

EXPLORING THALLIUM COMPOUNDS, CHEVREL
PHASES, AND OTHER CHALCOGENIDES AS
THERMOELECTRIC MATERIALS

A Dissertation

Presented to the Faculty of the Graduate School
of Cornell University

in Partial Fulfillment of the Requirements for the Degree of
Doctor of Philosophy

by

Michael Alan McGuire

August 2006

© 2006 Michael Alan McGuire

ALL RIGHTS RESERVED

EXPLORING THALLIUM COMPOUNDS, CHEVREL PHASES, AND OTHER CHALCOGENIDES AS THERMOELECTRIC MATERIALS

Michael Alan McGuire, Ph.D.

Cornell University 2006

In thermoelectric materials, the coupling between thermal and electrical currents allows for the direct conversion between heat and electricity. This makes possible the construction of refrigerators and electrical power generators with no moving parts which are compact, reliable, and vibration free. Devices made from the best materials for cooling near room temperature operate at only 10% of Carnot efficiency. This is significantly less efficient than a typical compressor based kitchen refrigerator, which operates at about 30% of the Carnot limit. Thermoelectric devices are currently used where the benefits of small size and/or dependability outweigh their cost in efficiency. It is clear that the development of widespread applications for thermoelectric devices must await the discovery of new materials with improved thermoelectric properties. In this dissertation, several experimental approaches to this problem are discussed. These include (1) new compounds containing the heavy element thallium, (2) the exploration of Chevrel phase materials for high temperature applications, (3) the search for new high symmetry materials, and (4) the chemical and physical manipulation of the properties of known thermoelectric materials. The investigations described in this work did not produce an improved thermoelectric material; however, they did lead to the discovery and characterization of many new compounds, some with interesting structural, electrical, and magnetic properties.

BIOGRAPHICAL SKETCH

Born on September 6, 1977 in Lawrenceburg, TN, Michael Alan McGuire is the second son of Bobby James McGuire and Roberta Edna McGuire. Although he can imagine enjoying science as a child, he mostly remembers fishing and playing with G.I. Joe figures. He has since outgrown action figures for the most part, but not fishing. He later, at about age 12, added hunting to his list of interests. Throughout high school and college Michael regularly enjoyed fishing and hunting squirrel, turkey, and deer. As a student at Lawrence County High School he was introduced to the wonders of physics and calculus by a teacher named Jerry Thomas. Michael seemed to have an aptitude for these subjects, and found them increasingly interesting. Somehow, the following year, he found himself at the University of Mississippi (Ole Miss) in Oxford, Mississippi, majoring in physics, and dating Laurel Elizabeth Qualls, who he met in high school and who was studying geology at the University of Tennessee at Martin. As an undergraduate his interest in physics (and Laurel) grew, and he was drawn towards theoretical elementary particle physics. However, his time working in the educational physics research group of Dr. Bruce Denardo studying the sinking of buoyant objects in bubbly water (which subsequently attracted some attention as a possible explanation for the disappearance of ships in the Bermuda Triangle, seriously) convinced him that experimental physics was the way to go. Having enjoyed his time at Ole Miss, and not knowing what else to do, Michael decided to stay there for two more years to earn a Master of Science degree in physics. During the summer between his senior year and first year of graduate school, he worked on an experiment with Dr. Lucien Cremaldi and Dr. Paul Rubinov, constructing and programming detectors for counting atmospheric muons. One afternoon Michael was electrocuted by a photomultiplier tube, and later began working as

a TA in optics and introductory physics labs. During his second year of graduate school he worked alongside a postdoc named Alem Teklu in the newly founded group of Dr. Veerle Keppens, building a probe for measuring the temperature dependence of the elastic constants of materials using the technique of resonant ultrasound spectroscopy. Although he found solid state physics research very interesting, and was not electrocuted while working in Dr. Keppens' lab, Michael wasn't sure of the direction he wanted to take after finishing his MS. As mysteriously as he had appeared at Ole Miss six years earlier, in the Fall of 2001 he found himself to be a graduate student in the physics department at Cornell University. Although it is probably not entirely coincidental that at the same time Laurel (*vide supra*) enrolled in graduate school at Syracuse University, just up the road. Near the end of his first year at Cornell, and thanks to the interdisciplinary nature of the physics program, he discovered Prof. Frank DiSalvo's research group in the Chemistry department next door, where he has spent a little over four years playing in the lab and researching thermoelectric materials. On May 31, 2003, Michael and Laurel were married, at the farm of his aunt Peggy Peppers, by her step-son Rev. Danny Huckaba. The ceremony took place within a few hundred yards of where he caught his first fish, and killed his first squirrel and his first deer. Upon completion of his PhD at Cornell, Michael will spend one year as a postdoctoral research associate in Prof. Robert Cava's group at Princeton University studying oxide superconductors, after which he will begin his appointment as a Wigner Fellow in the Materials Science and Technology Division at Oak Ridge National Laboratory.

to Laurel

ACKNOWLEDGEMENTS

As I sit down to write this, I feel the tremendous pressure of knowing that these Acknowledgements and the preceding Biographical Sketch are certainly the first parts (and likely the only parts) of this dissertation that will actually be read by other human beings, with the possible exception of my Committee. To further complicate matters, it is quite often the case that in attempting sincerity I achieve something that sounds more like sarcasm. So I make here the disclaimer that should sarcasm be detected by the reader in the following text it may be unintentional.

That being said, I am glad to have this opportunity to try to express my sincere appreciation to the many people who have helped make my time at Cornell both enjoyable and productive. At the top of that list, of course, is Prof. Francis J. DiSalvo. In addition, I am grateful to the other members of my Special Committee, Prof. Rob Thorne and Prof. Neil Ashcroft, for their time and effort.

It's hard to imagine a better research advisor than Frank. His unique mix of kindness, optimism, knowledge, and wisdom creates a research environment in which it is easy for students to flourish. There is a strong mutual trust between Frank and his group members, and I believe that this is an important part of the group culture. Because of this, much of our training comes from senior group members, which helps build trust and friendships among the students, postdocs, and visiting scientists, and is largely responsible for maintaining the groups high morale. As a result, there are many present and former group members who also deserve my thanks for making significant contributions to this work as well as for their friendship. Just as everyone who writes these sorts of things, I am sure that there are people who deserve to be mentioned here, but are, much to their

dismay, left out. It is up to the reader to decide whether such omissions were intentional or not.

I should start with Tom Reynolds. Tom was the first person I met in the group, and he taught me great deal about solid state chemistry and thermoelectrics, as well as many practical skills. One thing that comes to mind is that squirting acetone on suspect joints in a vacuum system (like the resistivity probe) is a handy way to find small leaks, but should not be used if clear fingernail polish was used to seal previous leaks. Tom was a good friend and teacher. Other members of the group who were invaluable during my formative years in the group include Chris Hoffmann, and Cora Lind, who were both very helpful around the lab, but about whom I have nothing particularly clever to say. Catherine "Catie" Oertel and Min "Fast Money" Yuan were and are good friends to me, and were pleasantly patient with my chemical ignorance. The same is true of Janet Hunting, whose kindness and helpfulness are rivaled only by Frank's. Dima Zherebtsov taught me a lot in the machine shop, and Craig Downie taught me to be suspicious of Texans. Yongkwan Dong dramatically increased my ability to make electrical contacts to small samples by teaching me to make a tiny "paint brush" by epoxying an eyelash to the end of a copper wire.

I enjoyed the opportunity to talk about physics, as well as gravy and biscuits, with "Angry" Mark Prochaska who occasional stopped by the office. I am also glad to have had the opportunity to get to know Neal Abrams. He has made several valiant attempts to help me understand his electrochemistry experiments, which do not go unappreciated. I am also grateful for the company he provided by moving into the instrument room, and for introducing me to the rock and roll music by changing the radio station. I also thank Neal and Jesse Reiherzer for helping me (and Laurel) out during a particularly frightening incident involving the tree nut which will not be named.

Laif Alden is the only graduate student who has been in the group for my entire time here. Although we never shared an office and we worked on different projects, Laif and I have much in common, and I consider him a true friend. He generally gets my references to *The Lord of the Rings* and *The Dark Tower*, and that means a lot to me. I spent three years sitting next to Mark Bailey, and by the end of that time I was able to understand up to about 70% of the things he said to me after he repeated it a couple of times. Mark is British and talks quietly and quickly. Mark is also a good chum, and patiently taught me how to do extended Hückel calculations, and how to think a little more like a chemist. He also introduced me to PG Tips, HobKnobs, and pepperoni and bacon pizza. Thanks, Mark.

I thank Chinmoy Ranjan for doing some DFT calculations for me, and Chandrani Roy Chowdhury for some good Indian cooking. I will remember them both for beating me (badly) at ping pong. I thank Francois Chevre for stimulating conversations about *Morrowind* and about butter, and for providing good cookies and liquor. Ali Schmidt is a vegan who spent a year or so working with me on Chevrel phase thermoelectrics. Even though she didn't eat animals or Oreo cookies, she was a good colleague and fun to work with.

Seriously, I have had only positive interactions with DiSalvo group members, present and past, and sincerely thank all of them (yes, including those not mentioned individually above) for contributing to my success and happiness at Cornell. I wish them all well in their lives and in their careers.

There are many other members of the Cornell community and collaborators from other institutions to whom I owe thanks. Kelly Case has been a good friend and is instrumental in almost everything that gets done in the group. I have left a few typos in this Dissertation just for her. Deb Hatfield's kindness and helpfulness, and especially her patience with my notoriously late forms, cer-

tainly do not go unappreciated. I also thank Emil Lobkovsky, John Hunt, John Sinnott, and other staff members of the chemistry and physics departments and CCMR, probably even Paul Mutolo. I am grateful for the opportunity to interact with excellent collaborators including Jeff Snyder and Franck Gascoin at JPL, Tom Scheidemantel and John Badding at Penn State, and Sami Malik at Diamond Innovations, Inc.

I thank my family, who have no idea what I've been doing or why I've been doing it, but who have been ever so supportive as they wait patiently for me to get a real job. Finally, I thank Laurel, for making me happy, and also for being my best friend for my five years at Cornell, as she will be for the rest of my life.

TABLE OF CONTENTS

1	Introduction to Thermoelectricity	1
1.1	Introduction to Thermoelectricity and the Thermoelectric Effects . . .	1
1.1.1	The Seebeck effect	1
1.1.2	The Peltier effect	3
1.1.3	The Thomson effect	4
1.2	Current Applications for Thermoelectric Devices	5
1.2.1	Cooling devices	7
1.2.2	Power generation devices	12
1.3	Survey of Thermoelectric Materials	16
1.3.1	Materials with high ZT at and below room temperature . . .	17
1.3.2	Materials with high ZT at high temperatures	22
1.4	Aims of This Work	32
	References	34
2	Theoretical Considerations	36
2.1	Thermodynamics of Coupled Flows	36
2.2	Device Equations and Efficiency	42
2.3	Bulk Materials	48
2.4	Low Dimensional Systems	59
2.5	Calculations of Thermoelectric Properties	61
2.6	Other Considerations for Devices	70
2.7	Comments about the Seebeck Coefficient	74
	References	80
3	Exploring Thallium Compounds as Thermoelectric Materials	82
3.1	Introduction and Motivation	83
3.2	General experimental details	85
3.3	Crystal Structures and Properties	89
3.3.1	$Tl_3Ti_2P_5S_{18}$	89
3.3.2	$Tl_2Cu_2SnS_4$	90
3.3.3	$Tl_5AgTi_6Se_{27}$	92
3.3.4	$Tl_3CuNb_2Se_{12}$	95
3.3.5	$Tl_2Cu_2SnTe_4$ and $Tl_2Ag_2SnTe_4$	100
3.3.6	$Tl_3Zr_{1.4}Sn_{1.6}Te_6$	103
3.3.7	$TlTiPS_5$	108
3.3.8	$Tl_2Au_2Sn_2Se_6$	109
3.3.9	$Tl_2TiCu_2S_4$ and $Tl_2TiCu_2Se_4$	117
3.3.10	$Tl_{1.71}Sn_{2.60}Bi_{7.71}Se_{15}$	117
3.3.11	$Tl_{11.5}Sb_{11.5}Cu_8Se_{27}$	133
3.4	Measured band gaps and comparisons between Tl and AM analogs	134

3.5	Tl coordination environments and lone pair activity	136
3.6	Conclusions	141
References		143
4	Tl₂AXTe₄ (A = Cd, Hg, Mn; X = Ge, Sn): Crystal Structure, Electronic Structure, and Thermoelectric Properties	145
4.1	Introduction	145
4.2	Experimental Details	146
4.3	Crystal Structure	152
4.4	Electronic Structure	158
4.5	Thermoelectric Properties: Tl ₂ AXTe ₄ A=Cd, Hg; X=Ge, Sn	168
4.6	Resistivity and Magnetization: Tl ₂ MnXTe ₄ X=Ge, Sn	174
4.7	Conclusions	176
References		177
5	Crystal Structure, Electronic Structure, and Thermoelectric Properties of AuTlSb: a New Pyrite Superstructure	179
5.1	Introduction	179
5.2	Experimental Details	180
5.3	Crystal Structure	186
5.4	Electronic Structure and Bonding	191
5.5	Thermopower and Electrical Resistivity	197
5.6	Conclusions	199
References		200
6	Chevrel Phase Thermoelectric Materials	202
6.1	Structure and Chemistry of Chevrel Phases	202
6.1.1	Mo ₆ Q ₈ compounds (Q = S, Se, Te)	206
6.1.2	Filled compounds of the type A _x Mo ₆ Q ₈	209
6.1.3	Cluster core substitutions: Mo _{6-x} M _x Q ₈	211
6.1.4	Substitutions on the Q sites: Mo ₆ Q _{8-y} X _y	212
6.2	Chevrel phase compounds as thermoelectric materials	212
6.2.1	Electronic structure of Chevrel phases	213
6.2.2	Thermoelectric properties of Chevrel phase compounds	215
6.2.3	Comparison of Cu _{3.1} Mo ₆ Se ₈ with other thermoelectric materials	219
6.3	Chevrel phase work at Cornell University	221
6.3.1	Previously reported work	222
6.3.2	Ti filled Chevrel phases	223
6.3.3	Synthesis of Ti _x Mo ₆ Se ₈	223
6.3.4	Structure and composition of Ti _x Mo ₆ Se ₈	224
6.3.5	TE properties of Ti _x Mo ₆ Se ₈	227

6.3.6	Discussion and Conclusions	230
References		232
7	Thermoelectric and structural properties of a new Chevrel phase:	
	Ti_{0.3}Mo₅RuSe₈	234
7.1	Introduction	234
7.2	Experimental	235
	7.2.1 Synthesis Methods	235
	7.2.2 Powder X-ray Diffraction	236
	7.2.3 Microprobe Analysis	237
	7.2.4 Property Measurements	237
7.3	Measured Compositions	238
7.4	Refined Crystal Structures of Mo ₅ RuSe ₈ and Ti _{0.3} Mo ₅ RuSe ₈	239
7.5	Thermoelectric Properties of Ti _{0.3} Mo ₅ RuSe ₈	243
7.6	Conclusions	245
References		247
8	Cu₄Mo₆Se₈: Synthesis, Crystal Structure, and Electronic Structure of a	
	New Chevrel Phase Structure-Type	248
8.1	Introduction	248
8.2	Experimental	249
	8.2.1 Synthesis Methods	249
	8.2.2 Characterization Techniques	252
	8.2.3 Electronic Structure Calculations	252
8.3	Results of Intercalation Studies	253
	8.3.1 Cu _x Mo ₆ S ₈	253
	8.3.2 Cu _x Mo ₆ Se ₈	254
	8.3.3 Cu _x Mo ₆ Te ₈	258
	8.3.4 Stability of Cu _x Mo ₆ Q ₈ (Q = S, Se) in Air	259
8.4	Crystal Structure of Cu ₄ Mo ₆ Se ₈	259
8.5	Electronic Structure of Triclinic Cu ₄ Mo ₆ Se ₈	268
8.6	Magnetic Susceptibility Measurements	275
8.7	Conclusions	275
References		278
9	Miscellaneous Materials	280
9.1	Introduction	280
9.2	The Layered Transition Metal Chalcogenides Ni ₃ Cr ₂ P ₂ S ₉ and	
	Ni ₃ Cr ₂ P ₂ Se ₉	281
	9.2.1 Discovery and synthesis of Ni ₃ Cr ₂ P ₂ Q ₉ (Q = S, Se)	283
	9.2.2 Crystal structure of Ni ₃ Cr ₂ P ₂ Se ₉	285
	9.2.3 Twinning and disorder in Ni ₃ Cr ₂ P ₂ Se ₉	293

9.2.4	Powder X-ray diffraction: $\text{Ni}_3\text{Cr}_2\text{P}_2\text{S}_9$ and $\text{Ni}_3\text{Cr}_2\text{P}_2\text{Se}_9$. . .	298
9.2.5	Thermoelectric properties	301
9.2.6	Magnetic properties of $\text{Ni}_3\text{Cr}_2\text{P}_2\text{S}_9$	303
9.2.7	Conclusions	316
9.3	Arsenic-Containing Bi_2Te_3 -Based Alloys	316
9.3.1	Synthesis of the Alloys	318
9.3.2	Powder X-ray Diffraction Results: Unit Cell Parameters . . .	320
9.3.3	Thermoelectric Properties	329
9.3.4	A Final Comment	333
9.3.5	Conclusions	335
9.4	High-Pressure, High-Temperature Treatment of PbTe	335
9.4.1	Conventional and HPHT synthesized PbTe	340
9.4.2	Effects of HPHT treatment of conventionally synthesized PbTe	345
9.4.3	Conclusion, comments, and future work with PbTe	348
	References	350
	10 Conclusions and Outlook for TE Materials Research	353

LIST OF TABLES

3.1	Single Crystal Refinement Data for $\text{Tl}_3\text{Zr}_{1.4}\text{Sn}_{1.6}\text{Te}_6$	106
3.2	Atomic Coordinates and Equivalent Isotropic Displacement Parameters for $\text{Tl}_3\text{Zr}_{1.4}\text{Sn}_{1.6}\text{Te}_6$	107
3.3	Anisotropic Displacement Parameters for $\text{Tl}_3\text{Zr}_{1.4}\text{Sn}_{1.6}\text{Te}_6$	108
3.4	Ruling out the subcell structure for $\text{Tl}_2\text{Au}_2\text{Sn}_2\text{Se}_6$	112
3.5	Single Crystal Refinement Data for $\text{Tl}_2\text{Au}_2\text{Sn}_2\text{Se}_6$	113
3.6	Atomic Coordinates and Equivalent Isotropic Displacement Parameters for $\text{Tl}_2\text{Au}_2\text{Sn}_2\text{Se}_6$	114
3.7	Anisotropic Displacement Parameters for $\text{Tl}_2\text{Au}_2\text{Sn}_2\text{Se}_6$	114
3.8	Single Crystal Refinement Data for $\text{Tl}_{1.71}\text{Sn}_{2.60}\text{Bi}_{7.71}\text{Se}_{15}$	125
3.9	Atomic Coordinates and Equivalent Isotropic Displacement Parameters for $\text{Tl}_{1.71}\text{Sn}_{2.60}\text{Bi}_{7.71}\text{Se}_{15}$	126
3.10	Anisotropic Displacement Parameters for $\text{Tl}_{1.71}\text{Sn}_{2.60}\text{Bi}_{7.71}\text{Se}_{15}$	127
3.11	Bond distances in $\text{Tl}_{1.71}\text{Sn}_{2.60}\text{Bi}_{7.71}\text{Se}_{15}$	128
3.12	Comparison of band gaps between Tl and alkali metal analogues.	137
3.13	Thallium - chalcogen bond distances.	139
4.1	Crystal data for $\text{Tl}_2\text{AGeTe}_4$	153
4.2	Crystal data for $\text{Tl}_2\text{ASnTe}_4$	154
4.3	Atomic positions and interatomic distances for $\text{Tl}_2\text{AGeTe}_4$	155
4.4	Atomic positions and interatomic distances for $\text{Tl}_2\text{ASnTe}_4$	156
4.5	Band gaps of Tl_2AXTe_4	169
5.1	Single Crystal Refinement Data for AuTlSb	184
5.2	Atomic Coordinates and Equivalent Isotropic Displacement Parameters for AuTlSb	185
5.3	Anisotropic Displacement Parameters for AuTlSb	185
5.4	Interatomic distances in AuTlSb	190
6.1	Measured compositions of $\text{Ti}_x\text{Mo}_6\text{Se}_8$ samples	227
7.1	Agreement Factors and Unit Cells for Mo_5RuSe_8 and $\text{Ti}_{0.3}\text{Mo}_5\text{RuSe}_8$	241
7.2	Atomic Coordinates for Mo_5RuSe_8 and $\text{Ti}_{0.3}\text{Mo}_5\text{RuSe}_8$	241
7.3	Interatomic distances in Mo_5RuSe_8 and $\text{Ti}_{0.3}\text{Mo}_5\text{RuSe}_8$	242
8.1	Single Crystal Refinement Data for $\text{Cu}_4\text{Mo}_6\text{Se}_8$	261
8.2	Atomic Coordinates and Equivalent Isotropic Displacement Parameters for $\text{Cu}_4\text{Mo}_6\text{Se}_8$	262
8.3	Anisotropic Displacement Parameters for $\text{Cu}_4\text{Mo}_6\text{Se}_8$	262
8.4	Interatomic distances in $\text{Cu}_4\text{Mo}_6\text{Se}_8$	267
8.5	Continuous symmetry measures for Chevrel phases	269
9.1	Single Crystal Refinement Data for $\text{Ni}_3\text{Cr}_2\text{P}_2\text{Se}_9$	286

9.2	Atomic Coordinates and Equivalent Isotropic Displacement Parameters for $\text{Ni}_3\text{Cr}_2\text{P}_2\text{Se}_9$	287
9.3	Anisotropic Displacement Parameters for $\text{Ni}_3\text{Cr}_2\text{P}_2\text{Se}_9$	288
9.4	Bond valence sums for $\text{Ni}_3\text{Cr}_2\text{P}_2\text{Se}_9$	292
9.5	Dependence of R values on atom assignments in $\text{Ni}_3\text{Cr}_2\text{P}_2\text{Se}_9$. . .	293
9.6	Bi_2Te_3 based alloy compositions	318
9.7	Bi_2Te_3 based alloy unit cells	325

LIST OF FIGURES

1.1	Illustration of the Peltier effect	4
1.2	Temperature measurement with a thermocouple	6
1.3	Diagram of a Peltier cooler	8
1.4	Photo of a commercial Peltier cooler	8
1.5	COP of a thermoelectric cooler	10
1.6	Diagram of a thermoelectric generator	13
1.7	Efficiency of a thermoelectric generator	14
1.8	Minimum S required to realize a particular ZT value	17
1.9	Good low temperature thermoelectric materials	18
1.10	Crystal structure of Bi_2Te_3	20
1.11	Crystal structure of CsBi_4Te_6	21
1.12	Good high temperature thermoelectric materials	23
1.13	Crystal structure of PbTe	24
1.14	Crystal structure of Si-Ge alloys	26
1.15	Skutterudite structure type	28
1.16	Half-Heusler structure type	29
1.17	Crystal structure of $\text{Yb}_{14}\text{MnSb}_{11}$	31
2.1	Diagram of a couple used to understand the thermoelectric effects	40
2.2	A schematic of a Peltier cooling couple.	44
2.3	A schematic of a TE generator	47
2.4	Umklapp scattering	56
2.5	Calculated doping dependence of the TE properties of Bi_2Te_3	65
2.6	Calculated transport distribution and TE properties of doped Bi .	67
2.7	Transient supercooling caused by current pulses.	73
2.8	A model for the high Seebeck coefficient in cobaltites.	79
3.1	The crystal structure of $\text{Tl}_3\text{Ti}_2\text{P}_5\text{S}_{18}$	90
3.2	Absorbance spectrum of $\text{Tl}_3\text{Ti}_2\text{P}_5\text{S}_{18}$	91
3.3	The crystal structure of $\text{Tl}_2\text{Cu}_2\text{SnS}_4$	92
3.4	Thermal conductivity of several thallium chalcogenides.	93
3.5	The crystal structure of $\text{Tl}_5\text{AgTi}_6\text{Se}_{27}$	94
3.6	Absorbance spectrum of $\text{Tl}_5\text{AgTi}_6\text{Se}_{27}$	96
3.7	The crystal structure of $\text{Tl}_3\text{CuNb}_2\text{Se}_{12}$	97
3.8	Resistivity of $\text{Tl}_3\text{CuNb}_2\text{Se}_{12}$	98
3.9	Absorbance spectrum of $\text{Tl}_3\text{CuNb}_2\text{Se}_{12}$	99
3.10	The crystal structure of $\text{Tl}_2\text{Ag}_2\text{SnTe}_4$	101
3.11	The crystal structure of $\text{Tl}_2\text{Cu}_2\text{SnTe}_4$	102
3.12	Resistivity and thermopower of $\text{Tl}_2\text{Cu}_2\text{SnTe}_4$	104
3.13	The crystal structure of $\text{Tl}_3\text{Zr}_{1.4}\text{Sn}_{1.6}\text{Te}_6$	107
3.14	The crystal structure of TlTiPS_5	108
3.15	Resistivity and thermopower of TlTiPS_5	110
3.16	The crystal structure of $\text{Tl}_2\text{Au}_2\text{Sn}_2\text{Se}_6$	111

3.17	Difference peaks in $\text{Tl}_2\text{Au}_2\text{Sn}_2\text{Se}_6$	115
3.18	Absorbance spectrum of $\text{Tl}_2\text{Au}_2\text{Sn}_2\text{Se}_6$	116
3.19	PXRD patterns from $\text{Tl}_2\text{TiCu}_2\text{S}_4$ and $\text{Tl}_2\text{TiCu}_2\text{Se}_4$	118
3.20	The crystal structure of $\text{Tl}_2\text{TiCu}_2\text{S}_4$ and $\text{Tl}_2\text{TiCu}_2\text{Se}_4$	119
3.21	Absorbance spectra of $\text{Tl}_2\text{TiCu}_2\text{S}_4$ and $\text{Tl}_2\text{TiCu}_2\text{Se}_4$	120
3.22	The crystal structure of $\text{Tl}_{1.71}\text{Sn}_{2.60}\text{Bi}_{7.71}\text{Se}_{15}$	123
3.23	A perspective view of the crystal structure of $\text{Tl}_{1.71}\text{Sn}_{2.60}\text{Bi}_{7.71}\text{Se}_{15}$	124
3.24	Measured thermoelectric properties of $\text{Tl}_{1.71}\text{Sn}_{2.60}\text{Bi}_{7.71}\text{Se}_{15}$	132
3.25	The crystal structure of $\text{Tl}_{11.5}\text{Sb}_{11.5}\text{Cu}_8\text{Se}_{27}$	134
3.26	Resistivity and thermopower of $\text{Tl}_{11.5}\text{Sb}_{11.5}\text{Cu}_8\text{Se}_{27}$	135
3.27	Thallium coordination environments.	138
3.28	Visualizing the lone pairs on Tl^{1+}	140
4.1	Powder X-ray diffraction patterns for Tl_2AXTe_4	149
4.2	Crystal structure of Tl_2AXTe_4	157
4.3	Comparison the electronic structures of KInTe_2 and TlInTe_2	160
4.4	Calculated band structures of $\text{Tl}_2\text{ASnTe}_4$	161
4.5	Calculated band structures of $\text{Tl}_2\text{AGeTe}_4$	161
4.6	Density of states for $\text{Tl}_2\text{CdSnTe}_4$	162
4.7	Density of states for $\text{Tl}_2\text{HgSnTe}_4$	163
4.8	Density of states for $\text{Tl}_2\text{MnSnTe}_4$	164
4.9	Density of states for $\text{Tl}_2\text{CdGeTe}_4$	165
4.10	Density of states for $\text{Tl}_2\text{HgGeTe}_4$	166
4.11	Density of states for $\text{Tl}_2\text{MnGeTe}_4$	167
4.12	Thermoelectric properties of Tl_2AXTe_4	170
4.13	Fits to the resistivity of Tl_2AXTe_4	171
4.14	Thermoelectric properties of doped $\text{Tl}_2\text{HgXTe}_4$	173
4.15	Magnetic susceptibility of $\text{Tl}_2\text{MnGeTe}_4$	175
5.1	Comparing the structures of AuSb_2 and AuTlSb	188
5.2	Ordering of the dimers in AuTlSb	189
5.3	Au coordination in AuTlSb	191
5.4	Band structure and DOS for AuTlSb	192
5.5	Band structure and DOS for AuSb_2	193
5.6	Calculated COOPs for AuTlSb	195
5.7	Calculated COOPs for AuSb_2	196
5.8	Resistivity and thermopower of AuTlSb	198
6.1	Views of the Chevrel phase cluster M_6Q_8	204
6.2	3-D network in Chevrel phases	205
6.3	Cavities in Chevrel phases	207
6.4	Known filling atoms for Chevrel phases	210
6.5	Locations of A atoms in $\text{A}_x\text{Mo}_6\text{Se}_8$	210
6.6	Molecular orbitals of the Mo_6Se_8 cluster	213
6.7	Band structure and DOS for Mo_6Se_8	214

6.8	TE properties of some Chevrel phases	217
6.9	TE properties of good high temperature thermoelectrics	220
6.10	Comparing $\text{Si}_{0.7}\text{Ge}_{0.3}$ and $\text{Cu}_{3.1}\text{Mo}_6\text{Se}_8$	221
6.11	Powder X-ray diffraction from $\text{Ti}_x\text{Mo}_6\text{Se}_8$	226
6.12	Thermoelectric properties of $\text{Ti}_x\text{Mo}_6\text{Se}_8$	228
6.13	Thermal conductivity of $\text{Ti}_{0.95}\text{Mo}_6\text{Se}_8$	230
7.1	Rieveld refinements for Mo_5RuSe_8 and $\text{Ti}_{0.3}\text{Mo}_5\text{RuSe}_8$	240
7.2	The Chevrel phase framework	243
7.3	Thermoelectric properties of $\text{Ti}_{0.3}\text{Mo}_5\text{RuSe}_8$	244
8.1	Copper intercalation apparatus	251
8.2	Intercalation of $\text{Cu}_2\text{Mo}_6\text{Se}_8$ made at 900 °C: PXRD	255
8.3	Intercalation of $\text{Cu}_2\text{Mo}_6\text{Se}_8$ made at 1200 °C: PXRD	257
8.4	Sheets in the structure of $\text{Cu}_4\text{Mo}_6\text{Se}_8$	263
8.5	Columns in the structure of $\text{Cu}_4\text{Mo}_6\text{Se}_8$	264
8.6	Coordination and displacement ellipsoids in $\text{Cu}_4\text{Mo}_6\text{Se}_8$	265
8.7	DFT band structure for $\text{Cu}_4\text{Mo}_6\text{Se}_8$	270
8.8	DFT DOS for $\text{Cu}_4\text{Mo}_6\text{Se}_8$	271
8.9	Calculated molecular orbitals for Mo_6Se_8 clusters	273
8.10	Evolution of bands from MOs in $\text{Cu}_4\text{Mo}_6\text{Se}_8$	274
8.11	Magnetic susceptibility of $\text{Cu}_x\text{Mo}_6\text{Se}_8$	276
9.1	PXRD of CrPS_4	283
9.2	Crystal structure of $\text{Ni}_3\text{Cr}_2\text{P}_2\text{Se}_9$	290
9.3	Coordination environments in $\text{Ni}_3\text{Cr}_2\text{P}_2\text{Se}_9$	291
9.4	Twinning in $\text{Ni}_3\text{Cr}_2\text{P}_2\text{Se}_9$	295
9.5	Difference peaks in $\text{Ni}_3\text{Cr}_2\text{P}_2\text{Se}_9$	296
9.6	Disorder in $\text{Ni}_3\text{Cr}_2\text{P}_2\text{Se}_9$	297
9.7	Powder patterns from $\text{Ni}_3\text{Cr}_2\text{P}_2\text{Q}_9$	299
9.8	Thermoelectric properties of $\text{Ni}_3\text{Cr}_2\text{P}_2\text{Q}_9$	304
9.9	Single crystal sample holder for the SQUID	307
9.10	M vs. H curves for $\text{Ni}_3\text{Cr}_2\text{P}_2\text{S}_9$ powder	308
9.11	Magnetic susceptibility of $\text{Ni}_3\text{Cr}_2\text{P}_2\text{S}_9$ powder	309
9.12	M vs. H curves for $\text{Ni}_3\text{Cr}_2\text{P}_2\text{S}_9$ crystals	311
9.13	Magnetic susceptibility of $\text{Ni}_3\text{Cr}_2\text{P}_2\text{S}_9$ crystals	312
9.14	Possible spin configurations in $\text{Ni}_3\text{Cr}_2\text{P}_2\text{S}_9$	315
9.15	Crystal structure of Bi_2Te_3	319
9.16	PXRD of $\text{Bi}_2\text{Te}_3\text{-Sb}_2\text{Te}_3\text{-Sb}_2\text{Se}_3\text{-As}_2\text{Te}_3$ alloys	322
9.17	PXRD of $\text{Bi}_2\text{Te}_3\text{-Sb}_2\text{Te}_3\text{-Sb}_2\text{Se}_3\text{-As}_2\text{Te}_3$ alloys	323
9.18	PXRD of $\text{Bi}_2\text{Te}_3\text{-Sb}_2\text{Te}_3\text{-As}_2\text{Te}_3$ alloys	324
9.19	Bi_2Te_3 based alloy unit cells	326
9.20	Selected diffraction peaks from Bi_2Te_3 alloys	330
9.21	Measured S of Bi_2Te_3 based alloys	332
9.22	Measured ρ of Bi_2Te_3 based alloys	333

9.23	Power factor of Bi_2Te_3 based alloys	334
9.24	Crystal structure of PbTe	336
9.25	Reported improvement in TE properties of PbTe	338
9.26	Pb-Te phase diagram	339
9.27	TE properties of HPHT synthesized PbTe	342
9.28	Composition maps of PbTe samples	344
9.29	Composition map of cast PbTe after HPHT	345
9.30	TE properties of HPHT treated PbTe	346
9.31	TE properties of annealed HPHT treated PbTe	347
9.32	Lattice thermal conductivity of PbTe samples	348

Chapter 1

Introduction to Thermoelectricity

1.1 Introduction to Thermoelectricity and the Thermoelectric Effects

Thermoelectricity describes the conversion between thermal energy and electrical energy. The coupling between the currents (flows) of these two types of energy is the source of thermoelectric phenomena. Electrical currents are carried by charged particles, electrons and/or holes. If any amount of entropy is associated with these particles a flow of heat will accompany the flow of charge. The manifestation of this coupling is described by three effects named for pioneers of thermoelectric research, Seebeck, Peltier, and Thomson (later Lord Kelvin). In what follows we will address each of these effects in turn.

1.1.1 The Seebeck effect

This effect was first described by Thomas Johann Seebeck in 1822 [1]. He constructed a closed loop made of two different metals and heated one of the two junctions. A compass needle around which the loop was wound deflected. Heating the junction created a magnetic field which exerted a torque on the magnetized needle. The immediate conclusion drawn by a student of science today is that the temperature gradient caused an electrical current to flow in the loop, generating a magnetic field. However, Seebeck drew a different analogy. He suspected that the source of the magnetic field generated by the temperature difference between the junctions must be related to the source of the earth's magnetic field, which he therefore concluded to be generated by the temperature difference

between the poles and the equator. Although his explanation of his observations was wrong, this was an important experimental discovery. It now bears his name, the Seebeck effect.

The term Seebeck effect is used to describe several different phenomena, or at least several different experimental arrangements in which it is realized. The first is that described above and observed first by Seebeck himself. An electromotive force (and thus an electrical current) is generated in a closed loop made of two different materials when a temperature difference exists between the two junctions. The second situation, closely related to the first, is an open circuit made from two different materials with a temperature difference between the junction and the open ends. In this case no current flows, but a voltage can be measured at the break in the circuit. The third situation is a single material between the ends of which a temperature difference exists. In this case a voltage difference is generated across the material. Clearly these three examples are intimately related and are all described by the same physics.

The third situation is the simplest since it involves only a single material. In this case the Seebeck coefficient S of the material is the ratio of the potential difference to the temperature difference across the sample: $S = \Delta V / \Delta T$. However, measuring ΔV requires attaching leads to the ends of the sample, creating two junctions between dissimilar materials and creating the second situation described above. Now a temperature difference exist across the sample and across the leads, and the measured voltage is $\Delta V = (S_{sample} - S_{leads}) \Delta T$. So only the difference between the Seebeck coefficient of the sample and that of the leads can be measured by this experiment. One must know S_{leads} to determine S_{sample} . It turns out that superconductors have $S = 0$ in the superconducting state (there is no entropy associated with the current in the superconducting ground state [2]). So measuring S using superconducting leads eliminates this problem; however,

such a measurement is not often practical. We will see below in our discussion of the Thomson effect that there are other measurements which can determine S without reference to a second material.

The Seebeck effect is the basis for thermocouples and thermoelectric power generation devices which will be described in the following Sections. We will see in the following Chapter that the Seebeck coefficient measures how much heat is carried by an electrical current in a material. Thinking of S in this way will make clear the relationships between S and the Peltier and Thomson coefficients described below. We also note that the sign or direction of the electrical current associated with a particular thermal current depends on the sign of the charge carriers. As a result, S is positive for holes and negative for electrons, and the measurement of S can be used to determine the sign of the dominant charge carriers in a material.

1.1.2 The Peltier effect

In about 1835, Jean Charles Athanase Peltier passed an electrical current through a junction between two dissimilar metals. He observed that the temperature of the junction changed in response to the current [3]. This effect was reversible. The direction of the current flow through the junction determined whether heat was absorbed or evolved. The Peltier coefficient Π is defined as the ratio of the rate of heat production Q to the electrical current I : $\Pi=Q/I$.

The connection between Π and the Seebeck coefficient S is straightforward. Different materials have different values of S , and so carry different amounts of heat with the same electrical current. If a junction is made between these two materials and a current I passed through it, the amount of heat brought into the junction by one material will not match the amount of heat carried away by the

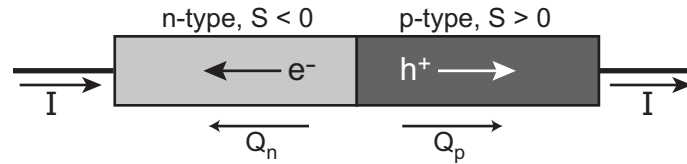


Figure 1.1: A diagram illustrating the Peltier effect at a junction between an n-type and p-type material. The arrows show the direction of the electrical current I , the electrons and holes, and the heat currents Q . The junction is cooled since both materials carry heat away from it.

other. Thus there will be a net amount of heat Q either dumped into or drawn away from the junction. The magnitude of Q (and therefore Π) will be proportional to the difference between the Seebeck coefficients of the two materials. This gives the relationship $Q \propto S_1 - S_2$. The largest Peltier heats are produced at the junction between two materials with Seebeck coefficients of opposite signs, since they are then carrying heat in opposite directions (see Figure 1.1).

The Peltier effect makes possible the construction of thermoelectric devices which act as heat pumps or refrigerators, as described later in this Chapter.

1.1.3 The Thomson effect

The final thermoelectric effect to be discussed is the Thomson effect. Unlike the Seebeck and Peltier effects, the description of the Thomson effect refers only to a single material. The effect was predicted and subsequently observed experimentally by William Thomson, after his explanation of the relationships between the Seebeck and Peltier effects [4]. If an electrical current I passes through a material in which a temperature gradient dT/dx exists, an amount of heat per unit volume Q is generated or absorbed along the length of the material. The Thomson coefficient τ is defined by $Q = \tau I (dT/dx)$. The reason that the Thomson heat is generated is that S for a particular material is temperature dependent.

Since S depends upon T , material in a temperature gradient can be viewed as a series of an infinite number of junctions between segments with different values of S . At each “junction” a Peltier heat is generated. The amount of heat per unit length will depend on how quickly S varies with position (dS/dx), and so $\tau \propto dS/dT$ (in fact, $\tau = TdS/dT$). In addition, thermodynamics demands that $S \rightarrow 0$ as $T \rightarrow 0$. So experimental measurements of $\tau(T)/T$ can be integrated from $T=0$ up to T to give $S(T)$ for a single material, without the use of a reference material.

The Thomson heat is generally small since S usually varies only slowly with temperature. This heat is typically neglected when modeling thermoelectric devices like those described in the following Sections and Chapter.

1.2 Current Applications for Thermoelectric Devices

Current thermoelectric materials research focuses on finding new materials from which to construct devices for cooling or power generation applications. However, the most important and widespread application of thermoelectricity is its use for measuring a temperature difference in the form of a thermocouple. In fact, thermocouples are used almost universally for the temperature measurements required for the characterization of thermoelectric materials. Therefore, before describing thermoelectric refrigerators and power generators, a brief explanation of how a temperature measurement is performed using a thermocouple is in order.

The diagram in Figure 1.2 shows how a temperature measurement is made using a thermocouple. The contact between materials A and B are made in the region at temperature T which is to be measured. The other ends of legs A and B are then each connected to material C at a reference temperature T_0 . The wires

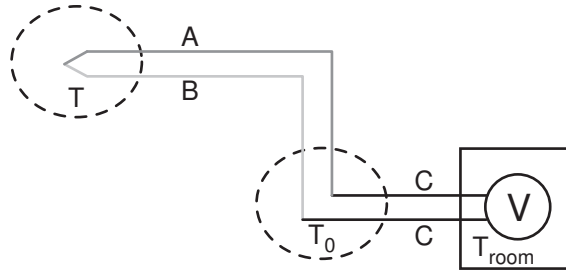


Figure 1.2: A diagram of the setup used for the measurement of temperature T using a thermocouple made of materials A and B . Material C connects the voltmeter V at room temperature to materials A and B at reference temperature T_0 .

of material C are then connected to the voltmeter V at room temperature. The measured voltage ΔV is then given by Equation 1.1.

$$\begin{aligned}\Delta V &= \int_{T_{room}}^{T_0} S_C dT + \int_{T_0}^T S_A dT + \int_T^{T_0} S_B dT + \int_{T_0}^{T_{room}} S_C dT \quad (1.1) \\ &= \int_{T_0}^T (S_A - S_B) dT\end{aligned}$$

The result is independent of T_{room} and material C . Knowledge of the $S_A(T)$ and $S_B(T)$, or even just the difference $S_A(T) - S_B(T)$, can be used to determine T from the measured value of ΔV . The reference junction at T_0 is often made in an ice point reference apparatus, which interestingly uses a thermoelectric device and feedback mechanism to maintain the temperature of an oil bath at 0°C . High precision measurements also require special isothermal connections at the voltmeter to ensure that T_{room} is the same for both legs.

When less precise temperature measurements are acceptable, such as in most high temperature furnaces, the reference junction (see Figure 1.2) can be omitted and room temperature used as a reference, leading to measurement errors on the order of the fluctuations of the ambient temperature. Another modi-

fication commonly employed for high temperature applications is the use of “extension grade” thermocouple wires. Often thermocouple wire used at high temperatures are expensive (for example Pt and a Pt/Rh alloy make up so called S-type thermocouples), and wires reaching from the furnace all the way to the temperature controller can be costly. Once these wires have reached far enough away from the furnace to be at a temperature that is near room temperature, they can be connected to less expensive wires which have been designed to have the same values of S at room temperature. These extensions then extend the rest of the way to the temperature controller. Extension grade wires are often made of copper that has been alloyed with various other metals to tune the Seebeck coefficient to match a particular value.

1.2.1 Cooling devices

Thermoelectric devices which act as heat pumps or refrigerators can be constructed according to Figure 1.3. Such a device takes advantage of the Peltier heat absorbed at a junction between an n-type and p-type material. The direction of the current is chosen so that in both legs the charge carriers, and therefore heat, are carried away from the junction. A real device is made up of many (sometimes hundreds) of these couples connected in series. A photograph of a small, commercially available Peltier cooling device is shown in Figure 1.4.

The efficiency of such a device depends on what materials are chosen for the two legs of the couple. This will be treated in detail in the following Chapter of this work. There we will see that the utility of a material for thermoelectric application increases with the parameter called the dimensionless thermoelectric figure of merit, symbolized by ZT and defined in Equation 1.2.

$$ZT = \frac{S^2 T}{\rho \kappa} \quad (1.2)$$

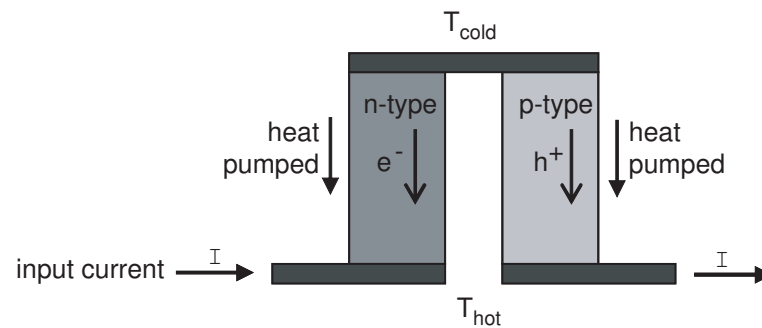


Figure 1.3: A schematic of a Peltier cooling device made from a junction between an n-type and a p-type material. The direction of the current is chosen so that heat is carried away from the cooler side at T_{cold} toward the hotter side at T_{hot} .

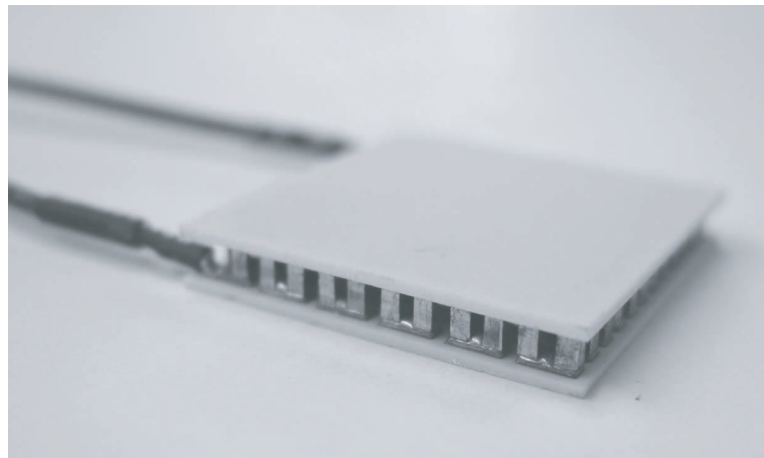


Figure 1.4: A photograph of a commercial Peltier cooling device. Note the pairs of legs, like those shown in Figure 1.3, connected in series.

Here S is the Seebeck coefficient, ρ is the electrical resistivity, κ is the thermal conductivity, and T is the absolute temperature. This dependence of thermoelectric efficiency on these three parameters is easy to understand. Large values of S lead to large Peltier heats. Small resistivities minimize the energy lost to Joule heating. Small thermal conductivities minimize the amount of “back conduction” of heat from the hot side to the cold side. Combined these lead to high ZT and efficient devices.

The dependence of thermoelectric efficiency on ZT will be derived in Chapter 2, where we will see that the Carnot efficiency is approached as $ZT \rightarrow \infty$. Figure 1.5 shows the coefficient of performance (the maximum value of the ratio of the heat pumped from the cold side to the input electrical power) for a thermoelectric cooler operating between $T_{hot} = 325$ K and various values for T_{cold} as a function of ZT . Carnot limits for these cases ($=T_{cold}/\Delta T$) are also listed on the plots. Note that for low ZT , the amount of heat pumped from cold to hot is smaller than the heat conducted from hot to cold, so $COP < 0$.

A good source of information about thermoelectric cooling applications is the web page of Marlow Industries (www.marlow.com). The company was recently acquired by II-VI Incorporated. Their single stage modules typically cool from about room temperature down to near -40 °C, or from 50 °C down to about -25 °C. Cooling to lower temperatures is realized in their multistage coolers, which can typically achieve $\Delta T_{max} = 80-120$ °C. Here we will review some of the applications in which Marlow’s thermoelectric coolers have been employed.

- Infrared sensors operate with higher sensitivity at lower temperatures, due simply to the suppression of thermal noise. Since thermoelectric coolers are small and vibration free (they have no moving parts), they are ideally

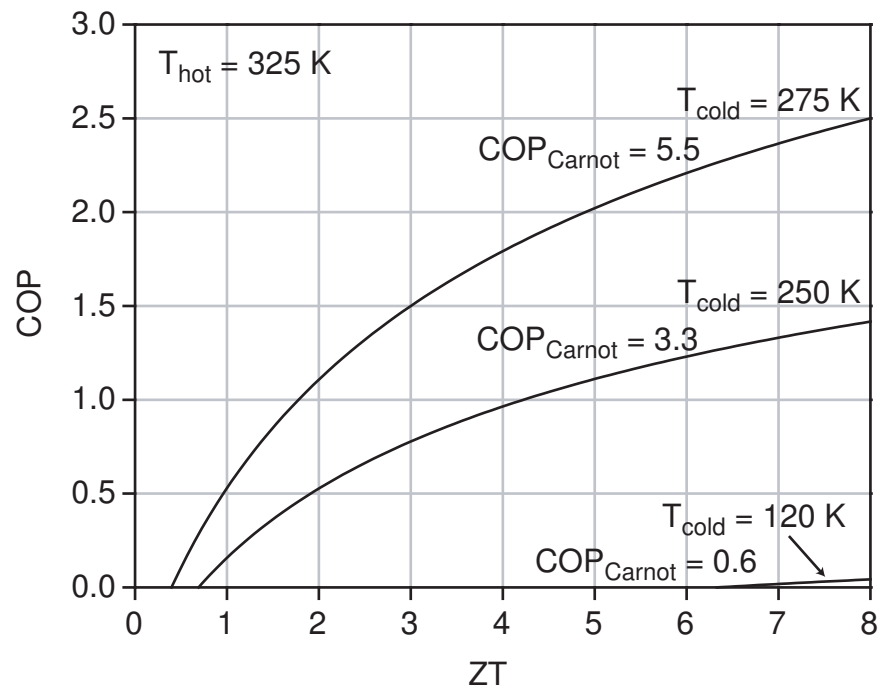


Figure 1.5: A plot of the coefficient of performance of a thermoelectric cooler versus the figure of merit ZT .

suiting for this application. They are used in night vision apparatuses by the military and by firefighters.

- High powered lasers used by the military require accurate temperature control close to room temperature. Thermoelectric modules are employed because they can be used for both cooling and heating (by reversing the direction of the current I in Figure 1.3).
- Thermoelectric coolers are used for refrigeration onboard the space station and shuttles, due to restrictions regarding freon and oils in the space environment.
- The LCD displays used in commercial aviation require brightness and contrast control to maintain readability over a wide range of ambient lighting conditions, from above the clouds in the daytime to on the ground at night. The backlighting for these displays is often produced by a Mercury vapor tube. The amount of vapor in the tube, and therefore the brightness of the backlight, is controlled by condensing or vaporizing Mercury on a spot in the tube which is temperature controlled using a thermoelectric device.
- In the biological and medical fields, thermoelectric devices are routinely used for temperature control. This includes controlling the temperature of columns used for high precision liquid chromatography, and the gels used for protein separation by electrophoresis. They are also used to control the temperature (heating and cooling) of liquid circulated through therapy pads and blankets. The quiet, maintenance free operation of thermoelectric modules is important for this application.
- The telecommunications industry uses small reliable thermoelectric devices to control the temperature of components like laser diodes.

- Thermoelectric devices are also used by the automobile industry for temperature controlled cup holders and seats, and by several companies which produce portable picnic coolers powered by automobile cigarette lighters.

The advantages of thermoelectric devices for heating and cooling applications are clear. They are compact and reliable, providing spot cooling or heating for temperature control. They have no moving parts, which makes them reliable and also vibration free. They are also electronically quiet, powered by a dc supply. The major disadvantage of thermoelectric devices (including the power generation devices which are addressed in the following Sections) is their low efficiencies. Typically these modules operate at about 10% of Carnot efficiency ($ZT \approx 1$ in Figure 1.5). For comparison, a compressor based home refrigeration unit operates at about 30% of Carnot efficiency [5]. Thermoelectric materials with $ZT \approx 4$ would be needed to match this. Thermoelectric devices are used in applications in which their advantages outweigh their cost in efficiency.

1.2.2 Power generation devices

Thermoelectric couples can also be used to generate electricity. This is illustrated in Figure 2.3. If one side is held at temperature T_{hot} and the other at a lower temperature T_{cold} , heat will flow through the legs, forcing oppositely charged carriers in opposite directions. This results in a net electrical current through an external load. A thermoelectric power generator is similar to a thermocouple, but the Seebeck voltage generated by the temperature difference is used to drive a current through a load. As in thermoelectric coolers, and for the same reasons, materials with high ZT (Equation 1.3) are needed for efficient thermoelectric generators.

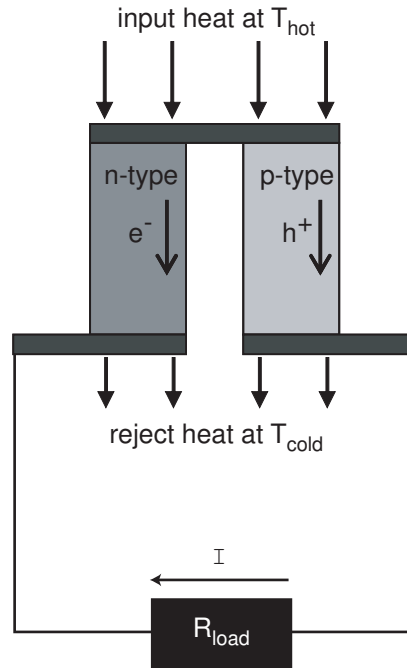


Figure 1.6: A Schematic of a thermoelectric power generation device made from a junction between an n-type and a p-type material.

Under optimal operating conditions (when the resistance of the load is equal to the internal resistance of the thermoelectric device) the efficiency of the generator is denoted by η^* , and is defined as the ratio of the power generated to the heat extracted from the hot reservoir. The Carnot limit for this efficiency is equal to $\Delta T/T_{hot}$. A plot showing the dependence of the efficiency of a thermoelectric generator on ZT is shown in Figure 1.7. The Carnot limit is approached as $ZT \rightarrow \infty$

There are two general classes of heat sources used to drive these devices. One is waste heat generated by some other process, like internal combustion engines or the stacks of industrial plants. The other is heat generated solely to run the device, such as heat from radioactive decay or a gas flame.

NASA uses thermoelectric modules to power instruments onboard space probes which are too far from the sun to use solar energy [6]. The heat source

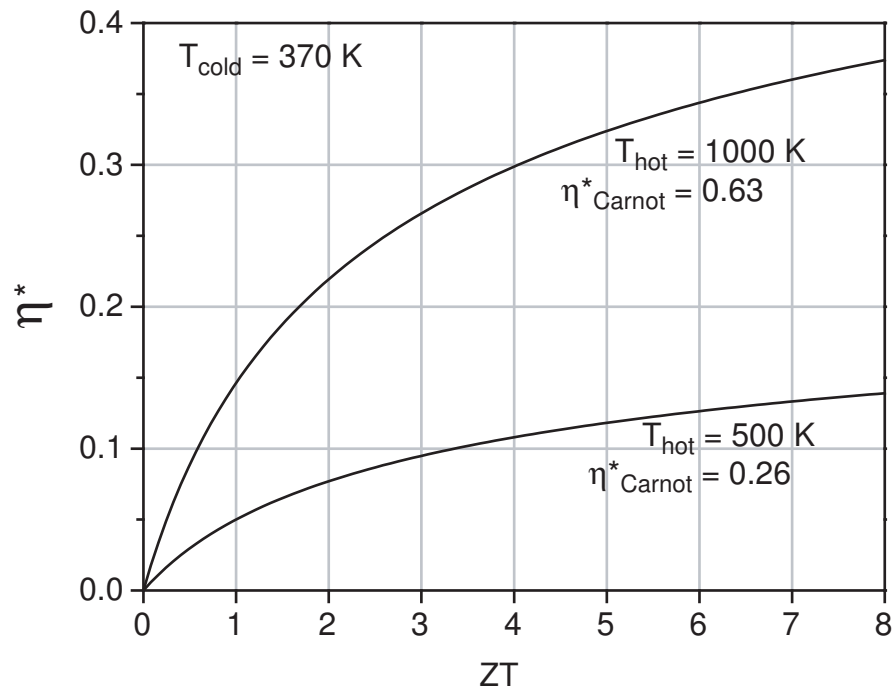


Figure 1.7: A plot of the dependence of the optimized efficiency η^* of a thermoelectric generator on the figure of merit ZT .

in these devices is the radioactive decay of a Pu containing material which is absorbed by a shielding layer, passed through the thermoelectric modules, and then radiated into space by fins attached to the cold side. The other common application for these devices is powering instruments in remote locations on earth, where solar power is not available or reliable enough. This includes natural gas pipeline monitoring stations, where a small amount of the gas is burned to generate heat to power the monitoring and communication instruments.

An area in which thermoelectric power generators have great potential but have not seen widespread use is waste heat recovery [6]. This is an attractive application since the thermal energy is “free”. When used, for example, to generate electricity using waste heat from an industrial plant’s smoke stacks, the efficiency of the devices need only be high enough to pay for the cost of the modules and their installation and maintenance. This technology also has the potential to significantly increase the efficiency of automobile engines, which generate tens of kilowatts of waste heat. Recovering even a small portion of this energy to power electronic components could decrease the load on the alternator, or even eliminate the need for an alternator, increasing the fuel efficiency of the vehicle. However, the added weight of the thermoelectric generator must be taken into account in this case. At this time, the performance and costs of these devices for automotive application is not well understood.

Regardless of the application, materials with high values of ZT are vital for any thermoelectric device (for cooling or power generation). In the following section, we will review a selection of known materials which show promising thermoelectric performance.

1.3 Survey of Thermoelectric Materials

In this Section we will give a brief review of some of the materials and classes of materials that are known to have good thermoelectric properties. We will begin by defining good thermoelectric properties by recalling the dimensionless thermoelectric figure of merit ZT , upon which thermoelectric efficiency depends. This parameter was introduced in the previous Section, and its relationship to efficiency (higher ZT gives higher efficiency) will be derived in the Chapter 2. For a material with Seebeck coefficient S , electrical resistivity ρ , and thermal conductivity κ , the thermoelectric figure of merit is given by

$$ZT = \frac{S^2 T}{\rho \kappa} = \frac{S^2 T}{\rho (\kappa_L + \kappa_{el})}. \quad (1.3)$$

We have split the total thermal conductivity into contributions from the lattice (subscript L) and from the electrical charge carriers (subscript el). The Wiedemann-Franz law relates κ_{el} and ρ through the equation $\kappa_{el} \rho = L_0 T$ where T is the absolute temperature and L_0 is a constant [2]. Good thermoelectric materials are those with high Seebeck coefficients, low electrical resistivities, and low lattice thermal conductivities. Current good thermoelectric materials have $ZT \approx 1$ at their optimal operating temperature.

Using the Wiedemann-Franz law, a relationship between a material's maximum ZT and its Seebeck coefficient can be derived, as shown in Eq. 1.4.

$$ZT = \frac{S^2 T}{\rho \kappa_{el} (1 + \kappa_L / \kappa_{el})} < \frac{S^2}{L_0}. \quad (1.4)$$

This is an upper bound on ZT since κ_L will always be greater than zero. For metals and heavily doped (degenerate) semiconductors $L_0 = (\pi^2/3)(k_B/e)^2 = 2.45 \times 10^{-8} \text{ V}^2/\text{K}^2$. For nondegenerate cases, L_0 can be larger or smaller than this value (but only changes by up to about 40%) depending on the energy dependence of the electron scattering [7]. However, good thermoelectric materials are

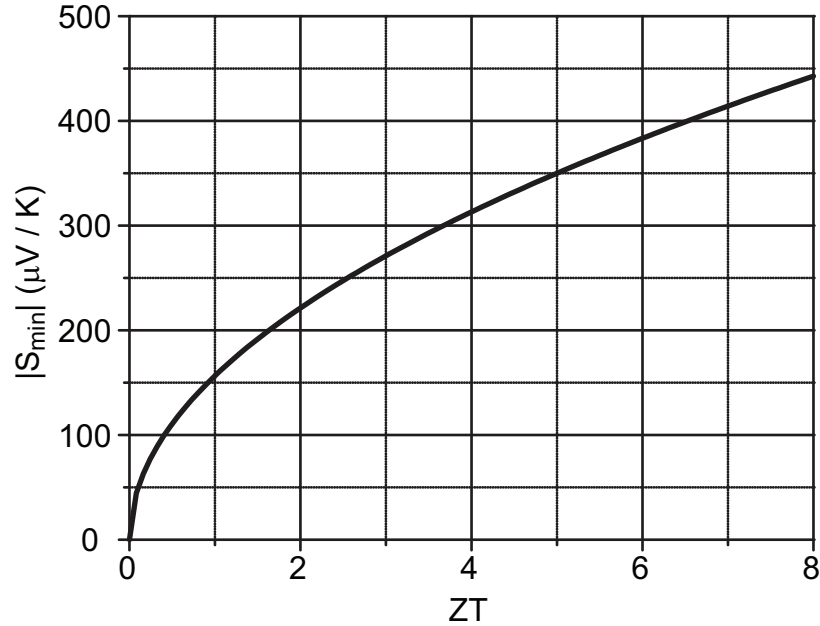


Figure 1.8: A plot of the relationship given in Eq. 1.4, showing the minimum absolute value of S needed to achieve a particular value of ZT .

usually best described as degenerate semiconductors. Eq. 1.4 shows that to realize a particular value of ZT , a certain minimum absolute value of S is required, regardless of the electrical and thermal conductivities. This relationship is plotted in Figure 1.8. For example, a material can not have $ZT=4$ with a Seebeck coefficient of less than about $310 \mu\text{V}/\text{K}$ (in absolute value).

1.3.1 Materials with high ZT at and below room temperature

The greatest need for new thermoelectric materials is for those which operate efficiently in cooling devices at and below room temperature [8]. The only materials commercially used in thermoelectric coolers today are Bi_2Te_3 based alloys. There are currently no known bulk materials that compete with these alloys near room temperature. At lower temperatures, where ZT of Bi_2Te_3 alloys is de-

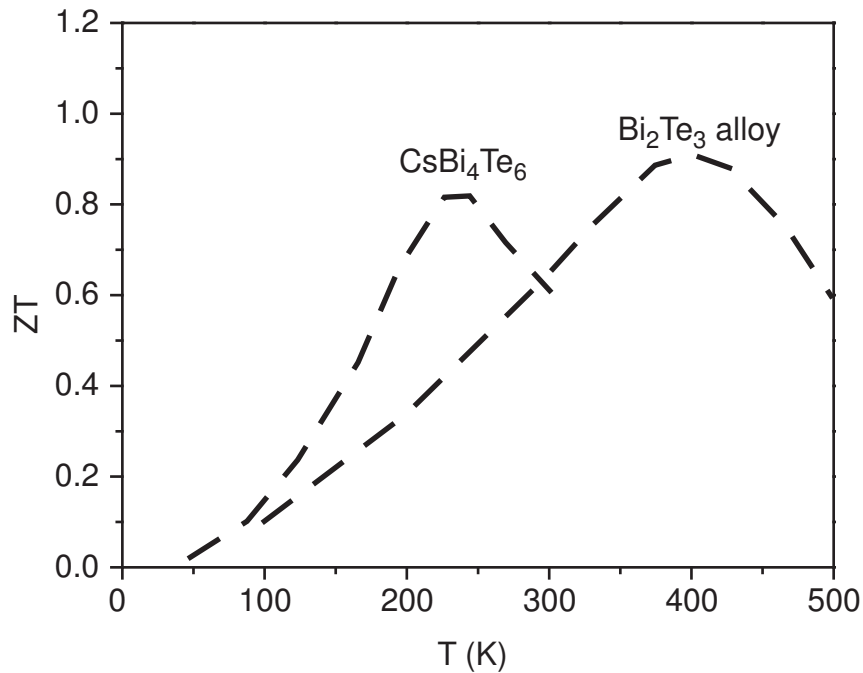


Figure 1.9: ZT as a function of temperature for Bi₂Te₃-alloys (from Ref. [10]) and CsBi₄Te₆(from Ref. [9]).

creased from its maximum which occurs between 300 K and 400 K, the ternary compound CsBi₄Te₆ has been found to have significantly higher ZT [9].

Figure 1.9 shows ZT as a function of temperature for these two materials. The shape of the curves is typical for semiconducting materials, increasing to a maximum and then decreasing as significant numbers of intrinsic carriers are excited across the band gap. The presence of carriers of both sign degrades S (they carry heat in opposite directions) and therefore decreases ZT. The temperature at which the peak in ZT occurs is related to the size of the band gap, and can be tuned in the Bi₂Te₃-alloys. The data in Figure 1.9 peak around 400 K and represent a material designed to be used in a power generation device. Samples used for cooling near room temperature have similar ZT curves which peak with $ZT \approx 1$ near 300 K. We will now briefly examine Bi₂Te₃-alloys and CsBi₄Te₆ individually.

Bi₂Te₃-based alloys

Bi₂Te₃ was one of the earliest materials to show promise for cooling applications [11, 12], and a good review of its properties, optimization, and use as a thermoelectric material is available [13]. Bi₂Te₃ crystallizes in the rhombohedral space group $R\bar{3}m$ ($a_H = 4.395 \text{ \AA}$, $c_H = 30.44 \text{ \AA}$), and adopts a layered crystal structure shown in Figure 9.15. The structure is composed of double-layers of edge sharing Bi centered octahedra with Te at the vertices. The layered structure leads to anisotropic transport properties. The thermoelectric properties are better in the plane of the layers than along the c-axis. Because of this, these materials are best used as oriented single crystals.

Bi₂Te₃ has $ZT \approx 0.7$ at room temperature (when appropriately doped). ZT is increased by alloying with the isostructural compound Sb₂Te₃. Alloying decreases the lattice thermal conductivity to about 2/3 of the value for pure Bi₂Te₃ by introducing disorder into the crystal structure. Its influence on the band gap of the material is also significant (Sb₂Te₃ has a band gap close to 0 eV.). Performance near room temperature is further enhanced by the addition of a small amount of Sb₂Se₃, which has a gap near 1.2 eV. This compound is not isostructural to the others so its influence on the gap of the alloy is not easily predictable. However, selenides usually have larger gaps than isostructural tellurides due simply to electronegativity differences. So addition of Sb₂Se₃ is believed to increase the band gap of the material and therefore push the onset of intrinsic conduction to higher temperatures. Typical alloy compositions are near (Bi₂Te₃)₂₅(Sb₂Te₃)₇₂(Sb₂Se₃)₃ doped with excess Te to give a p-type sample, and (Bi₂Te₃)₉₀(Sb₂Te₃)₅(Sb₂Se₃)₅ doped with SbI₃ to give a n-type sample. Typical values of the transport properties near room temperature for optimally doped alloys are: $|S| \approx 220 \mu\text{V/K}$, $\rho \approx 1 \text{ m}\Omega\text{cm}$, $\kappa \approx 15 \text{ mW/cmK}$.

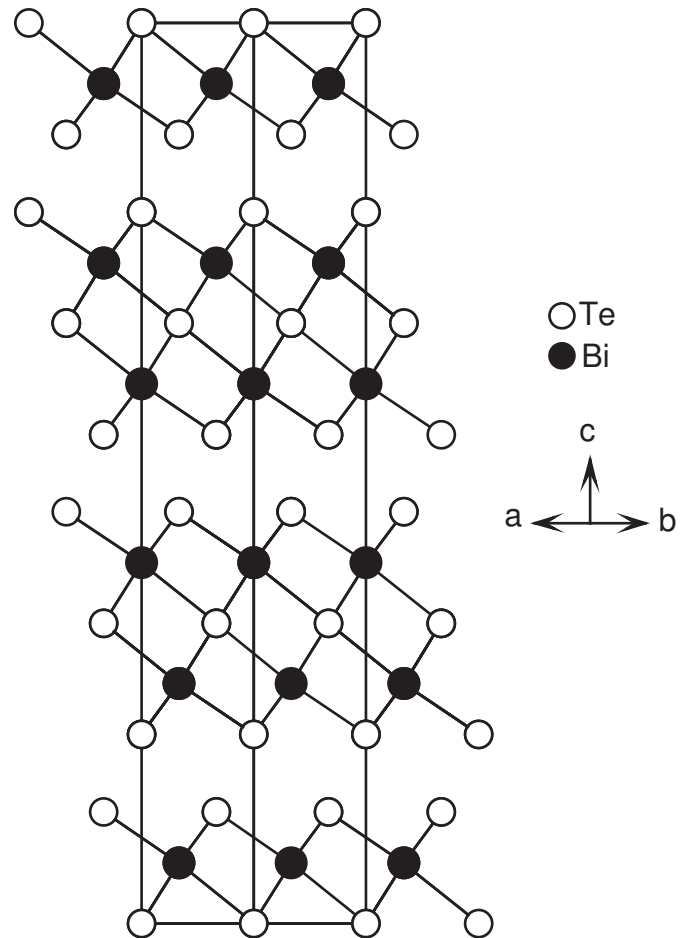


Figure 1.10: A view of the crystal structure of Bi_2Te_3 . The hexagonal unit cell is outlined. Only weak van der Waals interactions exist between the layers edge-sharing Bi-centered octahedra. This leads to easy cleavage of single crystals and fairly fragile devices.

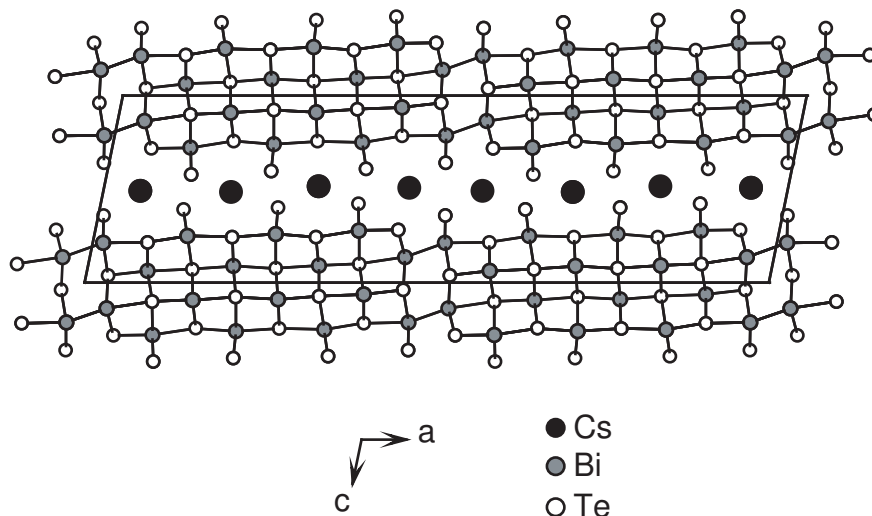


Figure 1.11: A view of the crystal structure of CsBi_4Te_6 .

CsBi_4Te_6

The crystal structure of this compound is shown in Figure 1.11 (space group $C2/m$, $a = 51.92 \text{ \AA}$, $b = 4.40 \text{ \AA}$, $c = 14.51 \text{ \AA}$, $\beta = 101.5^\circ$) [9]. The structure is composed of columns of stoichiometry Bi_2Te_3 along the b -axis. These columns are joined together in the a -direction by Bi-Bi bonds, forming infinite layers which are separated in the c -direction by Cs atoms. As with Bi_2Te_3 , the anisotropic structure leads to anisotropic transport properties. The best thermoelectric performance occurs along the b -axis, and the crystals grow as needles in this direction. The as prepared material is p -type, and its resistivity increases with temperature, which suggests that it is already a heavily (unintentionally) doped semiconductor. Band structure calculations suggest that it is a small band gap semiconductor. The authors performed an extensive survey of possible dopants to optimize ZT , and both n - and p -type doping was achieved, making this an exciting new system with possible commercial applications in lower temperature devices.

1.3.2 Materials with high ZT at high temperatures

There are many bulk materials with $ZT \approx 1$ at high temperatures, and we will give a brief survey of some of them here. Many of these systems have been studied and optimized by NASA for use in high temperature thermoelectric power generation devices. Figure 1.12 shows the temperature dependence of ZT for several of these materials. This Figure is adapted from Ref. [14] to include data for the half-Heusler compound HfNiSn from Ref. [10] and the Zintl phase $\text{Yb}_{14}\text{MnSb}_{11}$ from Ref. [15]. This Figure shows that each material has a particular temperature range over which it performs best. In real devices, like the radioisotope thermoelectric generators (RTG's) used by NASA, a large temperature difference exists between the hot and cold side, and so no single material performs well over the entire length of the legs. In practice, several materials can be segmented together along each leg, chosen so that the ones which operate best at high temperatures are closer to the hot side [14]. We will address this issue further in Chapters 2 and 6.

PbTe

Lead telluride (PbTe) is a common component of many thermoelectric power generation devices, and can be used up to 600 °C. The compound adopts the NaCl structure type ($a = 6.46 \text{ \AA}$), shown in Figure 9.24. The thermoelectric properties of PbTe have been recently reviewed [16]. PbTe can be doped p-type or n-type to achieve a maximum of $ZT \approx 0.8$ near 400 °C. Some doping can occur through departure from stoichiometry, but to make technologically useful materials external dopants are needed. Common n-type dopants are halogens, which substitute for Te and donate their extra valence electron to the conduction band. Common p-type dopants include Na, K, and Ag which substitute for Pb and cre-

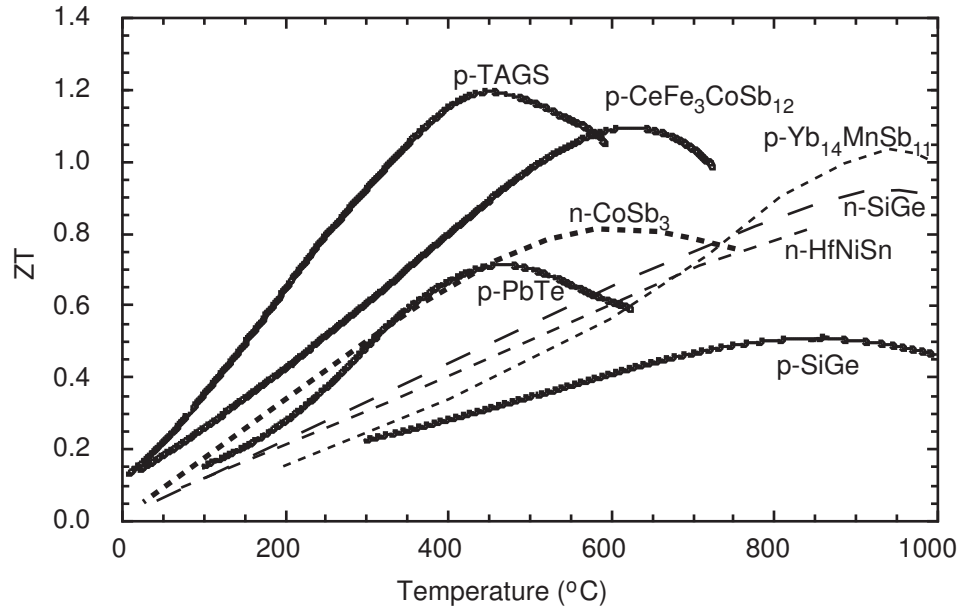


Figure 1.12: ZT as a function of temperature for good high-temperature thermoelectric materials [14, 10, 15]. The materials are labeled by whether they are p-type or n-type.

ate acceptors generating holes in the valence band. The thermoelectric properties of PbTe will be addressed further in Chapter 9 of this work.

TAGS

TAGS stands for Te-Ag-Ge-Sb (or tellurium-antimony-germanium-silver), and can be considered an alloy of AgSbTe_2 and GeTe . AgSbTe_2 adopts the NaCl structure type like PbTe (Figure 9.24) with Ag and Sb mixed on the cation sites. GeTe adopts a hexagonal structure below about 425 °C, and the NaCl structure type at higher temperatures. A typical alloy composition is $(\text{AgSbTe}_2)_{0.15}(\text{GeTe})_{0.85}$ [17], which has the NaCl structure above about room temperature. TAGS has high ZT near 400 °C (the data in Figure 1.12 reach $ZT=1.2$ at this temperature), and is commonly used in segmented power generation devices [17]. Values of $ZT>2$ have been reported for this system [18].

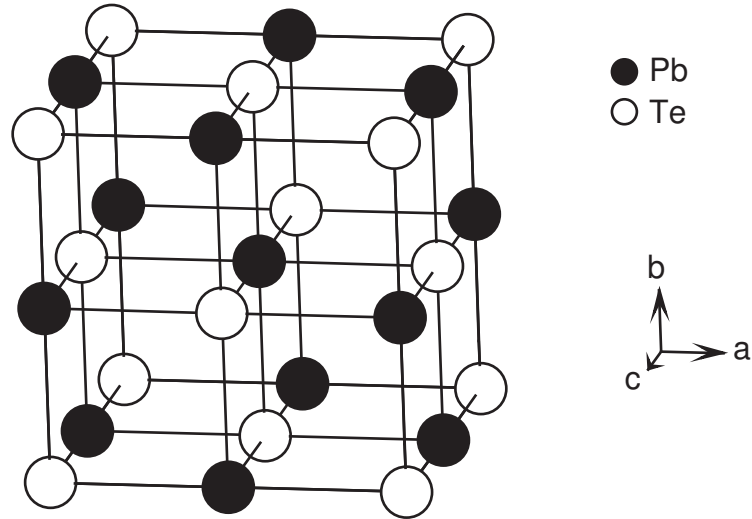


Figure 1.13: A view of the crystal structure of PbTe (NaCl structure type).

The earliest thermoelectric power generators used by NASA, starting in the 1950's, were based on PbTe and TAGS [6]. They operated between 550 °C and 150 °C with PbTe for the n-type leg and a segmented p-type leg composed of TAGS for the higher temperature segment and a SnTe-PbTe alloy for the lower temperature segment. They produced about 250 W of electrical power with a conversion efficiency near 8%.

Promising thermoelectric properties have also been observed recently in the related solid solution $(\text{AgSbTe}_2)_{0.05}(\text{PbTe})_{0.95}$, sometimes abbreviated LAST. Reports include n-type $ZT > 2$ near 525 °C [19]. It is believed that the thermoelectric properties of these materials is significantly influenced by their nanoscale structure, which is comprised of AgSb-rich nanodots imbedded in a PbTe rich matrix [20, 21]. However, other studies of these materials only found $ZT < 1$ [22, 23, 24]. A proposed explanation for these conflicting results is millimeter scale thermoelectric inhomogeneities [25]. The scanning Seebeck microprobe technique was used to show significant variation in S across a single sample of this material, including both n- and p-type behavior in the same specimen. Mea-

measurements of the various thermoelectric properties which determine ZT are often performed with different arrangements and geometries of contacts, and are sometimes measured on different pieces of cut from the bulk sample. Inhomogeneities on the mm scale could then be responsible for the discrepancy in the reported thermoelectric performance of LAST materials. It is clear that further careful examination of these materials is warranted to determine its utility for thermoelectric applications.

Si-Ge alloys

Silicon and germanium, and alloys of Si and Ge, adopt the diamond structure shown in Figure 1.14, made up of two interpenetrating fcc lattices displaced from each other by $(1/4, 1/4, 1/4)$. Silicon has electronic properties suitable for a good thermoelectric material. Tuomi defined the thermoelectric quality factor Q , which is determined by the properties of the electrons and holes in the energy bands of the semiconductor [26]. It is related to the B factor which is examined in detail in the following Chapter of this work. Good thermoelectric materials should have high quality factors. Silicon has one of the highest quality factors of any material [8]. However this parameter does not include the lattice thermal conductivity, which is very high in Si, 1000 mW/cmK at room temperature [27] (Bi_2Te_3 alloys have a lattice thermal conductivity near 10 mW/cmK [13]). This high thermal conductivity makes Si unusable in thermoelectric devices. However, alloying Si with Ge lowers the lattice thermal conductivity significantly, and the thermoelectric figure of merit ZT (Figure 1.12) is high, especially for n-type samples. Usual alloy compositions are near $\text{Si}_{0.7}\text{Ge}_{0.3}$.

Recent radioisotope thermoelectric generators used by NASA to power space probes have employed Si-Ge alloys. These materials have a lower sublimation rate than telluride compounds like PbTe and TAGS, and can therefore

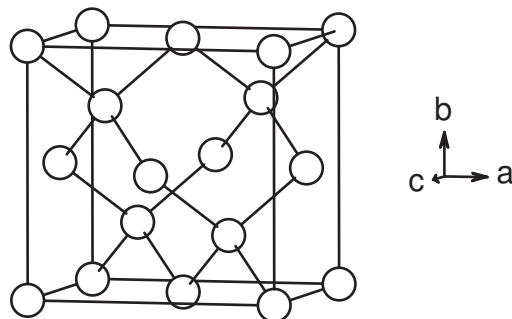


Figure 1.14: A view of the crystal structure of the Si-Ge alloys (the diamond structure type).

operate with a higher hot side temperature, up to 1000 °C typically [6]. These generators produced about 150 W of electric power, and a conversion efficiency near 8% is realized with a cold side temperature near 300 °C. This is about the same efficiency as a PbTe-TAGS based generators operating between 550 °C and 150 °C. The advantage of Si-Ge alloy based modules over the telluride based systems is the higher cold side temperature, which allows for smaller radiation fins and therefore higher efficiency per unit mass.

Skutterudites

Skutterudite is the mineral name for the compound CoAs_3 , and is commonly used to refer to any compound of the same structure type. The skutterudite crystal structure is cubic (space group $\text{Im}\bar{3}$) and is shown in Figure 1.15. The Co atoms are coordinated to Sb atoms in an octahedral arrangement. The octahedra tilt to share corners. In addition, Sb-Sb bonds are formed between corners of neighboring octahedra, forming Sb_4 square rings. This arrangement leaves a body-centered cubic array of voids in which the guest atoms reside. In the square rings, each Sb is bonded to two others, giving a formal charge of -1 for each Sb. The stoichiometry CoSb_3 gives a formal oxidation state of +3 for Co ($3d^5$). Binary

skutterudites have gaps or pseudo-gaps at their Fermi levels, however the sizes of the gaps (determined experimentally or theoretically) vary in the literature [28]. Filling atoms move the Fermi level away from the gap, and semiconducting behavior is usually maintained by compensating substitutions on the Co site. A typical composition is $\text{CeFe}_3\text{CoSb}_3$.

The thermoelectric properties of skutterudites have been extensively studied and recently reviewed (see Ref. [29] and references therein). Several compositions have shown ZT values in excess of 1 at high temperatures (above 600 °C). The filling atoms play an important role in decreasing the thermal conductivity of these materials. Even at low filling levels, for example 5% of La or Ce, can decrease the thermal conductivity by about one half, without the need for compensating substitutions on the Co sites. This is an active area of thermoelectric research, and there are many research groups currently working to optimize skutterudite thermoelectrics by studying various filler atoms and dopants.

Half-Heuslers

Half-Heusler materials are intermetallic compounds (although often referred to as alloys in the literature) with the composition XYZ. Typically X and Y are transition metals and Z is a main group element (although X and Y can also be alkali metals, alkaline earth elements, or lanthanides). The Half-Heusler structure type is cubic (space group $F\bar{4}3m$) and is shown in Figure 1.16. It can be described in several ways: three interpenetrating fcc lattices, a rock salt framework of X and Y with Z filling the cubic holes, or a zinc blende framework of X and Z with Y filling one half of the tetrahedral holes.

A recent review article summarizes the performance of half-Heusler compounds as thermoelectric materials [29]. These compounds are semiconductors if the total number of valence electrons per formula unit is either 8 (LiMgP) or

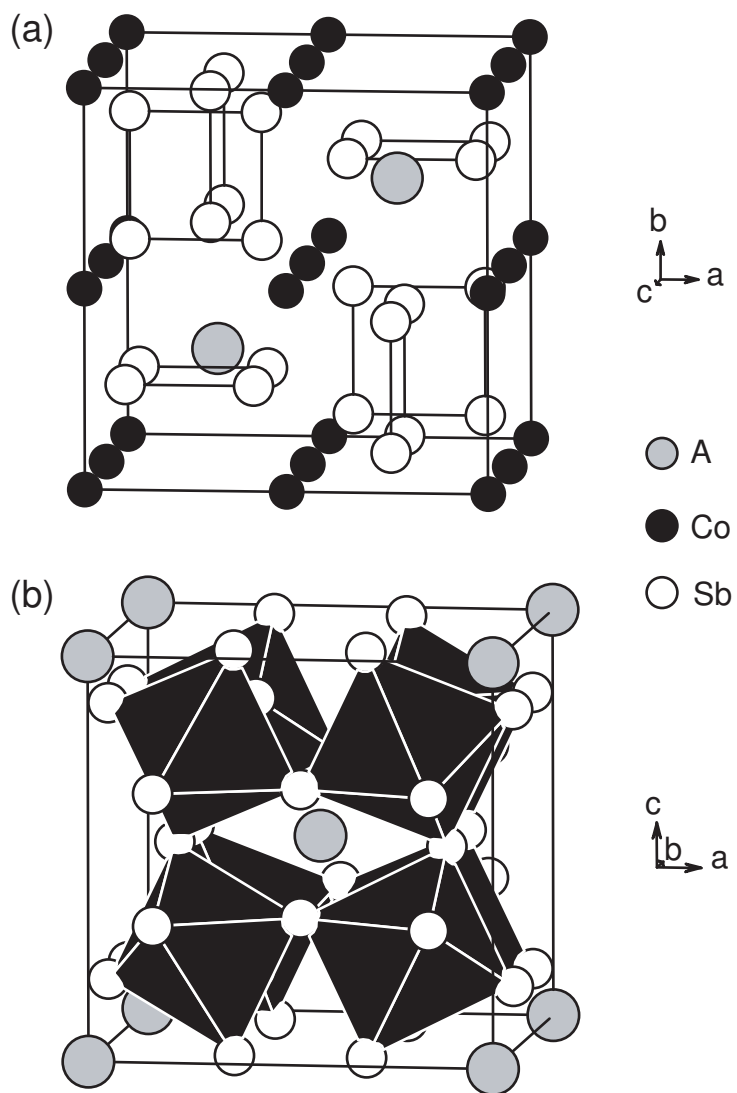


Figure 1.15: Two views of the crystal structure of a skutterudite of composition $A_x\text{CoSb}_3$. In (a) the Sb_4 rings are emphasized, while in (b) the Co centered octahedra are shown. Note that the choice of unit cell origin differs in the two views.

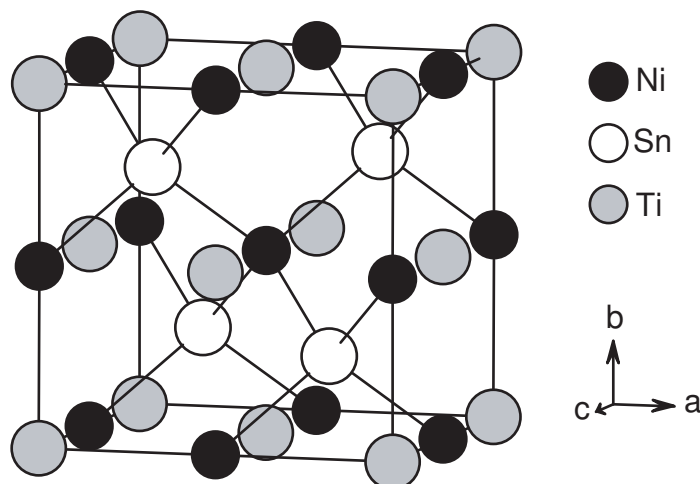


Figure 1.16: A view of the crystal structure of half-Heusler compounds.

18 (TiNiSn). The attractiveness of half-Heusler thermoelectrics comes from their high S and low ρ , however their thermal conductivity is too large for thermoelectric applications unless they are heavily alloyed. Charge carrier concentration is controlled by doping on the Z site, while the thermal conductivity is decreased by alloying on the X site. ZT as high as 1.4 has been reported at 700 K for the composition $Zr_{0.25}Hf_{0.25}Ti_{0.5}NiSn_{1-y}Sb_y$ [30], but has proven difficult to reproduce [31]. Near 1100 K, $ZT \approx 0.9$ is seen in Sb doped $Hf_{0.75}Zr_{0.25}NiSn$ (Figure 1.12 and Ref. [29]). Currently high ZT in half-Heusler thermoelectrics is only realized for n-type conduction.

Zintl phases

Conventional Zintl phases combine electropositive elements A (like alkali metals, alkaline earths, or rare earths) with one or more early p-block elements B. In more exotic Zintl phases B can also be a transition metal. Their structures are composed of covalently bonded frameworks (or sometimes clusters) of B atoms surrounding isolated A atoms. Simple, but powerful, electron counting rules

can be used to understand the electronic structure and bonding in these materials. The donation of electrons from the electropositive elements A results in unusual oxidation states for B. To satisfy their needs for filled octets the B atoms form bonds with one another, producing a covalent framework. The number of electrons donated by A and the number of valence electrons of B determine the connectivity in the B network, and thus control the adopted crystal structure.

Although some Zintl phases behave like semimetals, the closed shell nature of the B framework often results in semiconducting compounds with small band gaps between bonding and antibonding states. Since both the valence band and conduction band arise primarily from the covalent B framework and not the isolated A atoms, appropriate doping of these materials should produce mobile holes or electrons. In addition, aliovalent substitutions on the A sites represents an ideal doping strategy for Zintl phases. The substitutions should only affect the number of electrons donated to the B framework and have minimal influence on the mobility of the carriers. It has also been shown that the charge carrier concentration in Zintl phases can be tuned by "isovalent" substitutions (Yb^{2+} replacing Ca^{2+}), using the difference in electronegativity of the A atom to control the degree of electron transfer to the B framework [32]. These compounds also often adopt complex structures with large unit cells which lead to low lattice thermal conductivities.

This class of compounds has not been extensively studied for thermoelectric applications, with the exception of skutterudites and clathrates which can be classified as Zintl phases. Although the thermoelectric properties of only a few members of this large class of materials have been investigated, a high performance Zintl phase thermoelectric material has already been identified. The compound $\text{Yb}_{15}\text{MnSb}_{11}$ has $ZT > 1$ near 1000 °C (Figure 1.12 and Ref. [15]). The complex crystal structure of this compound is shown in Figure 1.17 (or-

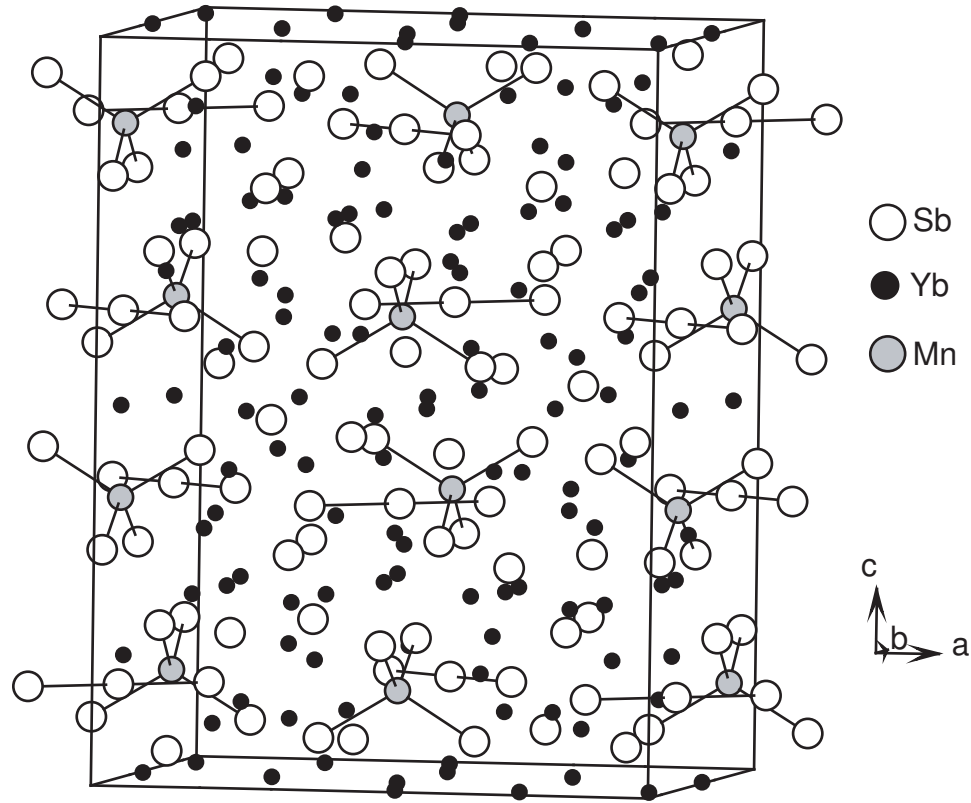


Figure 1.17: A view of the crystal structure of $\text{Yb}_{14}\text{MnSb}_{11}$.

thorhombic space group $I4_1/acd$). It is isostructural to the Zintl phase $\text{Ca}_{15}\text{AlSb}_{11}$ which contains isolated Sb^{3-} anions, linear $(\text{Sb}_3)^{7-}$ anionic units, and tetrahedral $(\text{AlSb}_4)^{9-}$ which exactly charge balance the Ca^{2+} cations. The p-type behavior of $\text{Yb}_{15}\text{MnSb}_{11}$ is attributed to the difference in valence state of the Mn atoms (formally 2+) and the Al atoms (formally 3+) in the electron precise analog $\text{Ca}_{15}\text{AlSb}_{11}$.

$\text{Yb}_{15}\text{MnSb}_{11}$ fills an important gap in Figure 1.12. Before its discovery, the best p-type materials for use at the highest temperatures (near 1000 °C) were Si-Ge alloys, with ZT values only near 0.4-0.5. This compound has the potential to replace Si-Ge alloys in high temperature thermoelectric generators, and further work is currently underway to optimize this material.

1.4 Aims of This Work

The previous Section shows that there are many materials that show good thermoelectric performance. However, the search for improved materials is still an active area of research. This is partly due to the increased awareness of the need for alternative energy sources and conversion mechanisms. As pointed out in the previous Section, the greatest needs are for materials with high ZT below room temperature, and for high ZT p-type materials for use near 1000 °C. Two general approaches are taken toward improved thermoelectric performance: (1) modification of known good thermoelectric materials through chemical substitutions (doping and alloying) and materials processing (fine grained and nanostructured materials), and (2) the search for new compounds which have the potential for enhanced thermoelectric properties. The incremental increases in ZT realized by the former approach are important, especially in materials which are currently used in commercial applications. However, the development of materials which operate efficiently in temperature ranges not covered by current materials (like 200 K and below), and the discovery of materials with ZT values that could open the way to new applications (competitive commercial refrigeration if $ZT \approx 4$ is achieved) is most likely to occur through investigation of new systems and the discovery and characterization of new solid state compounds. This is the primary approach to thermoelectric materials research in the DiSalvo group.

The two main experimental efforts described in this Dissertation are the investigation of structural and thermoelectric properties of new thallium containing compounds at and below room temperature, and the development of new Chevrel phase materials for high temperature applications. The former is a continuation of the work of a previous graduate student (Dr. Thomas K. Reynolds),

and includes the thermoelectric characterization of many of the compounds discovered and structurally characterized by him [33], as well as many other newly discovered Tl containing compounds. The Chevrel phase work was performed in collaboration with Dr. G. Jeffrey Snyder at NASA/JPL, and involved the synthesis and structural characterization of new and known Chevrel phase materials, as well as the preparation of single phase bulk samples for high temperature transport properties measurements carried out at JPL. Some results from aspects of our Chevrel phase work not presented here were reported in the Masters Thesis of Anneliese M. Schmidt [34]. In addition, the study of several “miscellaneous” materials are reported, including results from the study of complex anion systems, arsenic containing Bi_2Te_3 based alloys, and the effects of high-temperature high-pressure treatment of PbTe.

This work did not produce a high ZT material. However it did produce many new solid state compounds with interesting structural, electronic, and magnetic properties. In addition to the possibility of discovering high performance thermoelectrics, I believe that one of the most exciting aspects of the exploratory search for thermoelectric materials is the opportunity to discover and explore diverse classes of materials, and study their structure-property relationships. Examining the relationships between crystal structure and transport properties is a vital part of thermoelectrics research. Through the study of these relationships the researcher develops a powerful and diverse toolkit for determining and understating the crystal structure, electronic structure, and physical properties of materials.

Before presenting and discussing the experimental results, it is important to under the theory relevant to thermoelectric materials and devices. This is the topic of the following Chapter.

REFERENCES

- [1] T. J. Seebeck, *Abhandlungen der Deutschen Akademie der Wissenschaften zu Berlin*, 265 (1822–1823).
- [2] N. Ashcroft and N. Mermin, *Solid State Physics*, Holt, Rinehart and Winston, 1976.
- [3] J. C. Peltier, *Ann. Chim.* **LV1**, 371 (1834).
- [4] W. Thomson, *Proceedings of the Royal Society of Edinburgh*, 91 (1851).
- [5] F. DiSalvo, *Science* **285**, 703 (1999).
- [6] J. Yang and T. Caillat, *MRS Bull.* **31**, 224 (2006).
- [7] R. Heikes and R. Ure Jr., *Thermoelectricity: Science and Engineering*, Interscience Publishers Inc., 1st edition, 1961.
- [8] G. Mahan, *Solid State Physics Vol. 51*, pages 81–157, Academic Press, 1997.
- [9] D. Y. Chung et al., *J. Am. Chem. Soc.* **126**, 6414 (2004).
- [10] T. M. Tritt and M. A. Subramanian, *MRS Bull.* **31**, 188 (2006).
- [11] A. F. Ioffe, *Semiconductor Thermoelements and Thermoelectric Cooling*, Infosearch, 1957.
- [12] H. J. Goldsmid and R. W. Douglas, *Br. J. Appl. Phys.* **5**, 386 (1954).
- [13] W. Yim and F. D. Rosi, *Solid-State Electron.* **15**, 1121 (1972).
- [14] G. J. Snyder and T. Caillat, *MRS Proceedings* **793**, 37 (2004).
- [15] S. R. Brown, S. M. Kauzlarich, F. Gascoin, and G. J. Snyder, *Chem. Mater.* **18**, 1873 (2006).
- [16] Z. H. Dughaish, *Physica B* **322**, 205 (2002).
- [17] G. J. Snyder, *Appl. Phys. Lett.* **84**, 2436 (2004).
- [18] S. K. Plachkova, *Phys. Status Solidi A* **83**, 349 (1984).
- [19] K. F. Hsu et al., *Science* **303**, 818 (2004).
- [20] D. Blick et al., *Phys. Rev. Lett.* **93**, 146403 (2004).
- [21] J. P. Heremans, C. M. Thrush, and D. T. Morelli, *Phys. Rev. B* **70**, 225334 (2004).

- [22] H. Rodot, C.R. Acad. Sci. Hebd Seances Acad. Sci. D **249**, 1872 (1959).
- [23] A. Kosuga, M. Uno, K. Kurosaki, and S. Yamanaka, J. Alloys Compd. **387**, 52 (2005).
- [24] A. Kosuga, M. Uno, K. Kurosaki, and S. Yamanaka, J. Alloys Compd. **391**, 288 (2005).
- [25] N. Chen et al., Appl. Phys. Lett. **87**, 171903 (2005).
- [26] D. Tuomi, J. Electrochem. Soc. **131**, 2319 (1984).
- [27] G. A. Slack, *Solid State Physics Vol. 34*, pages 1–71, Academic Press, 1979.
- [28] K. Takegahara and H. Harima, Physica B **328**, 74 (2003).
- [29] G. S. Nolas, J. Poon, and M. Kanatzidis, MRS Bull. **31**, 199 (2006).
- [30] S. Sakurada and N. Shutoh, Appl. Phys. Lett. **86**, 2105 (2005).
- [31] S. R. Culp et al., Appl. Phys. Lett. **88**, 042106 (2006).
- [32] F. Gascoin et al., Adv. Funct. Mater. **15**, 1860 (2005).
- [33] T. K. Reynolds, *Design, Synthesis, and Characterization of New Materials for Thermoelectric Applications*, PhD thesis, Cornell University, 2003.
- [34] A. M. Schmidt, *Investigation of New Chevrel Phase Compounds for Improved Efficiency of Thermoelectric Power Generation Devices*, MS thesis, Cornell University, 2005.

Chapter 2

Theoretical Considerations

In this Chapter we will review the theory of thermoelectricity, thermoelectric (TE) conversion, and TE materials. We will begin by addressing the thermodynamics needed to understand thermoelectricity. Then we will see how TE devices can be constructed, and learn what material properties are needed to make the devices more efficient. The microscopic theory of the transport coefficients in bulk materials and low dimensional systems will then be treated. Significant progress has been made recently towards the calculation of TE properties from first principles, and we will review some of it here. We will conclude this Chapter by discussing in some detail the most mysterious (at least the least intuitive) transport coefficient, the Seebeck coefficient. This chapter has been adapted from a paper written by the author for his A-exam, at the request of Prof. N. W. Ashcroft.

2.1 Thermodynamics of Coupled Flows

In this section, we develop the quantitative theory of thermoelectricity by considering the coupling between flows of particles and heat (or entropy). The derivations are based on those found in Ref. [1]. We treat the coupled flows in the linear approximation, writing the relationships between the flows J , the forces X and the susceptibilities L as

$$J_i = \sum_j L_{ij} X_j. \quad (2.1)$$

Onsager has shown [2, 3] that the L matrix is symmetric if the flows and forces are chosen in such a way that the rate of entropy increase of the system Θ is given

by

$$\Theta = \sum_i J_i X_i. \quad (2.2)$$

We will derive an expression for Θ in the form of Equation 2.2 and identify the J 's and X 's.

Consider the rate of the increase of entropy of a unit volume inside the system. Denoting entropy per unit volume as s , internal energy per unit volume as u , concentration of particles as c , the electrochemical potential per unit volume as μ and temperature as T , we can write

$$ds = (du - \mu \cdot dc)/T. \quad (2.3)$$

We note that μ can be separated into contributions from the chemical potential and the electrical potential,

$$\mu = \mu_{chem} - e\phi, \quad (2.4)$$

with e being the magnitude of the electron charge. To get the rate of increase of entropy per unit time, we divide Equation 2.4 by dt , giving

$$\frac{ds}{dt} = \frac{1}{T} \frac{du}{dt} - \frac{\mu}{T} \frac{dc}{dt}. \quad (2.5)$$

By invoking conservation of energy and particle number, we can use continuity equations to replace time derivatives of the conserved quantities with their divergences to get

$$\frac{ds}{dt} = -\frac{1}{T} \nabla \cdot w + \frac{\mu}{T} \nabla \cdot J_N. \quad (2.6)$$

Here w is the energy flux and J is the particle flux. Now, we are interested in the quantity Θ which is given by the continuity equation

$$\Theta = \frac{ds}{dt} + \nabla \cdot J_s, \quad (2.7)$$

where J_s is the entropy flux. Writing out J_s in analogy with Equation 2.3 gives

$$\Theta = \frac{ds}{dt} + \nabla \cdot \left[\frac{1}{T} (w - \mu J_N) \right]. \quad (2.8)$$

Taking the divergence in Equation 2.8, and using Equation 2.6 for ds/dt , results in

$$\Theta = w \cdot \nabla (1/T) - J_N \cdot \nabla (\mu/T). \quad (2.9)$$

Now we must choose which fluxes to use, and then identify the corresponding forces. For TE applications, it is convenient to choose the particle flux and the entropy flux. We take the gradient in the second term on the right hand side of Equation 2.9 and get

$$\Theta = -J_N \cdot \frac{1}{T} \nabla \mu + [w - \mu J_N] \cdot \nabla (1/T). \quad (2.10)$$

The term in brackets in Equation 2.10 is recognized to be the product TJ_s , and we can now identify the forces.

$$\begin{aligned} X_N &= -\frac{1}{T} \nabla \mu \\ X_S &= T \nabla (1/T) \end{aligned} \quad (2.11)$$

The coupled flow equations can now be written in a form in which the L matrix is symmetric.

$$\begin{aligned} J_N &= -L_{NN} \frac{1}{T} \nabla \mu + L_{NS} T \nabla (1/T) \\ J_S &= -L_{NS} \frac{1}{T} \nabla \mu + L_{SS} T \nabla (1/T) \end{aligned} \quad (2.12)$$

We will next derive relationships between the elements of the L matrix and familiar transport coefficients. First we consider a situation in which no temperature gradient is present in the material. In this situation the first of Equation 2.12 gives, upon multiplication by e ,

$$J = \frac{L_{NN} e^2}{T} \nabla \phi, \quad (2.13)$$

where J is the electrical current density. We can identify this with Ohm's Law to see that the electrical conductivity is given by

$$\sigma = \frac{e^2 L_{NN}}{T} \quad (2.14)$$

The thermal conductivity at $J=0$ can be found by setting the right hand side of the first of Equation 2.12 to zero and substituting it into the second, eliminating $\nabla\mu$. This gives for the heat flow $q = T J_S$

$$q = - \left(L_{SS} - \frac{L_{SN}^2}{L_{NN}} \right) \nabla T. \quad (2.15)$$

From this we identify the thermal conductivity κ at zero electrical current as

$$\kappa = L_{SS} - \frac{L_{SN}^2}{L_{NN}}. \quad (2.16)$$

We note that the thermal conductivity at zero electric field is given simply by $\kappa_0 = L_{SS}$.

Finally, we *define* the Seebeck coefficient S as the ratio between the entropy current and the electrical current in the limit of vanishing temperature gradient. From Equation 2.12 this gives

$$S = \frac{J_S}{J} = \frac{L_{SN}}{e L_{NN}} = \frac{e L_{SN}}{T \sigma}. \quad (2.17)$$

We will show next that this is consistent with the definition of S given in the preceding section, and derive the relationships between τ , Π and S discussed there. To do this we write the first of Equation 2.12 in terms of the conventional transport coefficients and multiply by e/σ .

$$\frac{J}{\sigma} = -\frac{1}{e} \nabla\mu - S \nabla T \quad (2.18)$$

Here J/σ can be replaced by $\nabla\phi$ according to Ohm's Law. We will consider integrating this equation between points 1 and 2 in the circuit shown in Figure 2.8, made up of two dissimilar materials, a and b. We will call the difference in electrical potential between 1 and 2 V_0 and note that the chemical potential is the same at 1 and 2. Integrating Equation 2.18 from 1 to 2 then gives

$$J \int_1^2 \frac{1}{\sigma} dl = -V_0 - \int_1^2 S dT. \quad (2.19)$$

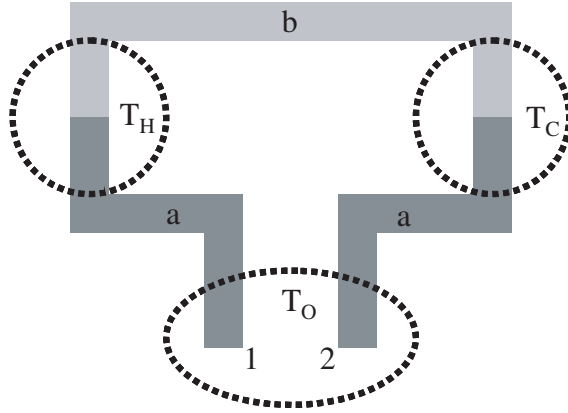


Figure 2.1: A thermoelectric couple made up of two materials a and b with junctions at two temperatures T_H and T_C .

In an open circuit situation, $J=0$, we have

$$V_0 = -[S_a(T_H - T_0) + S_b(T_C - T_H) + S_a(T_0 - T_C)]. \quad (2.20)$$

This reduces to

$$V_0 = (S_a - S_b) \Delta T, \quad (2.21)$$

showing that measurement of the open circuit voltage created by a temperature difference ΔT gives the Seebeck coefficient. In an actual experimental apparatus, material a represents the leads used to measure S of material b. Thus a voltmeter will report the difference between the Seebeck voltage ($S \Delta T$) of the sample and that of the leads. Corrections for the lead contribution must be made to determine the absolute Seebeck coefficient of the sample.

We will now consider the Peltier and Thomson heats in the circuit shown in Figure 2.8. We wish to arrive at an expression for the amount of heat exchanged between the circuit and the surroundings. We define dw as the difference between the amount of energy being transported into and out of a segment of the circuit of length dx . In the steady state, this must equal the amount of heat coming into that segment from the environment. We define $Q(x)$ as the amount of energy

coming in through the surface from the environment per unit length. With these definitions the steady state condition is

$$Q(x) = dw/dx. \quad (2.22)$$

To get an expression for dw/dx we will differentiate $w(x)$ obtained from the expression for entropy current density,

$$J_S = \frac{1}{T} (w - \mu J_N). \quad (2.23)$$

Solving Equation 2.23 for w , then replacing J_S using the second of Equations 2.12, followed by elimination of $\nabla\mu$ in favor of J_N using the first of Equations 2.12, ultimately results in the expression

$$w = (TeS + \mu) J_N - \kappa \frac{dT}{dx}. \quad (2.24)$$

Differentiation of Equation 2.24 gives, according to Equation 2.22,

$$Q(x) = \left(eS \frac{dT}{dx} + eT \frac{dS}{dx} + \frac{d\mu}{dx} \right) J_N - \frac{d}{dx} \left(\kappa \frac{dT}{dx} \right). \quad (2.25)$$

The first term on the right hand side of Equation 2.25 can be simplified using Equation 2.18 to obtain an expression containing three independent contributions to the heat being absorbed by the system from the environment, Q .

$$Q(x) = -TJ \frac{dS}{dx} - \frac{J^2}{\sigma} - \frac{d}{dx} \left(\kappa \frac{dT}{dx} \right) \quad (2.26)$$

The second term on the right hand side of Equation 2.26 is obviously the Joule heat which must be absorbed by the environment. The last term in Equation 2.26 is clearly the difference in the amount of heat brought into and carried away from a segment dx . This difference must be absorbed by the environment.

The first term contains both the Thomson and Peltier heats. It should not be surprising that they appear as a single term after the discussion in the preceding section highlighting their similar origins. If we consider a segment dx in one

of the arms of the circuit (a or b), this term tells us the amount of heat generated per unit length is

$$Q_\tau = -TJ \frac{dS}{dT} \frac{dT}{dx}. \quad (2.27)$$

We can identify the Thomson coefficient defined in Section 1 as

$$\tau = -T \frac{dS}{dT}. \quad (2.28)$$

To determine the heat generated by the first term in Equation 2.26 across an isothermal junction between a and b we must integrate this term across the junction (recall Q is the heat absorbed per unit length). This gives us, for the Peltier heat Q_Π (this is not a heat per unit length though we still use the symbol Q).

$$Q_\Pi = -TJ(S_b - S_a) \quad (2.29)$$

From here we identify the Peltier coefficient

$$\Pi = T(S_b - S_a). \quad (2.30)$$

We note that the relationships between τ , Π and S given by Equation 2.28 and Equation 2.30 agree with the predictions of the qualitative arguments of the previous Section.

It is clear then that a junction between two dissimilar legs in a thermoelectric couple through which an electrical current is flowing can absorb heat from its surroundings. This is the basis for thermoelectric refrigeration. The theory describing the performance of such devices, often called Peltier coolers, is the topic of the next section.

2.2 Device Equations and Efficiency

We have seen in the preceding section that cooling (or heating) can occur when current is passed through a junction between two materials. We wish now

to examine the theory of devices that would utilize this for refrigeration or power generation purposes, following Reference [1].

First we will discuss TE refrigeration. We will begin by considering the temperature distribution along a bar of length L carrying an electrical current density J . In the steady state, one end of this bar ($x=0$) is at temperature T_H , the other ($x=L$) is at T_C . Joule heating generates heat uniformly along the bar. We must solve the diffusion equation with a source term, due to this Joule heat.

$$\kappa \frac{d^2 T(x)}{dx^2} + J^2 \rho = 0 \quad (2.31)$$

This can easily be integrated twice, and with the boundary conditions described above we get

$$T(x) = \left(T_H - \frac{x}{L} \Delta T \right) + \frac{J^2 \rho}{2\kappa} x(L-x). \quad (2.32)$$

The rate at which the heat *exits* through the cold end of the rod is given by

$$q_C = \left[-A\kappa \frac{dT}{dx} \right]_{x=L} = \kappa \Delta T \frac{A}{L} + \frac{1}{2} I^2 \frac{\rho L}{A}. \quad (2.33)$$

Similarly the rate at which heat *enters* from the hot end is

$$q_H = \left[-A\kappa \frac{dT}{dx} \right]_{x=0} = \kappa \Delta T \frac{A}{L} - \frac{1}{2} I^2 \frac{\rho L}{A}. \quad (2.34)$$

The first terms on the right hand sides of Equation 2.33 and Equation 2.34 are the flows due to the temperature difference ΔT between the two ends. The second terms are due to the Joule heat. As expected, the difference between the heat coming in the hot end and leaving the cold end is simply the Joule heat. We also note that exactly one half of this Joule heat leaves through each end of the bar.

To this point we have made no mention of thermoelectric effects in this bar. If two such bars are joined at the cold end we can expect in addition to the heat flow given by Equation 2.33 a contribution due to the Peltier effect. To investigate this situation we consider the thermoelectric couple shown in Figure 2.2 made up of two materials, one n-type and one p-type.

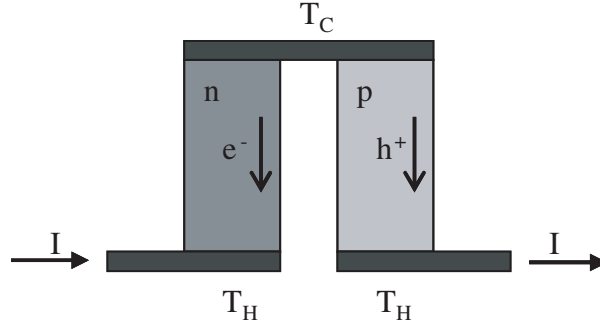


Figure 2.2: A TE couple, made by joining two materials, one n-type and one p-type, used to illustrate TE refrigeration. A current I is flowing through the couple, carrying heat away from the cold side (T_C) toward the hot side (T_H).

When a current I is passed through the couple as shown, charge carriers in both legs move downward. Since they carry heat as well as charge, heat is moved away from the top end, cooling it.

The standard measure of efficiency for a refrigerator is the coefficient of performance φ defined by

$$\varphi = \frac{q_C}{P}, \quad (2.35)$$

where P is the electrical power supplied to move the heat q_C away from the cold end.

We will now derive expressions for q_C and P for the couple shown above in Figure 2.2. In the steady state the heat removed from the cold end is given by Equation 2.33, with an additional term which accounts for the Peltier heat. With this additional term, and denoting R as the series resistance of the two legs, K as the parallel thermal conductance of the two legs and $\alpha = S_p - S_n$, we get from Equation 2.33 and Equation 2.29

$$q_C = \alpha T_C I - \frac{1}{2} I^2 R - K \Delta T. \quad (2.36)$$

The power supplied to the couple is given by the product of the current I and the applied voltage required to sustain this current. This voltage includes both the IR

drops along the legs and the Seebeck voltages across each leg. Thus, the power is given by

$$P = I^2 R + \alpha I \Delta T. \quad (2.37)$$

With Equation 2.36 and Equation 2.37 the coefficient of performance Equation 2.35 becomes

$$\varphi = \frac{\alpha T_C I - 1/2 I^2 R - K \Delta T}{\alpha I \Delta T + I^2 R}. \quad (2.38)$$

At this point we will make the simplifying assumptions that the two legs are made of materials with equal resistivities and thermal conductivities, and that $S_n = -S_p$. Making the substitutions $R = 2\rho L/A$, $K = 2\kappa A/L$ and $\alpha = 2S$ in Equation 2.38 gives, upon division by A ,

$$\varphi = \frac{S T_C J - 1/2 J^2 \rho L - \Delta T \kappa / L}{S J \Delta T + J^2 \rho L}. \quad (2.39)$$

The coefficient of performance Equation 2.39 depends on the current J . We can find the J which maximizes the COP for a couple with particular materials properties operating in a certain temperature range. The optimal J is then given by

$$J = \frac{\kappa \Delta T}{S L T_{avg}} \left[1 + \left(1 + \frac{S^2}{\rho \kappa} T_{avg} \right)^{1/2} \right]. \quad (2.40)$$

Putting this into Equation 2.39 to find the optimized coefficient of performance results in

$$\varphi^* = \frac{T_C}{\Delta T} \frac{\left(1 + \frac{S^2}{\rho \kappa} T_{avg} \right)^{1/2} - \frac{T_H}{T_C}}{\left(1 + \frac{S^2}{\rho \kappa} T_{avg} \right)^{1/2} + 1}. \quad (2.41)$$

From Equation 2.41 we see that the properties of the thermoelectric material appears only in the combination which is denoted by Z :

$$Z = \frac{S^2}{\rho \kappa} = \frac{S^2}{\rho (\kappa_L + \kappa_e)}. \quad (2.42)$$

Here we have split the thermal conductivity into the contribution from the lattice (subscript L) and that from the charge carriers (subscript e). Equation 2.41 also

shows that as Z becomes large, the coefficient of performance of the thermoelectric refrigerator approaches the Carnot limit of $T_C/\Delta T$.

We can also calculate the maximum temperature difference that this cooler can generate. This occurs when the Joule heat and thermally conducted heat transported into the cold junction exactly cancels the Peltier heat pumped away. That is, we set the right hand side of Equation 2.36 to zero, and find the current which maximizes ΔT for a given T_C . This current turns out to be $I=\alpha T_C/R$, and the resulting maximum temperature difference is

$$\Delta T_{max} = \frac{1}{2} Z T_C^2. \quad (2.43)$$

Similar considerations can be used to derive the efficiency of a TE power generation device, shown schematically in Figure 2.3. The efficiency of such a device η is defined as the ratio of the electrical power generated in the external load to the amount of heat that enters through the hot side.

$$\eta = \frac{I^2 R_{load}}{\alpha T_H I - \frac{1}{2} I^2 R + K \Delta T} \quad (2.44)$$

The open circuit voltage is equal to $\alpha \Delta T$, so the current is given by

$$I = \frac{\alpha \Delta T}{R_{load} + R}. \quad (2.45)$$

The expression for η obtained by combining Equations 2.44 and 2.45 can be optimized with respect to the load resistance. This gives an optimal value of

$$R_L = R \sqrt{1 + Z T_{avg}}. \quad (2.46)$$

The efficiency of the TE generator operating with the optimal load is then given by

$$\eta^* = \frac{\Delta T}{T_H} \frac{\sqrt{1 + Z T_{avg}} - 1}{\sqrt{1 + Z T_{avg}} + \frac{T_C}{T_H}}. \quad (2.47)$$

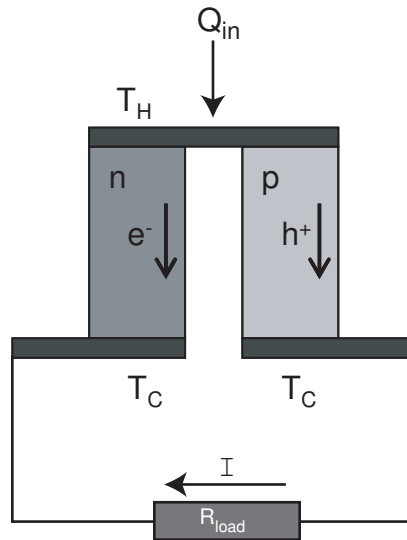


Figure 2.3: A TE couple used to illustrate TE power generation. Heat flow from T_H to T_C drives an electrical current through a load R_{load} .

So we see that both the maximum coefficient of performance (Equation 2.41) and the maximum temperature difference (Equation 2.43) of a TE refrigerator, and the maximum efficiency of a TE power generator (Equation 2.47), are all monotonically increasing functions of the parameter Z , which is called the TE figure of merit. Often the dimensionless product ZT is also called the figure of merit. This sets a very specific goal for TE materials researchers: find materials with large values of Z . This is a substantial challenge. The properties which determine Z , the Seebeck coefficient, electrical resistivity and thermal conductivity, can not be tuned independently. The electronic band structure of the material plays an important role in determining all three properties.

In what follows we will discuss the microscopic properties which lead to high ZT , and recent efforts toward first principle calculation of TE performance. Our main goal is to see how theory can lead us toward more promising TE materials.

2.3 Bulk Materials

We have learned that efficient TE materials must have high Seebeck coefficient (or thermopower) S , high electrical conductivity ρ and low thermal conductivity κ . In this section we will examine the microscopic materials properties necessary to realize this combination. In particular we will derive an expression which relates ZT for bulk semiconductors to microscopic materials parameters. The first part of this section, in which the dependence of ZT on the B parameter will be derived, is similar to the work in Refs. [4] and [5].

Using Equation 2.14 and Equation 2.17, and denoting the electronic thermal conductivity at zero electric field as κ_0 , we can write Equation 2.12 in the following form:

$$\begin{aligned} J_e &= -\sigma \left(\frac{\nabla\mu}{e} - E \right) - \frac{\sigma S}{T} \nabla T \\ J_Q &= -T\sigma S \left(\frac{\nabla\mu}{e} - E \right) - \kappa_0 \nabla T. \end{aligned} \quad (2.48)$$

We will now derive expressions for the electrical and thermal currents carried by electrons in a band, and then identify the transport coefficients by comparison with Equation 2.48.

We first consider the case of transport by a single conduction band. This is a reasonable simplification, since most good TE materials are highly doped semiconductors. The currents and fields will be directed only along x . For a single band the electrical and thermal currents are given by adding the contributions from each k state.

$$\begin{aligned} J_e &= \sum_k e v_x(k) g(k) \\ J_Q &= \sum_k [\epsilon(k) - \mu] v_x(k) g(k) \end{aligned} \quad (2.49)$$

Here $g(k)$ is the deviation from the equilibrium distribution function which will be determined by the Boltzmann equation. The expression for $g(k)$ is [6]

$$g(k) = \tau \left(-\frac{\partial f_0}{\partial \epsilon} \right) v_x \left[-e \left(\frac{\nabla \mu}{e} - E \right) - \frac{\epsilon - \mu}{T} \nabla T \right]. \quad (2.50)$$

Here f_0 is the Fermi-Dirac distribution function. Substitution of Equation 2.50 into Equation 2.49 allows the identification of the transport coefficients by comparison with Equation 2.48.

$$\begin{aligned} \sigma &= e^2 \sum_k v_x v_x \tau \left(-\frac{\partial f_0}{\partial \epsilon} \right) \\ T\sigma S &= e \sum_k v_x v_x \tau \left(-\frac{\partial f_0}{\partial \epsilon} \right) (\epsilon - \mu) \\ \kappa_0 &= \sum_k v_x v_x \tau \left(-\frac{\partial f_0}{\partial \epsilon} \right) (\epsilon - \mu)^2 \end{aligned} \quad (2.51)$$

The expressions Equation 2.51 allow the calculation of the transport coefficients for a single band from a knowledge of the band structure, the chemical potential and the scattering time. If multiple bands are present their contributions should be summed.

At this point we will make some simplifications. We'll consider anisotropic, parabolic bands and a constant relaxation time. The dispersion relation for one such conduction band, with band edge energy E_c , is

$$\epsilon(k) - E_c = \frac{\hbar^2}{2} \left[\frac{k_x^2}{m_x} + \frac{k_y^2}{m_y} + \frac{k_z^2}{m_z} \right]. \quad (2.52)$$

We'll imagine our TE material having N_c equivalent conduction bands, each described by Equation 2.52. The sums in Equation 2.51 can be converted into integral over the band energy by multiplication by the density of states. The density of states is determined by the dispersion relation (4.5) and is, noting that there are N_c equal contributions,

$$n(\epsilon) = N_c \frac{\sqrt{2}}{\hbar^3 \pi^2} \sqrt{m_x m_y m_z} (\epsilon - E_c)^{1/2}. \quad (2.53)$$

Each of the N_c bands contribute equally to the overall density of states. If we assume that transport only takes place along x then $v_x v_x = v^2 = 2(\epsilon - E_c)/m_x$. The first of Equation 2.51 can now be written as

$$\sigma = \frac{2^{3/2} N_c e \mu_x \sqrt{m_x m_y m_z}}{\hbar^3 \pi^2 k_B T} \int_{E_c}^{\infty} d\epsilon \frac{(\epsilon - E_c)^{3/2} e^{(\epsilon - \mu)/k_B T}}{(e^{(\epsilon - \mu)/k_B T} + 1)^2}. \quad (2.54)$$

Similar expression can be written for $T\sigma S$ and κ_0 . We have introduced the mobility $\mu_x = e\tau/m_x$. We now define $x = (\epsilon - E_c)/k_B T$ to make the integrals dimensionless, and the reduced chemical potential relative to the band edge $\xi = (\mu - E_c)/k_B T$. With these definitions the transport coefficients in Equation 2.51 become

$$\begin{aligned} \sigma &= \frac{2^{3/2} N_c e \mu_x \sqrt{m_x m_y m_z}}{\hbar^3 \pi^2} (k_B T)^{3/2} F_{3/2}(\xi) \\ S &= \left(\frac{k_B}{e} \right) \left[\frac{2^{3/2} N_c e \mu_x \sqrt{m_x m_y m_z}}{\sigma \hbar^3 \pi^2} (k_B T)^{3/2} F_{5/2}(\xi) - \xi \right] \\ \kappa_0 &= k_B \frac{2^{3/2} N_c \mu_x \sqrt{m_x m_y m_z}}{e \hbar^3 \pi^2} (k_B T)^{5/2} [F_{7/2}(\xi) - 2\xi F_{5/2}(\xi) + \xi^2 F_{3/2}(\xi)] \\ F_y(z) &= \int_0^{\infty} dx \frac{x^y e^{x-z}}{(e^{x-z} + 1)^2}. \end{aligned} \quad (2.55)$$

The coefficients in Equation 2.55 can now be put into the expression for ZT giving

$$\begin{aligned} ZT &= \frac{S^2 \sigma T}{\kappa_e + \kappa_L} = \frac{S^2 \sigma T}{\kappa_0 - S^2 \sigma T + \kappa_L} = \frac{F_{3/2}(\xi) \left[\frac{F_{5/2}(\xi)}{F_{3/2}(\xi)} - \xi \right]}{\left[F_{7/2}(\xi) - \frac{F_{5/2}(\xi)^2}{F_{3/2}(\xi)} \right] + \frac{1}{B}} \\ B &= \frac{2^{3/2}}{\hbar^3 \pi^2} \frac{k_B}{e} (k_B T)^{5/2} \frac{N_c \mu_x \sqrt{m_x m_y m_z}}{\kappa_L}. \end{aligned} \quad (2.56)$$

In the form of Equation 2.56 it is clear that ZT for this situation depends on the chemical potential and the B factor. The chemical potential is tunable by the experimentalist through doping. All of the relevant materials parameters appear in B. Mahan has shown that at optimal doping ZT is a monotonically increasing function of B. Thus materials with larger B values can have larger values of ZT, provided the optimal doping level can be realized.

Calculations which do not assume a constant relaxation time nor parabolic bands, and treat the presence of both electron and hole bands have been performed. The common result is that large B leads to large optimized ZT.

The case for an intrinsic semiconductor, both degenerate and non-degenerate, with energy dependent relaxation time has been studied recently by Mahan [7, 8]. The work is an extension of previous authors' treatments of this situation [9, 10, 11, 12]. He finds that ZT at optimal doping depends on B and the band gap E_G . ZT increases with increasing E_G and plateaus at about $10k_B T$. For classical statistics (non-degenerate case), in the limit of large E_G the following set of equations is derived for the saturation value of ZT.

$$\begin{aligned} (ZT)_{sat} &= \frac{\lambda(\lambda + 4)}{4\delta} \\ \lambda &= 2\delta - 4 - 2 \log \left(\frac{\lambda}{8B\delta} \right) \end{aligned} \quad (2.57)$$

Here $\delta=r+3/2$ where the relaxation time $\tau \sim \epsilon^r$. Mahan notes that for phonon and impurity scattering r has values between -1/2 and 3/2. So one expects δ to be between 2 and 3. One would like to keep the band gap near $10k_B T$ since larger values don't improve ZT for constant B, but can decrease B by increasing κ_L . Thus Equation 2.57 should only be used as a guide for estimating the maximum ZT possible for a material.

Most good thermoelectrics are highly doped semiconductors, so the applicability of classical statistics is questionable and Fermi-Dirac statistics should be used. The degenerate limit reduces to a single band problem. Mahan found that in this situation ZT depends only on B at optimal doping. He includes the dependence of the mobility on the carrier concentration, which previous authors have neglected, but finds that the results are not much changed. Mahan also shows the dependence of the optimal doping level on B. He finds that materials with low B values must be degenerately doped, so that the chemical potential moves

into the conduction band, while those with higher B values do not. This suggests another advantage of large B values, since it may be easier to reach the optimal doping level in such a material.

Sofo and Mahan also considered the effects of non-parabolic bands and different scattering mechanisms, beyond the relaxation time approximation [4]. They found again that large B is important for maximizing ZT . In this work they conclude that below $E_G=6k_B T$, ZT decreases with decreasing E_G due to the presence of minority carries (which lowers S by carrying the wrong charge along with the heat). For E_G above about $10k_B T$, ZT can either plateau, slightly decrease or continue to increase with increasing E_G depending on the band shape and scattering mechanism.

The conclusion is that B is the factor that should be maximized for good semiconductor thermoelectrics. The challenge has changed from finding a material with high ZT to finding a dopable semiconductor with large B . Here we recall the dependence of B on the material parameters,

$$B = \frac{N_c \mu_x \sqrt{m_x m_y m_z}}{\kappa_L}. \quad (2.58)$$

We'll now discuss how Equation 9.1 can lead experimentalist toward promising TE materials.

High mobility in the direction of transport is important. In an isotropic material $B \propto \tau m^{1/2}$, since $\mu=e\tau/m$. Thus one would like the high mobility in such a material to come from decreased scattering and not small band masses. Large effective masses are beneficial, and can be achieved in systems with d or f electrons which typically interact weakly with other orbitals. If the conduction or valence band extrema are composed mostly of d or f orbitals and thus relatively flat, m will be high. This is the case for the skutterudites [13], which are good thermoelectrics [14].

In an anisotropic material B has the following dependence on the effective masses and scattering time:

$$B = \tau \left(\frac{m_y m_z}{m_x} \right)^{1/2}. \quad (2.59)$$

Hence, large band anisotropy can be beneficial. One would like a small band mass in the direction of transport with large masses in the other two directions. This is the case for CsBi_4Te_6 . This compound has a layered crystal structure which leads to the anisotropic electronic structure [15]. CsBi_4Te_6 has high ZT in one direction below room temperature [16].

In both cases just described, low scattering rates are important for large B values. These low scattering rates can be achieved by reducing the electronegativity difference between atoms in the compound. Large electronegativity differences lead to charge separation between atoms. Then optical phonons can scatter charge carriers by creating electric fields due to the displacement of the charged atoms. The best thermoelectrics have low electronegativity differences.

Another important factor in B is the lattice thermal conductivity. This, of course, should be minimized. There are several ways of reducing κ_L . We'll discuss these within a simple model.

We consider the phonons as particles with a specific heat per unit volume c_v , which travel at an average speed (the speed of sound) v and collide with frequency described by the scattering time, or mean free time τ . Kinetic theory [6] gives for the thermal conductivity κ ,

$$\kappa = \frac{1}{3} c_v v^2 \tau. \quad (2.60)$$

To lower κ we can lower the specific heat of the phonons, decrease the speed of sound, or increase the phonon scattering. Often increasing phonon scattering also increases electron scattering, which can lower B as discussed above. However it is a common way of improving thermoelectric performance.

Alloying produces irregularities in the crystal lattice from which phonons can scatter, and is a common way of decreasing thermal conductivity in TE materials. The best TE materials near room temperature are alloys of Bi_2Te_3 and Sb_2Te_3 and Sb_2Se_3 [11]. The alloying reduces κ to about 2/3 of that for pure Bi_2Te_3 . Alloying can also effect the electrical properties and can serve as a means to tune the band gap [17].

Another way of decreasing κ is to include loosely bound atoms in oversized atomic cages in the crystal structure [18]. These atoms are often called "rattlers" and provide low energy optical phonon modes that can interact strongly with and scatter the acoustic phonons. Since the acoustic phonons usually carry most of the heat, the rattlers decrease the thermal conductivity. This effect was first recognized in Polydiacetylene single crystals [19]. In this compound, massive side groups are attached to the polymer backbone. The motion of these side groups is modeled using several two-level-systems, giving nice agreement with the experimentally measured thermal conductivity. This mechanism is similar to the tunneling states which are used to describe the thermal conductivity of amorphous materials [20]. Indeed, the presence of rattlers sometimes leads to glass-like temperature dependence of the thermal conductivity [21] (and ultrasonic attenuation [22]) in crystalline materials. Slack proposed the idea of an electron-crystal phonon-glass, which would conduct electricity like a crystal but conduct heat like a glass [18]. These materials would be made up of an extended covalent network which includes channels or cavities in which loosely bound guest atoms can "rattle". The germanium clathrates are an example of this concept, and have shown interesting TE properties [23]. Sales and coworkers have suggested that atomic displacement parameters (ADP's) can be a useful tool for TE researchers [24]. These are some of the first data to be determined for new compounds. Unusually large ADP's can be a signature of rattlers.

Slack also noted that most of the heat is carried by the acoustic phonons [25]. Typically optical phonons carry little heat. This is because, in most crystals, the optical phonon branches have less dispersion and therefore lower group velocities. According to Equation 2.60 κ_L varies with v^2 . If there are N atoms in the unit cell, the thermal energy is split between 3 heat carrying acoustic branches and $3N-3$ non-heat carrying optical branches. Large N can therefore lead to lower values of κ_L .

Yet another way of achieving low thermal conductivity is the use of heavy atoms. The utility of heavy atoms can be shown by consideration of a 1-D chain of atoms of mass M separated by a distance a with nearest neighbor interactions described by the force constant K . This leads to the dispersion relation [6]

$$\omega(k) = 2\sqrt{\frac{K}{M}} \left| \sin \frac{1}{2}ka \right|. \quad (2.61)$$

The group velocity is determined by $d\omega/dk$,

$$v(k) = \pm a\sqrt{\frac{K}{M}} \cos \frac{1}{2}k. \quad (2.62)$$

positive for $0 \leq k \leq \pi/a$, negative for $-\pi/a \leq k \leq 0$. Larger atomic masses lead to lower sound velocities which by Equation 2.60 lead to lower thermal conductivities.

Near room temperature the most important intrinsic source of phonon scattering is the phonon-phonon interactions known as umklapp processes [6]. Due to the presence of the periodic potential, collisions need only to conserve the phonon wave vector to within a reciprocal lattice vector \mathbf{K} , and umklapp processes denote those collisions in which $\mathbf{K} \neq 0$. A diagram of a two phonon umklapp process is shown in Figure 2.4.

Two phonons with wave vectors \mathbf{k}_1 and \mathbf{k}_2 come in, and one phonon with wave vector \mathbf{k}_3 leaves the interaction. Since the vector sum of \mathbf{k}_1 and \mathbf{k}_2 (Figure 2.4) is outside the first Brillouin zone (BZ), it is returned to the first BZ by

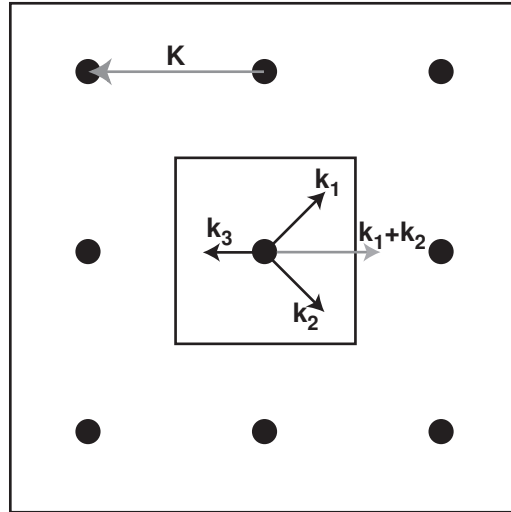


Figure 2.4: An umklapp process in which phonons with wave vectors \mathbf{k}_1 and \mathbf{k}_2 interact, with the help of a reciprocal lattice vector \mathbf{K} , to produce a phonon \mathbf{k}_3 with momentum opposite to that of the vector sum $\mathbf{k}_1 + \mathbf{k}_2$.

the addition of a reciprocal lattice vector \mathbf{K} . The net result is that the phonons are scattered “backwards”. These types of processes will occur only if there are populated phonon modes with wave vectors large enough to combine to reach outside the first BZ. Since only low wave vector (low energy) phonon modes are populated significantly at low temperatures, umklapp process “turn on” above a particular temperature. Below this temperature, phonons are scattered at a temperature independent rate by point defects, grain boundaries, and at the sample surfaces (neglecting any electron-phonon interactions which might give a temperature dependence to the phonon scattering time τ). Thus, at low temperatures, the thermal conductivity increases as the specific heat increases, like T^3 . To achieve low thermal conductivity, it is advantageous to have umklapp scattering begin at temperatures far below the operation temperature. Large direct-space unit cell volumes lead to small first BZ volumes in k -space, and thus allow umklapp scattering to occur for smaller wave vectors and thus at lower temperatures. Alternatively, if the phonon energy increases slowly with increasing k , then

modes with large k can be populated even at low temperatures. This too allows umklapp scattering to occur at lower temperatures. The dispersion relation given above (Equation 2.52) shows that the phonon energy will increase slowly with k when the ratio K/M is small. Thus heavy atoms (large M) and weak bonds (small K) will enhance umklapp scattering. The Debye temperature Θ_D is a measure of a “characteristic” phonon energy, and so a low Debye temperature suggests that a material will have low thermal conductivity at room temperature. Note that heavy atoms play a dual role in lowering κ by decreasing both v and τ in 2.60.

Finally, the degeneracy of the band extremum N_c appears in B. This should be large for good thermoelectrics. One would like to have as many bands as possible contributing to the electronic transport. Very little work has been done toward increasing this parameter. There are two contributions to N_c . One is accidental degeneracy, having other band extrema within about $k_B T$ of the lowest conduction band or highest valence band. The other is the degeneracy imposed by the symmetry of the crystal structure. The symmetry operations of the crystal can produce equivalent band extrema. In the highest symmetry cubic systems $N_c=48$ for a general position in the Brillouin zone. In the lowest symmetry case $N_c=1$ for a general position. High symmetry structures therefore have greater potential than low symmetry structures. The best TE at room temperature, Bi_2Te_3 based alloys, have $N_c=6$. It is trigonal ($R\bar{3}m$) and has the band extrema at a general position, according to DFT calculations and experiment [26]. If spin-orbit interactions are not included in these calculations the band extrema occur at a high symmetry point and $N_c=2$. So it seems that SO coupling can also help to increase N_c . Heavy atoms exhibit stronger SO coupling, so their inclusion may help increase N_c as well as decrease κ_L .

In summary, these are the suggestions that the theory described above provides to the experimentalist searching for improved TE materials:

1. Examine semiconductors (which can be heavily doped) with a band gap around $10k_B T$, where T is the temperature of operation.
2. Include transition metals or rare earth elements, since d and f orbitals generally produce bands with large m_i .
3. Look for compounds with indirect band gaps which typically lead to large m_i .
4. Examine systems in which there is little electronegativity difference among the atoms. This will improve the mobility by decreasing polar scattering.
5. Try alloying similar compounds to reduce κ_L .
6. Investigate complex structures with many atoms per unit cell. This gives more optical modes which can lower κ_L . Complex structures may also be more likely to have band extrema away from special positions, leading to larger N_c . Large unit cells may also lead to increased umklapp scattering of phonons.
7. Look for structures with open channels or cavities in which rattling guest atoms can reside, or for compounds with evidence of rattling (large ADP's). This will reduce κ_L .
8. Include heavy atoms. This will reduce κ_L by decreasing sound speeds, and it can improve N_c through SO coupling.
9. Focus on high symmetry structures. These can have high values of N_c imposed by symmetry.
10. Take advantage of anisotropy. Small effective masses in the direction of transport along with large effective masses perpendicular to transport are advantageous.

2.4 Low Dimensional Systems

In the previous section the advantages of anisotropy in the electronic structure were noted. This has led to interest in the TE properties of quantum well devices, in which thin layers of the TE material are sandwiched between layers of a wide band gap material. This confines the charge carriers to move in two dimensions. Recently Hicks and Dresselhaus have proposed large improvements in ZT for such systems [5, 27].

In their treatment only the lowest energy level corresponding to the confinement in the direction perpendicular to the layers is considered. The dispersion relation is then, for parabolic bands within the layers,

$$\epsilon(k) = \frac{\hbar^2}{2} \left[\frac{k_x^2}{m_x} + \frac{k_y^2}{m_y} + \frac{(\pi/a)^2}{m_z} \right]. \quad (2.63)$$

Here a is the thickness of the TE layer. The calculations proceed similarly to those presented in the previous section. Hicks and Dresselhaus find that ZT is a function of the chemical potential and B_{2D} which is given by

$$B_{2D} = \frac{1}{\hbar^2 \pi} \frac{k_B}{e} (k_B T)^2 \frac{\mu_x \sqrt{m_x m_y}}{a \kappa_L}. \quad (2.64)$$

The thickness of the TE layer is seen to be a new parameter which can be used to increase B.

They calculate that for Bi_2Te_3 layers $Z_{2D}T$ can be increased by a factor of 13 over the bulk value by decreasing a to 5 Å. This is true for layers prepared in the a-c plane. For layers in the a-b plane $Z_{2D}T$ is still increased over the bulk value, but only by a factor of three. In a separate work they find that in a quantum well device, bismuth metal ($Z_{2D}T=8$ at 10 Å) actually outperforms Bi_2Te_3 ($Z_{2D}T=5$ at 10 Å), suggesting that one need not start with a high ZT bulk material to achieve high $Z_{2D}T$.

In their work, Hicks and Dresselhaus point out that in addition to the direct dependence of B_{2D} on a in 2.64, decreasing a can increase B indirectly by decreasing κ_L . If the layer thickness becomes comparable to the intrinsic phonon scattering length of the material (about 10 \AA for Bi_2Te_3), κ_L can be dominated by interface scattering. Even at larger values of a , interface scattering can appreciably affect κ_L . Thus decreasing a can decrease κ_L , improving B_{2D} .

Based on the discussion above, quantum wells seem promising for TE applications. However, Mahan and Lyon [28], and Sofo and Mahan [29], have found that a more careful treatment of the problem predicts much more modest improvements than those reported above. In particular they consider the effects of the electrically insulating barrier material that separates the TE layers. They note that these layers will conduct heat, but will do no TE pumping. Thus they simply add to the lattice thermal conductivity, decreasing B and the figure of merit. Making these layers thinner will help with this problem. However, thin barriers allow tunneling between TE layers which broadens the subbands in the directions parallel to the superlattice.

Instead of the flat band model used by Hicks and Dresselhaus, Sofo and Mahan use the more realistic Kronig-Penney model. In the limit of thick barrier layers these are equivalent. However, Sofo and Mahan note that when the period of the superlattice (thickness of TE layer plus barrier layer) becomes small, mixing between the wells produces dispersion in the lowest subband. This makes the system more three dimensional and the advantage of the anisotropy is diminished. They show that for large periods the optimized chemical potential lies above the lowest subband. ZT increases with decreasing period until the lowest subband broadens such that the chemical potential lies within it. Then ZT decreases as the period is further reduced. Their calculations for Bi_2Te_3 based superlattices showed a maximum enhancement of about a factor of two.

Thus 2-D quantum well superlattices (and 1-D quantum wires [5]) can have improved TE properties. However interactions between subbands in neighboring wells must be considered, and these systems will always be plagued by the parasitic heat conduction of the supporting materials used to construct the devices.

2.5 Calculations of Thermoelectric Properties

Much theoretical work has been directed at a microscopic calculation of the transport properties of TE materials. Here we review the results from some recent work, mainly by Mahan and coworkers. In particular, Mahan [30] has introduced the transport distribution, abbreviated TD and symbolized by Ξ , and used it to calculate and optimize thermoelectric performance. The thermopower, electrical conductivity and electronic thermal conductivity can all be calculated from the TD. Also, the TD has some physical significance that gives an alternative view of what makes a good TE material.

First we recall the scalar form of the transport coefficients given above in Equation 2.51 and include the k dependence of v and τ explicitly.

$$\begin{aligned}\sigma &= e^2 \sum_k v_k^2 \tau_k \left(-\frac{\partial f_0}{\partial \epsilon} \right) \\ T\sigma S &= e \sum_k v_k^2 \tau_k \left(-\frac{\partial f_0}{\partial \epsilon} \right) (\epsilon - \mu) \\ \kappa_0 &= \sum_k v_k^2 \tau_k \left(-\frac{\partial f_0}{\partial \epsilon} \right) (\epsilon - \mu)^2\end{aligned}\tag{2.65}$$

The sums over can be changed to an integral over energy giving, for example

$$\sigma = e^2 \int_{-\infty}^{\infty} \left(-\frac{\partial f_0}{\partial \epsilon} \right) \sum_k [v_k^2 \tau_k \delta(\epsilon - \epsilon(k))] d\epsilon.\tag{2.66}$$

In Equation 2.66 the delta function picks out all of the k states that contribute to the integral at energy ϵ . Mahan defines the TD as

$$\Xi(\epsilon) = \sum_k v_k^2 \tau_k \delta(\epsilon - \epsilon(k)). \quad (2.67)$$

In terms of the TD, the transport coefficients can be written as,

$$\begin{aligned} \sigma &= e^2 \int_{-\infty}^{\infty} \left(-\frac{\partial f_0}{\partial \epsilon} \right) \Xi(\epsilon) d\epsilon \\ S &= \frac{ek_B}{\sigma} \int_{-\infty}^{\infty} \left(-\frac{\partial f_0}{\partial \epsilon} \right) \Xi(\epsilon) \left(\frac{\epsilon - \mu}{k_B T} \right) d\epsilon \\ \kappa_0 &= k_B T \int_{-\infty}^{\infty} \left(-\frac{\partial f_0}{\partial \epsilon} \right) \Xi(\epsilon) \left(\frac{\epsilon - \mu}{k_B T} \right)^2 d\epsilon. \end{aligned} \quad (2.68)$$

To regain the tensor form of the transport coefficients, the tensor form of the TD is used by replacing v_k^2 by the outer product $v_k v_k$ in Equation 2.67.

All of the material dependent parameters (the electronic structure and scattering times) are included in the TD. Knowledge of the band structure and a model for the carrier scattering mechanisms allows calculation of ZT as a function of temperature and chemical potential μ .

Scheidemantel et al. point out the TD is relatively easy to calculate and can provide a means of comparison between materials, and for screening new potential TE materials [26]. The TD can be thought of as a weighted density of states, which weights states by how they contribute to conduction along particular directions. Since $\partial f_0 / \partial \epsilon$ is sharply peaked around $\epsilon = \mu$, one can approximate the TD as linear over the range of integration: $\Xi(\epsilon) = \alpha(\epsilon - \mu) + \beta$. It follows that the TE power factor $PF = S^2 / \rho$ is proportional to α^2 / β . Thus TE performance will be best when $\Xi(\epsilon)$ has a large slope and small height. In the limit of an isotropic material with constant scattering time the TD is proportional to the density of states. In such a case, optimal doping should occur when the chemical potential reaches edge of rapid increase (or decrease) in the DOS. Sharp peaks in the DOS (which

can correspond to sharp peaks in the TD) can lead to good TE performance. This was noted above when the benefit of narrow f or d bands was discussed.

Scheidemantel and coworkers calculated the thermoelectric properties of the most studied thermoelectric material, Bi_2Te_3 based alloys [26]. In this work, the authors use first-principles calculations to obtain the electronic structure of the material. The scattering mechanisms are modeled empirically. However they note that many of the parameters describing the scattering can be obtained from their calculations. The precision of this method is lower than that of the more empirical models that use many experimental results to parameterize band structures and scattering. However, this technique has much promise in the realm of new materials, where empirical data may be scarce and only crystal structure data are available.

The authors use the local density approximation (LDA) with the linear augmented plane wave (LAPW) method to calculate band structures. Spin-orbit coupling is found to be essential to obtaining the correct electronic structure. The scattering mechanisms are described by experimentally determined parameters at this stage, with hope of eventually calculating many or all of these from first principles. Doping is very important in thermoelectric materials and must be treated by the calculation. They use a rigid band model, in which the band structure does not change with doping level. This should be acceptable at low doping levels, but would certainly be inaccurate at doping levels in which the bonding in the compounds is significantly changed. Doping is simulated simply by displacing the Fermi level up (n-type) or down (p-type). Experimentally determined lattice thermal conductivities were used. All calculations were performed at 300 K.

The authors show the dependence of the TE properties on the in-plane conductivity σ_{xx} as a function of doping. Their results are reproduced in the

figure below. The dashed line represents reported experimental data. First they show the results for the in-plane thermopower S_{xx} . The only parameter used to fit theoretical results to the experimental data is a single, constant relaxation time. The agreement is quite good, especially on the n-doped side. The authors also show the calculated conductivity anisotropy, measured by σ_{xx}/σ_{zz} , at different doping levels, along with experimental data. The strong disagreement at high doping (high conductivity) is attributed to the possible failure of the rigid band model at those doping levels. Using the same isotropic scattering time as used to fit the thermopower data above gives the dashed line, which agrees well with experiment. Even better agreement can be achieved by the use of a small (5%) anisotropy in the scattering time (solid line).

The effects of doping on ZT are also calculated, and show reasonable agreement with experimental results. In this work, the authors state that they are working to incorporate a better model for the scattering into their calculations. They regard this paper as "the first step toward the ultimate goal of a parameter free evaluation of thermoelectric transport coefficients."

The same group also used this method to study the pressure dependence of the thermoelectric properties of Sb_2Te_3 [31]. The stress (hydrostatic and uniaxial) was determined by fitting the total energy surface calculated for 312 different values of the hexagonal lattice parameters a and c . Interesting behavior, including improved TE properties and metallization (under uniaxial stress) are predicted. One of the most interesting results of this work is that upon metallization, Sb_2Te_3 retains a non-negligible thermopower ($\sim 100\mu\text{V}/\text{K}$) which is not typical of a metal. This is due to the special behavior of the TD under uniaxial stress. The DOS for states below the Fermi energy increases with applied stress, and their velocities do not decrease. The states above the Fermi energy change relatively little. This leads to an asymmetric TD near the Fermi energy which is

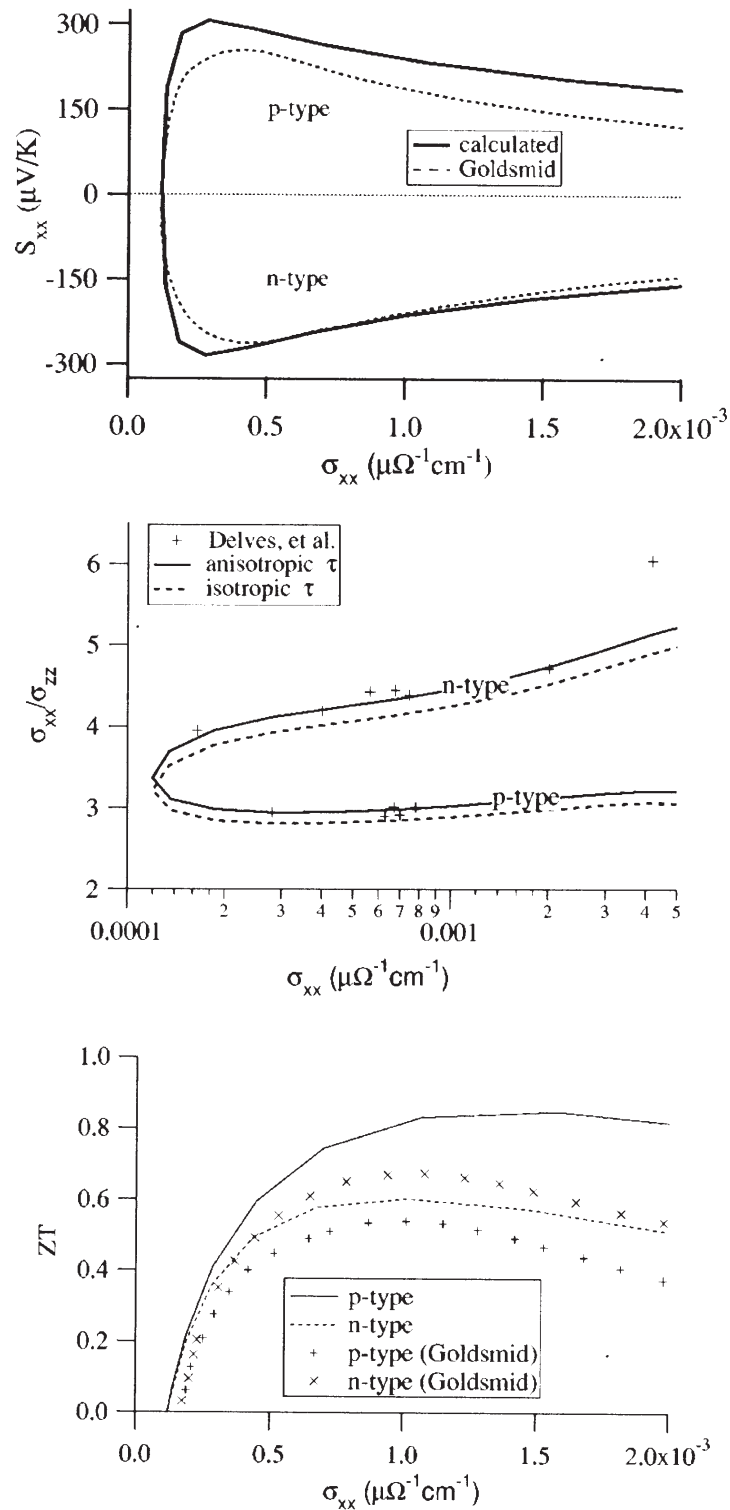


Figure 2.5: Figures taken from Ref. [26] showing the dependence of the calculated TE properties of Bi_2Te_3 alloy on doping level, and how they compare to experimental values.

responsible for the large thermopower. As a result, the TE power factor increases by more than a factor of four at pressures near 4 GPa.

Later this group used the TD to study the TE properties of bismuth metal [32]. They use the rigid band model for doping and a constant relaxation time. The calculated values for the x and z components of the thermopower of $S_{xx} = -107 \mu\text{V}/\text{K}$ and $S_{zz} = -47 \mu\text{V}/\text{K}$ agree well with experimental values of $-103 \mu\text{V}/\text{K}$ and $-50 \mu\text{V}/\text{K}$, respectively.

They note two pronounced peaks in the power factor as a function of doping that exceed that of Bi_2Te_3 . The peaks in the PF are found where the TD has, in particular, a steep slope. They go on to calculate ZT as a function of doping and find a maximum of $ZT = 1.4$, significantly higher than Bi_2Te_3 alloys at 300K. They suggest tin as a possible dopant (about 1 atomic % is needed to maximize ZT).

Mahan has written many other papers on the theory of thermoelectricity. Including the effects of inhomogeneous doping [33]. Since T varies as a function of distance along the TE element, so does the optimum doping concentration which is a function of T. Inhomogeneous doping can take advantage of this to improve the overall efficiency. This will be addressed again in a later Section of this Chapter, in which segmented TE generators are discussed.

The final paper that will be discussed in this section is an article by Mahan and Sofo entitled "The best thermoelectric" [30]. This is also the paper in which they first introduced the TD. In this work they discuss upper bounds on ZT and what electronic structure is needed to attain those values. They begin by making the following definitions, and introducing the Bohr radius a_0 , to simplify the forms of the transport coefficients given in Equation 2.65:

$$\begin{aligned} \sigma_0 &= \frac{e^2}{\hbar a_0} \\ I_n &= \int_{-\infty}^{\infty} dx \frac{e^x}{(e^x - 1)^2} s(x) x^n \end{aligned} \quad (2.69)$$

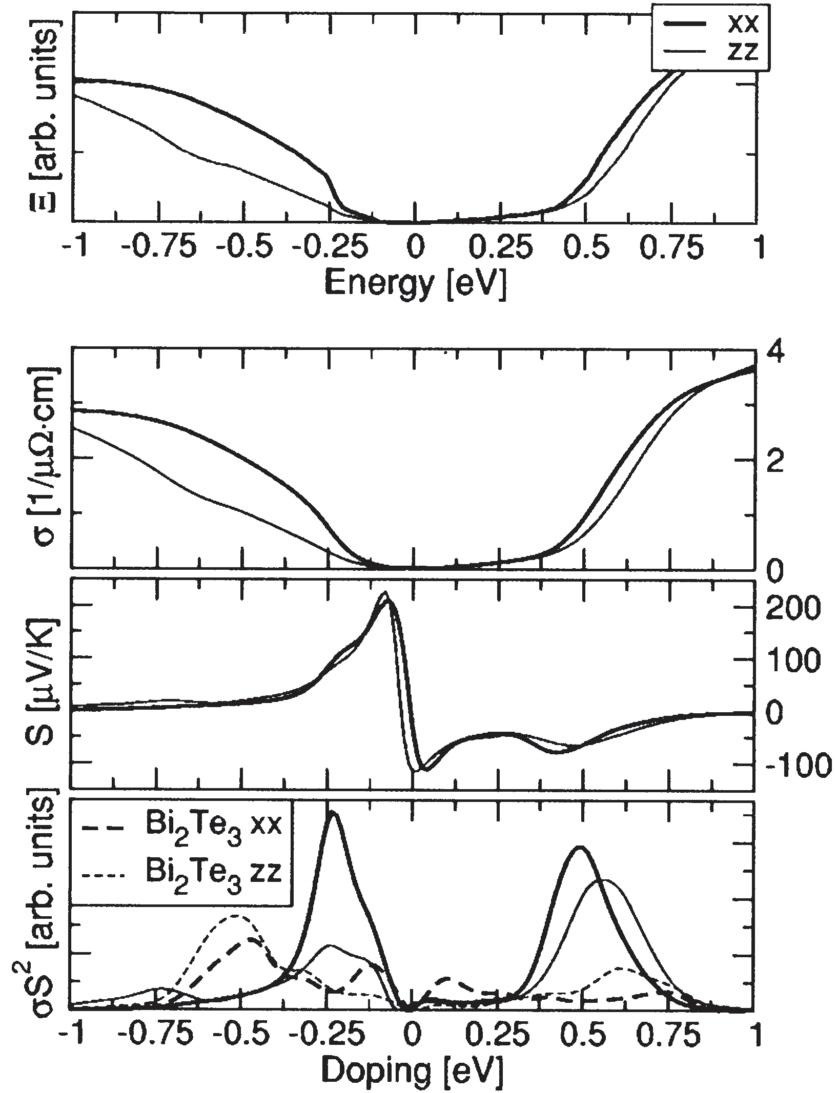


Figure 2.6: Figure from Ref. [32]. The TD as a function of energy measured from the Fermi level, and the conductivity σ , thermopower S and PF of Bi as a function of the chemical potential (doping). Calculations for Bi_2Te_3 are shown for comparison.

$$s(x) = \hbar a_0 \Xi (\mu + x k_B T).$$

The transport coefficients are then given by

$$\begin{aligned}\sigma &= \sigma_0 I_0 \\ \sigma S &= \left(\frac{k_B}{e}\right) \sigma_0 I_1 \\ \kappa_0 &= \left(\frac{k_B}{e}\right)^2 T \sigma_0 I_2.\end{aligned}\tag{2.70}$$

Using Equation 2.70 the TE figure of merit ZT can be written as

$$\begin{aligned}ZT &= \frac{\xi}{1 - \xi + A} \\ \xi &= \frac{I_1^2}{I_0 I_2}, A = \frac{1}{\alpha I_2}, \alpha = \left(\frac{k_B}{e}\right)^2 \frac{T \sigma_0}{\kappa_L}.\end{aligned}\tag{2.71}$$

So, all that is needed to calculate ZT is the lattice thermal conductivity and the TD or equivalently $s(x)$. It can be proved that $\xi \leq 1$. The authors found that ZT is maximized as $\xi \rightarrow 1$ and $A \rightarrow 0$. Clearly A can never equal zero since κ_L can not be reduced to zero. Thus ZT is bounded and can not be infinite. For $\xi = 1$, $ZT = 1/A$. This is the upper bound on ZT . From Equation 2.71 and the definition of σ_0 then,

$$ZT \leq \frac{1}{A} = \frac{\kappa_0}{\kappa_L}.\tag{2.72}$$

The authors find that the only $s(x)$ that gives $\xi = 1$ is the Dirac delta function. They proceed then to find the maximum ZT for a material with $s(x)$ given by

$$s(x) = f(x) \delta(x - b).\tag{2.73}$$

The integrals in Equation 2.70 can then be calculated and give

$$\begin{aligned}\sigma &= \sigma_0 D(b) f(b) \\ S &= \left(\frac{k_B}{e}\right) b \\ \kappa_0 &= \left(\frac{k_B}{e}\right)^2 T \sigma_0 D(b) f(b) b^2 \\ D(x) &= \frac{e^x}{(e^x + 1)^2}.\end{aligned}\tag{2.74}$$

These give $ZT = \kappa_0 / \kappa_L$. To maximize ZT then, κ_0 must be maximized. They consider the case where $f(x) = C$, independent of x , and maximize the function $b^2 D(b)$. This occurs for $b = 2.4$. That is, the resonance in the TD should be $2.4k_B T$ above or below the chemical potential. This gives $S = 207 \mu V / K$, which agrees well with experimental values for good thermoelectrics. Finally, the optimal ZT is

$$(ZT)_{max} = 0.44 \left(\frac{k_B}{e} \right)^2 \frac{\sigma_0 T C}{\kappa_L}. \quad (2.75)$$

The authors note that the highest value of the power factor known occurs in the intermetallic compound $YbAl_3$. The rare-earth f-levels (nature's closest approximation to a delta function) are known to be near the chemical potential. This supports their conclusion that good TE should have a sharp peak in the TD (or DOS) near the chemical potential. This is consistent with the arguments given in the general discussion of bulk materials above, which suggested using d or f levels to get flat bands to increase the effective masses. Here this same effect is manifested in a rapid change in the TD. The benefit of a rapidly changing TD near the Fermi level has already been pointed out above.

The authors then consider the maximum ZT for a compound containing rare earth elements with the density of f-levels denoted by n . The DOS is then assumed to have the form $N(\epsilon) = n \delta(\epsilon - b k_B T)$. For parabolic bands the TD can be written as

$$\Xi(\epsilon) = N(\epsilon) v(\epsilon)^2 \tau(\epsilon). \quad (2.76)$$

This, along with Equation 2.73 and Equation 2.75, gives an expression for the maximum ZT of such a compound:

$$(ZT)_{max} = 0.15 \frac{v^2 \tau n k_B}{\kappa_L}. \quad (2.77)$$

Assuming typical values for the parameters, they derive a maximum of $ZT = 14$. This more than 10 times higher than any known material's ZT at room tempera-

ture. Finally, they go on to consider the effect of a constant background in addition to the delta function in the density of states, and find that this significantly decreases the maximum ZT.

2.6 Other Considerations for Devices

In addition to the work on the microscopic theory of the transport coefficients of TE materials described above, there have been some recent theoretical considerations of actual TE devices. In this section we will discuss the compatibility of materials used in segmented devices, and the effect of "transient supercooling" of a Peltier junction.

One of the most important applications of TE devices is their use in radioisotope thermoelectric generators (RTG's) by NASA. These devices use heat generated by radioactive decay of PuO_2 to generate the electricity needed to power space probes that are too far from the sun to use solar power. Temperature differences across the devices of several hundreds of degrees are common. In this situation, the temperature dependence of the TE materials' properties can not be ignored. There is no single material which performs well over such a large temperature range. Several different materials are segmented in series, those with the best ZT at high temperature at the hot side, those that perform well at lower temperature nearer the cool side. This can significantly improve the overall efficiency.

Snyder and Ursell [34] write the efficiency of a TE material used for power generation with temperature dependent transport properties in the following way [35].

$$\eta = \frac{J \int_{T_C}^{T_H} S dT - J^2 \int_0^l \rho dx}{JT_H S + \kappa \nabla T} \quad (2.78)$$

They define the quantity they call the relative current density,

$$u = \frac{J}{\kappa \nabla T}. \quad (2.79)$$

The reduced efficiency η_r is defined as the ratio of the efficiency to the Carnot efficiency given by $\eta_C = \Delta T/T_H$. Using Equation 2.78 in the limit of small temperature difference, and the definition Equation 2.79 the authors write the reduced efficiency as

$$\eta_r = \frac{u \frac{S}{Z} (1 - u \frac{S}{Z})}{u \frac{S}{Z} + \frac{1}{ZT}}. \quad (2.80)$$

This can then be optimized to find the value of u which gives the best efficiency. They define this optimal u to be the compatibility factor (CF) for that material:

$$CF = \frac{\sqrt{1 + ZT} - 1}{ST}. \quad (2.81)$$

Materials that are segmented together should have similar values of CF if they are expected make positive contributions to the overall efficiency.

Thus, having materials with high ZT at different temperatures is not sufficient to build an efficient segmented generator. The authors state that the compatibility factors should not vary by more than a factor of two between the different materials in each leg of the generator. Compatibility is a considerable obstacle to the development of high temperature TE generators. Currently there is no commercial p-type material that can work efficiently in the 800-1000°C range except Si-Ge alloys. Unfortunately these alloys are not compatible with the other materials used in the p-type leg of these devices. Si-Ge has a larger S and larger ρ than the other materials, giving it a comparable ZT . However, S appears in the denominator of Equation 2.81. This gives Si-Ge a CF that is too low to be efficiently segmented into the generators. There is a need for a new p-type material to replace Si-Ge.

We will now discuss the effect of transient supercooling. In the steady state, the maximum temperature drop for optimized Bi_2Te_3 alloys is 82 K. A

pulsed current input can create transient cooling which exceeds this value. This effect can be understood in the following way. The Peltier cooling occurs at the cold junction, while the Joule heating occurs throughout the material. Thus a pulse of current produces a pulse of cooling beyond the steady state situation before the Joule heat arrives at the cold junction. Of course, after the pulse the excess Joule heat arrives and heats the cold junction to a temperature above the steady state value. Thonhauser et al. have considered theoretically the effect of the peak shape on the magnitude of this supercooling effect [36].

They consider a TE material (denoted by subscript t) and the metal contact (subscript m) at the cold end. That is, they treat one leg of the couple in Figure Equation 2.2. The temperature distribution in the TE and metal is determined by the heat equation, and matching the temperature and heat flux at their interface $x=a$. They assume no temperature dependence in the materials' properties. Introducing c to represent the specific heat, they write

$$\begin{aligned}
 c_t \frac{\partial}{\partial t} T_t(x, t) &= \kappa_t \frac{\partial^2}{\partial x^2} T_t(x, t) + \rho_t J(t)^2 \\
 c_m \frac{\partial}{\partial t} T_m(x, t) &= \kappa_m \frac{\partial^2}{\partial x^2} T_m(x, t) + \rho_m J(t)^2 \\
 \kappa_t \frac{\partial T_t}{\partial x}(a, t) - S J(t) T_t(a, t) &= \kappa_m \frac{\partial T_m}{\partial x}(a, t) \\
 T_t(a, t) &= T_m(a, t).
 \end{aligned} \tag{2.82}$$

The solution to Equation 2.82 was determined numerically using the properties of optimized Bi_2Te_3 alloy for the TE material and copper for the metal. They keep the hot side at 300K and solve for the temperature at the top of the copper contact. Current pulses of varying shapes, but with identical lengths and maximum heights, are superimposed on the optimal steady state current. The pulses had time dependence proportional to t^p , where $p=0, 1/3, 1/2, 1, 2, 3, 4, 5$. The height and length of the pulses were those which maximized the temperature drop for

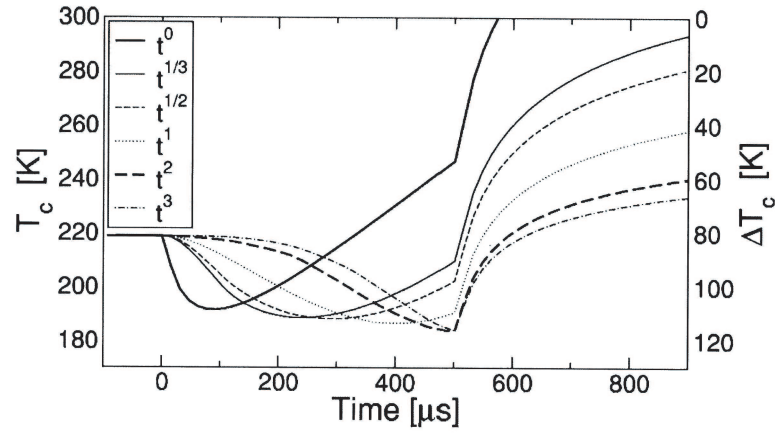


Figure 2.7: Figure from Ref. [36]. The calculated cold side temperature of a Bi_2Te_3 TE device subjected to current pulses with time dependence t^p superimposed on the optimal steady state current.

the $p=0$ case. The results are summarized in Figure 2.7. They find that the supercooling is greatest for $p=2$.

With $p=2$ the maximum temperature drop of 116 K is attained. This is 34 K greater than the steady state temperature drop, and 8 K greater than the simple T_0 pulse. An effective ZT can be calculated from Equation 2.43 for this situation, by comparing it to the steady state ZT :

$$\frac{(ZT)_{eff}}{ZT} = \frac{\Delta T_{p=2}}{(T_H - \Delta T_{p=2})^2} \frac{(T_H - \Delta T_{SS})^2}{\Delta T_{SS}}. \quad (2.83)$$

This gives $ZT_{eff}/ZT=2.01$ for $p=2$, significantly greater than $ZT_{eff}/ZT=1.76$ for the $p=0$ case. The parameters (duration, maximum height) of a pulse with a quadratic time dependence can be further optimized, and the authors report that initial investigations into this results in several more degrees of supercooling, at least.

Miner et al. considered constructing a thermoelectromechanical refrigerator based on transient supercooling [37]. Mechanical cantilevers would be used to make periodic contact between the cold substrate and the cold end of the Peltier

cooler. They consider periodic pulses of constant amplitude ($p=0$) with the duration and height optimized to give the maximum supercooling. The authors calculate, in a manner similar to Thonhauser et al. discussed above, that if the cold substrate is in contact with the Peltier cooler when the pulse is on, and not in contact between pulses, a steady state temperature difference of 108 K can be achieved.

2.7 Comments about the Seebeck Coefficient

We will conclude this work by discussing in more detail the Seebeck coefficient S . Of the transport coefficients S , σ and κ , the Seebeck coefficient is certainly the least familiar and intuitive. It is not as easy to attach a physical meaning to S . In addition, it has been the author's experience in reading the TE materials literature that the many diverse equations for S found in papers' Introductions can be bewildering. Here we will discuss what S really is, and some formulas for it, valid in different situations.

Using arguments of kinetic theory, one can deduce a simple formula for S for the free electron theory of metals [6]. For the average velocity of charge carriers crossing a plane due to the different thermal energies of the particles on either side one finds

$$v_Q = -\frac{\tau}{3m} \frac{c_v}{n} \nabla T. \quad (2.84)$$

Here τ is the mean free time or scattering time and m , c_v , and n are the electronic mass, specific heat and density, respectively. The diffusion of the charged particles causes a separation of charge in the material, which produces an electric field. In the steady state, the average velocity imparted to the carriers by this electric field is equal to that originating from the thermal gradient (Equation 2.84). The ratio of the electric field to the temperature gradient gives the Seebeck coefficient.

In this case,

$$S = -\frac{c_v}{3ne}. \quad (2.85)$$

The specific heat can be calculated in the Drude and Sommerfeld models.

$$\begin{aligned} S_{Drude} &= -\frac{k_B}{2e} = -430\mu V/K \\ S_{Sommerfeld} &= -\frac{\pi^2}{6} \frac{k_B}{e} \left(\frac{k_B T}{E_{Fermi}} \right) = -\left(\frac{k_B T}{E_{Fermi}} \right) \cdot 140\mu V/K. \end{aligned} \quad (2.86)$$

This is one of the classic failures of the Drude model. Metals have S on the order of a few $\mu V/K$, which the Sommerfeld model predicts correctly. However, semiconductors with low carrier concentration, which can be described by classical statistics, have S on the order of that predicted by the Drude model. We note here that since c_V is the heat capacity per unit volume, and n is the number of electrons per volume, we can write $S=C/3e$ where C is the heat capacity per electron. Thus, S in this model is proportional to the ratio of how much heat the electrons carry to how much charge they carry. So large S is realized by having a large heat capacity per charge carrier.

We will move away from the free electron picture now, and consider transport in bands. In particular we recall here that S can be written in terms of the transport distribution (denoted in this work by $\Xi(\epsilon)$ and abbreviated as TD, the notation used by Mahan, but called $\sigma(\epsilon)$ in most earlier references). As shown earlier in Equation 2.68,

$$\begin{aligned} S &= \frac{k_B}{e} \left[\frac{\int_{-\infty}^{\infty} \left(-\frac{\partial f_0}{\partial \epsilon} \right) \Xi(\epsilon) \left(\frac{\epsilon - \mu}{k_B T} \right) d\epsilon}{\int_{-\infty}^{\infty} \left(-\frac{\partial f_0}{\partial \epsilon} \right) \Xi(\epsilon) d\epsilon} \right] \\ \Xi(\epsilon) &= \sum_k v_k^2 \tau_k \delta(\epsilon - \epsilon(k)). \end{aligned} \quad (2.87)$$

The integrands in Equation 2.87 are significantly different from zero only near the Fermi level. They can thus be evaluated using the Sommerfeld expansion [6]

giving

$$S = \frac{\pi k_B}{3 e} k_B T \left[\frac{d}{d\epsilon} \log \Xi(\epsilon) \right]_{\epsilon=E_{Fermi}} . \quad (2.88)$$

It is common to see some variation of this form of S in the materials literature, for both metals and semiconductors. According to Equation 2.88, large S is obtained by having a strong energy dependence of the TD near the Fermi level. Equation 2.87 shows that this can arise through the energy dependence of the velocity, scattering time or DOS. The edge of a band of large effective mass is a good place to find a rapid change in the DOS with energy. It's not clear that the treatment leading to Equation 2.88, geared toward metals, should apply in this situation, but the result is consistent with the interpretation of a "good" TD described by Scheidemantel et al. [26] discussed above.

It is also instructive to derive S by applying Maxwell-Boltzmann statistics to a doped semiconductor with small carrier density [8]. The calculation will be similar to that in the earlier discussion of bulk materials, but more general since we will not specify the form of the deviation $g(k)$ from the equilibrium distribution. We will however restrict ourselves to the case of zero temperature gradient, and consider the electric field to be the only driving force. The conductivity σ and the product $T\sigma S$ can then be read off by comparison of Equations 2.48 and 2.49, adapted to these conditions. We find the following expression for S, analogous to Equation 2.55:

$$\begin{aligned} S &= \frac{k_B}{e} \left[\frac{r_1}{r_2} - \xi \right] \\ \xi &= (\mu - E_C) / k_B T \\ r_n &= \sum_k v_k g(k) [\epsilon(k) / k_B T]^n . \end{aligned} \quad (2.89)$$

The quantity ξ can be related to the carrier density n .

$$n = N_C \left(\frac{m k_B T}{2\pi\hbar} \right)^{3/2} f(\xi)$$

$$f(\xi) = \frac{2}{\sqrt{\pi}} \int_0^{\infty} \sqrt{x} e^{\xi-x} dx = e^{\xi} \quad (2.90)$$

$$x = \epsilon(k)/k_B T$$

Using Equation 2.90 to replace ξ in Equation 2.89 gives for the Seebeck coefficient,

$$S = \left(\frac{k_B}{e} \right) \left[\frac{r_1}{r_2} + \ln(n_0) - \ln(n) \right]. \quad (2.91)$$

This expression tells us that S decreases as the carrier concentration n increases. Since the conductivity increases with n it can be shown that the power factor has a maximum at some optimal carrier concentration (that this is true experimentally and occurs at 10^{18} - 10^{21} cm⁻³ has been known since Ioffe's initial investigations into TE materials [38]).

Finally we will address briefly the case of strongly correlated systems. These systems are currently receiving much attention in condensed matter physics, including TE materials research. In deriving transport coefficients for systems with large correlations, the one electron Boltzmann theory used above should be replaced by the Kubo formulation [39]. A formula for the Seebeck coefficient for these systems which is similar to those derived above from Boltzmann transport theory but with the Hubbard Hamiltonian H replacing the band energy.

$$S = \frac{k_B}{e} \frac{1}{k_B T} \left[\frac{S_2}{S_1} - \mu \right]$$

$$S_i = \frac{e^2}{2k_B T} \int_0^{\infty} d\tau T r \left[\exp \left(\frac{\mu \sum_j -H}{k_B T} \right) \cdot (v_i v_1(\tau) + v_1(\tau) v_i) \right] \quad (2.92)$$

Here v_1 and v_2 are the velocity and energy flux operators, respectively. At high temperatures, the ratio S_1/S_2 becomes temperature independent and will be overwhelmed by the chemical potential $\mu = -T(\partial s / \partial N)_{E,V}$ where s is the entropy. If g is the degeneracy of the high temperature state, S becomes

$$S = \frac{k_B}{e} \frac{\partial}{\partial N} \ln [g]. \quad (2.93)$$

It is clear from Equation 2.93 why S is often said to measure the entropy per carrier. When Equation 2.93 is applied to spinless fermions the well-known Heikes formula is produced.

This concludes our survey of the Seebeck coefficient and the forms in which it often appears in the literature: Equations 2.86, 2.88, 2.91 and 2.93. Finally, we will discuss the application of Equation 2.93 to a class of materials of current interest.

This formula has been applied recently to the sodium cobaltites $\text{Na}_x\text{Co}_2\text{O}_4$ by Koshibae et al. [40]. These compounds have Co in both the 3+ and 4+ oxidation states, the ratio of the two determined by x . They are metallic, but have Seebeck coefficients near $100\mu\text{V}/\text{K}$. They define M as the total number of Co^{4+} ions, $N-M$ the total number of Co^{3+} sites, and g_3 and g_4 as the electronic degeneracy of the Co^{3+} and Co^{4+} ions, respectively. The total degeneracy then is given by

$$g = g_3^{N-M} g_4^M \frac{N!}{M! (N-M)!}. \quad (2.94)$$

Applying Stirling's approximation, and noting $x=M/N$, gives for the thermopower

$$S = -\frac{k_B}{e} \left[\ln \left(\frac{g_3}{g_4} \right) + \ln \left(\frac{x}{1-x} \right) \right]. \quad (2.95)$$

The thermopower is composed of one term due to the difference in degeneracy of the two sites, and one term due to the configurational entropy. When taken alone, the second term is the Heikes formula mentioned above. The value of x is determined by the stoichiometry of the compound, and the authors specialize to $x=0.5$, typical for these materials. This eliminates the second term in Equation 2.95, giving

$$S = -\frac{k_B}{e} \ln \left(\frac{g_3}{g_4} \right). \quad (2.96)$$

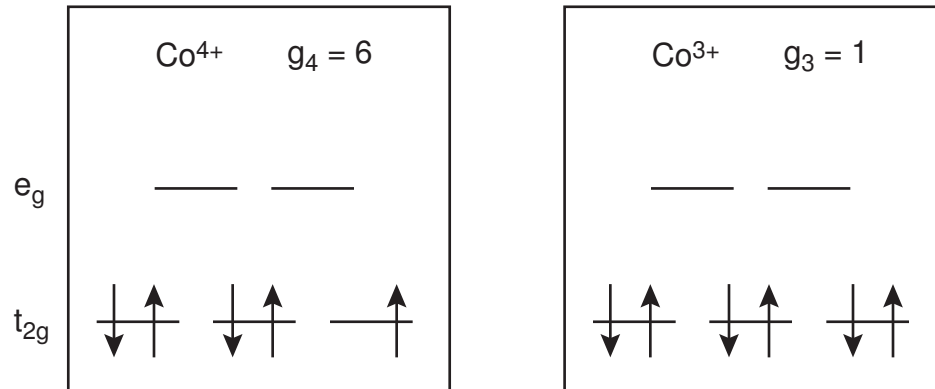


Figure 2.8: The 3d orbital of Co split by an octahedral field, showing the large difference in degeneracy between the Co^{3+} and Co^{4+} configurations.

The thermopower is high if the hopping is between states with a large difference in degeneracy.

The authors consider the Co d orbitals split by the octahedral field. For the spin configurations shown above, this gives a thermopower of $Q=(k_B/e)\ln(6)$. Higher thermopowers are realized if excited states are considered. The authors note that the presence of the low spin state of Co^{3+} ($g=1$) is important in achieving high thermopowers. The authors suggest that this mechanism may be applied to other systems.

REFERENCES

- [1] R. Heikes and R. Ure Jr., *Thermoelectricity: Science and Engineering*, Interscience Publishers Inc., 1st edition, 1961.
- [2] L. Onsager, Phys. Rev. **37**, 405 (1931).
- [3] L. Onsager, Phys. Rev. **38**, 2265 (1931).
- [4] J. Sofo and G. Mahan, Phys. Rev. B **49**, 4565 (1994).
- [5] L. Hicks and M. Dresselhaus, Phys. Rev. B **47**, 12727 (1993).
- [6] N. W. Ashcroft and N. D. Mermin, *Solid State Physics*, Saunders College, 1st edition, 1976.
- [7] G. Mahan, Journal of Applied Physics **65**, 1578 (1989).
- [8] G. Mahan, Solid State Physics **51**, 81 (1997).
- [9] P. Price, Philos. Mag. **46**, 1252 (1955).
- [10] P. Price, Phys. Rev. **104**, 1223 (1956).
- [11] R. Chasmar and R. Stratton, J. Electron. Control **7**, 52 (1959).
- [12] D. Tuomi, J. Electrochem. Soc. **131**, 2319 (1984).
- [13] L. Nordstrom and D. Singh, Phys. Rev. B **53**, 1103 (1996).
- [14] G. . Nolas, M. Kaeser, R. T. Littleton IV, and T. M. Tritt, Applied Physics Letters **77**, 1855 (2000).
- [15] P. Larson et al., Phys. Rev. B **65**, 045205 (2002).
- [16] D.-Y. Chung et al., Science **287**, 1024 (2000).
- [17] R. Dornhaus and G. Nimtz, *Narrow Gap Semiconductors*, Springer, 1st edition, 1976.
- [18] G. Slack, *CRC Handbook of Thermoelectrics*, chapter New Materials and Performance Limits for Thermoelectric Cooling, pages 407–440, CRC Press, 1995.
- [19] M. N. Wybourne et al., Phys. Rev. Lett. **53**, 580 (1984).
- [20] E. R. Grannan et al., Phys. Rev. Lett. **60**, 1402 (1988).
- [21] J. L. Cohn et al., Phys. Rev. Lett. **82**, 779 (1999).
- [22] V. Keppens et al., Phil. Mag. Lett. **80**, 807 (2000).

- [23] G. Nolas, J. Cohn, G. Slack, and S. Schujman, *Applied Physics Letters* **73**, 178 (1998).
- [24] B. C. Sales et al., *Mater. Res. Soc. Symposium Proceedings* **626** (2001).
- [25] G. A. Slack, *Solid State Physics* **34**, 1 (1979).
- [26] T. J. Scheidemantel et al., *Phys. Rev. B* **68**, 125210 (2003).
- [27] L. Hicks, T. Harman, and M. Dresselhaus, *Applied Physics Letters* **63**, 3230 (1993).
- [28] G. Mahan and H. Lyon Jr., *Journal of Applied Physics* **76**, 1899 (1994).
- [29] J. Sofo and G. Mahan, *Applied Physics Letters* **65**, 2690 (1994).
- [30] G. D. Mahan and J. O. Sofo, *Proc. Natl. Acad. Sci.* **93**, 7436 (1996).
- [31] T. Thonhauser et al., *Phys. Rev. B* **68**, 085201 (2003).
- [32] T. Thonhauser, T. Scheidemantel, and J. Sofo, *Applied Physics Letters* **85**, 588 (2004).
- [33] G. Mahan, *Journal of Applied Physics* **70**, 4551 (1991).
- [34] G. J. Snyder and T. S. Ursell, *Phys. Rev. Lett.* **91**, 148301 (2003).
- [35] B. Sherman, R. Heikes, and W. Ure Jr., *J. Appl. Phys.* **31**, 1 (1960).
- [36] T. Thonhauser, G. Mahan, L. Zikatanov, and J. Roe, *Applied Physics Letters* **85**, 3247 (2004).
- [37] A. Miner, A. Majumdar, and U. Ghoshal, *Applied Physics Letters* **75**, 1176 (1999).
- [38] A. Ioffe, *Semiconductor Thermoelements and Thermoelectric Cooling*, Infosearch, 1957.
- [39] P. M. Chaikin and G. Beni, *Phys. Rev. B* **13**, 647 (1976).
- [40] W. Koshibae et al., *Phys. Rev. B* **62**, 6869 (2000).

Chapter 3

Exploring Thallium Compounds as Thermoelectric Materials

This Chapter is an extension of some of the work reported in the dissertation of Dr. Thomas K. Reynolds [1]. Many new compounds are discussed here. Since they were discovered near the end of Dr. Reynolds' graduate studies, only the crystallography and a few diffuse reflectance spectroscopy measurements were described in his dissertation. In the current work, we report further characterizations which have been performed on many of these materials, including measured thermoelectric properties, measured band gaps, and results from electron localization function calculations which confirm the presence of stereoactive lone pairs on Tl^{1+} . We will not discuss in detail the synthetic procedures that yielded the single crystals, and give only brief descriptions of the crystal structures, since these have been discussed before. There are a few exceptions: $Tl_3Zr_{1.4}Sn_{1.6}Te_6$, $Tl_2TiCu_2S_4$, $Tl_2TiCu_2Se_4$, and $Tl_{1.71}Sn_{2.60}Bi_{7.71}Se_{15}$ were discovered by the author and did not appear in Dr. Reynolds' dissertation, and a new crystal structure is presented for $Tl_2Au_2Sn_2Se_6$, showing the previously reported solution to be a subcell of the true structure. Diffuse reflectance spectra are included here in those cases in which they were not reported previously. The density functional theory and electron localization function calculations reported here were performed by Prof. Ram Seshadri at UCSB. This Chapter has been adapted from a paper published in *Chemistry of Materials*. * Further results from

*Reproduced in part with permission from M. A. McGuire, T. K. Reynolds, and F. J. DiSalvo, *Chem. Mater.* **17**, 2875 (2005). Copyright 2005 American Chemical Society.

our investigations into Tl containing systems are presented in the following two Chapters.

3.1 Introduction and Motivation

One major area of current TE research is the synthesis and characterization of new alkali metal (AM) chalcogenide compounds. AM compounds show a great diversity of structural features including isolated metal-chalcogenide units, 1-d chains, 2-d layers and 3-d networks [2]. However the low electronegativity of AM's can lead to large band gaps and increased scattering of charge carriers. The resulting higher values of resistivity are not optimal for TE applications. The reactivity of AM's also may lead to compounds that are unstable when exposed to air or moisture, adding considerable complexity to devices that would utilize them. Despite these possible disadvantages, some AM compounds have been discovered which show promising TE properties. In particular the figure of merit of CsBi_4Te_6 exceeds that of optimized Bi_2Te_3 alloys below about 250 K [3]. We would like to take advantage of the rich chemistry of AM's while avoiding the properties that hinder TE performance. Tl may be an interesting element in this respect, since it can behave as a pseudo-AM.

In contrast to other group 13 elements, Tl prefers the 1+ oxidation state (although Tl^{3+} is known), and the many similarities between the chemistry of AM and Tl have been noted [4]. In addition, many Tl analogs of AM solid state compounds are known to exist, especially among the oxides. This leads us to believe that the diversity seen in AM chalcogenide compounds may also exist in Tl containing systems.

The electronegativity of Tl (2.04) is much higher than that of any AM, which should lead to less ionic compounds with smaller band gaps and thus

higher carrier mobility. Thallium is also heavier than any stable AM. Inclusion of heavy atoms is a well-established route towards low thermal conductivity. Finally, compounds containing Tl tend to be less sensitive to air and moisture than AM compounds (also related to Tl's less electropositive nature). Unlike AM's, Tl^{1+} has a lone pair of electrons that can be stereoactive and may lead to an even greater diversity of structures. Based on these observations we believe that investigation of Tl containing chalcogenides may lead to the discovery of improved TE materials.

Quaternary Tl-chalcogenide systems have been little studied. The current version of the Inorganic Crystal Structure Database (ICSD) lists twenty quaternary Tl sulfides, only five quaternary Tl selenides and only two quaternary Tl tellurides. Undoubtedly one reason for the lack of extensive study of these systems to date is the high toxicity of Tl. This can limit the range of applications of Tl based TE materials. As a reference we can compare the toxicity of Tl ($\text{LD}_{50} = 4.5 \text{ mg/kg man}$) to that of Pb ($\text{LD}_{50} = 155 \text{ mg/kg man}$) and Bi ($\text{LD}_{50} = 221 \text{ mg/kg man}$), as reported on Material Safety Data Sheets. It is interesting to note that the known mechanism of Tl toxicity is related to its similarity to AMs. Cell membranes cannot distinguish between Tl and potassium, and Tl interferes with vital potassium dependent processes [5]. Despite this high toxicity, if a high-performance material is discovered it may find use in niche applications, and with proper device and safety engineering may be suitable for commercial use. In addition, even if the materials could not be used, they may provide a proof of principle by showing that the goal of $ZT = 4$ in bulk materials is achievable.

The thermoelectric properties of some ternary Tl compounds have already been investigated. The ternary compound Tl_2SnTe_5 (isostructural to K_2SnTe_5 and Cs_2SnTe_5) has a figure of merit at room temperature equal to that of non-optimized Bi_2Te_3 ($ZT = 0.6$) [6]. Tl_9BiTe_6 was found to have extremely low ther-

mal conductivity, and $ZT = 1.2$ at 500°C [7]. Above about 300°C , TlSbTe_2 performs as well as PbTe and the filled skutterudites [8].

We have begun our study of quaternary Tl-chalcogenide systems both by attempting to synthesize analogs of known AM compounds and by investigating phase diagrams such as Tl-M1-M2-X where M1 and M2 are transition or main group metals and X is S, Se or Te. This has led to the discovery of many new compounds, some analogous to known AM's compounds and some adopting new structure types. Our results demonstrate both the similarities and differences between the solid state chemistry of Tl and AM's.

In this Chapter we present 13 Tl containing multinary chalcogenides. The structures are discussed and compared to known AM compounds. In general Tl will be treated as a simple single electron donor in the description of crystal structures. This means that we will focus on the framework composed of the non-Tl atoms and consider the Tl atoms as filling spaces between structural units (chains and layers). Due to the less ionic nature of Tl, this viewpoint may not be as valid as it is for AM's. So we must keep in mind that this construction is used only to aid in the visualization of the crystal structures, and that there may be significant mixing between Tl and chalcogen orbitals in bands at or near the Fermi level. This mixing should result in less anisotropic physical properties than the views of the crystal structures shown might suggest. The coordination of Tl in these compounds are presented in a separate section, with emphasis on the activity of the lone pair of electrons on Tl^{1+} .

3.2 General experimental details

WARNING: As noted above, Tl is *extremely* toxic. In addition, when exposed to moisture Tl forms TlOH which is easily absorbed through skin. Contact

with Tl and its compounds should be carefully avoided. Appropriate gloves (e.g. nitrile) should be worn at all times while working with Tl containing materials. Thallium compounds should be disposed of with other hazardous solid waste. Gloves, weighing papers, kimwipes, etc. which are contaminated with Tl should be disposed of in a separate waste container.

All of the compounds reported here were synthesized from the elements. Since thallium metal will tarnish slowly in air, it was handled in an argon filled glove box. Chunks were cut from the 0.5 inch diameter rod with wire cutters used only for this purpose and weighed inside the glove box and placed in capped glass vials. Appropriate amounts of the other elements were then weighed out and loaded into carbon coated silica tubes. In most cases the loadings were chosen to match the stoichiometry of known alkali metal compounds. Others were chosen to make cursory studies of quaternary phase diagrams (combinations equivalent to mixing common binary chalcogenides in several different ratios). The Ar filled vials were removed from the glove box and the Tl was added to the silica tubes. The tubes were then quickly (to limit the exposure of Tl to air) attached to a vacuum line for sealing. The tubes were heated over 24 hours to 800°C, held at this temperature for 172 hours and then cooled over 200 hours to 300°C at which point the furnace was turned off and allowed to cool to room temperature. Crystals were extracted from the resulting polycrystalline mass for examination. Exceptions to this general synthetic procedure are noted in the discussions of the individual compounds below.

The elemental compositions of the crystals were investigated with a JEOL 8900R electron microprobe operating in energy dispersive mode at 15 kV and between 5 and 20 nA. Standardless, semi-quantitative analysis was used to determine approximate ratios of elements in the crystals. Single crystals were mounted in poly(butenes) oil and bathed in a cold nitrogen stream (175 ± 5 K) for single

crystal x-ray diffraction on a Bruker SMART CCD diffractometer. The program SMART was used to collect the data and the program SAINT was used to integrate the data and refine the unit cells based on strong reflections [9]. Absorption corrections were made with SADABS [10], and space groups were determined by the program XPREP [11]. Crystal structure solutions and refinements were carried out using SHELXS97 and SHELXL97 within the WingX program suite [12].

In compounds containing heavy elements (like Tl or even Te), crystal structure refinement is often complicated by strong absorption and truncation of high angle data. Both lead to unaccounted for peaks in the Fourier difference map. Since strong X-ray scatterers (high Z elements) have significant scattering power even at high angles, truncation of high angle data often leads to fluctuations (peaks and holes) near the heavy atom in the electron density map calculated from the measured reflections, at a distance roughly equal to the d-spacing corresponding to the cutoff in 2θ). Poor absorption correction often results in peaks at high symmetry positions. In the structure refinements for Tl compounds we are sometimes left with a few unassigned peaks and holes from $\pm 2 \text{ e}\text{\AA}^{-3}$, up to perhaps $\pm 5\text{-}6 \text{ e}\text{\AA}^{-3}$. For comparison, a peak corresponding to a carbon atoms typically is $3\text{-}6 \text{ e}\text{\AA}^{-3}$, depending of course on the displacement parameters. Geometry is the most useful tool in determining whether a difference peak is due to a missing atom, or an experimental artifact. If the distance between the peak and neighboring atoms is in the range expected for a typical chemical bond (roughly 1.5 \AA up to 3.5 \AA), then it may indicate a missing atom, or be due to poor absorption correction if at a high symmetry position. If a peak or hole appears at the same position as a atom in the structure, it may indicate that the atom has been misidentified, and should be changed to one of higher or lower Z, respectively. If a peak or hole is closer to a heavy atom than a typical bond ($< 1\text{\AA}$), it is most

likely due to truncation at about that resolution. Large difference peaks or holes will be addressed in the discussion of the crystal structures presented below.

Band gaps were estimated using diffuse reflectance spectroscopy with a Shimadzu UV-3101PC spectrophotometer. BaSO_4 was used as a 100% reflectance standard [13]. Sharp increases in the absorbance vs. energy plots were identified as the signature of the onset of excitation across an energy gap. The gap was estimated as the energy at which this onset occurred. The onset was approximated as the intersection of a line fit to the increase in absorbance spectra and the baseline estimated from the low energy data. In some cases, experimental difficulties (unaccounted for dips in the spectra below about 0.7 eV and noisy data near the point at which the instrument switches between two different detectors around 1.4 eV) precluded precise determination of the band gap.

Thermoelectric properties were measured in a home built apparatus. This apparatus has been described elsewhere [14]. For the current investigations liquid nitrogen was used as the cryogen and data are reported between about 80 K and 300 K. Thermal conductivity measurements were performed using the four-point steady state technique on polycrystalline pellets. The pellets were cold pressed in a 3/8" x 3/16" rectangular, hardened steel pellet press and sintered as described below. The samples were contacted with silver epoxy (Epotek H20E). The measured data were corrected for the heat loss through thermocouples and heater leads which was measured in a separate experiment. At the same time the thermopower was measured using the chromel legs of the thermocouples and was corrected for the chromel contribution. Either an AC resistance bridge (Linear Research Inc. LR-700) or two lockin amplifiers (Stanford Research Systems model 830) were used for the four point resistivity measurements. These measurements were carried out on the polycrystalline pellets used for the ther-

mal conductivity measurements described above. Electrical contacts were made using a silver paste (Dupont, Conductor Composition 4922N).

Measurements of standards and reference materials using our apparatus and techniques suggests that the maximum absolute uncertainties in the values of the measured properties are about 15% for thermal conductivity and about 5% for thermopower and electrical resistivity. The TE properties of some compounds were not investigated for various reasons. Colored transparent compounds suggest band gaps greater than 1.8 eV, and they are likely to be too resistive. Some compound have not been prepared as single phase bulk samples, and single crystals of appropriate dimensions for properties measurements have not been grown. Some compounds that were made single phase as polycrystalline pellets could not be fully characterized because of high contact and/or sample resistance.

3.3 Crystal Structures and Properties

3.3.1 $\text{Tl}_3\text{Ti}_2\text{P}_5\text{S}_{18}$

This compound is isostructural to the AM compound $\text{K}_3\text{Ti}_2\text{P}_5\text{S}_{18}$ [15], but was discovered in an attempt to make the Tl analog of the known compound $\text{NaTi}_2\text{P}_3\text{S}_{12}$ [16]. The structure is shown in Figure 3.1. The compound is monoclinic (C2/c) and forms black needles. Chains of composition $[\text{Ti}_2\text{P}_5\text{S}_{18}]^{3-}$ separated by Tl atoms run diagonally in the ac plane. In these chains, Ti is coordinated to six S atoms in a distorted octahedral geometry, and P is tetrahedrally coordinated by S. The TiS_6 octahedra are formed by edge bridging of three tetrahedral PS_4 units to each Ti. These tetrahedra then either corner share with other PS_4 tetrahedra or edge share with distorted Ce centered octahedra to form the chains. Tl(2) is disordered over two sites, each half occupied. This disorder is

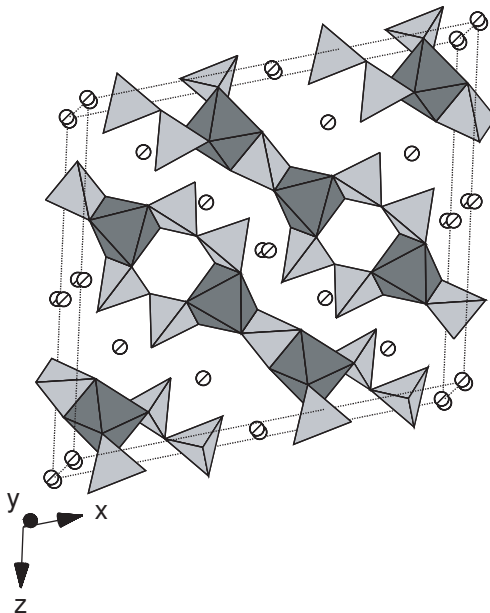


Figure 3.1: A view of the crystal structure of $\text{Tl}_3\text{Ti}_2\text{P}_5\text{S}_{18}$ showing Ti centered octahedra (dark) and tetrahedral PS_4 units (light) and Tl atoms (striped).

not seen in the AM compound. Both Tl(1) and Tl(2) are again irregularly coordinated by eight S atoms in one-sided environments which could accommodate lone pairs (*vide infra*). Attempts to make this compound in bulk gave a mixture of the target phase and a minor ($\sim 10\%$) unidentified impurity phase. The band gap of $\text{Tl}_3\text{Ti}_2\text{P}_5\text{S}_{18}$ was estimated from the absorbance spectrum of this product. The spectrum is shown in Figure 3.2. The band gap was measured to be approximately 1.3 eV, consistent with the black color of this compound.

3.3.2 $\text{Tl}_2\text{Cu}_2\text{SnS}_4$

Elements were loaded in a 2:2:1:4 ratio in an attempt to make the Tl analog of the known compound $\text{Rb}_2\text{Cu}_2\text{SnS}_4$ [17]. The reaction product contained black block-like crystals of $\text{Tl}_2\text{Cu}_2\text{SnS}_4$ which is isostructural to the AM compound. The structure (Figure 3.3) is orthorhombic, space group Ibam , and is made up of $[\text{Cu}_2\text{SnS}_4]^{2-}$ layers separated by Tl. The layers are formed by chains made up

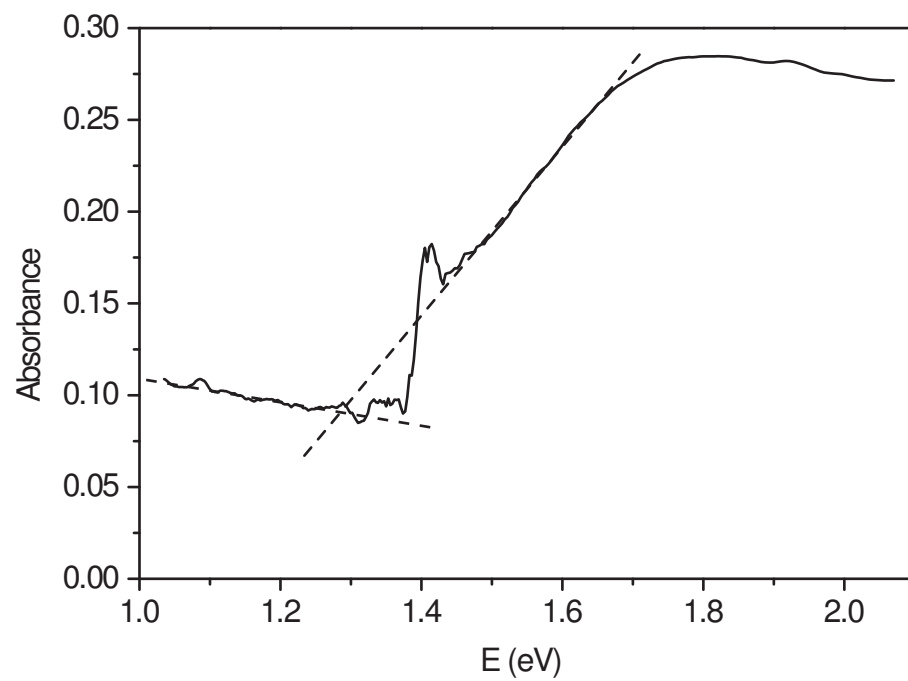


Figure 3.2: The measured absorbance spectrum of $\text{Tl}_3\text{Ti}_2\text{P}_5\text{S}_{18}$ used to approximate the band gap. A gap of 1.3 eV is estimated from this data.

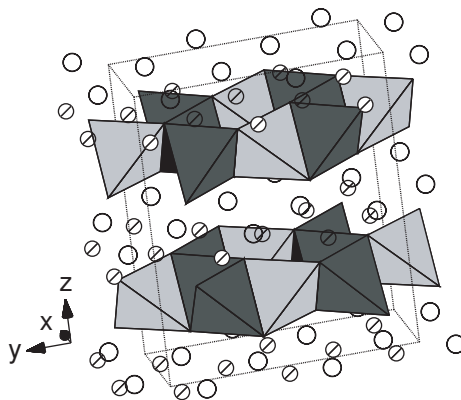


Figure 3.3: A view of the crystal structure of $\text{Tl}_2\text{Cu}_2\text{SnS}_4$ showing Sn (light) and Cu (dark) centered tetrahedra and Tl atoms (striped).

of edge sharing CuS_4 tetrahedra running parallel to the a axis and joined by Sn atoms forming SnS_4 tetrahedra. Between the layers Tl has slightly distorted cubic coordination by S (*vide infra*).

This compound was made as a single phase polycrystalline powder by reaction of the elements at 700°C for 2 days, annealing for 7 days at 300°C , and then grinding, pressing a pellet and annealing at 400°C for 4 days. This material was then pressed into a rectangular pellet and sintered at 400°C for 4 days.

The thermal conductivity of the polycrystalline pellet was measured. Figure 3.4 shows the thermal conductivity of this compound, and of the other compounds which were measured. The thermal conductivity of $\text{Tl}_2\text{Cu}_2\text{SnS}_4$ is very low, less than half that of optimized Bi_2Te_3 alloys at room temperature [18]. High sample and/or contact resistance prevented the measurement of resistivity and thermopower.

3.3.3 $\text{Tl}_5\text{AgTi}_6\text{Se}_{27}$

This compound was discovered in a successful attempt to synthesize the Tl analog to the known compounds $\text{Cs}_5\text{AgTi}_6\text{Se}_{27}$ and $\text{Rb}_5\text{AgTi}_6\text{Se}_{27}$ [19]. Black

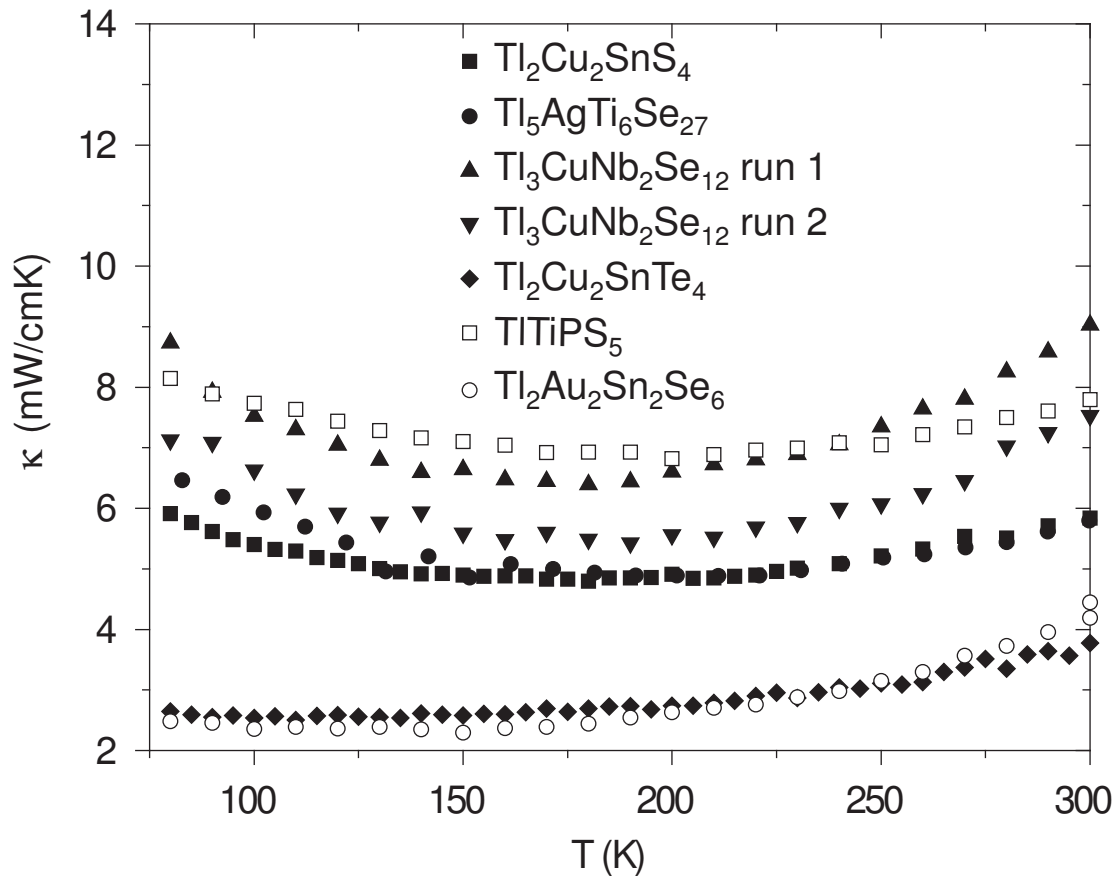


Figure 3.4: The measured thermal conductivities of six of the compounds reported here. Based on measurements of reference materials and on estimated errors in geometrical measurements, the uncertainty of the κ measurements is estimated to be about $\pm 15\%$.

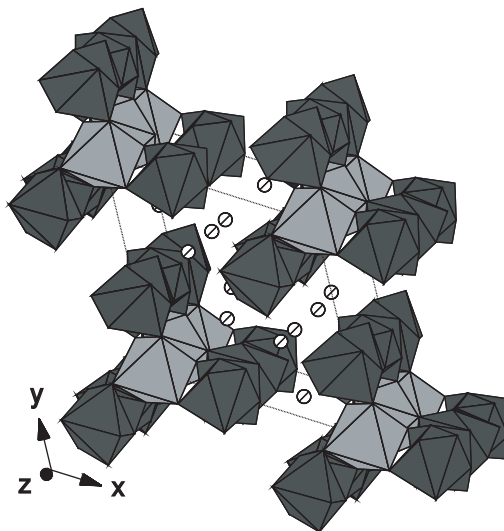


Figure 3.5: A view of the crystal structure of $\text{Tl}_5\text{AgTi}_6\text{Se}_{27}$ showing Ti centered polyhedra (dark), Ag centered octahedral (light) and Tl atoms (striped).

needles were recovered from the reaction product and were determined to have the target composition. The AM analogs also form as black needles. As in many AM compounds, these are properly Zintl phases where the octet rule is satisfied by forming direct Se-Se single bonds. The structure is trigonal (space group $P3_1c$), and is shown in Figure 3.5. Ti is in an irregular seven coordinate environment, bonded to Se. The Ti polyhedra face share in pairs, and these pairs then share trans-edges to form 1-D chains along the hexagonal c -axis. The Ag ions reside between these chains, and are in octahedral coordination by Se. The Ag centered octahedra join three chains of Ti centered polyhedra together in isolated groups. Tl(1) is irregularly coordinated by six Se atoms. Tl(2) is coordinated by nine Se atoms in a distorted tri-capped trigonal prism. Tl(3) is coordinated to nine Se atoms in a symmetrical, but one-sided, environment (*vide infra*).

The Se-Se dimers have a formal charge of 2- and the structural formula can be written $\text{Tl}_5\text{AgTi}_6(\text{Se}_2)_{12}\text{Se}_3$. The formal charge on Ti is 4+, while Ag and Tl are both 1+. Ti has an irregular coordination, bonded to 4 Se-Se dimers and

one Se^{2-} anion. The Ti atom is bonded to both Se atoms of two of the dimers, but only one Se atom of the other two dimers. The distances between the pairs of Se atoms vary from 2.35 Å to 2.37 Å. The Se-Se bond distance in elemental Se is about 2.4 Å [20]. All other Se-Se distances in this structure are greater than 3.0 Å. This coordination of Ti by Se is unusual, since Ti is often nearly octahedrally coordinated by six Se anions.

A stoichiometric mixture of the elements was reacted at 500°C for 2 days, and cooled to room temperature over 2 days. All reflections in the powder X-ray diffraction pattern of the product could be indexed to the target compound except one small peak which is attributed to unreacted Se. A rectangular pellet of this compound was then pressed and sintered at 300°C for 10 days.

Figure 3.4 shows the measured thermal conductivity of this sample. The thermal conductivity is very low, less than half that of optimized Bi_2Te_3 alloys at room temperature. At 300 K the thermopower was measured to be $-820 \mu\text{V}/\text{K}$, indicating n-type conduction. The measured resistivity at 300 K was $1.2 \times 10^4 \Omega \text{ cm}$. This is too large for TE applications, but is an order of magnitude lower than $\text{Cs}_5\text{AgTi}_6\text{Se}_{27}$, which has a resistivity at room temperature of $2.5 \times 10^5 \Omega \text{ cm}$ [19].

The band gap of this material was estimated from its absorbance spectrum. The spectrum is shown in Figure 3.6. The band gap was measured to be approximately 0.8 eV, consistent with the black color of this compound.

3.3.4 $\text{Tl}_3\text{CuNb}_2\text{Se}_{12}$

This compound was made in a successful attempt to synthesize the Tl analog of the known compound $\text{K}_3\text{CuNb}_2\text{Se}_{12}$ [21]. This compound crystallizes in the monoclinic space group $\text{P}2_1/\text{n}$ as black needles, the same color as the AM analogue. In this structure (Figure 3.7) the Nb atoms are coordinated to seven

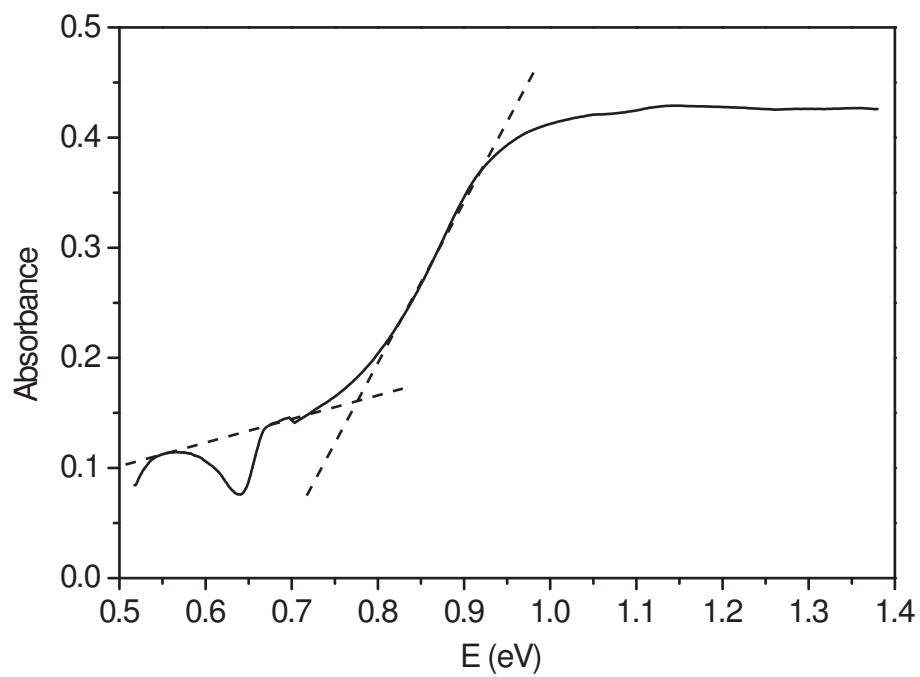


Figure 3.6: The measured absorbance spectrum of $\text{Tl}_5\text{AgTi}_6\text{Se}_{27}$ used to approximate the band gap. A gap of 0.8 eV is estimated from this data.

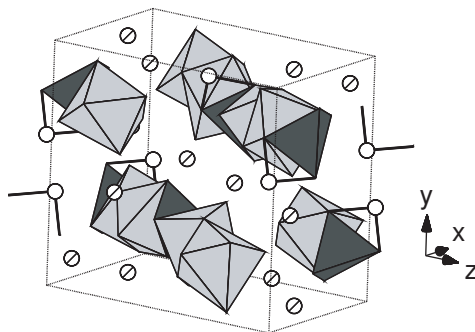


Figure 3.7: A view of the crystal structure of $\text{Tl}_3\text{CuNb}_2\text{Se}_{12}$ showing Nb centered polyhedra (light), Cu centered tetrahedra (dark), Se atoms (white) and Tl atoms (striped).

Se atoms in a distorted pentagonal bipyramid. These polyhedra are paired by face sharing and each member of the pair edge shares with a CuSe_4 tetrahedron forming chains running perpendicular to the b-axis. Tl atoms reside between these chains. In this structure, Tl(1) has irregular seven-fold coordination and Tl(2) irregular eight-fold coordination by Se. Tl(3) is in a distorted mono-capped cubic environment, coordinated by nine Se atoms (*vide infra*). There is a substantial amount of Se-Se bonding in this structure. In each CuSe_4 unit, two of the Se atoms are bonded to the same Se atom outside the chain forming Se trimers. There is also Se-Se bonding within the chains. Around each Nb four of the five Se atoms that make up the distorted pentagon are bonded forming two dimers. Dimers are also formed by Se atoms coordinated to neighboring Nb centered polyhedra. The interatomic distances between paired Se atoms range from 2.36 Å to 2.47 Å. The next closest Se-Se contact is 2.81 Å which is shorter than the typical Se-Se van der Waals contact of 3.80 Å [22], but we do not consider it to be a single bond. With these assignments, the composition can be written as $\text{Tl}_3\text{CuNb}_2(\text{Se}_3)(\text{Se}_2)_3\text{Se}_3$. Counting each Se dimer and trimer as 2-, and assigning 1+ to both Tl and Cu gives a formal charge of 5+ for Nb.

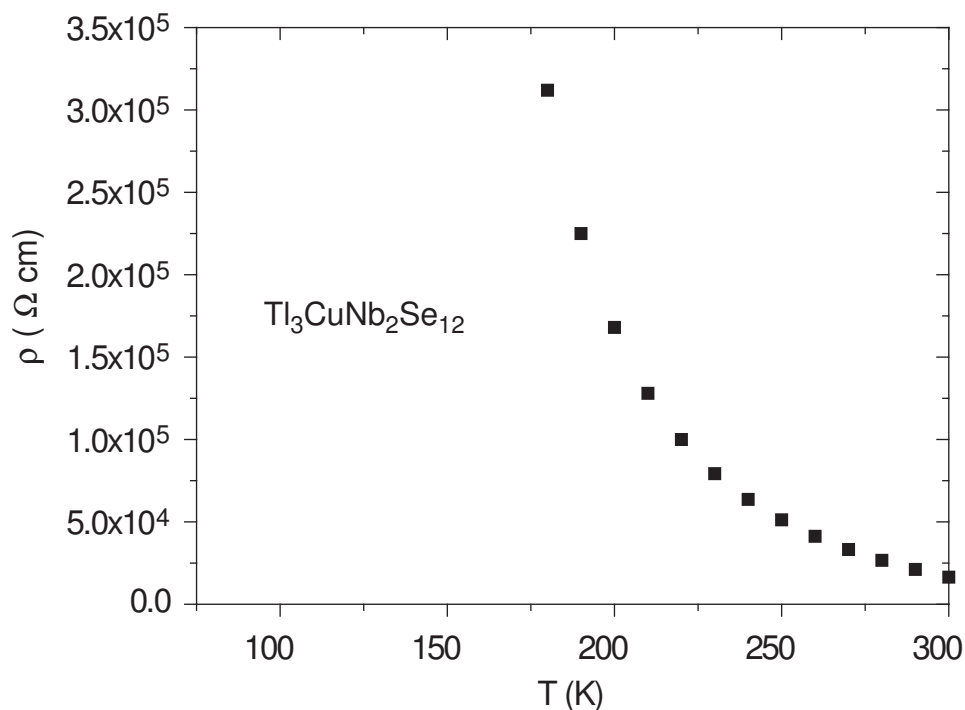


Figure 3.8: The measured resistivity of $\text{Tl}_3\text{CuNb}_2\text{Se}_{12}$. The uncertainty of these measurements is estimated to be about $\pm 5\%$, and arises primarily from the geometrical measurements.

This compound was made as a single phase powder by reacting the elements at 500°C and then annealing for 7 days at 300°C . The product was then pressed into a rectangular pellet and sintered at 300°C for 4 days. The results of TE properties measurements on the polycrystalline pellet are presented in Figures 3.4 and 3.8. This compound shows p-type semiconducting behavior, with high resistivity. The thermopower could only be measured near room temperature due to the increasing resistance as T decreased. The measured value at 300 K was $+770 \mu\text{V}/\text{K}$, indicating p-type conduction. The thermal conductivity was measured twice, with the sample being removed from the measurement apparatus and then later remounted. The measurements show acceptable reproducibility, and low thermal conductivity. The band gap of this material was estimated from

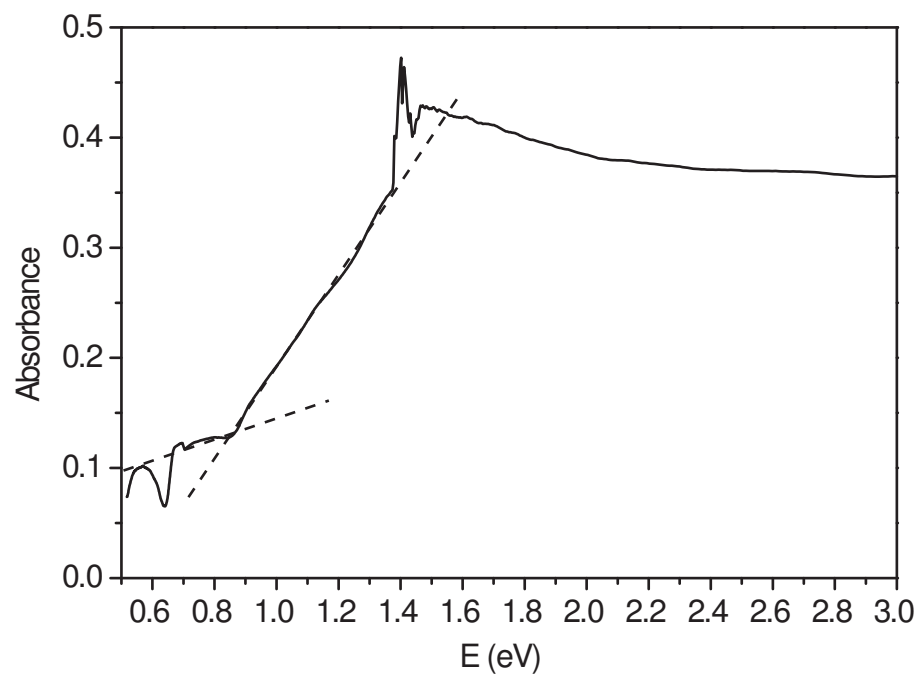


Figure 3.9: The measured absorbance spectrum of $\text{Tl}_3\text{CuNb}_2\text{Se}_{12}$ used to approximate the band gap. A gap of 0.8 eV is estimated from this data.

its absorbance spectrum. The spectrum is shown in Figure 3.9. The band gap was measured to be approximately 0.8 eV, consistent with the black color of this compound.

3.3.5 $\text{Tl}_2\text{Cu}_2\text{SnTe}_4$ and $\text{Tl}_2\text{Ag}_2\text{SnTe}_4$

These compounds were discovered in attempts to make Tl analogs of the known compound $\text{K}_2\text{Ag}_2\text{SnTe}_4$ [23]. $\text{Tl}_2\text{Ag}_2\text{SnTe}_4$ is isostructural to the AM compound (Figure 3.10). $\text{Tl}_2\text{Cu}_2\text{SnTe}_4$ is not; however, it is very similar (Figure 3.11). Both Tl compounds form block-like black crystals, as does $\text{K}_2\text{Ag}_2\text{SnTe}_4$. All three compounds are tetragonal ($\overline{I}42m$) and have channels running along the c-axis in which Tl atoms reside. The Tl atoms are in a distorted square anti-prismatic environment, coordinated by Te atoms. The framework surrounding these channels is different in each case and is made up of Sn and Cu/Ag atoms in tetrahedral coordination.

In these compounds the Sn atom is at the corners (and center) of the unit cell and is tetrahedrally coordinated by Te. The differences among the structures are due to the different sites and occupancies of the Cu or Ag atoms. In $\text{Tl}_2\text{Ag}_2\text{SnTe}_4$ there are two sites partially occupied by Ag. One is at $(0,0,1/2)$ and has occupancy 0.29. The other is displaced from this high symmetry position to (x,y,z) , and thus forms eight equivalent sites around the first Ag atom. These sites have occupancy 0.22 and large displacement ellipsoids suggesting perhaps further positional disorder. In $\text{Tl}_2\text{Cu}_2\text{SnTe}_4$ the site at $(0,0,1/2)$ is vacant and only the fourfold site is occupied by Cu. The occupancy of this site is 0.5. In all of these compounds the tetrahedrally coordinated metal atoms form chains along the c axis. The metal atoms which are offset from high symmetry positions form bonds to Te atoms coordinated to symmetry equivalent metal atoms in neigh-

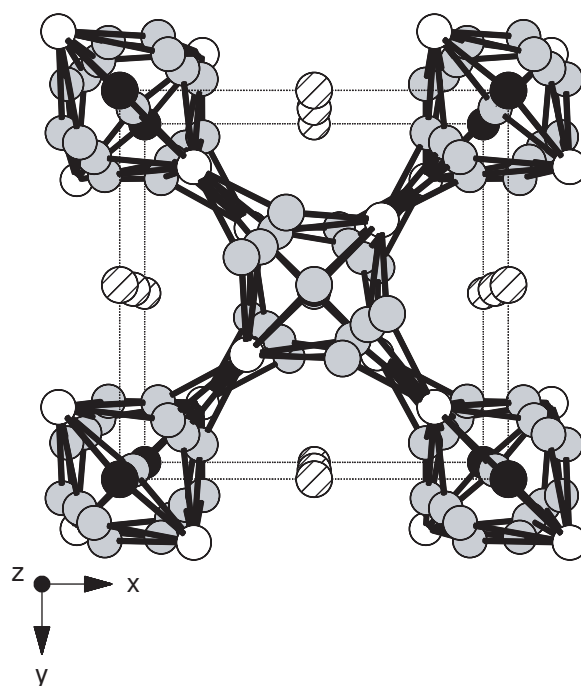


Figure 3.10: A view of the crystal structure of $\text{Tl}_2\text{Ag}_2\text{SnTe}_4$ viewed along the c-axis showing Te atoms (white), Sn atoms (dark), Ag atoms (medium) and Tl atoms (striped).

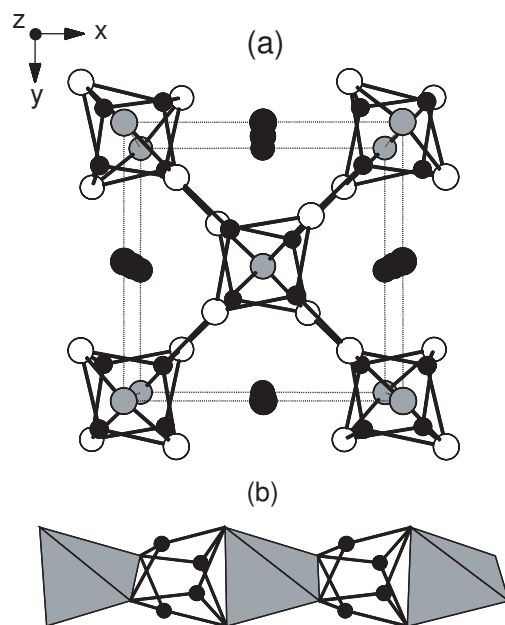


Figure 3.11: (a) A view of the crystal structure of $\text{Tl}_2\text{Cu}_2\text{SnTe}_4$ viewed along the c -axis showing Te atoms (white), Sn atoms (medium), Cu atoms (small, dark) and Tl atoms (large, dark). (b) Part of a chain of composition Cu_2SnTe_4 composed of SnTe_4 tetrahedra joined by Cu atoms.

boring chains. This inter-chain bonding makes the non-Tl containing part of the structure three dimensional. The Tl atoms in these structures are found in distorted square antiprisms (*vide infra*) between the chains.

These compounds have the structural features desired for good thermoelectric materials. A three dimensional covalent network is present which could provide for good electrical transport properties, while the Tl atoms in open channels may act as “rattlers” to scatter heat carrying phonons to keep the lattice thermal conductivity low.

Attempts to make $\text{Tl}_2\text{Ag}_2\text{SnTe}_4$ in bulk resulted in the target compound as the majority phase along with SnTe and other unidentified phases. However, the Cu analogue was made as a single phase powder, by reacting the elements at 500°C for 2 days, and then grinding and annealing a pressed pellet at 300°C for 4 days. A rectangular pellet of this material was pressed and annealed at 400°C for one week, and the thermoelectric properties were measured.

The results of the properties measurements are presented in Figures 3.4 and 3.12. This p-type semiconducting compound has extremely low thermal conductivity, and a moderate thermopower. However, the resistivity of this material is too high to be useful for thermoelectric applications, unless the carrier density can be increased by suitable doping. The very low thermal conductivity of this compound could be partially due to the disordered Cu atoms.

3.3.6 $\text{Tl}_3\text{Zr}_{1.4}\text{Sn}_{1.6}\text{Te}_6$

This compound was discovered during an investigation of the Tl-Zr-Sn-Te phase diagram. It was synthesized by heating a stoichiometric mixture of the elements to 800°C over 24 hours, soaking at this temperature for 100 hours, then cooling to 400°C over 100 hours. It forms black needles, crystallizes in the

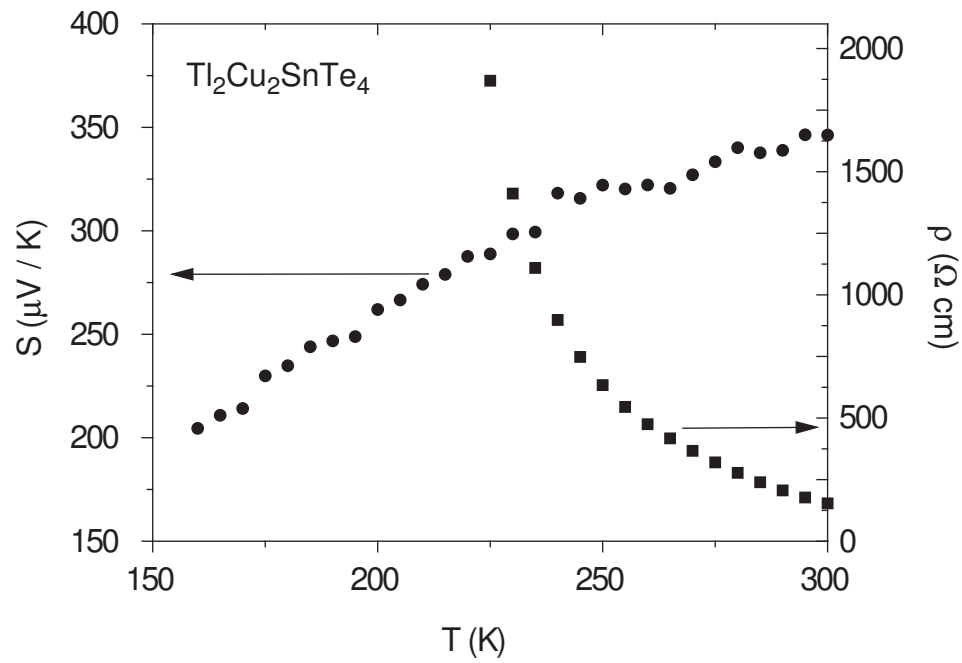


Figure 3.12: The measured resistivity (circles) and thermopower (squares) of $Tl_2Cu_2SnTe_4$. Based on measurements of reference materials and on estimated errors in geometrical measurements, the uncertainty of the ρ and S measurements is estimated to be about $\pm 5\%$.

rhombohedral space group $R\bar{3}m$ and is isostructural to NaInSe_2 [24]. The crystal structure data are reported in Table 3.1. Atomic positions and occupancies, and atomic displacement parameters are given in Table 3.2 and Table 3.3, respectively. The largest Fourier difference peak ($5.181 \text{ e}\text{\AA}^{-3}$) is located 0.87 \AA from Tl, and is attributed to truncation of the diffraction data at $\theta = 30.45^\circ$. The only other peaks larger than $2 \text{ e}\text{\AA}^{-3}$ are close to Te (0.68 and 1.23 \AA).

The structure is shown in Figure 3.13, and consists of sheets of edge sharing octahedra with Te atoms at the vertices. The centers of the octahedra are randomly occupied equally by Zr and Sn. The sheets are separated by Tl which has distorted octahedral coordination by Te atoms in the sheets (*vide infra*). Charge balance is achieved if the Zr/Sn site is split equally and Sn has a charge of $2+$. Single crystal x-ray data refinement of the occupancy of this site, requiring the total occupancy to be unity, results in 46% Zr and 54% Sn. This is consistent with the results from standardless energy dispersive electron microprobe analysis of several single crystals which gave an average Zr/Sn ratio of 0.8. It is not surprising that Zr^{4+} and Sn^{2+} are found sharing the same site. They have similar covalent radii (1.45 \AA and 1.41 \AA , respectively), and have similar bond distances to Te in their binary phases (2.96 - 3.13 \AA in ZrTe_3 [25] and 3.16 \AA in SnTe [26]). These are similar to the (Zr/Sn)-Te distance seen in $\text{Tl}_3\text{Zr}_{1.4}\text{Sn}_{1.6}\text{Te}_6$ (3.01 \AA).

This compound is also isostructural to the compound TlSbTe_2 which has shown interesting thermoelectric properties [8]. Attempts to synthesize $\text{Tl}_3\text{Zr}_{1.4}\text{Sn}_{1.6}\text{Te}_6$ in bulk have resulted in a multiphase mixture containing the target compound as the majority phase ($\sim 90\%$) and Tl_4SnTe_3 .

Table 3.1: Single crystal refinement data for $\text{Tl}_3\text{Zr}_{1.4}\text{Sn}_{1.6}\text{Te}_6$.

Empirical formula	$\text{Tl}_3\text{Zr}_{1.4}\text{Sn}_{1.6}\text{Te}_6$
Formula weight	1696.4 g/mol
Temperature	175(5) K
Wavelength	0.71073 Å
Crystal system	Rhombohedral
Space Group	$R\bar{3}m$
Unit cell dimensions	$a = 4.344(6)$ Å $c = 23.43(6)$ Å
Volume	$382.8(12)$ Å ³
Absorption Correction	SADABS (based on equivalents)
Color	Black
Z	1
Calculated density	4.897 g/cm ³
Absorption coefficient	30.671 mm ⁻¹
F(000)	460
θ range	2.61° to 30.45°
Limiting indices	$-6 \leq h \leq 6$ $-6 \leq k \leq 5$ $-29 \leq l \leq 32$
Reflections collected/unique	1618 / 181 [R(int) = 0.0683]
Completeness to $\theta=30.45^\circ$	98.9%
Refinement method	Full-matrix least-squares on F^2
Data/restraints/parameters	181 / 0 / 9
Goodness-of-fit on F^2	1.098
Final R indices ($I > 2\sigma(I)$) ^(a,b)	$R_1 = 0.0407$, $wR_2 = 0.0930$
R indices (all data) ^(a,b)	$R_1 = 0.0444$, $wR_2 = 0.0941$
Largest diff. peak and hole	5.181 and -2.767 eÅ ⁻³

$${}^a R_1 = \frac{\sum ||F_o| - |F_c||}{\sum |F_o|} \quad {}^b wR_2 = \frac{[\sum w(F_o^2 - F_c^2)^2 / \sum w(F_o^2)^2]}{1/2}$$

$$w^{-1} = [\sigma(F_o^2) + (aP)^2 + bP] \text{ where } P = [\max(F_o^2, 0) + 2F_c^2] / 3$$

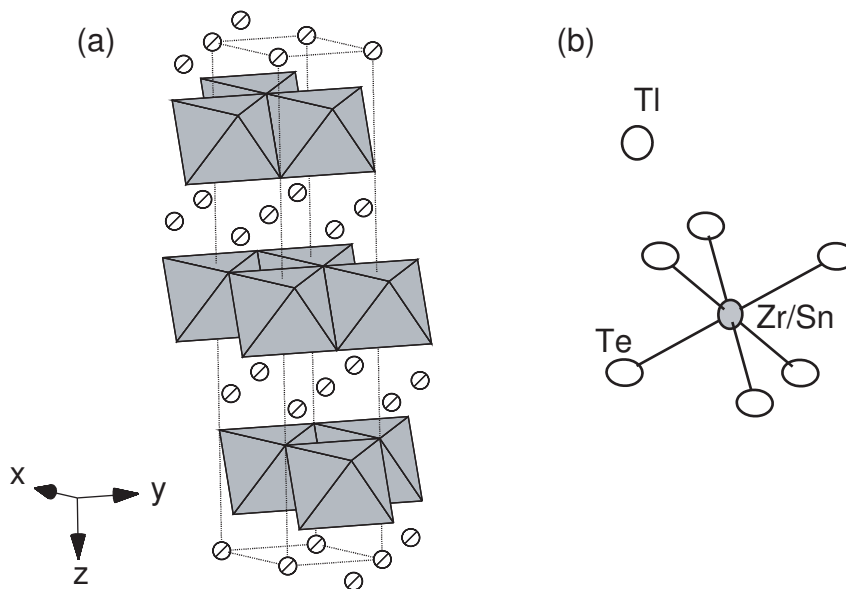


Figure 3.13: (a) A view of the crystal structure of $\text{Tl}_3\text{Zr}_{1.4}\text{Sn}_{1.6}\text{Te}_6$ showing mixed Sn/Zr centered octahedra (grey) and Tl atoms (striped). (b) Displacement ellipsoids in $\text{Tl}_3\text{Zr}_{1.4}\text{Sn}_{1.6}\text{Te}_6$.

Table 3.2: Atomic coordinates, equivalent isotropic displacement parameters (\AA^2), and occupancies for $\text{Tl}_3\text{Zr}_{1.4}\text{Sn}_{1.6}\text{Te}_6$. U_{eq} is defined as one third of the trace of the orthogonalized U_{ij} tensor.

Atom	x	y	z	U_{eq}	Occ.
Tl(1)	0	0	0.2374(1)	0.0164(2)	1
Zr(1)	0	0	0.5	0.033(2)	0.54(3)
Sn(1)	0	0	0.5	0.020(4)	0.46(3)
Te(1)	0	0	0	0.0075(4)	1

Table 3.3: The anisotropic displacement parameters (\AA^2) for the compound $\text{Tl}_3\text{Zr}_{1.4}\text{Sn}_{1.6}\text{Te}_6$. The exponent of the anisotropic displacement factor is of the form: $-2\pi^2(h^2a^*U_{11}+\dots+2hka^*b^*U_{12})$.

Atom	U_{11}	U_{22}	U_{33}	U_{23}	U_{13}	U_{12}
Tl(1)	0.023(1)	0.023(1)	0.013(1)	0	0	0.011(1)
Zr(1)	0.010(1)	0.010(1)	0.016(1)	0	0	0.005(1)
Sn(1)	0.010(1)	0.010(1)	0.016(1)	0	0	0.005(1)
Te(1)	0.016(1)	0.016(1)	0.020(1)	0	0	0.008(1)

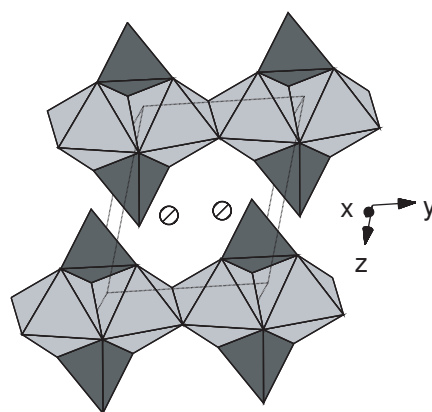


Figure 3.14: A view of the crystal structure of TlTiPS_5 showing PS_4 tetrahedra (dark) and Ti centered octahedra (light). Striped circles represent Tl.

3.3.7 TlTiPS_5

An attempt was made to synthesize the Tl analog of the known quaternary compounds RbTiPS_5 and KTiPS_5 [27]. The reaction product contained black needles of the composition TlTiPS_5 . The Tl and K compounds are not isostructural (TlTiPS_5 is triclinic ($P\bar{1}$) whereas the AM compounds are monoclinic), however they have very similar structural features. The crystal structure of TlTiPS_5 is shown in Figure 3.14. Infinite 1-d chains of composition $[\text{TiPS}_5]^{1-}$ run along the b-axis. Ti is coordinated to S in a distorted octahedral geometry, and P is tetrahedrally coordinated to S. The octahedra share edges to form the chains. The P

atom is bonded to three S atoms in the chain (at the juncture of two edge sharing octahedra) and to one S atom outside the chain. In the AM compounds these same chains are seen. However in these compounds the chains are not staggered along the direction of the chains as they are in the Tl compound (see Figure 3.14). The staggering of the chains seen in the Tl compound results in the lowering of the crystal symmetry from monoclinic to triclinic. The staggering also results in a less symmetrical environment for the Tl ion than is seen for K and Rb. This could be due to the influence of the Tl lone pair (*vide infra*).

This compound was prepared as a single phase polycrystalline powder by reacting the elements together at 500°C for 2 days, then cooling to room temperature over 2 days. A rectangular pellet was pressed from this material and sintered at 300°C for 4 days.

The pellet was used for thermoelectric properties measurements, and the results are shown in Figures 3.4 and 3.15. This compound is an n-type semiconductor with high resistivity and relatively low thermal conductivity.

3.3.8 $\text{Tl}_2\text{Au}_2\text{Sn}_2\text{Se}_6$

This compound was discovered in an attempt to make the Tl analog of $\text{K}_2\text{Au}_2\text{Sn}_2\text{Se}_6$ [28]. Black plate-like crystals of composition $\text{Tl}_2\text{Au}_2\text{Sn}_2\text{Se}_6$ were recovered from the reaction product. The AM compound was reported to crystallize in the space group $P4/mcc$ with unit cell axes $a = 8.251 \text{ \AA}$ and $c = 19.961 \text{ \AA}$. The strong x-ray diffraction peaks could be indexed with a similar unit cell ($a_0 = 8.097 \text{ \AA}$, $c_0 = 20.069 \text{ \AA}$) and systematic absences suggested the same space group $P4/mcc$. However, weak supercell reflections (on the order of 1-2% of the strongest reflections) clearly indicated a larger unit cell with $a = 11.451 \text{ \AA}$ ($= a_0\sqrt{2}$) and $c = 20.071 \text{ \AA}$.

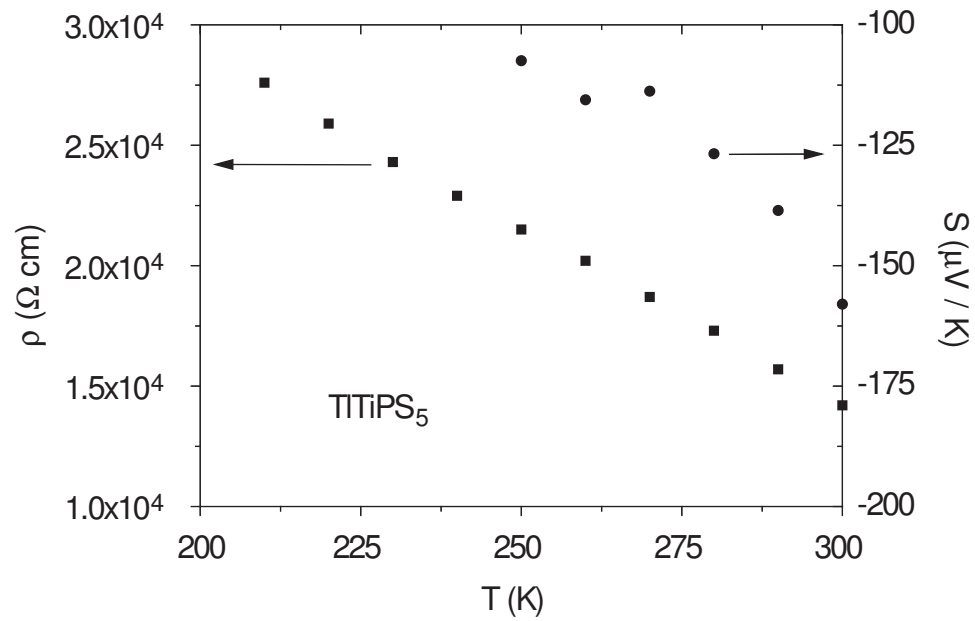


Figure 3.15: The measured resistivity (squares) and thermopower (circles) of TlTiPS₅. Based on measurements of reference materials and on estimated errors in geometrical measurements, the uncertainty of the ρ and S measurements is estimated to be about $\pm 5\%$.

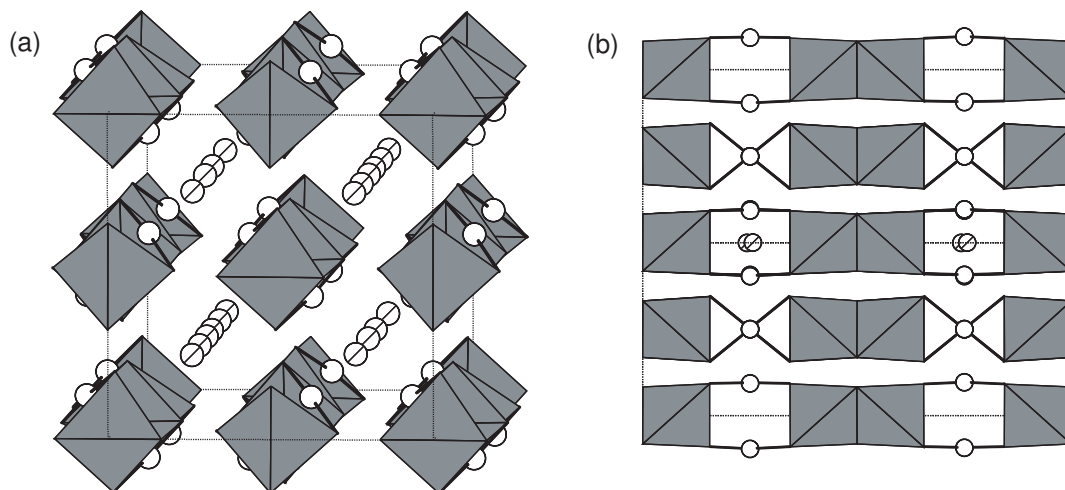


Figure 3.16: (a) The crystal structure of $\text{Tl}_2\text{Au}_2\text{Sn}_2\text{Se}_6$ viewed nearly down the c -axis, showing Sn centered tetrahedra, Tl atoms (striped) and Au atoms (white). (b) A view down the $[110]$ axis, showing the displacement of the Tl(4) atoms. In this view Tl(1)-Tl(3) are eclipsed by the Sn_2Se_6 units.

The data were integrated using the $11.451 \text{ \AA} \times 20.071 \text{ \AA}$ unit cell, and the reflections sorted based on whether or not they are allowed by the a_0, c_0 subcell. The results are summarized in Table 3.4, and clearly indicate that the data is inconsistent with the subcell. We proceeded to solve the structure in the $11.451 \text{ \AA} \times 20.071 \text{ \AA}$ unit cell. Systematic absences suggested only the space group $P4/ncc$. The crystal data are reported in Table 3.5. The atomic positions and occupancies, and the the atomic displacement parameters are given in Table 3.6 and Table 3.7, respectively.

The crystal structure is shown in Figure 3.18. It is made up of chains along the c -axis. The chains have composition $[\text{Au}_2\text{Sn}_2\text{Se}_6]^{2-}$, and contain pairs of edge sharing SnSe_4 tetrahedra linked by Au in linear coordination. The Tl atoms are between these chains. One Tl atom is split between two sites, Tl(2) and Tl(3), which are 2.6 \AA apart.

One K atom in $\text{K}_2\text{Au}_2\text{Sn}_2\text{Se}_6$ was reported to have large displacement parameters, elongated along the c -axis [28]. The authors stated that this may indi-

Table 3.4: Reflections used for the single crystal refinement of the structure of $\text{Tl}_2\text{Au}_2\text{Sn}_2\text{Se}_6$, divided into groups which are allowed by the a_0, c_0 subcell or not allowed by the a_0, c_0 subcell.

	Allowed by subcell	Not allowed by subcell
# measured	13523	13640
# with $I/\sigma > 3$	7212	2688
# with $I/\sigma > 10$	5016	846
maximum I/σ	21.4	20.2
average I/σ	7.0	1.9
maximum I	9998	122
average I	168	7.3

cate positional disorder. The same large displacement ellipsoids were seen for the equivalent Tl atom when the structure was solved in the smaller unit cell. However, in the larger unit cell, this site corresponds to two sites in different positions, each displaced slightly with respect to the subcell structure (Figure 3.16). In the larger cell, these Tl atoms (both Tl(4)) then have nearly spherical displacement ellipsoids (Table 3.7). This small displacement is the primary difference between the structures solved in the different unit cells. Due to the weakness of the supercell reflections observed for this compound, and the smaller scattering power of K with respect to Tl, we believe that the supercell may have been overlooked in $\text{K}_2\text{Au}_2\text{Sn}_2\text{Se}_6$.

We will now address the largest Fourier difference peaks observed in the refinement of the crystal structure of $\text{Tl}_2\text{Au}_2\text{Sn}_2\text{Se}_6$. Three difference peaks are greater than $2 \text{ e}\text{\AA}^{-3}$ and not close to heavy atoms. The location of the two strongest, labeled Q(1) ($5.89 \text{ e}\text{\AA}^{-3}$) and Q(2) ($3.87 \text{ e}\text{\AA}^{-3}$), are shown in Figure 3.17. The relationship between the location of the Q sites and those of the Tl and Au atoms suggest possible disorder or twinning in the crystal. The locations of the

Table 3.5: Single crystal refinement data for $\text{Tl}_2\text{Au}_2\text{Sn}_2\text{Se}_6$.

Empirical formula	$\text{Tl}_2\text{Au}_2\text{Sn}_2\text{Se}_6$
Formula weight	1513.81 g/mol
Temperature	175(5) K
Wavelength	0.71073 Å
Crystal system	Tetragonal
Space Group	P4/ncc
Unit cell dimensions	a = 11.4513(7) Å c = 20.071(3) Å
Volume	2632.0(4) Å ³
Absorption Correction	SADABS (based on equivalents)
Color	Black
Z	8
Calculated density	7.641 g/cm ³
Absorption coefficient	66.895 mm ⁻¹
F(000)	4992
θ range	2.03 ° to 33.14 °
Limiting indices	-13 ≤ h ≤ 16 -8 ≤ k ≤ 17 -30 ≤ l ≤ 24
Reflections collected/unique	22199 / 2527 [R(int) = 0.0521]
Completeness to $\theta=30.45^\circ$	100.0%
Refinement method	Full-matrix least-squares on F ²
Data/restraints/parameters	2527 / 0 / 62
Goodness-of-fit on F ²	1.063
Final R indices (I > 2σ(I)) ^(a,b)	R ₁ = 0.0379, wR ₂ = 0.0858
R indices (all data) ^(a,b)	R ₁ = 0.0787, wR ₂ = 0.1017
Largest diff. peak and hole	5.890 and -4.771 eÅ ⁻³

$${}^a R_1 = \frac{\sum ||F_o| - |F_c||}{\sum |F_o|} \quad {}^b wR_2 = \frac{[\sum w(F_o^2 - F_c^2)^2 / \sum w(F_o^2)^2]^{\frac{1}{2}}}{\sum w(F_o^2)^2}$$

$$w^{-1} = [\sigma(F_o^2) + (aP)^2 + bP] \quad \text{where } P = [\max(F_o^2, 0) + 2F_c^2] / 3$$

Table 3.6: Atomic coordinates and equivalent isotropic displacement parameters (\AA^2) for $\text{Tl}_2\text{Au}_2\text{Sn}_2\text{Se}_6$. U_{eq} is defined as one third of the trace of the orthogonalized U_{ij} tensor.

Atom	x	y	z	U_{eq}	Occ.
Tl(1)	0.2500	0.7500	0.5912(1)	0.015(1)	1
Tl(2)	0.2500	0.2500	0.5634(4)	0.016(2)	0.121(3)
Tl(3)	0.2500	0.2500	0.4342(1)	0.015(1)	0.879(3)
Tl(4)	0.7500	0.7500	0.7570(1)	0.024(1)	1
Au(1)	0.4039(1)	0.9039(1)	0.7500	0.013(1)	1
Au(2)	0.0935(1)	0.9065(1)	0.7500	0.012(1)	1
Sn(1)	0.0030(1)	0.4989(1)	0.5880(1)	0.008(1)	1
Se(2)	-0.1644(1)	0.4990(1)	0.5002(1)	0.008(1)	1
Se(3)	0.5032(1)	0.8157(1)	0.6558(1)	0.010(1)	1
Se(6)	-0.0032(1)	0.8135(1)	0.8436(1)	0.009(1)	1

Table 3.7: The anisotropic displacement parameters (\AA^2) for the compound $\text{Tl}_2\text{Au}_2\text{Sn}_2\text{Se}_6$. The exponent of the anisotropic displacement factor is of the form: $-2\pi^2(h^2a^{*2}U_{11}+\dots+2hka^*b^*U_{12})$.

Atom	U_{11}	U_{22}	U_{33}	U_{23}	U_{13}	U_{12}
Tl(1)	0.012(1)	0.011(1)	0.024(1)	0	0	0.000(1)
Tl(2)	0.011(2)	0.011(2)	0.024(4)	0	0	0
Tl(3)	0.012(1)	0.012(1)	0.020(1)	0	0	0
Tl(4)	0.024(1)	0.024(1)	0.025(1)	0	0	0
Au(1)	0.015(1)	0.015(1)	0.008(1)	-0.001(1)	0.001(1)	-0.001(1)
Au(2)	0.014(1)	0.014(1)	0.008(1)	-0.001(1)	-0.001(1)	-0.001(1)
Sn(1)	0.009(1)	0.009(1)	0.005(1)	0.000(1)	0.000(1)	-0.001(1)
Se(2)	0.007(1)	0.010(1)	0.008(1)	-0.001(1)	0.001(1)	0.000(1)
Se(3)	0.013(1)	0.008(1)	0.008(1)	0.001(1)	-0.001(1)	0.000(1)
Se(6)	0.013(1)	0.007(1)	0.009(1)	0.000(1)	-0.002(1)	0.000(1)

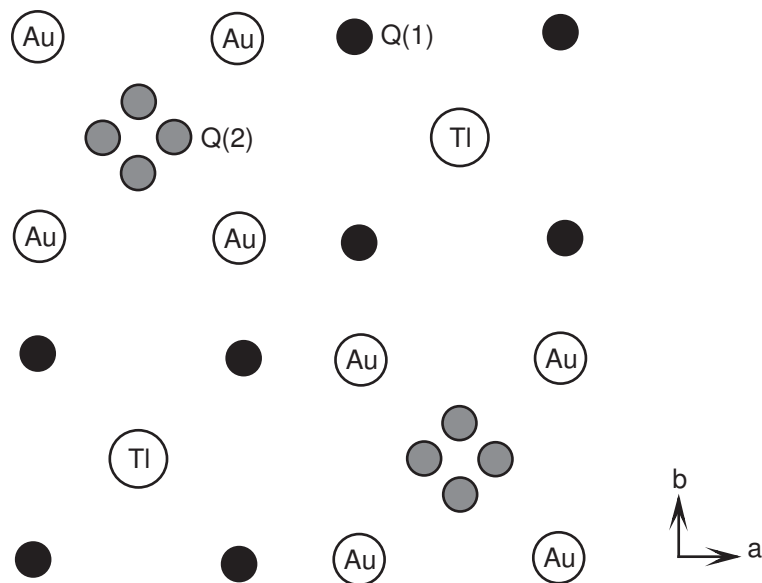


Figure 3.17: A plane from the $\text{Tl}_2\text{Au}_2\text{Sn}_2\text{Se}_6$ structure parallel to the c axis containing Au(1), Au(2), and Tl(4), showing the location of the two strongest difference peaks Q(1) and Q(2).

only other peak larger than $2 \text{ e}\text{\AA}^{-3}$ show a similar relationship to positions of Se atoms. Since even the strongest Q was relatively weak, the level of twinning or disorder is expected to be small, and no efforts were made to further resolve the issue.

This compound was prepared as a single phase sample by first reacting the elements together at 700°C , then grinding and annealing a pressed pellet at 400°C . A rectangular pellet of this material was pressed and sintered at 400°C for 7 days.

Resistivity and thermopower could not be measured due to poor electrical contacts, however thermal conductivity was measured and is presented in Figure 3.4. This compound has extremely low thermal conductivity, especially at low temperatures, similar to $\text{Tl}_2\text{Cu}_2\text{SnTe}_4$ presented above.

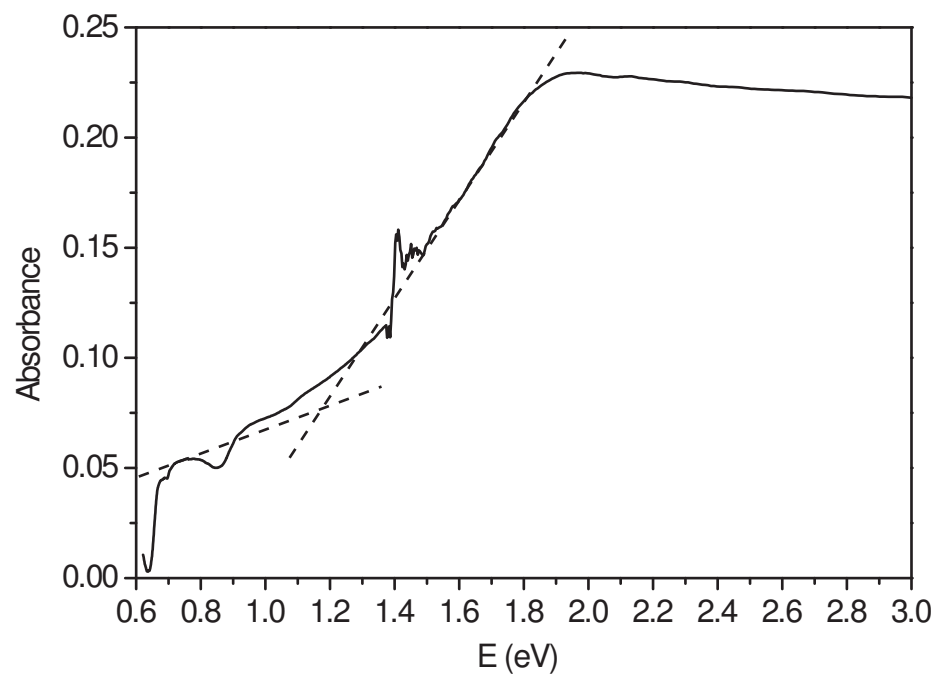


Figure 3.18: The measured absorbance spectrum of $\text{Tl}_2\text{Au}_2\text{Sn}_2\text{Se}_6$ used to approximate the band gap. A gap of 1.2 eV is estimated from this data.

The band gap of this material was estimated from its absorbance spectrum. The spectrum is shown in Figure 3.18. The band gap was measured to be approximately 1.2 eV, consistent with the black color of this compound.

3.3.9 $\text{Tl}_2\text{TiCu}_2\text{S}_4$ and $\text{Tl}_2\text{TiCu}_2\text{Se}_4$

Single phase samples of these two compounds were made by reacting stoichiometric mixtures of the elements at 800 °C for two days followed by cooling to room temperature over eight days. The sulfide is a very dark red color, while the selenide is black. Single crystal X-ray structure determinations were precluded due to poor crystallinity of the plate-like crystals. Although no single crystal structure was determined for these two compounds, powder X-ray diffraction data suggest that they are isostructural to the known AM compounds $\text{Rb}_2\text{TiCu}_2\text{S}_4$ and $\text{Cs}_2\text{TiCu}_2\text{Se}_4$, which form layered structures in the space group $P4_2/mcm$ [29]. The PXRD patterns are shown in Figure 3.19. The structure (Figure 3.20) contains sheets of edge sharing Cu and Ti centered tetrahedra with S or Se at the vertices. These sheets are separated by Tl atoms.

Diffuse reflectance spectroscopy was used to estimate the band gap of these compounds. The measured absorbance spectra are displayed in Figure 3.21. From these plots, the estimated band gaps are 1.4 eV for $\text{Tl}_2\text{TiCu}_2\text{S}_4$ and 1.1 eV for $\text{Tl}_2\text{TiCu}_2\text{Se}_4$. As is usually the case, the selenide has a smaller band gap than the isostructural sulfide.

3.3.10 $\text{Tl}_{1.71}\text{Sn}_{2.60}\text{Bi}_{7.71}\text{Se}_{15}$

In his dissertation, Dr. Thomas K. Reynolds reported the structure and thermoelectric properties of the compound $\text{Tl}_{0.91}\text{Sn}_{3.18}\text{Bi}_{6.91}\text{Se}_{14}$ [1]. Resistivity measurements showed metallic behavior, with a room temperature value near

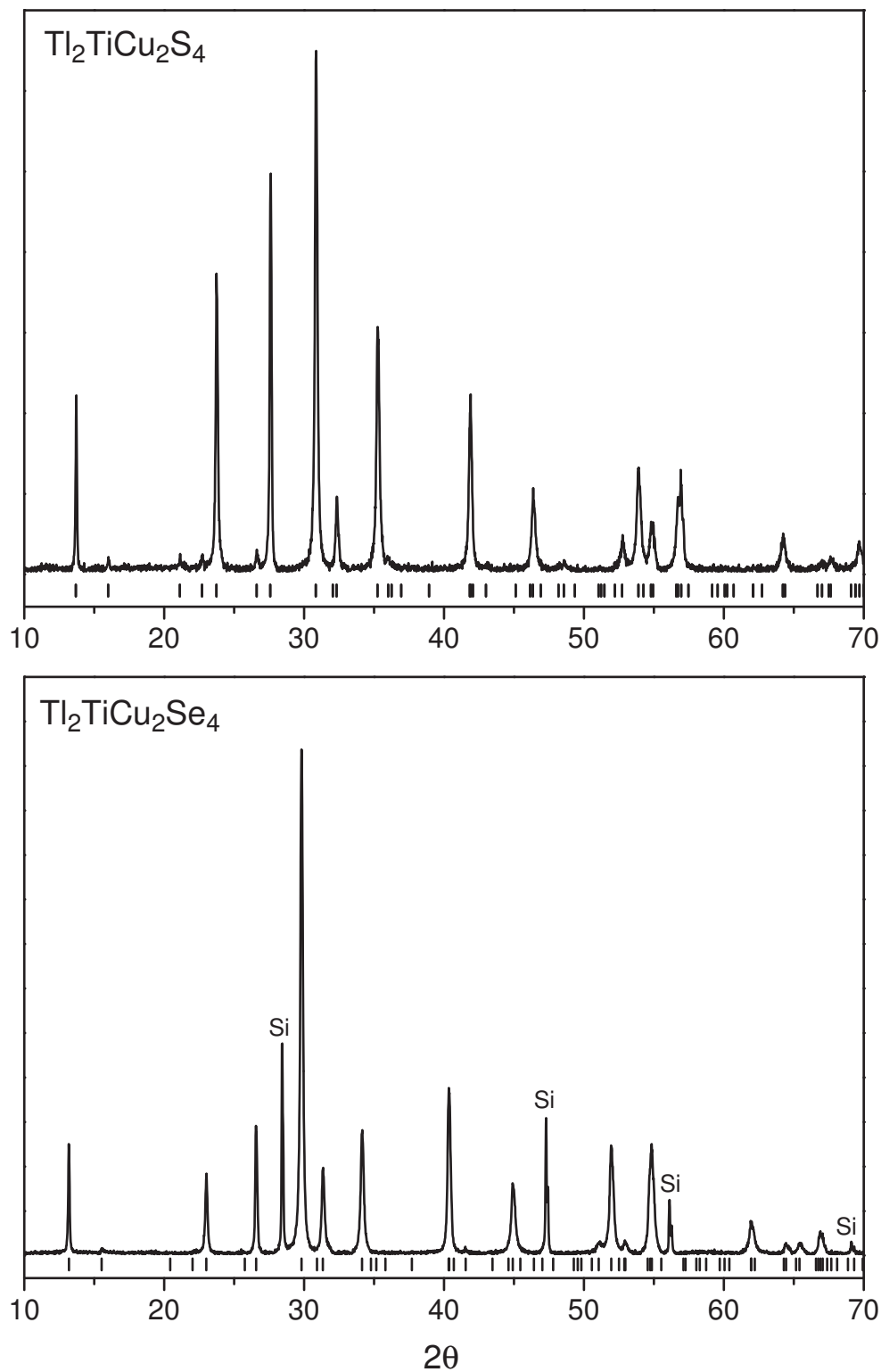


Figure 3.19: Measured PXRD patterns for $\text{Tl}_2\text{TiCu}_2\text{S}_4$ and $\text{Tl}_2\text{TiCu}_2\text{Se}_4$. The tick marks locate the predicted peak positions based on the refined unit cell constants and the space group of the AM analogues ($P4_2/mcm$). An internal Si standard was mixed into the selenide sample.

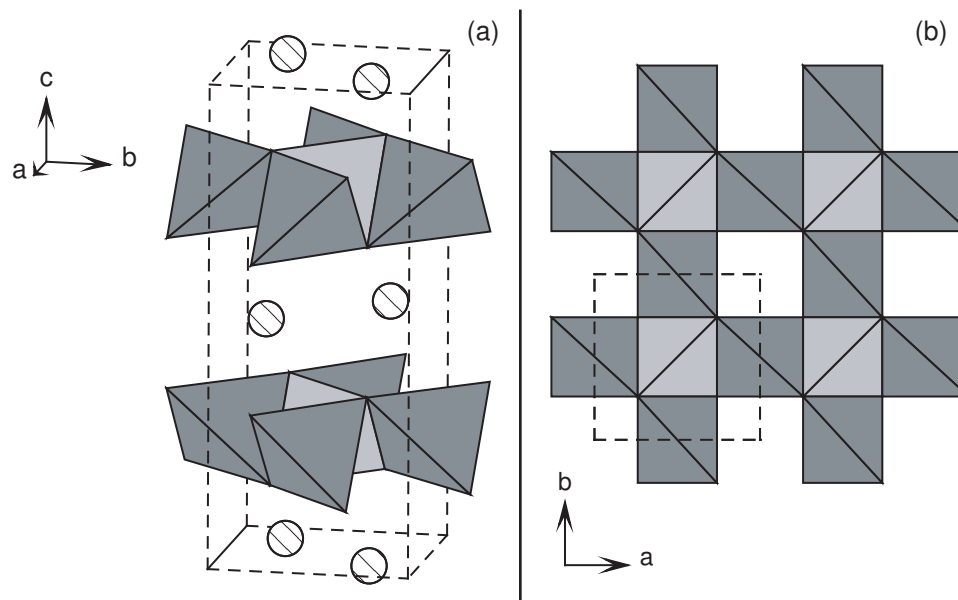


Figure 3.20: Views of the structure type adopted by $\text{Tl}_2\text{TiCu}_2\text{S}_4$ and $\text{Tl}_2\text{TiCu}_2\text{Se}_4$, showing Cu centered tetrahedra (dark) and Ti centered tetrahedra (light) with S or Se at the vertices and Tl atoms (striped circles). In (a) the layered structure is emphasized, while (b) shows a single $[\text{TiCu}_2\text{Q}_4]^{2-}$ layer viewed down the c axis.

0.8 $\text{m}\Omega\text{cm}$. The compound was n-type with a room temperature thermopower of about $-90 \mu\text{V}/\text{K}$. The thermal conductivity was not measured, but is expected to be at least as low as the alkali metal compounds $\text{K}_{1-x}\text{Sn}_{4-x}\text{Bi}_{11+x}\text{Se}_{21}$ and $\text{K}_{1+x}\text{Sn}_{4-2x}\text{Bi}_{7+x}\text{Se}_{15}$ which have thermal conductivities in the range 10-14 mW/cmK at room temperature [30, 31]. From this an estimated ZT of 0.2-0.3 is calculated. However, there were difficulties with crystal structure solution, and attempts were made to synthesize more crystals of this compound for further study. The elements were loaded in a 1:3:7:14 ratio, and heated at 700°C for one day, then cooled to 300°C over four days. This reaction produced a large number of needlelike crystals up to 1 cm long and from 10 to 50 microns thick. Resistivity measurements showed these needles to be semiconducting, with resistivity values significantly higher than those reported for $\text{Tl}_{0.91}\text{Sn}_{3.18}\text{Bi}_{6.91}\text{Se}_{14}$. This sug-

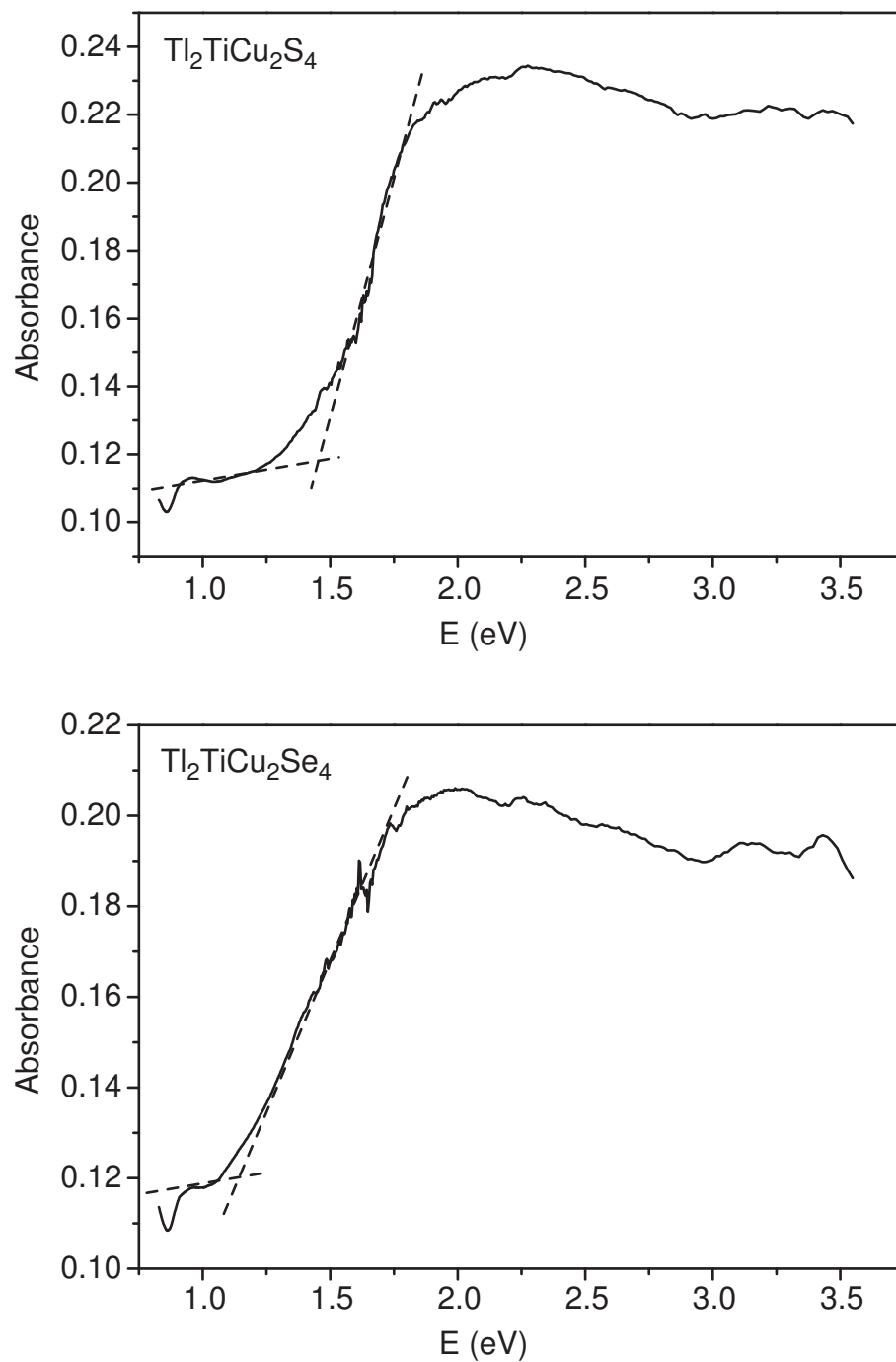


Figure 3.21: The measured absorbance spectra of $\text{Tl}_2\text{TiCu}_2\text{S}_4$ and $\text{Tl}_2\text{TiCu}_2\text{Se}_4$ used to approximate the band gaps. From this data, the estimated gaps are 1.4 eV for the sulfide and 1.1 eV for the selenide.

gested that these were crystals of a different compound, and the characterization of this new compound was pursued.

Single crystal X-ray diffraction studies showed that these crystals indeed were not isostructural to the previously reported compound. X-ray experiments on two needles gave the same structure, and the refinement results from the second crystal (which was smaller and had a lower R_{int} value) are shown in Table 3.8. Views of the structure of $Tl_{1.71}Sn_{2.60}Bi_{7.71}Se_{15}$ are shown in Figures 3.22 and 3.23. The structure is made up of stepped sheets and columns, both composed of edge sharing octahedra with Se atoms at their vertices. Atom positions, equivalent isotropic displacement parameters, and site occupancy factors are given in Table 3.9. Refined anisotropic displacement parameters are listed in Table 3.10, and the ellipsoids are shown in Figure 3.22.

Some attention must be given to how the occupancies of the metal sites were assigned. At first, all of these octahedral sites were refined as mixed Bi/Sn. When this was done, four sites were seen to be nearly pure Bi (>95%). For subsequent refinement, these four sites were assigned as Bi. The remaining five octahedral sites were left as mixtures of Bi and Sn. In addition, there is one metal site that is eight coordinate, with longer bonds to Se (all >3.35 Å). Based on these long Se distances, this site is identified as Tl. This site also has larger displacement ellipsoids than the octahedral sites (see Figure 3.22 and Table 3.9). Finally, there are two sites which are coordinated to eight Se atoms, each with some distances similar to those seen in the octahedral sites, and some similar to those seen for the Tl site. These sites were assigned as a mixture of Tl and Sn. Like the pure Tl sites in this compound, these sites have relatively large displacement parameters. This along with the elongated displacement ellipsoids on one of the Se atoms to which this site is bonded (see Figure 3.22) are likely to be indications of positional disorder. The position of this Se atom should depend on whether Tl or Sn occu-

pies the neighboring site. It is impossible to exclude the possibility of some Bi on the Tl/Sn sites as well. Similar atom assignments used in the refinement of the alkali metal analogue, and other members of the so called grand homologous series of compounds reported by Kanatzidis and coworkers (*vide infra*). When the assignments described above were used, and the occupancy ratios were allowed to refine freely, the resulting composition proved to be nearly charge-balanced: $\text{Tl}_{1.74}\text{Sn}_{2.68}\text{Bi}_{7.58}\text{Se}_{15}$ ($R_1 = 0.0333$, $wR_2 = 0.0636$ for $I > 2\sigma I$). Assigning the formal charges of +1 for Tl, +2 for Sn, +3 for Bi gives a total of 29.8 positive charges per formula unit, almost exactly matching the 15 Se^{2-} ions. This supports the atom assignments used in the refinements. For the final refinement cycle, exact charge balance was enforced, giving the composition $\text{Tl}_{1.71}\text{Sn}_{2.60}\text{Bi}_{7.71}\text{Se}_{15}$, with no significant impact on the agreement factors (Table 3.8). Of the seven Fourier difference peaks greater than $2 \text{ e}\text{\AA}^{-3}$, six are less than 0.85 \AA from a Bi or Tl atom, and the remaining one is near a Se atom ($d = 0.80 \text{ \AA}$).

A list of distances between the all the metal atom sites and Se is given in Table 3.11. Inspection of this list reveals that some of the "octahedral" sites described above may be better described as square-pyramidal. These include Bi(1), Bi(2), Bi/Sn(6), and Bi/Sn(9). Excluding the single long bonds of these sites, the Bi-Se and Bi/Sn-Se distances in $\text{Tl}_{1.71}\text{Sn}_{2.60}\text{Bi}_{7.71}\text{Se}_{15}$ range from 2.71 \AA to 3.16 \AA . For comparison, the Bi-Se distances in Bi_2Se_3 are between 2.89 \AA and 3.03 \AA [32], and the Sn-Se distances in SnSe are $2.75\text{-}3.47 \text{ \AA}$ [33]. Typically, $\text{Tl}^{1+}\text{-Se}$ distances are longer than this: for example 3.45 \AA in TlInSe_2 [34]. This is in agreement with the longer Tl-Se distances seen in $\text{Tl}_{1.71}\text{Sn}_{2.60}\text{Bi}_{7.71}\text{Se}_{15}$ of $3.36\text{-}3.52 \text{ \AA}$ for Tl(1), and $2.88\text{-}3.55 \text{ \AA}$ for the mixed Tl/Sn sites.

As note above, Kanatzidis has reported several alkali metal compounds which have structural features similar to those found in $\text{Tl}_{1.71}\text{Sn}_{2.60}\text{Bi}_{7.71}\text{Se}_{15}$ and $\text{Tl}_{0.91}\text{Sn}_{3.18}\text{Bi}_{6.91}\text{Se}_{14}$. These series of compounds are described in terms

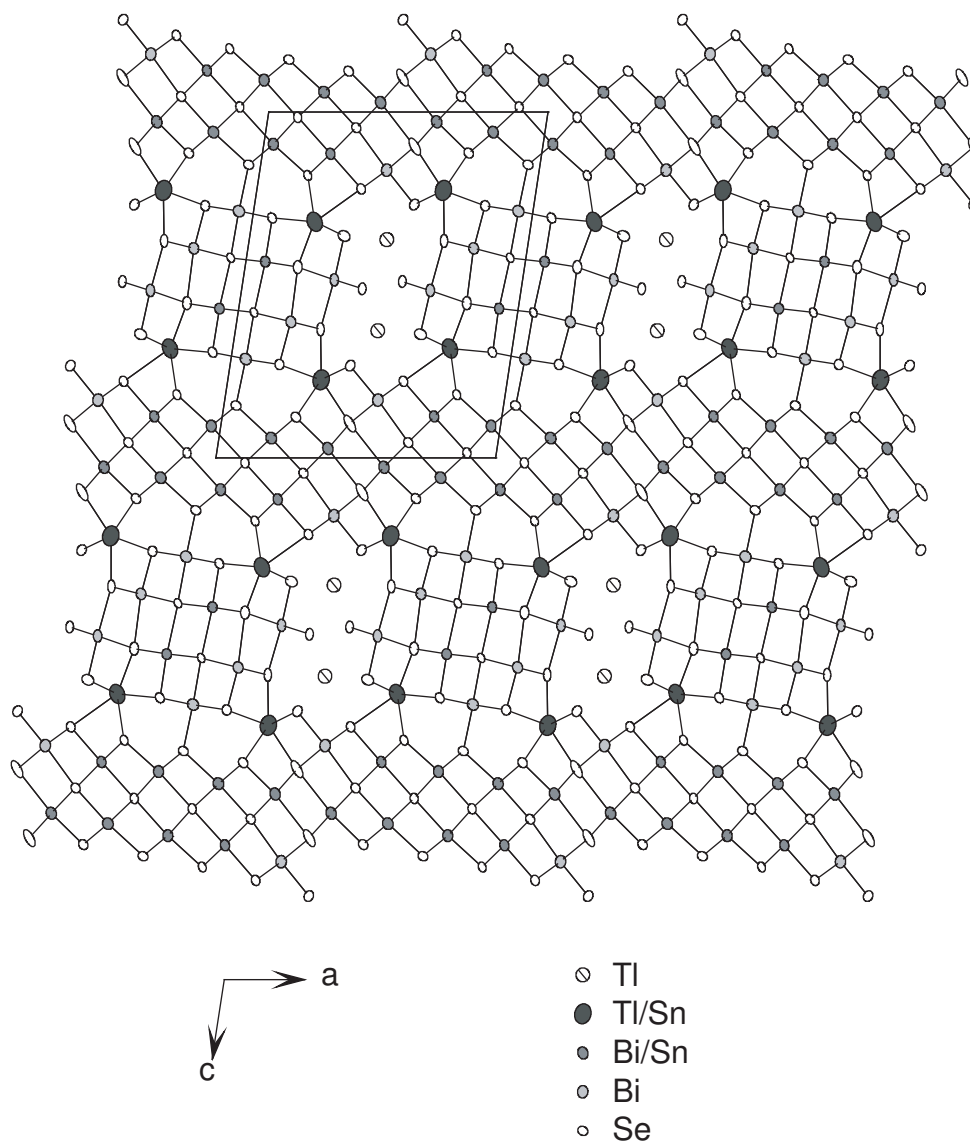


Figure 3.22: A view down the b-axis of the crystal structure of $\text{Tl}_{1.71}\text{Sn}_{2.60}\text{Bi}_{7.71}\text{Se}_{15}$ showing displacement ellipsoids (95 % probability level). The dotted lines are the unit cell edges.

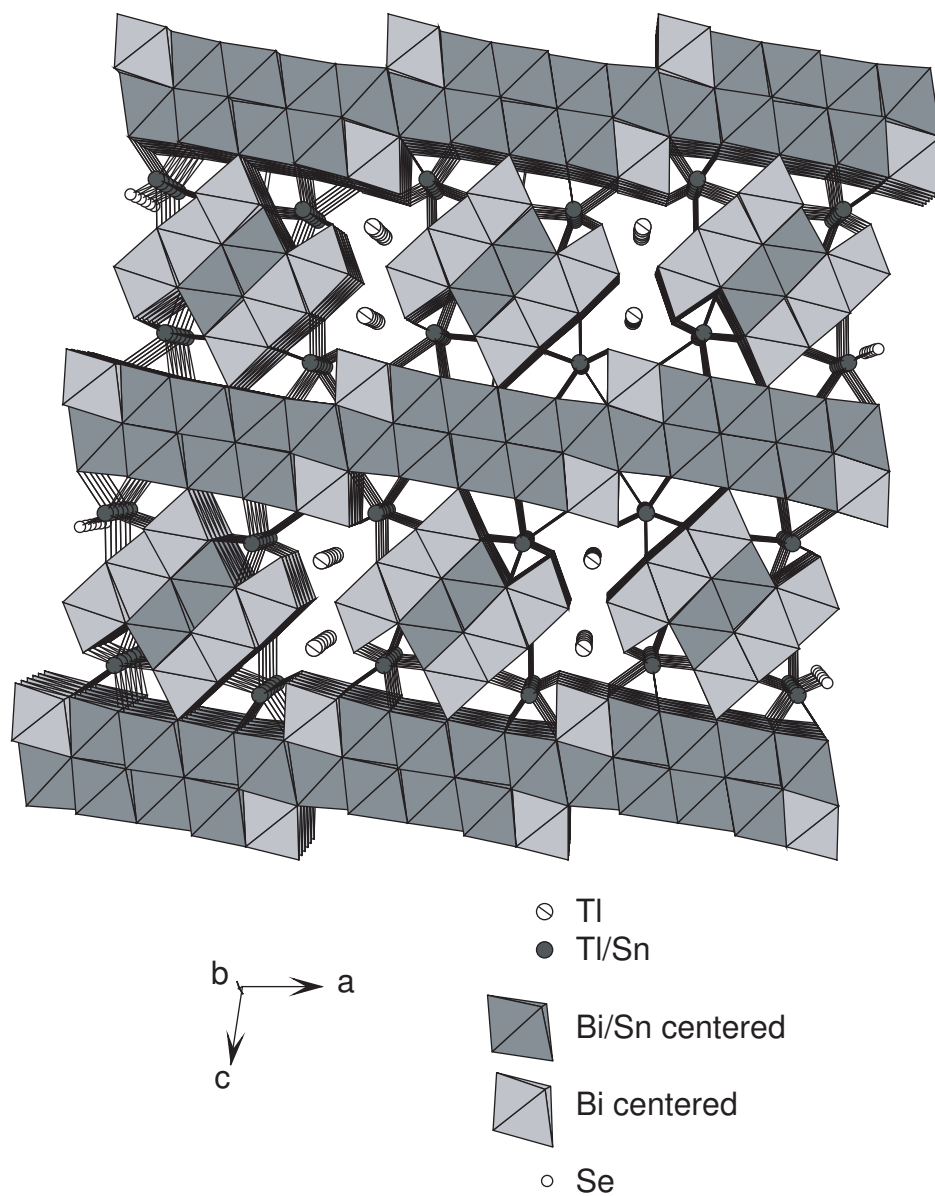


Figure 3.23: A perspective view of the crystal structure of $\text{Tl}_{1.71}\text{Sn}_{2.60}\text{Bi}_{7.71}\text{Se}_{15}$ showing the stepped layers and the columns, both made up of edge sharing octahedra.

Table 3.8: Single crystal refinement data for $\text{Tl}_{1.71}\text{Sn}_{2.60}\text{Bi}_{7.71}\text{Se}_{15}$.

Empirical formula	$\text{Tl}_{1.71}\text{Sn}_{2.60}\text{Bi}_{7.71}\text{Se}_{15}$
Formula weight	3267.04
Temperature	175(5) K
Wavelength	0.71073 Å
Crystal system, space group	Monoclinic, $P2_1/m$
Unit cell dimensions	$a = 17.2015(15)$ Å $\alpha = 90^\circ$ $b = 4.1577(4)$ Å $\beta = 98.673(7)^\circ$ $c = 21.504(3)$ Å $\gamma = 90^\circ$
Volume	1520.4(3) Å ³
Z, Calculated density	2, 7.137 g/cm ³
Absorption coefficient	66.397 mm ⁻¹
F(000)	2694
Crystal size	0.120 x 0.030 x 0.010 mm ³
Theta range for data collection	1.42 to 28.28 °
Limiting indices	$-22 \leq h \leq 22, -5 \leq k \leq 5, -28 \leq l \leq 28$
Reflections collected / unique	23370 / 4297 [R(int) = 0.0594]
Completeness to theta = 28.28 °	100.0 %
Refinement method	Full-matrix least-squares on F ²
Data / restraints / parameters	4297 / 1 / 170
Goodness-of-fit on F ²	1.019
Final R indices [I > 2σ(I)]	R ₁ = 0.0334, wR ₂ = 0.0641
R indices (all data)	R ₁ = 0.0560, wR ₂ = 0.0717
Largest diff. peak and hole	3.112 and -2.812 eÅ ⁻³

$${}^a R_1 = \frac{\sum ||F_o| - |F_c||}{\sum |F_o|} \quad {}^b wR_2 = \left[\frac{\sum w(F_o^2 - F_c^2)^2}{\sum w(F_o^2)^2} \right]^{\frac{1}{2}}$$

$$w^{-1} = [\sigma(F_o^2) + (aP)^2 + bP] \text{ where } P = [\max(F_o^2, 0) + 2F_c^2] / 3$$

Table 3.9: Atomic coordinates, equivalent isotropic displacement parameters (\AA^2), and occupancies for $\text{Tl}_{1.71}\text{Sn}_{2.60}\text{Bi}_{7.71}\text{Se}_{15}$. U_{eq} is defined as one third of the trace of the orthogonalized U_{ij} tensor.

Atom	x	y	z	U_{eq}	Occ.
Tl(1)	0.5087(1)	0.2500	0.6317(1)	0.022(1)	1
Bi(1)	0.8066(1)	0.2500	0.3938(1)	0.013(1)	1
Bi(2)	0.4530(1)	0.2500	0.1678(1)	0.015(1)	1
Bi(3)	0.3257(1)	0.2500	0.4847(1)	0.012(1)	1
Bi(4)	0.0526(1)	0.2500	0.7138(1)	0.015(1)	1
Bi(5)	0.7567(1)	0.2500	0.8796(1)	0.013(1)	0.918(3)
Sn(5)	0.7567(1)	0.2500	0.8796(1)	0.013(1)	0.082(3)
Bi(6)	0.0690(1)	0.2500	0.4321(1)	0.013(1)	0.785(7)
Sn(6)	0.0690(1)	0.2500	0.4321(1)	0.013(1)	0.215(7)
Bi(7)	0.1865(1)	0.2500	0.9421(1)	0.015(1)	0.823(7)
Sn(7)	0.1865(1)	0.2500	0.9421(1)	0.015(1)	0.177(7)
Bi(8)	0.0341(1)	0.2500	0.0926(1)	0.015(1)	0.625(7)
Sn(8)	0.0341(1)	0.2500	0.0926(1)	0.015(1)	0.375(7)
Bi(9)	0.6054(1)	0.2500	0.0278(1)	0.015(1)	0.553(7)
Sn(9)	0.6054(1)	0.2500	0.0278(1)	0.015(1)	0.447(7)
Tl(10)	0.7761(1)	0.2500	0.6831(1)	0.028(1)	0.388(8)
Sn(10)	0.7761(1)	0.2500	0.6831(1)	0.028(1)	0.612(8)
Tl(11)	0.3332(1)	0.2500	0.7737(1)	0.031(1)	0.315(8)
Sn(11)	0.3332(1)	0.2500	0.7737(1)	0.031(1)	0.685(8)
Se(11)	0.0697(1)	0.2500	0.3059(1)	0.011(1)	1
Se(12)	0.8937(1)	0.2500	0.9850(1)	0.010(1)	1
Se(13)	0.3213(1)	0.2500	0.0451(1)	0.010(1)	1
Se(14)	0.6279(1)	0.2500	0.7781(1)	0.010(1)	1
Se(15)	0.0432(1)	0.2500	0.8481(1)	0.012(1)	1
Se(16)	0.1741(1)	0.2500	0.1832(1)	0.011(1)	1
Se(17)	0.8241(1)	0.2500	0.2706(1)	0.011(1)	1
Se(18)	0.0565(1)	0.2500	0.5792(1)	0.009(1)	1
Se(19)	0.5697(1)	0.2500	0.4894(1)	0.011(1)	1
Se(20)	0.3035(1)	0.2500	0.6278(1)	0.012(1)	1
Se(21)	0.8118(1)	0.2500	0.5522(1)	0.013(1)	1
Se(22)	0.5706(1)	0.2500	0.2672(1)	0.012(1)	1
Se(23)	0.7368(1)	0.2500	0.1184(1)	0.011(1)	1
Se(24)	0.3368(1)	0.2500	0.3579(1)	0.015(1)	1
Se(25)	0.4593(1)	0.2500	0.9003(1)	0.020(1)	1

Table 3.10: The anisotropic displacement parameters (\AA^2) for the compound $\text{Tl}_{1.71}\text{Sn}_{2.60}\text{Bi}_{7.71}\text{Se}_{15}$. The exponent of the anisotropic displacement factor is of the form: $-2\pi^2(h^2a^2U_{11}+\dots+2hka^*b^*U_{12})$.

Atom	U_{11}	U_{22}	U_{33}	U_{23}	U_{13}	U_{12}
Tl(1)	0.0219(3)	0.0211(4)	0.0232(4)	0.000	0.0032(3)	0.000
Bi(1)	0.0122(3)	0.0130(3)	0.0155(3)	0.000	0.0034(2)	0.000
Bi(2)	0.0130(3)	0.0142(3)	0.0185(3)	0.000	0.0023(2)	0.000
Bi(3)	0.0088(3)	0.0097(3)	0.0183(3)	0.000	0.0029(2)	0.000
Bi(4)	0.0155(3)	0.0143(3)	0.0154(3)	0.000	0.0041(2)	0.000
Bi/Sn(5)	0.0111(3)	0.0118(3)	0.0157(4)	0.000	0.0037(2)	0.000
Bi/Sn(6)	0.0115(3)	0.0121(4)	0.0143(4)	0.000	0.0026(3)	0.000
Bi/Sn(7)	0.0149(4)	0.0137(4)	0.0170(4)	0.000	0.0041(3)	0.000
Bi/Sn(8)	0.0129(4)	0.0136(4)	0.0177(5)	0.000	0.0031(3)	0.000
Bi/Sn(9)	0.0142(4)	0.0122(4)	0.0187(5)	0.000	0.0049(3)	0.000
Tl/Sn(10)	0.0303(6)	0.0132(5)	0.0433(8)	0.000	0.0141(5)	0.000
Tl/Sn(11)	0.0306(6)	0.0135(6)	0.0472(9)	0.000	0.0030(5)	0.000
Se(11)	0.0101(7)	0.0117(8)	0.0120(8)	0.000	0.0042(6)	0.000
Se(12)	0.0081(6)	0.0092(7)	0.0130(8)	0.000	0.0029(6)	0.000
Se(13)	0.0104(7)	0.0091(7)	0.0113(8)	0.000	0.0034(6)	0.000
Se(14)	0.0093(6)	0.0095(7)	0.0127(8)	0.000	0.0033(6)	0.000
Se(15)	0.0122(7)	0.0140(8)	0.0101(8)	0.000	0.0031(6)	0.000
Se(16)	0.0080(6)	0.0123(8)	0.0117(8)	0.000	0.0037(6)	0.000
Se(17)	0.0099(7)	0.0110(8)	0.0126(8)	0.000	0.0024(6)	0.000
Se(18)	0.0076(6)	0.0101(7)	0.0101(8)	0.000	0.0037(6)	0.000
Se(19)	0.0070(6)	0.0081(7)	0.0165(9)	0.000	0.0018(6)	0.000
Se(20)	0.0067(6)	0.0098(8)	0.0204(9)	0.000	0.0032(6)	0.000
Se(21)	0.0094(7)	0.0103(8)	0.0203(9)	0.000	0.0030(6)	0.000
Se(22)	0.0102(7)	0.0120(8)	0.0136(9)	0.000	-0.0001(6)	0.000
Se(23)	0.0113(7)	0.0099(8)	0.0118(8)	0.000	0.0038(6)	0.000
Se(24)	0.0178(8)	0.0147(8)	0.0135(9)	0.000	0.0048(6)	0.000
Se(25)	0.0209(8)	0.0093(8)	0.0346(11)	0.000	0.0199(8)	0.000

Table 3.11: Distances from metal atoms sites to neighboring Se atoms (Å) in $\text{Tl}_{1.71}\text{Sn}_{2.60}\text{Bi}_{7.71}\text{Se}_{15}$.

Tl(1)	3.3557(14)	Bi(4)	2.9053(17)	Bi/Sn(8)	2.8600(17)
	3.3557(14)		2.9173(18)		2.8685(12)
	3.3803(19)		2.9418(11)		2.8685(12)
	3.4350(15)		2.9418(11)		3.0454(13)
	3.4350(15)		2.9527(11)		3.0454(13)
	3.4445(14)		2.9527(11)		3.0810(17)
	3.4445(14)				
	3.4895(18)	Bi/Sn(5)	2.8360(11)	Bi/Sn(9)	2.7518(17)
	3.5180(15)		2.8360(11)		2.9099(14)
			2.8657(17)		2.9099(14)
Bi(1)	2.7100(18)		3.0135(17)		2.9936(13)
	2.8030(10)		3.0667(12)		2.9936(13)
	2.8030(10)		3.0667(12)		3.429(2)
	3.1290(11)				
	3.1290(11)	Bi/Sn(6)	2.7163(18)	Tl/Sn(10)	2.8896(14)
	3.3945(19)		2.9048(11)		2.8896(13)
			2.9048(11)		2.970(2)
Bi(2)	2.7130(17)		2.9802(11)		3.3509(14)
	2.8461(11)		2.9802(11)		3.3509(14)
	2.8461(11)		3.2008(18)		3.4996(19)
	3.0671(14)				3.5481(17)
	3.0671(14)	Bi/Sn(7)	2.8758(12)		3.5481(17)
	3.2079(17)		2.8758(12)		
			2.9436(17)	Tl/Sn(11)	2.8773(13)
Bi(3)	2.7514(10)		2.9546(17)		2.8773(13)
	2.7514(10)		3.0553(13)		3.103(2)
	2.7618(19)		3.0553(13)		3.215(2)
	3.1566(19)				3.4308(15)
	3.1578(12)				3.4308(15)
	3.1578(12)				3.4633(17)
					3.4633(17)

of homologies, the evolution of structures through the expansion of modular units in various dimensions as the composition is changed. Kanatzidis has reported “the grand homologous series” $A_m(M_6Se_8)_m(M_{5+n}Se_{9+n})$ [30], “the homologous superseries” $A_m[M_{1+l}Se_{2+l}]_{2m}[M_{1+2l+n}Se_{3+3l+n}]$ [35], “the megaserries” $A_m[M_{1+l}Se_{2+l}]_{2m}[M_{2l+n}Se_{2+3l+n}]$ [36], and the homologous series of telluride compounds $CsPb_mBi_3Te_{5+m}$ [37]. Here M are main group metals (Sb, Bi, Sn, Pb), A are alkali metals (K, Rb, Cs), and l, m, and n are integers. In each series the values of the integers (l, m, n) determines the size and shape of the columns and stepped layers that make up the structure (note that there are only layers and no columns in the Te series).

The Tl compound reported here, $Tl_{1.71}Sn_{2.60}Bi_{7.71}Se_{15}$, is isostructural to the $l = 2, m = 2, n = 6$ member of $A_m[M_{1+l}Se_{2+l}]_{2m}[M_{2l+n}Se_{2+3l+n}]$. This formula then predicts a composition of $Tl_1M_{11}Se_{15}$, $M = Bi, Sn$. For $Tl^{1+}, Bi^{3+}, Sn^{2+}$, and Se^{2-} there is a unique Sn/Bi ratio that balances the formal charges with this chemical formula; that is, the ratio that satisfies both $1 + 3[Bi] + 2[Sn] = 30$ and $[Bi] + [Sn] = 11$, where [M] represents the stoichiometric coefficient of element M. The solution is $Tl_1Sn_4Bi_7Se_{15}$. However, if Tl is allowed to mix onto the M sites, the chemical formula is no longer constrained. In the reported AM compounds, the resulting chemical formula is typically written as, for example, $K_{1+x}Sn_{4-2x}Bi_{7+x}Se_{15}$, in which case the compound with $x = 0.46$ is known [31]. This formula reflects the fact that two divalent atoms can be replaced by one monovalent atom and one trivalent atom without disturbing the charge balance. As pointed out above, the refinement for the Tl compound was carried out under the restraint of charge neutrality. The resulting formula can be written as $Tl_{1+x}Sn_{4-2x}Bi_{7+x}Se_{15}$ with $x = 0.71$.

Several needlelike crystals of $Tl_{1.71}Sn_{2.60}Bi_{7.71}Se_{15}$ were used for electrical resistivity and thermopower measurements. All resistivity measurements

showed activated behavior, with room temperature resistivity values around 100 m Ω cm. Some variability was seen in the resistivity magnitudes, which may be attributed to inaccuracies in the measurements of the cross sectional areas of the thin needles, or to varying doping states of the individual crystals due to varying Tl/Bi/Sn ratios. Similar variation was seen in the thermopower measurements. All showed the compound to be n-type, and an increase in the magnitude of S with increasing temperature, but the values at room temperature varied between -200 μ V/K and -450 μ V/K. Representative data are shown in Figure 3.24. These data were chosen because we have the most confidence in the geometrical measurements as well as the thermal and electrical contacts. In addition, these data sets (S and ρ) were measured on the same crystal, and thus represent a single doping state. This material has high thermopower, but is too resistive for TE applications.

Also shown in Figure 3.24 is a logarithmic plot of the resistivity versus $1/T$. This plot would be linear if the observed decrease in resistivity with increasing temperature were due only (or even primarily) to an increase in charge carrier density n caused by activation from localized dopant states or across a band gap. That the curve is not linear suggests neither of these models accurately describes the system. This could be due to combination of intrinsic and extrinsic activation, or to a strong temperature dependence of the carrier mobility μ ($\rho(T) = en(T)\mu(T)$). It is also possible that at low temperatures, when the resistivity of the sample is large, the total resistance is no longer small compared with the input impedance of the instrument. For example, the sample resistance at the lowest temperature was about 120 k Ω . At room temperature, the contact resistance was on the order of 1 k Ω , and may have increased upon cooling. High sample resistance would cause the measured resistivity value to be lower than the true value. This may be responsible for the deviation from linearity in the log

plot shown in Figure 3.24, which appears to be stronger at lower temperatures. If this is indeed the cause for the nonlinear nature of the $\log(\rho)$ vs. $1/T$ data, then a linear fit to higher temperature data may still give a meaningful estimate of the activation energy or band gap. Such a fit is shown in Figure 3.24, and from it a band gap of 0.08 eV or activation energy of 0.04 eV is derived.

Kanatzidis and coworkers have measured the band gaps of several similar alkali metal compounds using diffuse reflectance spectroscopy [38]. The values range from a low of 0.3 eV for $K_{1-x}Sn_{3-x}Bi_{11+x}Se_{20}$ up to a high of 0.62 eV for $Cs_{1+x}Pb_{3-2x}Bi_{7+x}Se_{14}$. These are significantly higher than the estimated gap of $Tl_{1.71}Sn_{2.60}Bi_{7.71}Se_{15}$ of 0.08 eV. The direct analogue $K_{1.46}Sn_{3.09}Bi_{7.45}Se_{15}$ ($K_{1+x}Sn_{4-2x}Bi_{7+x}Se_{15}$ with $x = 0.45$) has a measured band gap of 0.39 eV, and resistivity and thermopower at room temperature of $9 \text{ m}\Omega\text{cm}$, $-70 \text{ }\mu\text{V/K}$. The TE power factor (S^2/ρ) of these two compounds are $0.54 \text{ }\mu\text{W/cmK}^2$ for $K_{1+x}Sn_{4-2x}Bi_{7+x}Se_{15}$ and $2.2 \text{ }\mu\text{W/cmK}^2$ for $Tl_{1.71}Sn_{2.60}Bi_{7.71}Se_{15}$.

The value of the thermal conductivity is needed to determine the figure of merit ZT. These measurements could not be performed on the small single crystals, so we will estimate it from the measured data from the alkali metal analogs. Kanatzidis et al. have measured the thermal conductivity of a bulk ingot of $K_{1.46}Sn_{3.09}Bi_{7.45}Se_{15}$, and found a room temperature value of 14 mW/cmK . This was uncorrected for radiative losses, and the true value is therefore expected to be lower. Subtracting the electronic component using the Wiedemann-Franz law gives $\kappa_{Lattice} = 13.2 \text{ mW/cmK}$. The electronic thermal conductivity of $Tl_{1.71}Sn_{2.60}Bi_{7.71}Se_{15}$ is small, only about 0.1 mW/cmK , due to its relatively high resistivity. It is likely that this is less than the error due to radiative losses in the measurement of the AM compound. Therefore we use 13 mW/cmK as a conservative estimate of the thermal conductivity of $Tl_{1.71}Sn_{2.60}Bi_{7.71}Se_{15}$, keeping in mind that the actual value should be lower than this due to the substitution

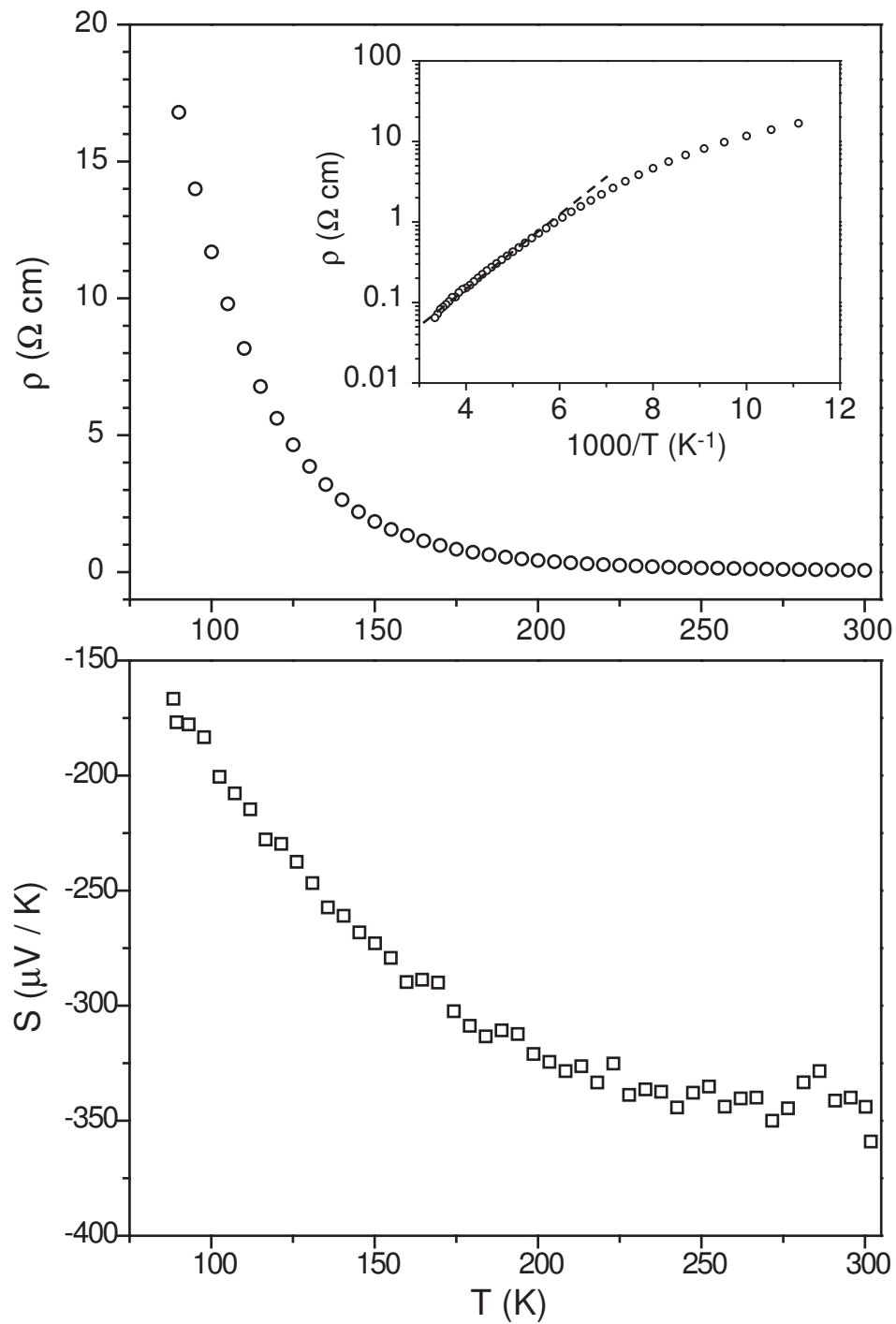


Figure 3.24: The measured electrical resistivity ρ and thermopower S of $\text{Tl}_{1.71}\text{Sn}_{2.60}\text{Bi}_{7.71}\text{Se}_{15}$. Based on measurements of reference materials and on estimated errors in geometrical measurements, the uncertainty of the ρ and S measurements is estimated to be about $\pm 5\%$.

of the heavier element Tl for K, and the increased amount of disorder (larger value of x in the chemical formula). This gives an estimate for the $ZT \approx 0.05$ at 300 K for $\text{Tl}_{1.71}\text{Sn}_{2.60}\text{Bi}_{7.71}\text{Se}_{15}$. This is not a high ZT . It is significantly lower than that of the best member of the AM homologous series ($ZT \approx 0.2$ at 300 K in $\text{K}_{1.25}\text{Pb}_{3.50}\text{Bi}_{25}\text{Se}_{15}$). However, it is higher than that of the direct AM analogue ($ZT \approx 0.01$ at 300 K in $\text{K}_{1.46}\text{Sn}_{3.09}\text{Bi}_{7.45}\text{Se}_{15}$). Interestingly, this estimated increase in performance is not due to lower resistivity or lower thermal conductivity, but to enhanced thermopower. Perhaps the Tl analogue of $\text{K}_{1.25}\text{Pb}_{3.50}\text{Bi}_{25}\text{Se}_{15}$ should be investigated.

3.3.11 $\text{Tl}_{11.5}\text{Sb}_{11.5}\text{Cu}_8\text{Se}_{27}$

This compound was discovered during an investigation of the quaternary phase diagram. The elements were combined in a 2:2:2:5 ratio and the reaction product contained crystals of the title composition in the form of silver needles. $\text{Tl}_{11.5}\text{Sb}_{11.5}\text{Cu}_8\text{Se}_{27}$ is not isostructural to any known AM phase and crystallizes in the monoclinic space group $P2_1/m$. The crystal structure is shown in Figure 3.25 and includes Cu in tetrahedral coordination and Sb in both square pyramidal and octahedral coordination, common coordination environments for both elements. These polyhedra form a framework with channels running along the b direction in which the Tl atoms reside. Three of the Tl sites are partially occupied by Sb and are coordinated by Se in either square pyramidal or distorted octahedral geometry. Four are fully occupied by Tl and have seven-fold coordination by Se (*vide infra*). The ratio of Tl:Sb on one site is 1:3, and on the other two it is 3:1. This mixed occupancy balances the formal charges. Mixed occupancy of Tl and Sb is also seen in TlSbSe_2 , which has one site occupied by equally by Tl and Sb [39],

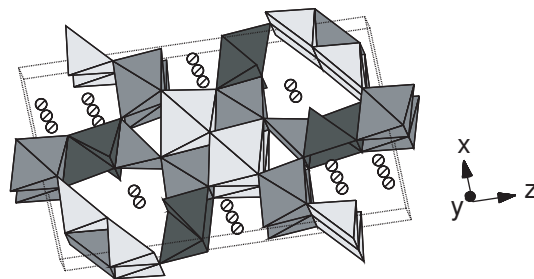


Figure 3.25: The crystal structure of $\text{Tl}_{11.5}\text{Sb}_{11.5}\text{Cu}_8\text{Se}_{27}$ showing Cu centered tetrahedra (dark), Sb centered polyhedra (medium), mixed Tl/Sb centered polyhedra (light) and Tl atoms (striped).

and Tl_9SbSe_6 , which has one site with 80% Tl and 20% Sb and another with 20% Tl and 80% Sb [40].

This compound was prepared as a single phase bulk sample in the form of a silver-colored ingot by heating the elements at 800°C for two days, and then slow cooling to 400°C over four days.

Pieces broken away from a single phase ingot of this material were used for thermopower and resistivity measurements. The results of these measurements are shown in Figure 3.26, and indicate that $\text{Tl}_{11.5}\text{Sb}_{11.5}\text{Cu}_8\text{Se}_{27}$ is a p-type semiconductor.

3.4 Measured band gaps and comparisons between Tl and AM analogs

As pointed out in the introduction, we expect the higher electronegativity of Tl to lead to lower band gaps and higher mobilities than found in isostructural AM compounds. Measured band gaps for eight of the compounds presented here are shown in Table 3.12, along with comparisons between Tl and AM analogues. Four of the AM materials for which we discovered Tl analogs have band gaps reported in the literature. In each case we found the Tl compound to have

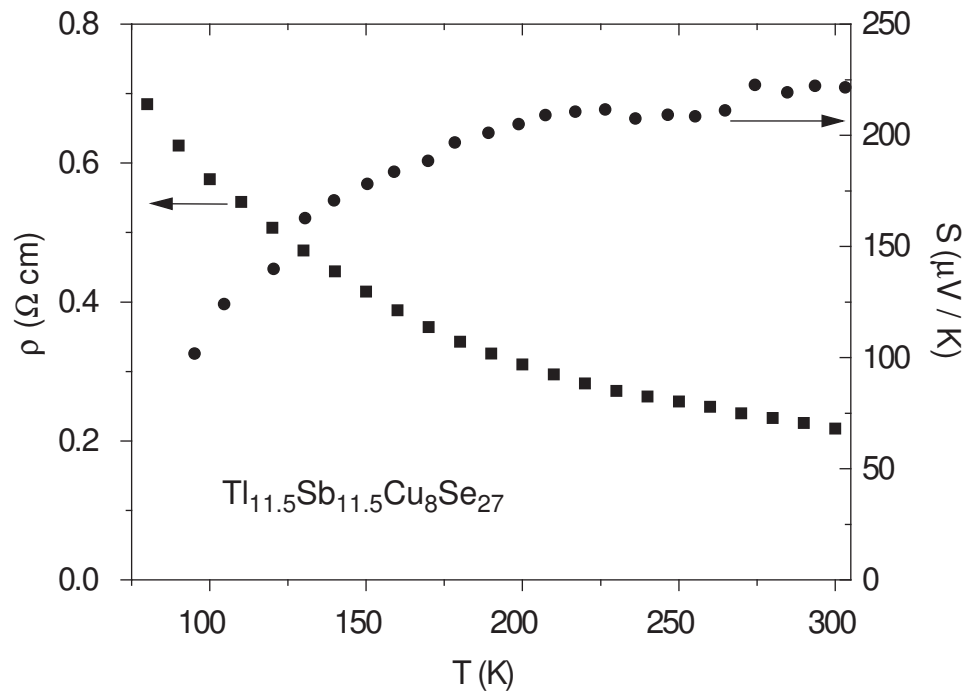


Figure 3.26: The measured resistivity (squares) and thermopower (circles) of $\text{Tl}_{11.5}\text{Sb}_{11.5}\text{Cu}_8\text{Se}_{27}$. Based on measurements of reference materials and on estimated errors in geometrical measurements, the uncertainty of the ρ and S measurements is estimated to be about 5%.

a smaller band gap than the AM compound. In the only case in which resistivity data is available for the AM compound, the Tl analog was found to have a lower resistivity. These results are consistent with the expectation that the lower electronegativity of Tl should lead to improved electrical properties.

3.5 Tl coordination environments and lone pair activity

The coordination environments of the Tl atoms in all of the structures presented above are shown in Figure 3.27. For those compounds with several crystallographically distinct Tl sites, the coordination around each site is shown and labeled. If different sites have very similar environments, only one is shown. Brief descriptions of the environments are given in the discussions of individual compounds above. Table 3.13 lists the range of distances between Tl and S, Se or Te that we consider to be a bond in each compound. It is important to note that often there is no obvious large gap in the Tl-chalcogen interatomic distance histogram to be used in defining the cut-off between those contacts considered to be bonds and those not considered to be bonds.

In Figure 3.27, Tl is seen to adopt a wide variety of coordination environments, from almost cubic to very irregular, with coordination numbers from five to ten. There are many instances in which the coordination is obviously one-sided. This suggests that the lone pair on Tl in these situations is stereoactive, and is protruding into the vacant part of the coordination environment. The compounds are loosely arranged from top to bottom based on the asymmetry of the arrangement of chalcogens around the Tl atom. Thus the environments near the bottom of the figure are more likely to have active lone pairs than those at near top. We note that the most asymmetric environments tend to occur in the lower symmetry space groups.

Table 3.12: Measured band gaps of Tl compounds, and comparisons between Tl and AM analogs.

Compound	Color	E_{Gap} (eV)	
$Tl_2Cu_2SnS_4^a$	black	1.4	
$Rb_2Cu_2SnS_4$ [17]	orange	2.08	
$Tl_3Ti_2P_5S_{18}$	black-gold	1.3	
$K_3Ti_2P_5S_{18}$ [15]	red-brown	1.61	
$Tl_2CeP_2S_7^{a,b}$	yellow	2.4	
$K_2LaP_2S_7$ [41]	colorless	> 3.5	
$Tl_2Au_2Sn_2Se_6$	black	1.2	
$K_2Au_2Sn_2Se_6$ [28]	red	2.28	
$Tl_2TiCu_2S_4$	dark red	1.4	
$Rb_2TiCu_2S_4$ [29]	orange	2.2	
$Tl_2TiCu_2Se_4$	black	1.1	
$Cs_2TiCu_2Se_4$ [29]	orange-red	~ 2	
$Tl_5AgTi_6Se_{27}^c$	black	0.8	($1.2 \times 10^4 \Omega \text{ cm}$)
$Cs_5AgTi_6Se_{27}$ [19]	black		($2.5 \times 10^5 \Omega \text{ cm}$)
$Tl_3CuNb_2Se_{12}^d$	black	0.8	
$TlTiPS_5^{a,e}$	black	1.3	
$Tl_2BiP_2S_7^{a,e}$	red	1.8	

^a Measured diffuse reflectance spectra are presented in Ref. [1].

^b We expect the Ce f electron to be localized and have little effect on the band gap.

^c No band gap data available for AM analogue, room temperature resistivities are compared in parentheses.

^d No data available for AM analogue.

^e No isostructural AM analogue known.

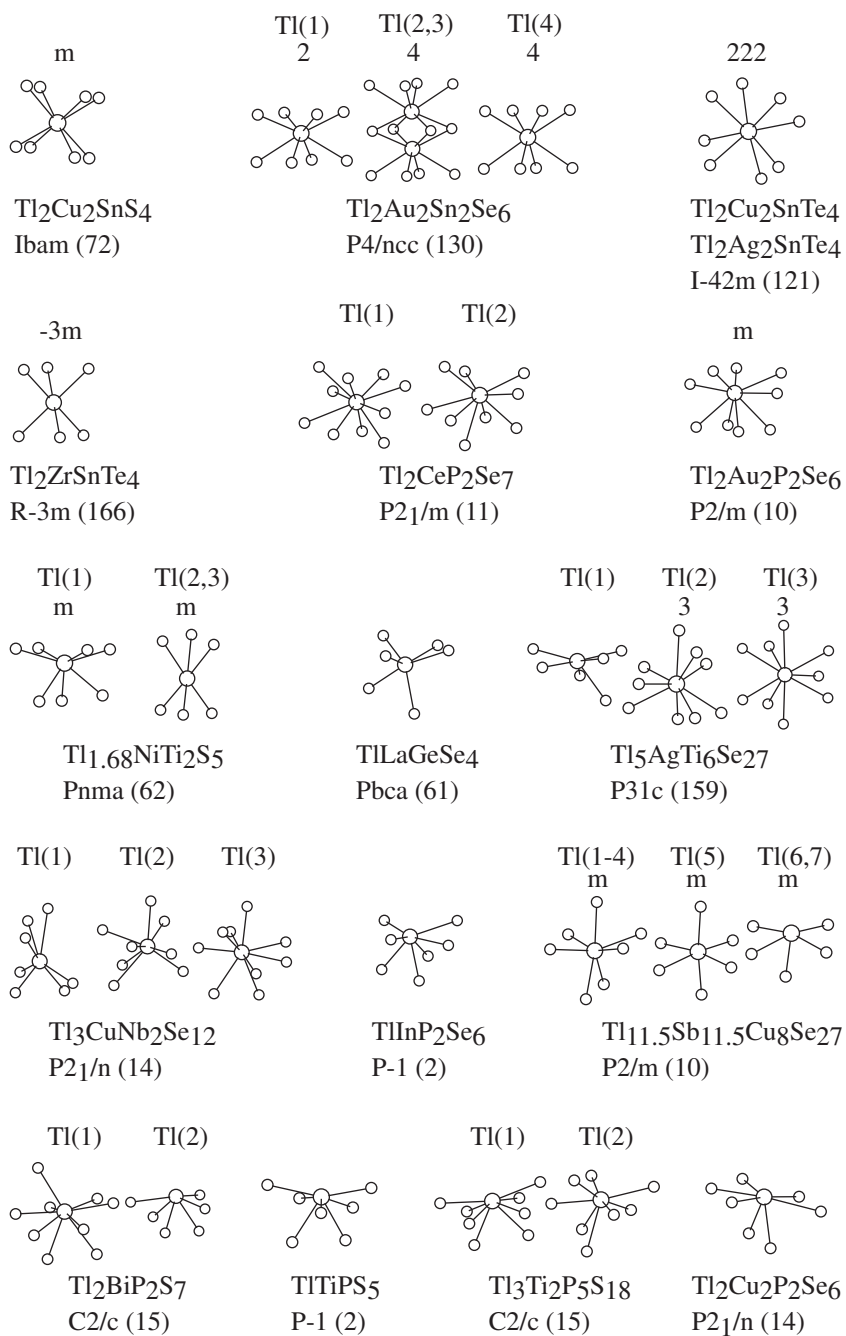


Figure 3.27: The coordination environments of Tl atoms in the compounds presented here. Each unit is labeled by the compound name and space group, and the site symmetry (if any) of the Tl site.

Table 3.13: Distances between Tl and coordinating chalcogens for all 17 structures. The column "Bond distances" correspond to the bonds shown in Figure 3.27. The next closest chalcogen distances are also listed.

Compound	Bond distances	Shorted non-bond dist.
$\text{Tl}_2\text{CeP}_2\text{S}_7$	3.232-3.758	4.416
$\text{Tl}_3\text{Ti}_2\text{P}_5\text{S}_{18}$	3.160-3.600	3.847
$\text{Tl}_2\text{Cu}_2\text{SnS}_4$	3.277-3.402	4.813
$\text{Tl}_5\text{AgTi}_6\text{Se}_{27}$	3.221-3.707	3.851
$\text{Tl}_3\text{CuNb}_2\text{Se}_{12}$	3.034-3.709	3.762
$\text{Tl}_2\text{Cu}_2\text{SnTe}_4$	3.550-3.570	> 5
$\text{Tl}_2\text{Ag}_2\text{SnTe}_4$	3.571-3.711	> 5
$\text{Tl}_3\text{Zr}_{1.4}\text{Sn}_{1.6}\text{Te}_6$	3.368	> 5
TlTiPS_5	3.168-3.527	3.682
$\text{Tl}_2\text{Au}_2\text{Sn}_2\text{Se}_6$	3.250-3.586	> 5
TlLaGeSe_4	3.242-3.516	3.899
$\text{Tl}_2\text{BiP}_2\text{S}_7$	3.137-3.598	3.681
$\text{Tl}_{1.68}\text{NiTi}_2\text{S}_5$	2.997-3.545	3.911
$\text{Tl}_2\text{Cu}_2\text{P}_2\text{Se}_6$	3.321-3.766	3.919
$\text{Tl}_2\text{Au}_2\text{P}_2\text{Se}_6$	3.208-3.650	4.799
$\text{TlInP}_2\text{Se}_6$	3.205-3.815	4.003
$\text{Tl}_{11.5}\text{Sb}_{11.5}\text{Cu}_8\text{Se}_{27}$	2.734-3.673	4.505

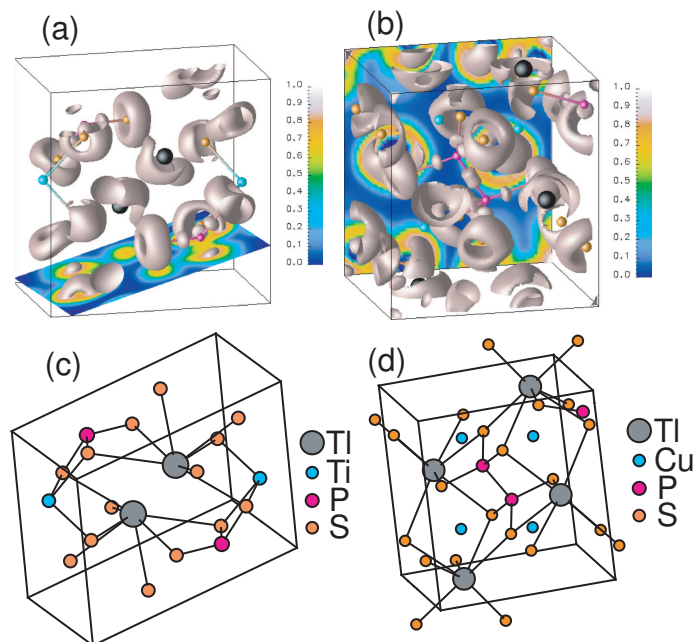


Figure 3.28: The results of ELF calculations for TlTiPS_5 (a) and $\text{Tl}_2\text{Cu}_2\text{P}_2\text{Se}_6$ (b). Ball and stick models oriented the same as the ELF figures are shown in (c) for TlTiPS_5 and (d) for $\text{Tl}_2\text{Cu}_2\text{P}_2\text{Se}_6$.

Density functional calculations of the electronic structure were performed for two of these compounds, TlTiPS_5 and $\text{Tl}_2\text{Cu}_2\text{P}_2\text{Se}_6$, using the LMTO method as implemented in the Stuttgart TB LMTO ASA program. The lone pairs were visualized using the Electron Localization Function [42]. The results are shown in Figure 3.28. Also shown in Figure 3.28 are a ball and stick model of the structure oriented in the same way as in the ELF calculation. The ball and stick figure shows the coordination environment on the Tl atoms, and it is expected that the lone pair should point away from the coordinating chalcogens and into the empty part of the Tl coordination spheres. The figure shows electron density distributed around the chalcogen atoms, and also one sided lobes of electron density on each Tl atom. These lobes correspond to the lone pairs. Comparison the ELF plots and the ball and stick models shows that the lone pairs indeed point into the gaps in the Tl coordination environments. These results show that the lone pair of

electron on Tl in chalcogenide compounds can be stereoactive. This is in contrast to AM's and may be partly responsible for the structural differences between Tl and AM compounds. In particular, TlTiPS₅ is similar but not isostructural to KTiPS₅ (*vide supra*). The coordination of Tl in TlTiPS₅ is more asymmetric than that of K in KTiPS₅. This is due to a slight staggering of the [TiPS₅]¹⁻ chains which opens a gap in the Tl coordination sphere. The ELF calculations (Figure 3.28) show that the lone pairs indeed reside in this gap.

3.6 Conclusions

We draw several conclusions from our investigation of quaternary thallium chalcogenide systems. First, it is clear that these are fertile grounds for new materials. This work has produced many new compounds (close to 30) with a wide variety of structural features and networks, from one- to three-dimensional. The chemistry of Tl chalcogenides may be as rich as that of AM chalcogenides. Some of the compounds we have discovered are isostructural to known AM compounds, but some are not. Perhaps the AM analogs of some of these new Tl compounds exist. We have shown evidence that the lone pair on Tl may influence the adopted crystal structure, and may be responsible for some of the differences between Tl and AM compounds.

We have also seen evidence for some potential advantages of Tl chalcogenides over AM chalcogenides as TE materials. We have seen little evidence for sensitivity to air or moisture in these compounds (a few pellets visibly tarnished in air after a few weeks). In every case in which a comparison can be made, the Tl compound was found to have a significantly smaller band gap or lower resistivity than the isostructural AM analog. Some of the compounds were also shown to have extremely low thermal conductivity. There are no thermal con-

ductivity data for isostructural alkali metal compounds with which to compare. However, it is very likely that the thermal conductivity of the Tl compounds will be lower than that of the AM compounds simply due to the larger mass of Tl. We have shown several examples of thermal conductivity less than half that of optimized Bi_2Te_3 alloys. These alloys typically have a thermal conductivity of 15 mW/cmK at room temperature, with a lattice contribution of approximately 10 mW/cmK [18]. It is possible that the low thermal conductivities seen for these Tl compounds can be further decreased through alloying between suitable compounds.

Despite these advantages, we have not yet found a material with promising TE properties. Most of the compounds do show semiconducting behavior with low thermal conductivities, but the electrical resistivities are too large. It is possible that these materials can be doped to carrier concentrations that would improve their TE performance. We have made no attempt yet to study the doping behavior of these compounds. One challenge associated with complex, multinary compounds is doping without the formation of compensating defects. Our samples were not prepared with the ultra-high purity starting materials and extreme care required to synthesize truly intrinsic samples, and yet the measured resistivities are high. This suggests that any unintentional doping is, in fact, being compensated. As prepared, none of the Tl compounds that we have investigated to date can compete with the thermoelectric properties of Bi_2Te_3 alloys, or the AM compound CsBi_4Te_6 [3]. However, the number and diversity of potential new compounds seems large, and several ternary Tl compounds have shown promise. This gives us hope that an advanced thermoelectric material will be found among Tl chalcogenides.

REFERENCES

- [1] T. K. Reynolds, *Design, Synthesis, and Characterization of New Materials for Thermoelectric Applications*, PhD thesis, Cornell University, 2003.
- [2] A. Gutzmann, C. Naether, and W. Bensch, *Acta Crystallogr.* **C60**, i11 (2004).
- [3] D.-Y. Chung et al., *Science* **287**, 1024 (2000).
- [4] N. Greenwood and A. Earnshaw, *Chemistry of the Elements*, Pergamon Press, 1984.
- [5] S. Galván-Arzate and A. Santamaría, *Toxicol. Lett.* **99**, 1 (1998).
- [6] J. Sharp, B. Sales, D. Mandrus, and B. Chakoumakos, *Appl. Phys. Lett.* **74**, 3794 (1999).
- [7] B. Woelfing, C. Kloc, J. Teubner, and E. Bucher, *Phys. Rev. Lett.* **86**, 4350 (2001).
- [8] K. Kurosaki, H. Uneda, H. Muta, and S. Yamanaka, *J. Alloys Compd.* **376**, 43 (2004).
- [9] SMART and SAINT: Data collection and processing software for the SMART system, Bruker Analytical X-ray Instruments, Inc., Madison, WI, 1995.
- [10] SADABS program for absorption correction, G.M. Sheldrick for Bruker Analytical X-ray Instruments, Inc., Madison, WI, 2000.
- [11] XPREP program for determination of space groups, Bruker Analytical X-ray Instruments, Inc., Madison, WI, 2000.
- [12] L. Farrugia, *J. Appl. Cryst.* **32**, 837 (1999).
- [13] M. Kanatzidis and A. Sutorik, *Prog. Inorg. Chem.* **43**, 151 (1995).
- [14] T. K. Reynolds, M. A. McGuire, and F. J. DiSalvo, *J. Solid State Chem.* **177**, 3038 (2004).
- [15] V. Derstroff, W. Tremel, G. Regelsky, J. Schmedt auf der Günne, and H. Eckert, *Solid State Sciences* **4**, 731 (2002).
- [16] X. Cieren et al., *J. Solid State Chem.* **121**, 230 (1996).
- [17] J.-H. Liao and M. Kanatzidis, *Chem. Mater.* **5**, 1561 (1993).
- [18] W. Yim and F. D. Rosi, *Solid-State Electron.* **15**, 1121 (1972).
- [19] F. Huang and J. Ibers, *Inorg. Chem.* **40**, 865 (2001).

- [20] P. Cherin and P. Unger, *Inorg. Chem.* **6**, 1589 (1967).
- [21] Y.-J. Lu and J. Ibers, *Inorg. Chem.* **30**, 3317 (1990).
- [22] A. A. Bondi, *J. Phys. Chem.* **68**, 441 (1964).
- [23] J. Li, H.-Y. Guo, D. Proserpio, and A. Sironi, *J. Solid State Chem.* **117**, 247 (1995).
- [24] R. Hoppe, W. Lidecke, and F. C. Frorath, *Z. Anorg. Allg. Chem.* **309**, 49 (1961).
- [25] R. Seshadri et al., *J. Mater. Chem.* **8**, 2869 (1998).
- [26] E. I. Rogacheva, G. V. Gorne, S. A. Laptev, A. V. Arinkin, and T. B. Vesiene, *J. Solid State Chem.* **43**, 364 (1982).
- [27] J. Do, K. Lee, and H. Yun, *J. Solid State Chemistry* **125**, 30 (1996).
- [28] S. Loeken and W. Tremel, *Z. Anorg. Allg. Chem.* **624**, 1588 (1998).
- [29] F. Huang and J. Ibers, *Inorg. Chem.* **40**, 2602 (2001).
- [30] A. Mrotzek, D.-Y. Chung, N. Ghelani, T. Hogan, and M. Kanatzidis, *Chem. Eur. J.* **7**, 1915 (2001).
- [31] K.-S. Choi et al., *Chem. Mater.* **13**, 756 (2001).
- [32] S. Nakajima, *J. Phys. Chem. Solids* **24**, 479 (1963).
- [33] T. Cattopadhyay, J. Pannetier, and H. von Schnering, *J. Phys. Chem. Solids* **47**, 879 (1986).
- [34] D. Mueller, G. Eulenberger, and H. Hahn, *Z. Anorg. Alg. Chem.* **398**, 207 (1973).
- [35] A. Mrotzek, L. Iordanidis, and M. Kanatzidis, *Chem. Commun.* **40**, 1648 (2001).
- [36] A. Mrotzek and M. Kanatzidis, *Acc. Chem. Res.* **36**, 111 (2003).
- [37] K.-F. Hsu, S. Lal, T. Hogan, and M. Kanatzidis, *Chem. Commun.* **13**, 1380 (2002).
- [38] A. Mrotzek, L. Iordanidis, and M. Kanatzidis, *Inorg. Chem* **40**, 6204 (2001).
- [39] K. Wacker and P. Buck, *Mater. Res. Bull.* **15**, 1105 (1980).
- [40] A. Gaeumann and P. Bohac, *J. Less-Common Met.* **31**, 314 (1973).
- [41] C. Evenson, IV and P. Dorhout, *Inorg. Chem.* **40**, 2884 (2001).
- [42] R. Seshadri, *Proc. Indian Acad. Sci.* **113**, 487 (2001).

Chapter 4

Tl_2AXTe_4 (A = Cd, Hg, Mn; X = Ge, Sn):

Crystal Structure, Electronic Structure, and Thermoelectric Properties

In this Chapter, six new thallium chalcogenides are reported, and their crystal structure, electronic structure, and thermoelectric properties are discussed. The electronic structure calculations were performed by Dr. Thomas J. Scheidemantel at the Pennsylvania State University. This Chapter is adapted from a paper published in *Chemistry of Materials*.*

4.1 Introduction

In the previous Chapter we showed experimentally that Tl containing materials have measured band gaps consistently smaller than their isostructural alkali metal analogues [1]. Many of the Tl compounds also had very low thermal conductivities. These results led us to further explore Tl compounds. Our continued investigation into Tl chalcogenides led to the discovery of the six isostructural compounds Tl_2AXTe_4 (A=Cd, Hg, Mn, X=Ge, Sn). These compounds are the first examples of a new structure type, which can be viewed as an ordered superstructure of the known compound TlInTe_2 , which in turn is a superstructure of the TlSe structure type. In what follows, we present the syntheses, crystal structure, calculated electronic structures, and measured TE properties of these new compounds. We also compare the calculated electronic structure of the par-

*Reproduced in part from M. A. McGuire, T. J. Scheidemantel, J. V. Badding, and F. J. DiSalvo, *Chem. Mater.* **17**, 6186 (2005). Copyright 2005 American Chemical Society.

ent structure TlInTe_2 with that of its isostructural alkali metal analogue KInTe_2 . The calculations show the influence that Tl has near the Fermi level, which was mentioned in the previous Chapter. They also demonstrate the decrease in the band gap which was shown experimentally to accompany the substitution of Tl for an alkali metal.

4.2 Experimental Details

In these syntheses, Tl metal was weighed in an Ar filled glove box and placed into capped vials. The other reactants were weighed in air and loaded into silica tubes which had been coated with carbon to prevent reaction between the silica and the samples. The Tl was then added to the tube, and the tube was quickly attached to a vacuum line for sealing. The evacuated, sealed silica tubes were heated in electric furnaces. $\text{Tl}_2\text{CdGeTe}_4$, $\text{Tl}_2\text{CdSnTe}_4$, $\text{Tl}_2\text{MnGeTe}_4$, and $\text{Tl}_2\text{MnSnTe}_4$ were synthesized by reaction of the elements in 2:1:1:4 molar ratios. For $\text{Tl}_2\text{HgGeTe}_4$, and $\text{Tl}_2\text{HgSnTe}_4$ containing compounds, Tl, HgTe, Ge or Sn, and Te were reacted in a 2:1:1:3 molar ratio.*

Reaction temperature profiles which produced the single crystals used for structure determinations were as follows: $\text{Tl}_2\text{CdGeTe}_4$: 12 h to 500°C, 24 h at 500°C, 100 h to 30°C; $\text{Tl}_2\text{CdSnTe}_4$: 24 h to 800°C, 100 h at 800°C, 300 h to 200°C; $\text{Tl}_2\text{HgGeTe}_4$: 24 h to 800°C, 48 h at 800°C, 200 h to 300°C; $\text{Tl}_2\text{HgSnTe}_4$: 24 h to 500°C, 100 h at 500°C, 100 h to 100°C; $\text{Tl}_2\text{MnGeTe}_4$: 12 h to 500°C, 24 h at 500°C, 100 h to 30°C; $\text{Tl}_2\text{MnSnTe}_4$: 24 h to 900°C, 100 h at 900°C, 200 h to 400°C. At the

*Starting materials: Tl rod, 99.9%, Alfa Aesar; Cd shot 99.999% United Mineral and Chemical Corp.; Hg 99.999% Alfa Aesar; Mn powder 99.95% Gallard Schlesinger; Ge pieces 99.9999% Gallard Schlesinger; Sn mossy 99.9% Allied Chemical; Te ingot 99.999% Research Organinc/Inorganic Chemical Corporation. HgTe was made by heating the elements in an evacuated sealed silica tube at 500°C for two days.

end of each profile the furnace was turned off and allowed to cool naturally to room temperature.

Single crystals extracted from the reaction products were analyzed using energy dispersive x-ray spectroscopy on a JEOL 8900R electron microprobe. The measurements confirmed the presence of all four elements in approximately 2:1:1:4 ratios for many of the crystals which were analyzed. Some crystals of known binary and ternary tellurides (CdTe, SnTe, HgTe, TlTe, Tl_2GeTe_5 , Tl_2SnTe_5) were also found in the reaction products. However, the target compounds were the majority phase in each case. Based on the microprobe results and powder X-ray diffraction patterns, we estimate the yields of these reactions to be 50-70%, with the exception of $\text{Tl}_2\text{HgGeTe}_4$ which gave a nearly single phase product (yield of $\sim 90\%$).

Crystals from these reactions which looked similar to those determined by microprobe measurements to have the target composition were then selected for single crystal structure determinations. The crystals were mounted in poly(butenes) oil and bathed in a cold nitrogen stream (175 ± 5 K) for single crystal x-ray diffraction on a Bruker SMART CCD diffractometer. The program SMART was used to collect the data, and the program SAINT was used to integrate the data and refine the unit cells based on all strong reflections.[2] Absorption corrections were made with SADABS [3], and space groups were determined with the program XPREP [4]. Crystal structure solutions and refinements were carried out using SHELXS-97 and SHELXL-97 within the WingX program suite [5].

Attempts to make the Mn compounds as single-phase materials failed. However, polycrystalline, single-phase samples of $\text{Tl}_2\text{CdGeTe}_4$, $\text{Tl}_2\text{CdSnTe}_4$, $\text{Tl}_2\text{HgGeTe}_4$, and $\text{Tl}_2\text{HgSnTe}_4$ were successfully synthesized. The room temperature powder X-ray diffraction (PXRD) results are shown in Figure 9.7. These diffraction patterns were indexed using the program TREOR [6] (excluding the

impurity peaks in the Mn containing compounds). The tick marks in Figure 9.7 locate the predicted peak positions for each compound, based on the indexed cells from PXRD and the space group $I\bar{4}2m$ determined from the single crystal diffraction results. The single phase samples described above were prepared in the following ways. For the Hg compounds, stoichiometric amounts of Tl, HgTe, Ge or Sn, and Te were heated to 500°C over 36 hours, then held at this temperature for five days, at which point the furnace was turned off and allowed to cool naturally to room temperature. The products were then ground and pressed into cylindrical pellets (5/16 in. diameter) and annealed for seven days at 300°C. The resulting materials were single phase as determined by PXRD. Doped samples of the Hg compounds were made in the same way, only with Pb, HgI₂, Ga₂Te₃, or As₂Te₃ added to the starting mixture.[†] The level of doping was chosen to provide about 10¹⁹ charge carriers per cubic centimeter. Bulk samples of the Cd compounds were made by reacting the elements at 500°C for four days, then cooling to room temperature over four days. Several subsequent anneals for 4-7 days each at 250-300°C were required to obtain single phase samples.

These single phase powders were cold pressed in a 3/8 in. x 3/16 in. rectangular, hardened steel pellet press, and then sintered at 300°C for two weeks. The thickness of the pellets ranged from 0.32-0.36 cm. The measured densities of the polycrystalline pellets after sintering were 80-90% of the single crystal densities.

Thermoelectric properties (electrical resistivity, thermal conductivity, and thermopower) of the Cd and Hg compounds were measured in a home built

[†]Pb granular 99.99% Fisher Scientific Co.; Ga unspecified company, unknown purity; As pieces 99.99% Alfa Aesar; HgI₂ powder 99% Mallinckrodt; As₂Te₃ was made by heating the elements to 500°C for one day, then grinding and heating at 400°C for four hours and then 350°C for several days; Ga₂Te₃ was made by heating the elements to 650°C for one day and then at 825°C for six hours.

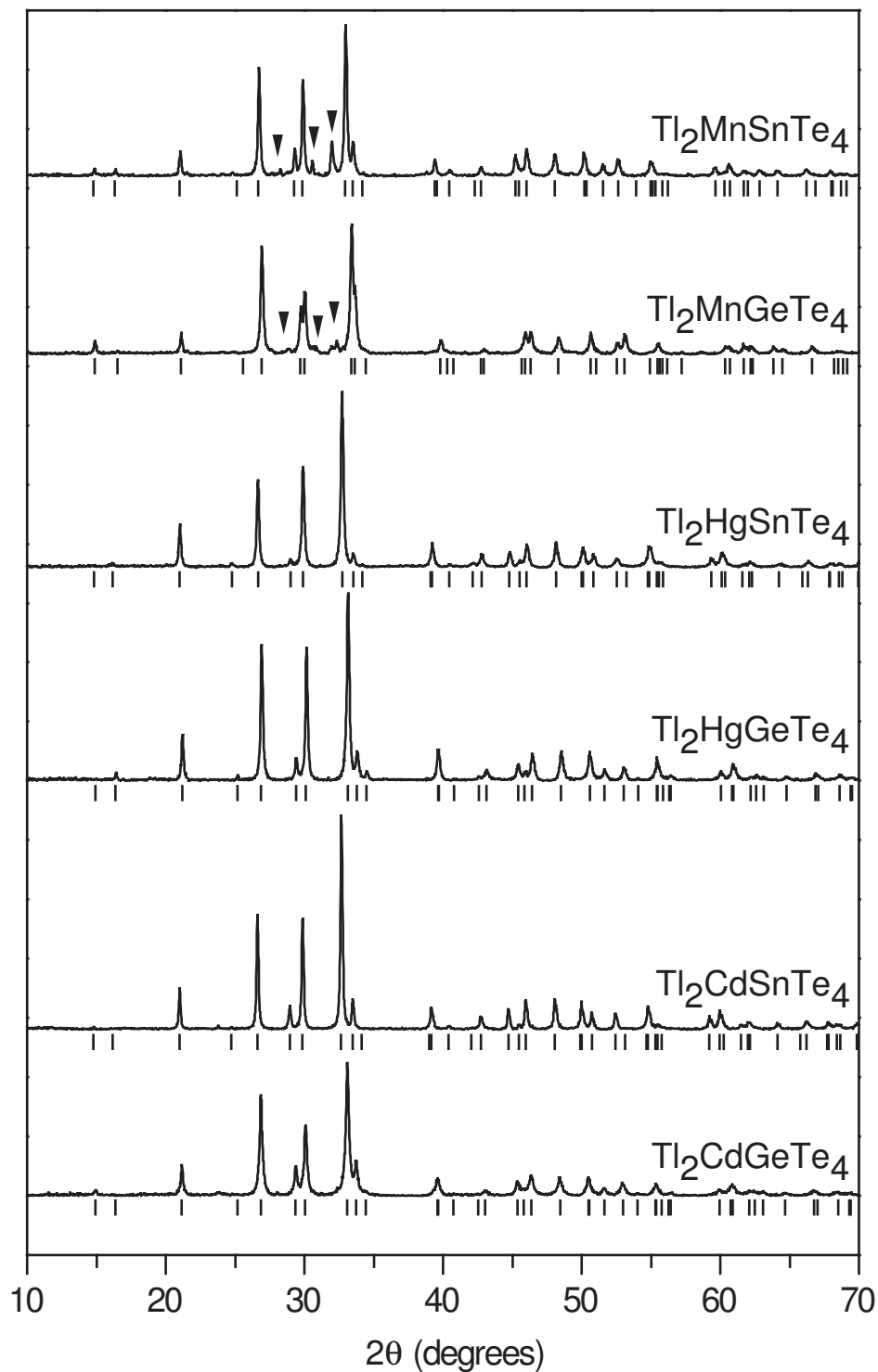


Figure 4.1: The measured powder X-ray diffraction patterns for the six compounds reported here. The ticks mark the predicted peak positions for each compound. The arrows indicate impurity peaks in the Mn compounds.

apparatus which has been described elsewhere [7]. For the current investigations liquid nitrogen was used as the cryogen and data are reported between about 80 K and 300 K. In some cases large values of the total resistance (sample plus contacts) became too large for our instrumentation. In these instances, the data only extends down to the lowest temperature at which the measurements could be made. Thermal conductivity measurements were performed using the four-point steady state technique. The samples were contacted with silver epoxy (Epotek H20E). The measured data were corrected for the heat loss through thermocouples and heater leads which was measured in a separate experiment. At the same time, thermopower was measured using the chromel legs of the thermocouples and was corrected for the chromel contribution. An AC resistance bridge (Linear Research Inc. LR-700) was used for the four-point resistivity measurements. These measurements were carried out on the same pellets used for the thermal conductivity and thermopower measurements. Copper foil was used for the current leads, and 40 AWG copper wires were used for the voltage leads. Electrical contacts were made using a silver paste (Dupont, Conductor Composition 4922N). TlGaTe_2 and TlInTe_2 have been shown to exhibit non-linear I-V behavior [8, 9]. Tests at room temperature on the Tl_2AXTe_4 samples used in the current study showed that these materials were Ohmic over the range of current densities used in the investigation. Measurements of standards and reference materials using our apparatus and techniques suggests that the maximum absolute uncertainties in the values of the measured properties are about 15% for thermal conductivity and about 5% for thermopower and electrical resistivity.

The room temperature resistivity measurements on the Mn compounds were performed on small ($\sim 400 \mu\text{m}$) crystals extracted from the reaction products and contacted with gold wires ($d=0.002 \text{ in.}$) and silver paste (Dupont, Con-

ductor Composition 4922N). After the measurements, microprobe analysis of the crystals confirmed their compositions to be $\text{Tl}_2\text{MnGeTe}_4$ and $\text{Tl}_2\text{MnSnTe}_4$.

Approximately ten milligrams of crystals of $\text{Tl}_2\text{MnGeTe}_4$ were collected, and ground into powder for magnetic susceptibility measurements. Powder X-ray diffraction showed the powder to be single phase. The magnetic susceptibility measurements were performed using a Quantum Design Magnetic Properties Measurement System. The sample (7.3 mg) was loaded into a gel cap and then mounted in a plastic drinking straw which was attached to the measurement apparatus. DC magnetization measurements were performed in a field of 5 T from 5K to 400K. The diamagnetic moment of an empty gel cap was measured and subtracted from the raw data to give the moment of the sample.

Electronic structures of the six compounds were calculated using density functional theory. The full potential linearized augmented plane wave method was used to solve the Kohn-Sham equations self consistently with the exchange-correlation interaction included according to the generalized gradient approximation of Perdew, Burke, and Ernzerhof [10, 11]. To this end, the calculations were conducted using the WIEN2k code. For convergence, 1000 k-points in the entire Brillouin zone, corresponding to 99 k-points in the irreducible wedge, were used. The R-kmax parameter was set to 10 resulting in approximately 10,000 stars in the interstitial region for each compound. Spherical harmonics up to $L = 6$ were included in the ion core, resulting in 900 basis function in the expansion. The muffin tin radii used were 2.6 for Tl, 2.5 for Te, 2.6 for Hg, 2.4 for Ge, 2.5 for Sn, 2.5 for Cd and 2.3 for Mn, with all radii listed as multiples of the bohr radius. States within the energy window from -7.0 Ry up to 3.5 Ry were included in calculating the spin orbit interaction. This energy range is larger than the default to allow a more accurate spin orbit correction. Spin-polarized calculations were performed on $\text{Tl}_2\text{MnGeTe}_4$ and $\text{Tl}_2\text{MnSnTe}_4$.

4.3 Crystal Structure

Results from the single crystal structure refinements for all six compounds are presented in Tables 4.1 and 4.2. Several significant residual peaks were found in the Fourier difference map for $\text{Tl}_2\text{HgGeTe}_4$. All but two of the twenty highest peaks ($2.1\text{--}4.9 \text{ e}\text{\AA}^{-3}$) are all located within 1.5 \AA of heavy atoms (Tl, Hg, Te) and therefore attributed to truncation of the high angle X-ray data. The remaining two peaks are 1.35 \AA and 0.92 \AA from Ge, and may indicate a small amount of Ge positional disorder. However, their distances to Te (2.4 and 2.2 \AA) are shorter than typical Ge-Te bonds (*vide infra*). Atomic positions, displacement parameters, and interatomic distances are given in Tables 4.3 and 4.4. The crystal structure is shown in Figure 7.2. All compounds are isostructural and crystallize in the non-centrosymmetric, tetragonal space group $I\bar{4}2m$. The structure is an ordered superstructure of the TlSe structure type.[12] TlSe (space group $I4/mcm$) consists of 1-d chains of edge sharing Tl^{3+} centered tetrahedra, with Se at the vertices, separated by Tl^{1+} ions. The tetrahedrally coordinated Tl^{3+} can be replaced with other trivalent atoms, as in TlMSe_2 $M=\text{Al, Ga, In}$, and TlMTe_2 $M=\text{Ga, In}$. In Tl_2AXTe_4 , this tetrahedral site is occupied by divalent and tetravalent atoms in alternation along the chains (Figure 7.2), and the formal charges can be assigned as $[\text{Tl}^{1+}]_2[\text{A}^{2+}][\text{X}^{4+}][\text{Te}^{2-}]_4$.

If the A and X atoms shared the tetrahedral sites instead of being ordered along the chains, this would result in a centrosymmetric structure, isostructural to TlInTe_2 , with space group $I4/mcm$. Inspection of the systematic absence conditions showed no evidence for a c-glide along the a direction, and no evidence of site mixing was seen during the structure refinements. This ensures that the A and X cations are ordered along the chains. The non-zero Flack absolute structure parameters seen for several of these compounds (Tables 4.1 and 4.2) are then

Table 4.1: Crystallographic information for the Ge containing compounds reported here.

	$\text{Tl}_2\text{CdGeTe}_4$	$\text{Tl}_2\text{HgGeTe}_4$	$\text{Tl}_2\text{MnGeTe}_4$
a (Å)	8.3825(19)	8.3571(11)	8.399(3)
c (Å)	7.0775(18)	7.0684(14)	6.963(3)
V (Å ³)	497.3(2)	493.67(13)	491.2(3)
size (μm ³)	100x50x30	100x100x40	150x30x30
θ range (°)	3.44 to 30.41	3.45 to 28.56	3.43 to 30.41
Reflections coll. / unique	2921 / 404	2372 / 345	3478 / 405
R_{int}	0.0442	0.0894	0.054
completeness to θ max (%)	100	98.6	100
Data/parameters	404 / 14	345 / 15	405 / 14
GOF on F ²	1.217	1.166	1.127
R_1 I>2σ(I)	0.0234	0.0488	0.0255
wR ₂ I>2σ(I)	0.0505	0.1166	0.0508
R_1 all data	0.0253	0.0502	0.0302
wR ₂ all data	0.0509	0.1172	0.0524
Flack param.	0.019(15)	0.27(3)	0.064(19)
Largest diff. peak/hole (eÅ ⁻³)	1.311/-2.176	4.893/-3.118	1.640/-3.056

$$R_1 = \frac{\sum ||F_o| - |F_c||}{\sum |F_o|} \quad wR_2 = \left[\frac{\sum w(F_o^2 - F_c^2)^2}{\sum w(F_o^2)^2} \right]^{\frac{1}{2}}$$

$$w^{-1} = [\sigma(F_o^2) + (aP)^2 + bP] \quad \text{where } P = [\max(F_o^2, 0) + 2F_c^2] / 3$$

Table 4.2: Crystallographic information for the Sn containing compounds reported here.

	Tl ₂ CdSnTe ₄	Tl ₂ HgSnTe ₄	Tl ₂ MnSnTe ₄
a (Å)	8.4250(4)	8.397(4)	8.4503(13)
c (Å)	7.2171(5)	7.157(6)	7.1078(15)
V (Å ³)	512.27(5)	504.6(6)	507.55(15)
size (μm ³)	200x70x10	100x70x40	50x30x20
θ range (°)	3.42 to 30.44	3.43 to 30.45	3.41 to 30.46
Reflections coll. / unique	5638 / 424	2845 / 418	3939 / 422
R _{int}	0.0531	0.0409	0.0603
completeness to θ max (%)	100	100	100
Data/parameters	424 / 15	418 / 15	422 / 15
GOF on F ²	1.133	1.164	1.135
R ₁ I>2σ(I)	0.0221	0.0264	0.0286
wR ₂ I>2σ(I)	0.0480	0.0544	0.0580
R ₁ all data	0.0224	0.0277	0.0368
wR ₂ all data	0.0481	0.0548	0.0599
Flack param.	0.442(18)	0.317(13)	0.56(7)
Largest diff. peak/hole (eÅ ⁻³)	1.627/-2.083	1.181/-3.736	0.989/-2.786

$$R_1 = \frac{\sum ||F_o| - |F_c||}{\sum |F_o|} \quad wR_2 = \left[\frac{\sum w(F_o^2 - F_c^2)^2}{\sum w(F_o^2)^2} \right]^{\frac{1}{2}}$$

$$w^{-1} = [\sigma(F_o^2) + (aP)^2 + bP] \quad \text{where } P = [\max(F_o^2, 0) + 2F_c^2] / 3$$

Table 4.3: Atomic coordinates, displacement parameters, and interatomic distances for the Ge containing compounds reported here.

	Tl₂CdGeTe₄	Tl₂HgGeTe₄	Tl₂MnGeTe₄
Atomic coordinates			
x Te	0.1749(1)	0.1757(1)	0.1729(1)
z Te	-0.2252(1)	0.2254(2)	0.2316(1)
Isotropic displacement parameters (Å ²)			
Tl	0.019(1)	0.017(1)	0.019(1)
A	0.014(1)	0.015(1)	0.015(1)
X	0.009(1)	0.008(1)	0.008(1)
Te	0.010(1)	0.007(1)	0.009(1)
Interatomic distances (Å)			
Tl-Te	3.4808(7)	3.4697(8)	3.5011(10)
	3.6548(7)	3.6425(9)	3.6262(10)
Tl-Tl	3.5388(9)	3.5342(7)	3.4815(13)
A-Te	2.8430(7)	2.8428(14)	2.7765(9)
X-Te	2.6156(7)	2.6177(14)	2.6110(9)

Table 4.4: Atomic coordinates, displacement parameters, and interatomic distances for the Sn containing compounds reported here.

	Tl₂CdSnTe₄	Tl₂HgSnTe₄	Tl₂MnSnTe₄
Atomic coordinates			
x Te	0.1821(1)	0.1826(1)	0.1794(1)
z Te	0.2396(1)	0.2406(1)	0.2468(2)
Isotropic displacement parameters (Å ²)			
Tl	0.021(1)	0.018(1)	0.021(1)
A	0.013(1)	0.013(1)	0.013(1)
X	0.010(1)	0.009(1)	0.008(1)
Te	0.012(1)	0.009(1)	0.012(1)
Interatomic distances (Å)			
Tl-Te	3.5379(4)	3.5244(16)	3.5658(9)
	3.6138(4)	3.5918(17)	3.5884(9)
Tl-Tl	3.6086(3)	3.579(3)	3.5539(8)
A-Te	2.8705(7)	2.8542(16)	2.7992(12)
X-Te	2.7743(7)	2.7689(15)	2.7702(11)

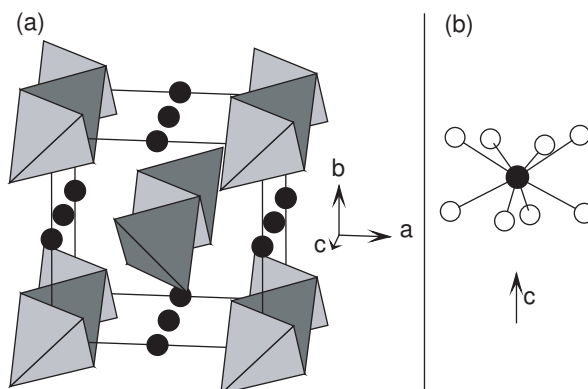


Figure 4.2: (a) A view of the crystal structure of Tl_2AXTe_4 ($A = Cd, Hg, Mn$; $X = Ge, Sn$). The Tl atoms (dark circles) separate chains of edge sharing A centered tetrahedra (medium grey) and X centered tetrahedra (light grey) with Te at the vertices. (b) The distorted square anti-prismatic coordination of Tl by Te (open circles).

attributed to presence of a racemic mixture in the crystals used for diffraction studies. The refinements for these compounds were carried out using the appropriate twinning law (inversion of all indices).

In all six compounds Tl, A and X are located at the positions $(0, 1/2, 0)$, $(0, 0, 1/2)$ and $(0, 0, 0)$, respectively. Te is at (x, x, z) , where x and z for each compound are given in Tables 4.1 and 4.2. The Tl^{1+} ion is coordinated to eight Te atoms, two from each of four neighboring $[AXTe_4]^{2-}$ chains, in a distorted square anti-prismatic environment (Figure 7.2). This relatively symmetric environment suggests that the Tl^{1+} lone pair is not stereo-chemically active.

Interatomic distances in each compound are listed in Tables 4.4 and 4.1. The A-Te and X-Te distances are similar to those found in the literature for the corresponding cation oxidation state in tetrahedral coordination: Cd-Te = 2.81Å in CdTe [13], Hg-Te = 2.79Å in HgTe [14], Mn-Te = 2.75Å in K_2MnTe_2 [15], Ge-Te = 2.62-2.64Å in Tl_2GeTe_5 [16], Sn-Te = 2.79Å in Tl_2SnTe_5 [17]. The Tl-Te distances are also consistent with those found in similar known compounds: 3.55-3.71Å in $Tl_2Cu_2SnTe_4$ and $Tl_2Ag_2SnTe_4$ [1], 3.57Å in $TlGaTe_2$ [18], 3.60Å in $TlInTe_2$ [18].

Although we know of no alkali metal compound which is strictly isostructural to Tl_2AXTe_4 , the structure is quite similar to that of $\text{Cs}_2\text{MnSnTe}_4$ [19]. The same $[\text{MnSnTe}_4]^{2-}$ chains exist in this compound, and are separated by Cs^{1+} ions. However the arrangement of the chains within in the unit cell is different, and the compound is orthorhombic. The structure is also similar to that of $\text{K}_2\text{Ag}_2\text{SnTe}_4$ [20], and its Tl analogues $\text{Tl}_2\text{Ag}_2\text{SnTe}_4$ and $\text{Tl}_2\text{Cu}_2\text{SnTe}_4$ [1]. In these compounds the divalent A in Tl_2AXTe_4 is replaced by two monovalent ions (Cu or Ag) distributed over four positions surrounding the site occupied by A. There are several known alkali metal analogues of the parent structure TlInTe_2 . One example is KInTe_2 [21]. Below we will compare the calculated electronic structure of these two compounds, and see the effect of replacing K with Tl.

4.4 Electronic Structure

The electronic structures of these compounds were investigated with density functional theory (DFT) calculations, using the full potential linearized augmented plane wave method. First a test calculation was performed on the compound TlGaTe_2 . This proved to be in agreement with previous investigators results, with the exception of the value of the band gap [22]. Our calculation showed a small positive gap while Okazaki et al. calculated a small negative gap [22]. Experimentally TlGaTe_2 is a semiconductor, in agreement with our calculation. However, it is well known that band gaps determined from DFT calculations can be unreliable, and are often underestimated. The density of states (DOS) are reported as number of states per eV per unit cell, so that integration of the DOS curve up to the Fermi level gives to total number of electrons per unit cell.

We then proceeded to calculate and compare the electronic structures of the isostructural compounds KInTe_2 [21] and TlInTe_2 [18], from which the Tl_2AXTe_4 structure can be derived (*vide supra*). The results are shown in Figure 4.3. We see that replacing K with Tl decreases the calculated band gap. This is consistent with the many experimental examples, which we have previously documented, of the smaller band gaps in Tl compounds compared to their alkali metal analogues [1]. More importantly, we also see (Figure 4.3) that the contribution from Tl near the Fermi level, although small, is significantly larger than that of K. This is a direct result of the less electropositive nature of Tl, allowing significant mixing between Tl and Te orbitals near the Fermi level. This means that transport properties should be less anisotropic in a “layered” or “chain-like” Tl compound than in its alkali metal analogue. This is also reflected in the band structures shown in Figure 4.3. More dispersion is seen in the bands of TlInTe_2 than in K analogue, especially in the highest valence band.

The calculated band structures of $\text{Tl}_2\text{CdSnTe}_4$, $\text{Tl}_2\text{HgSnTe}_4$ and $\text{Tl}_2\text{MnSnTe}_4$ are shown in Figure 4.4, and the band structures for the corresponding Ge compounds are shown in Figure 4.5. The calculated density of states (DOS) are displayed in Figures 4.6, 4.7, and 4.8 for the Sn compounds, and Figures 4.9, 4.10, and 4.11 for the Ge analogues. In these Figures, the top panels display the total DOS, with a closer view around the Fermi level in the insets. The lower panels show the normalized projected density of states (PDOS). There is little difference between these results for the Sn compounds and those found for the Ge compounds, so only the Sn compounds will be discussed in detail here.

The calculated band structures of $\text{Tl}_2\text{CdSnTe}_4$ and $\text{Tl}_2\text{HgSnTe}_4$ are seen to be quite similar, with the main difference being the magnitude of the gap. Experimentally, $\text{Tl}_2\text{HgSnTe}_4$ behaves like a semiconductor (*vide infra*), though the

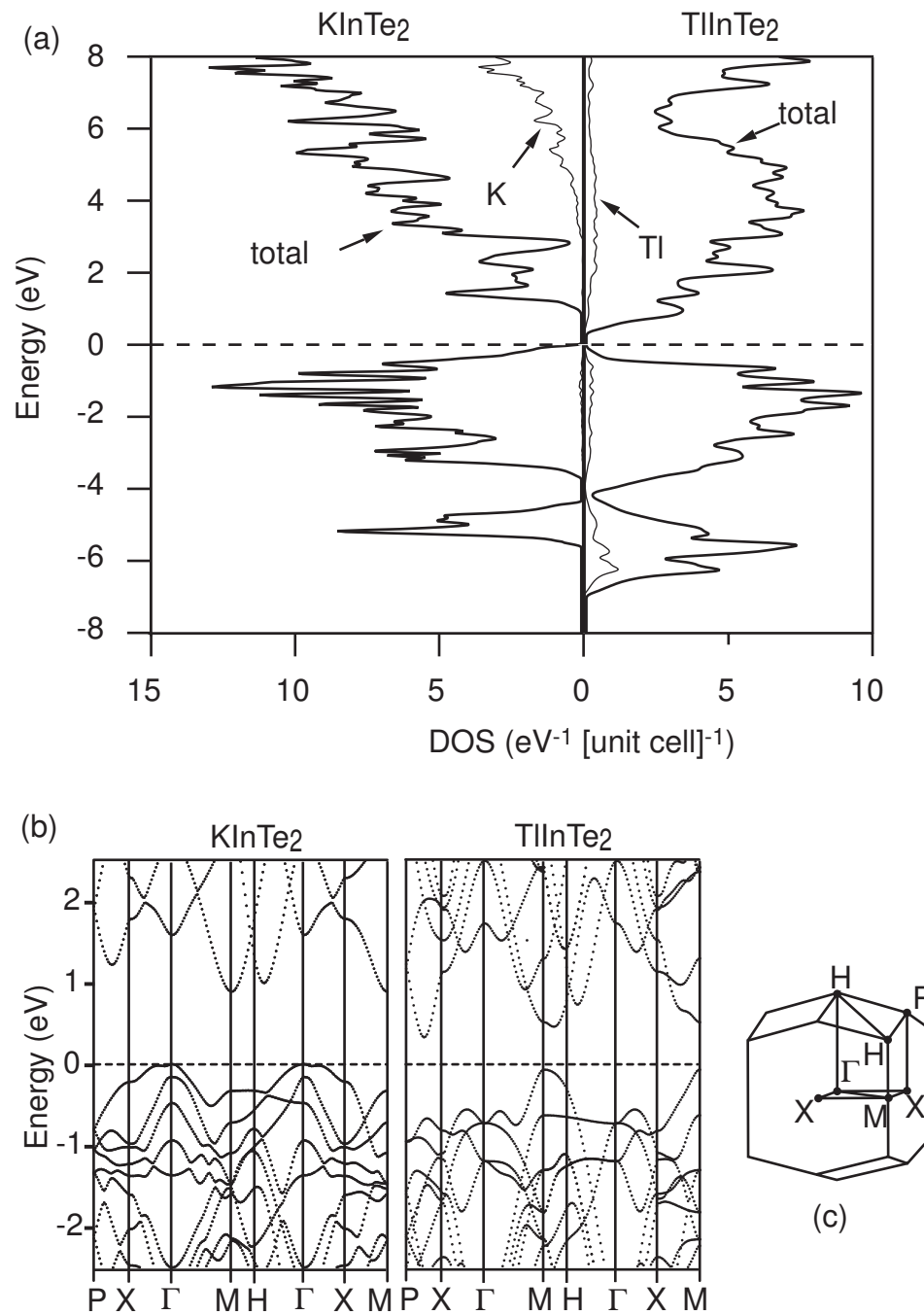


Figure 4.3: (a) The calculated density of states per unit cell for KInTe_2 and TlInTe_2 . Also shown are the K and Tl projections. (b) The calculated band structure of KInTe_2 and TlInTe_2 . (c) The first Brillouin zone for the body centered tetragonal lattice, showing the special points as labeled in the band structures. The dashed line in (a) and (b) is the Fermi level ($E = 0$ eV).

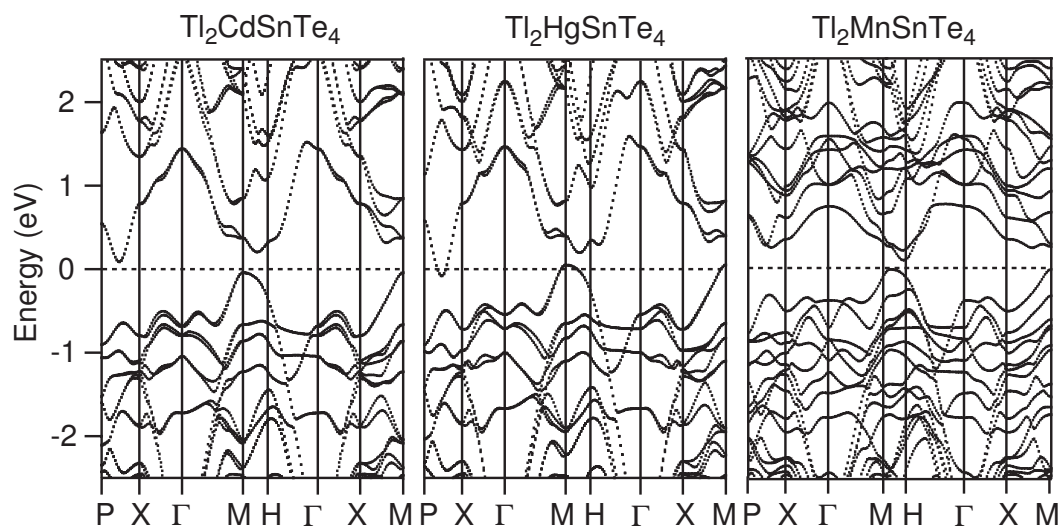


Figure 4.4: The calculated band structures of $\text{Tl}_2\text{CdSnTe}_4$, $\text{Tl}_2\text{HgSnTe}_4$ and $\text{Tl}_2\text{MnSnTe}_4$. The Fermi level is the dashed line at $E = 0$ eV.

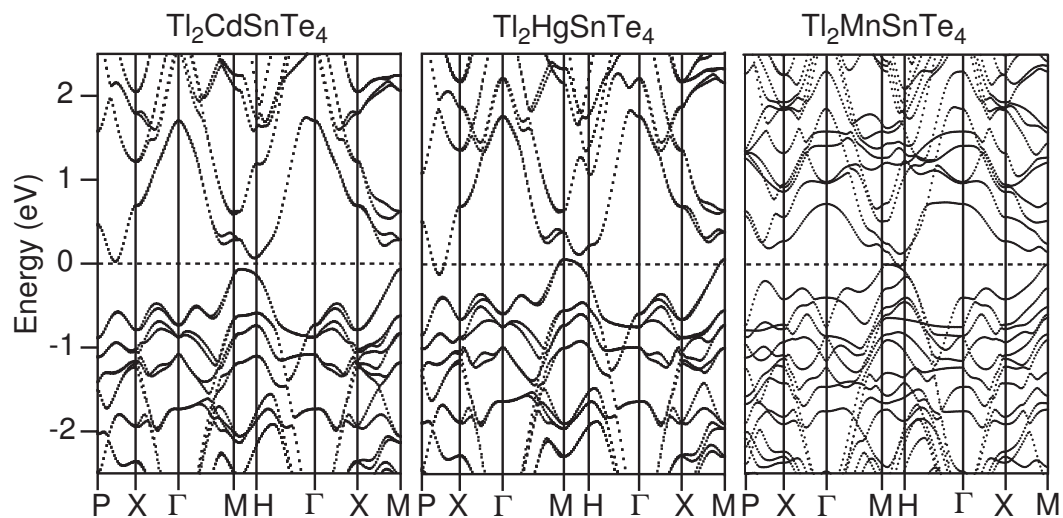


Figure 4.5: The calculated band structures of $\text{Tl}_2\text{CdGeTe}_4$, $\text{Tl}_2\text{HgGeTe}_4$ and $\text{Tl}_2\text{MnGeTe}_4$. The Fermi level is the dashed line at $E = 0$ eV.

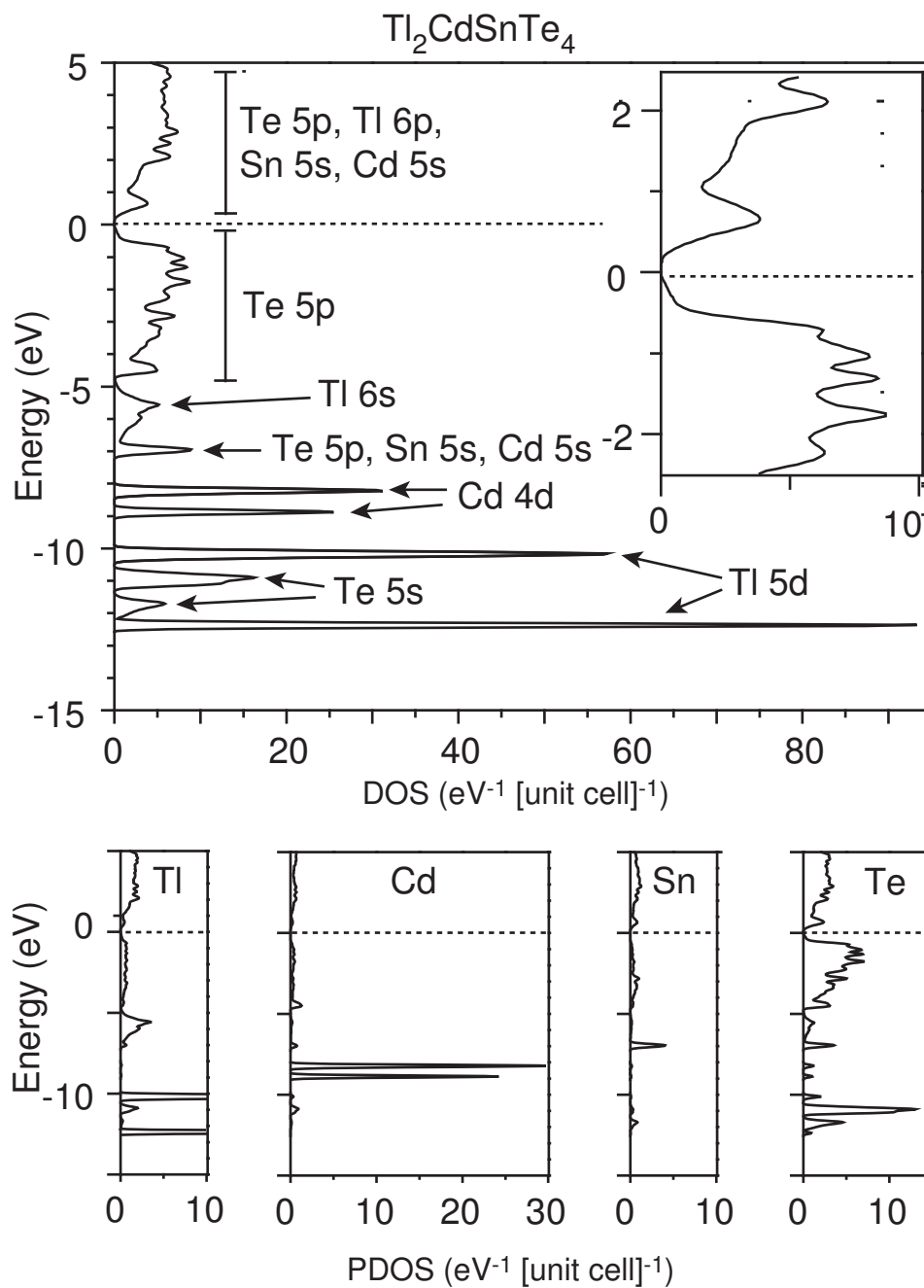


Figure 4.6: The calculated density of states (DOS) per unit cell and projected densities of states (PDOS) for $\text{Tl}_2\text{CdSnTe}_4$. The Fermi level (dotted line) is at $E = 0$ eV.

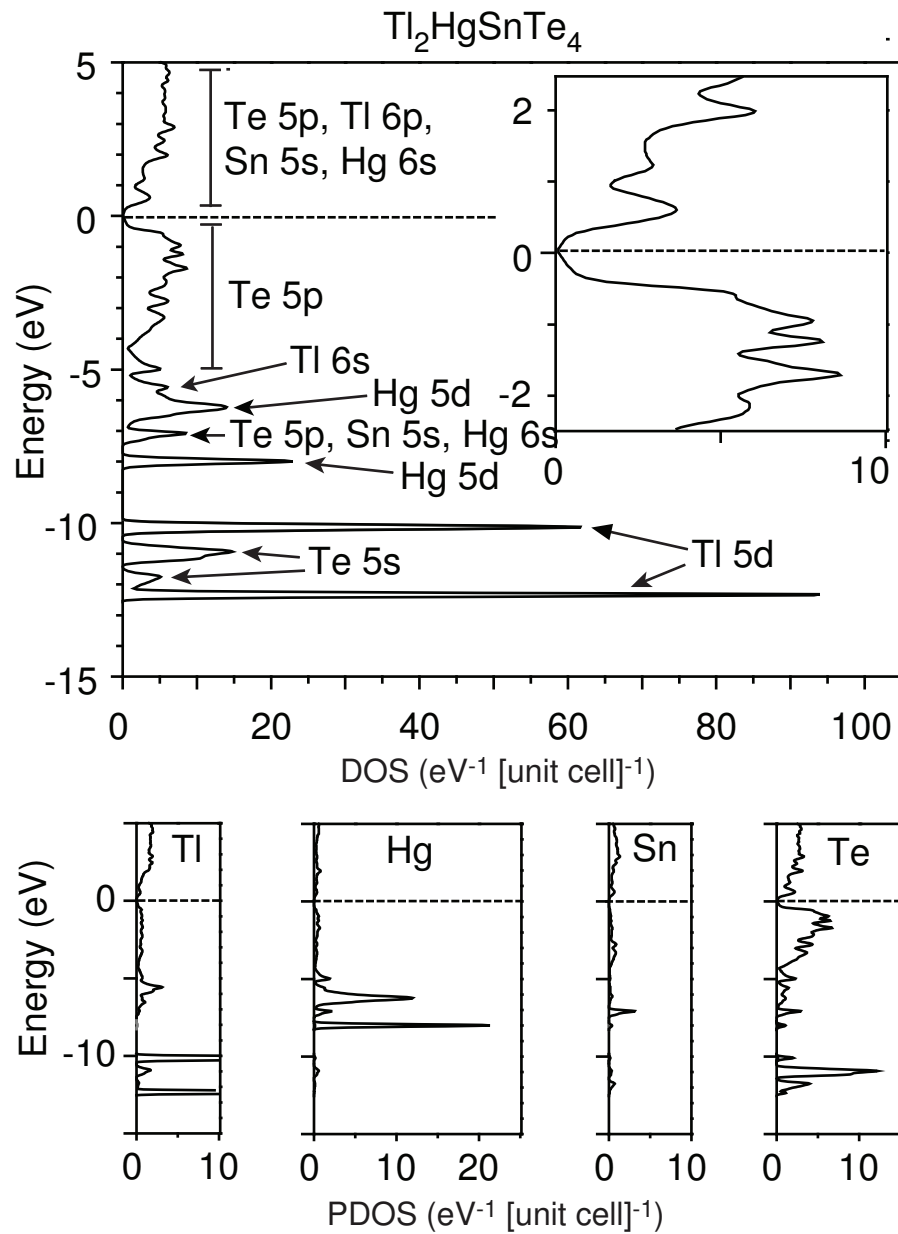


Figure 4.7: The calculated density of states (DOS) per unit cell and projected densities of states (PDOS) for $\text{Tl}_2\text{HgSnTe}_4$. The Fermi level (dotted line) is at $E = 0$ eV.

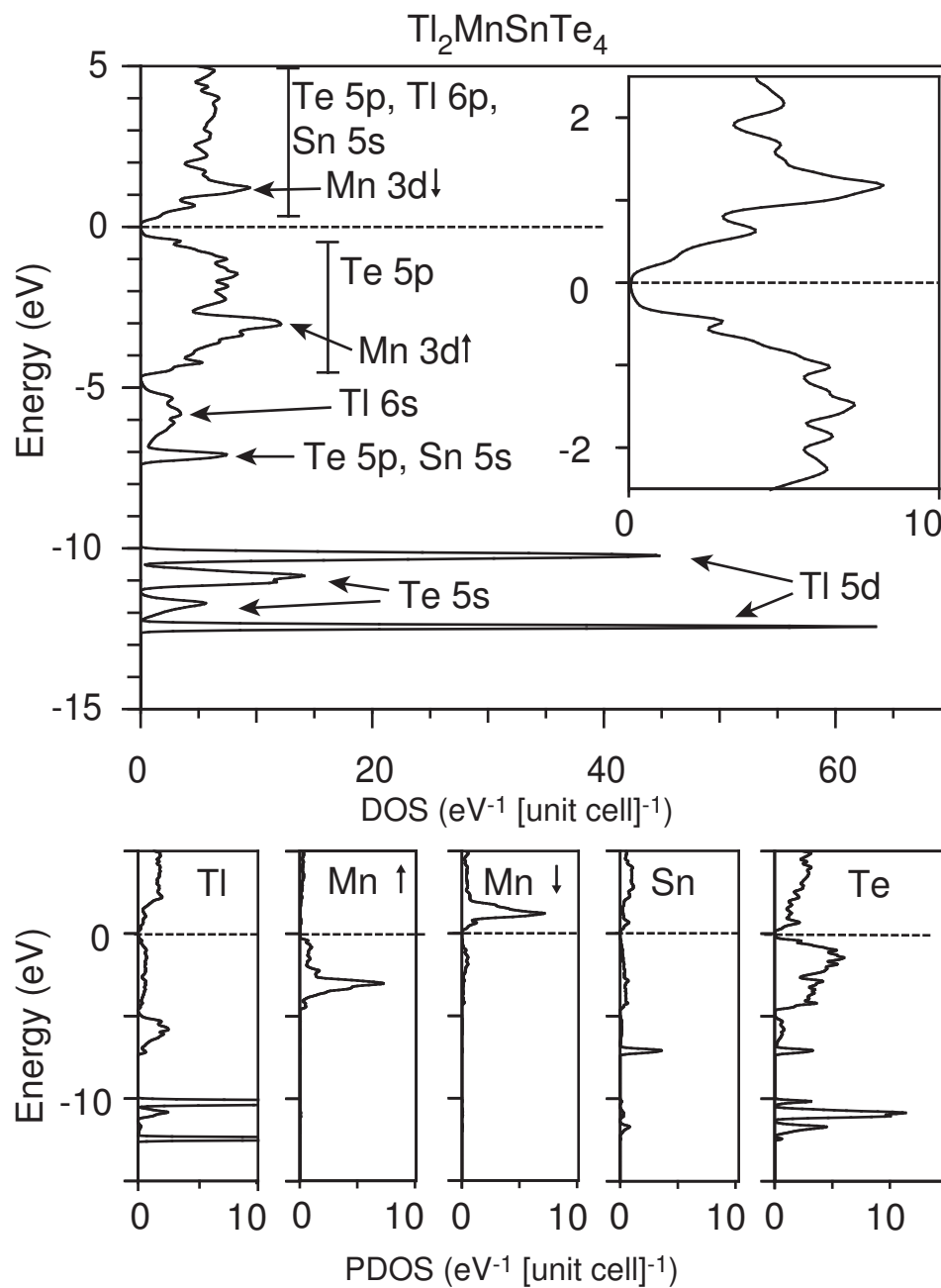


Figure 4.8: The calculated density of states (DOS) per unit cell and projected densities of states (PDOS) for $\text{Tl}_2\text{MnSnTe}_4$. The Fermi level (dotted line) is at $E = 0$ eV.

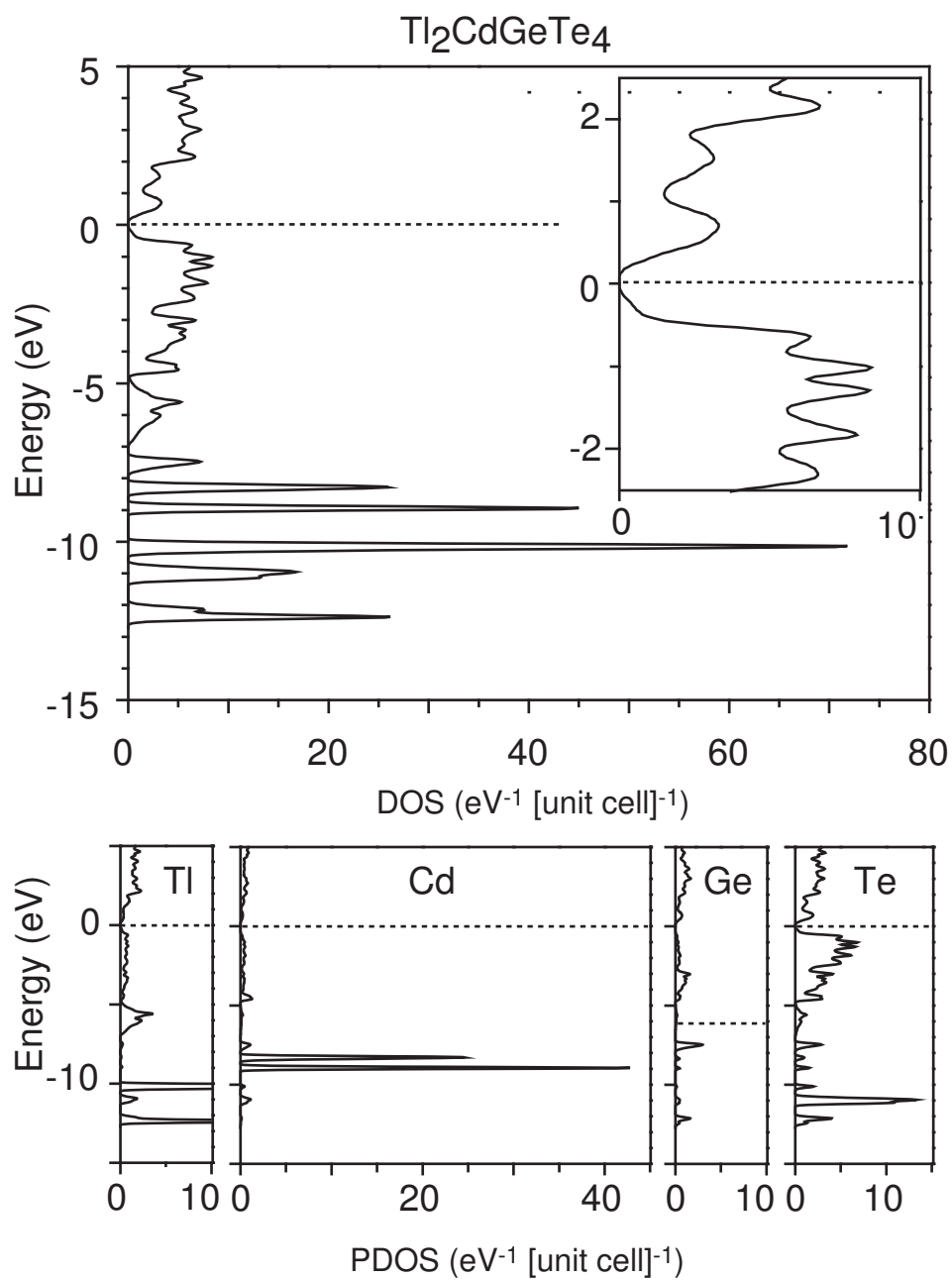


Figure 4.9: The calculated density of states (DOS) per unit cell and projected densities of states (PDOS) for $\text{Tl}_2\text{CdGeTe}_4$. The Fermi level (dotted line) is at $E = 0$ eV.

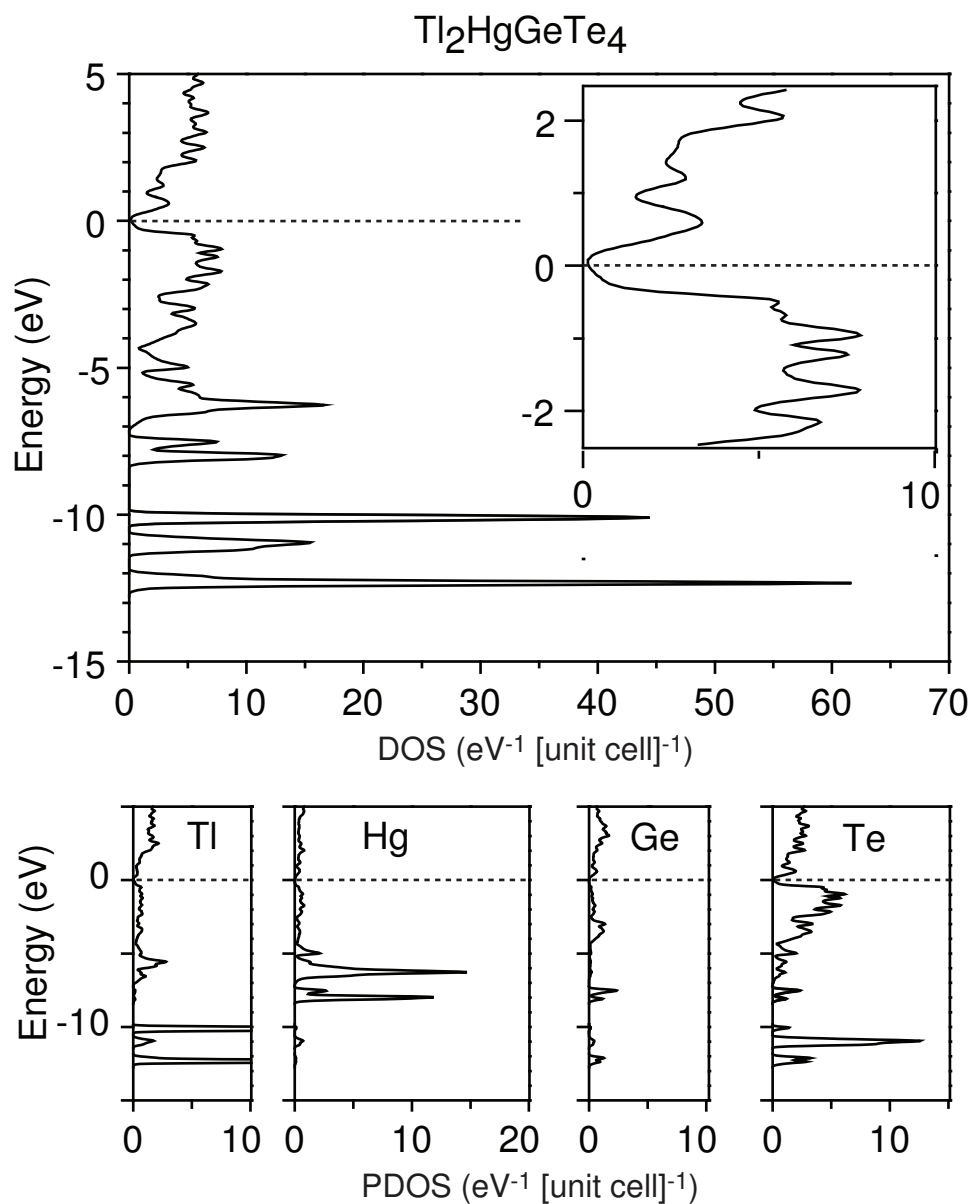


Figure 4.10: The calculated density of states (DOS) per unit cell and projected densities of states (PDOS) for $\text{Tl}_2\text{HgGeTe}_4$. The Fermi level (dotted line) is at $E = 0$ eV.

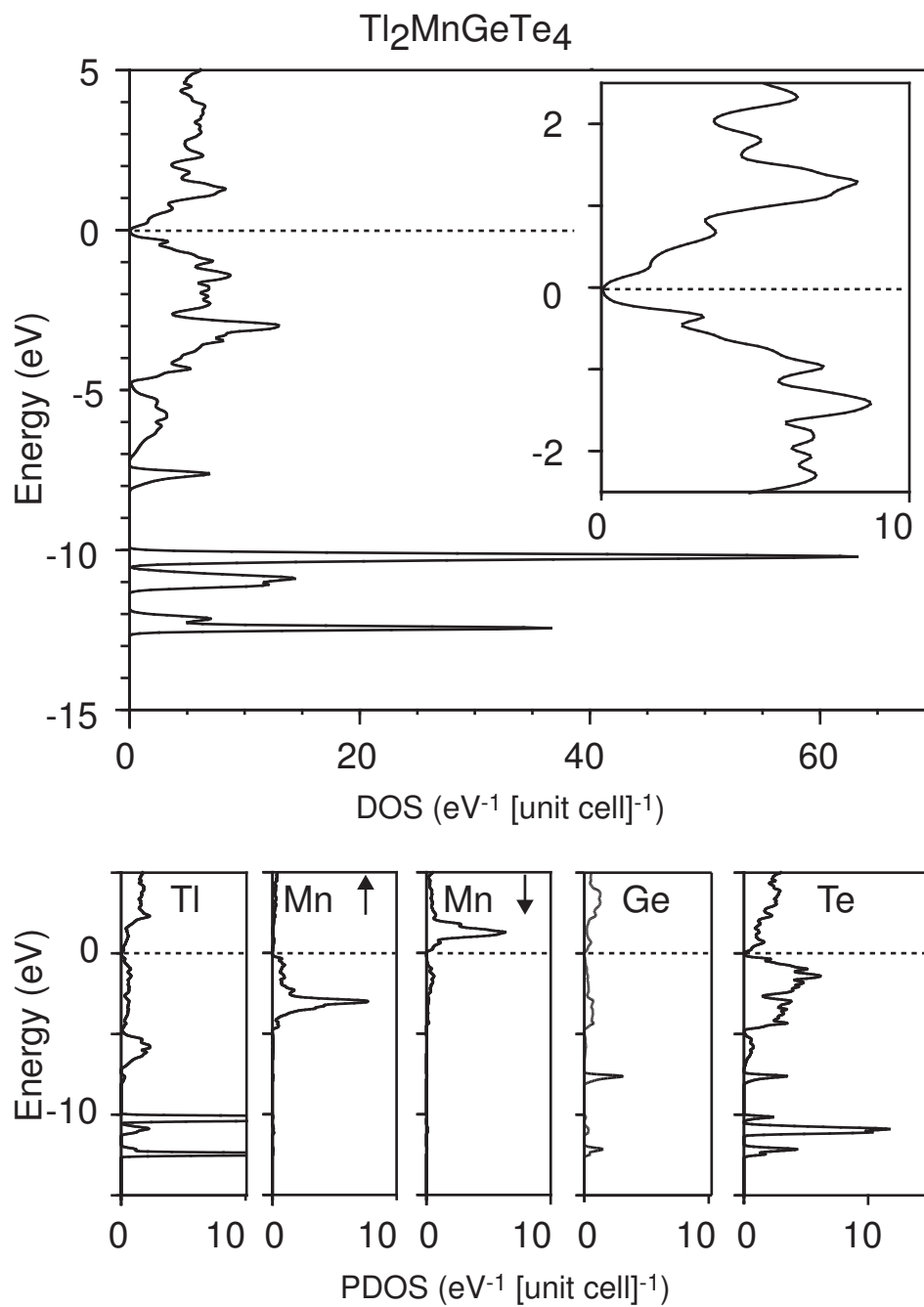


Figure 4.11: The calculated density of states (DOS) per unit cell and projected densities of states (PDOS) for $\text{Tl}_2\text{MnGeTe}_4$. The Fermi level (dotted line) is at $E = 0$ eV.

calculations predict this material to be a semimetal with a small band overlap (Figure 4.4). This suggests that the gap has been underestimated by the calculation, a common problem with DFT calculations. The same discrepancy was pointed out above for previous calculations on TlGaTe_2 [22].

In the top panels of Figures 4.6, 4.7 and 4.8 the DOS curves are labeled by the atomic states which make the predominant contributions, as identified by the calculated PDOS. The states near the Fermi level are found to arise primarily from the Te atoms, and are identified as the Te 5p bands. The conduction bands contain significant contributions from the cations as well. The filled core levels of Tl (5d and 6s), Cd/Hg (4d/5d), and Te (5s) are visible. The Sn 4d levels are below -15 eV.

Initial, non-spin-polarized calculations predicted $\text{Tl}_2\text{MnSnTe}_4$ to be metallic, with the Fermi level passing through the middle of narrow, half filled Mn 3d bands. This suggested that these compounds may in fact be Mott insulators. Electrical resistivity and magnetization measurements supported this hypothesis by showing the Mn compounds to be magnetic semiconductors (*vide infra*). Thus, spin-polarized calculations were performed. These calculations showed (Figures 4.4, 4.5, 4.8, and 4.11) that the Mn 3d bands are indeed split into spin-up bands which are filled, and spin-down bands which are unfilled, confirming that these compounds are Mott insulators.

4.5 Thermoelectric Properties: Tl_2AXTe_4 A=Cd, Hg; X=Ge, Sn

The thermoelectric properties of these four compounds, measured on polycrystalline pellets, are shown in Figure 4.12. They are seen to be semiconductors with moderately high thermopower at room temperature and very low thermal conductivity. The plateau in the $\rho(T)$ curve for $\text{Tl}_2\text{HgGeTe}_4$ below about

200 K suggests some unintentional doping may be present in this sample. The Hg compounds have room temperature resistivities one to two orders of magnitude lower than the Cd compounds. The resistivities of all four compounds show activated behavior. Activation energies were estimated from linear fits to $\ln(\rho)$ vs. $1000/T$, assuming $\rho \propto \exp(-E_a/k_B T)$. These plots are shown in Figure 4.13. The resulting values of E_a , along with band gap values derived from the band structure calculations, are summarized in Table 4.5. If the activation is due to excitation across the band gap, the corresponding energy gap equals $2E_a$.

In Figure 4.12 the Cd compounds are seen to have $S > 0$ while the Hg compounds have $S < 0$. This shows that the dominant charge carriers are holes in the Cd compounds and electrons in the Hg compounds. This may be due to the greater dispersion seen in the conduction band of the Hg compounds (Figures 4.5 and 4.4). The temperature dependence of the measured thermal conductivity

Table 4.5: Activation energies E_a from fitting resistivity data, and band gaps E_G determined from electronic structures (eV).

Compound	fitted E_a	calculated E_G
$\text{Tl}_2\text{CdGeTe}_4$	0.08	0.10
$\text{Tl}_2\text{CdSnTe}_4$	0.06	0.13
$\text{Tl}_2\text{HgGeTe}_4$	0.08	-0.18
$\text{Tl}_2\text{HgSnTe}_4$	0.11	-0.13

in Figure 4.12 is typical for that of crystalline materials. The thermal conductivity of all four materials is very low. For comparison, at room temperature optimized Bi_2Te_3 based alloys have $\kappa = 15$ mW/cmK, with a lattice contribution of $\kappa_L = 10$ mW/cmK [23]. Due to the relatively high resistivity of these Tl compounds (Figure 4.12), there is expected to be little electronic contribution to κ . The measured

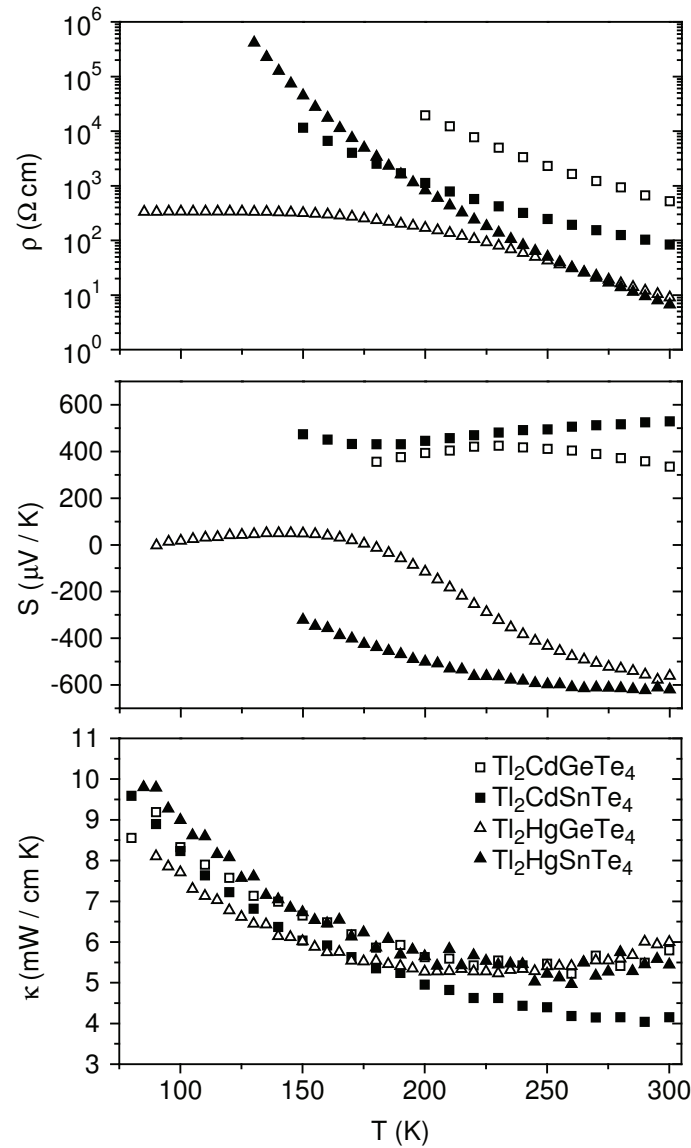


Figure 4.12: The measured resistivity (ρ), thermopower (S) and thermal conductivity (κ) of Tl_2AXTe_4 ($A = \text{Cd}, \text{Hg}; X = \text{Ge}, \text{Sn}$). Based on measurements of reference materials and on estimated errors in geometrical measurements, the uncertainty of the ρ and S measurements is estimated to be about 5%, and the uncertainty of the κ measurements is estimated to be about 15%.

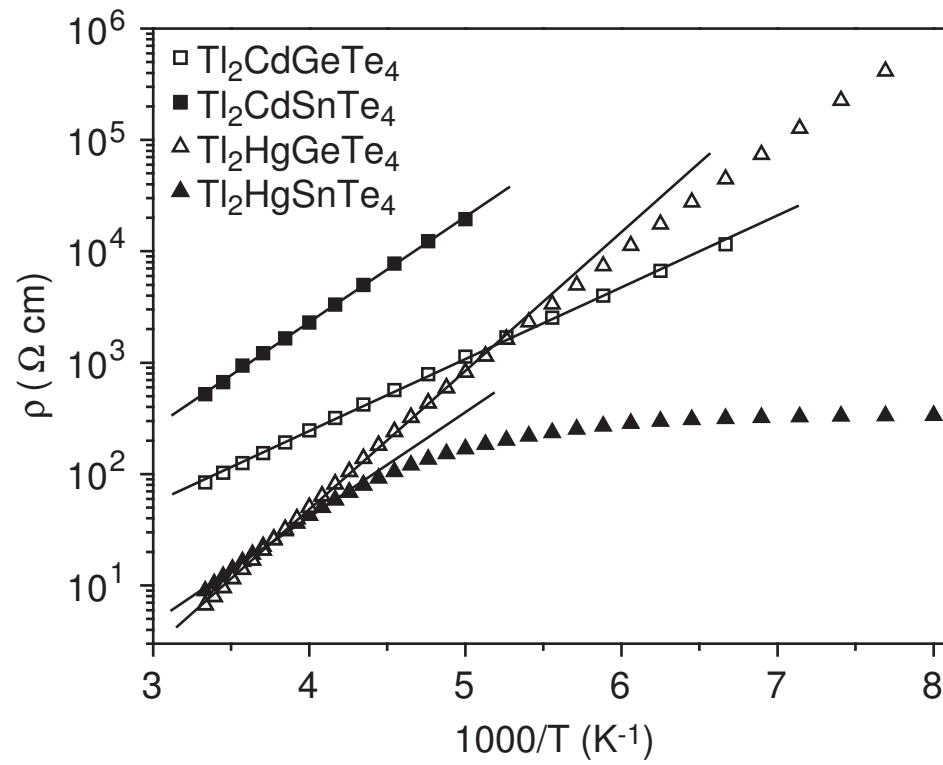


Figure 4.13: Linear fits to $\ln(\rho)$ vs. $1000/T$ used to estimate activation energies.

value of κ is essentially equal to κ_L . Other Tl chalcogenides, as noted above, have also been found to have low thermal conductivities, with values comparable to these materials.

Since these compounds were found to have low κ and high S at room temperature, but ρ values too high for TE applications, we tried to prepare doped samples, aiming to decrease ρ while retaining moderately high values of S . The nominally undoped Hg compounds exhibited significantly lower ρ , and higher magnitudes of S than the Cd compounds (Figure 4.12), so we restricted our study to $\text{Tl}_2\text{HgGeTe}_4$ and $\text{Tl}_2\text{HgSnTe}_4$. Several dopants were tested: Pb to substitute for Tl (n-type), As (n-type) and Ga (p-type) for Ge, and I for Te (n-type). The target doping density was $10^{19}/\text{cm}^3$. Since this corresponds to a concentration of only about 0.1 percent, any second phases which may have formed as a result of the doping were undetectable by X-ray diffraction. The results are shown in Figure 4.14. The attempted doping produced no significant change in κ . At room temperature the resistivity of $\text{Tl}_2\text{HgGeTe}_4$ was decreased by about an order of magnitude (to $0.9 \Omega\text{cm}$ for I doping), but is seen to be still too high for good TE performance. Although at lower temperatures the resistivity of $\text{Tl}_2\text{HgSnTe}_4$ was decreased by doping, little difference is seen in the room temperature values. The thermopower decreased significantly upon doping, by about a factor of two in most cases.

The high resistivities of the doped samples suggest that the target carrier concentration was not achieved. This could be due to the formation of compensating defects, which often occurs when doping multinary compounds. Since the doped compounds also had only moderate thermopowers, we did not pursue the doping of these materials further.

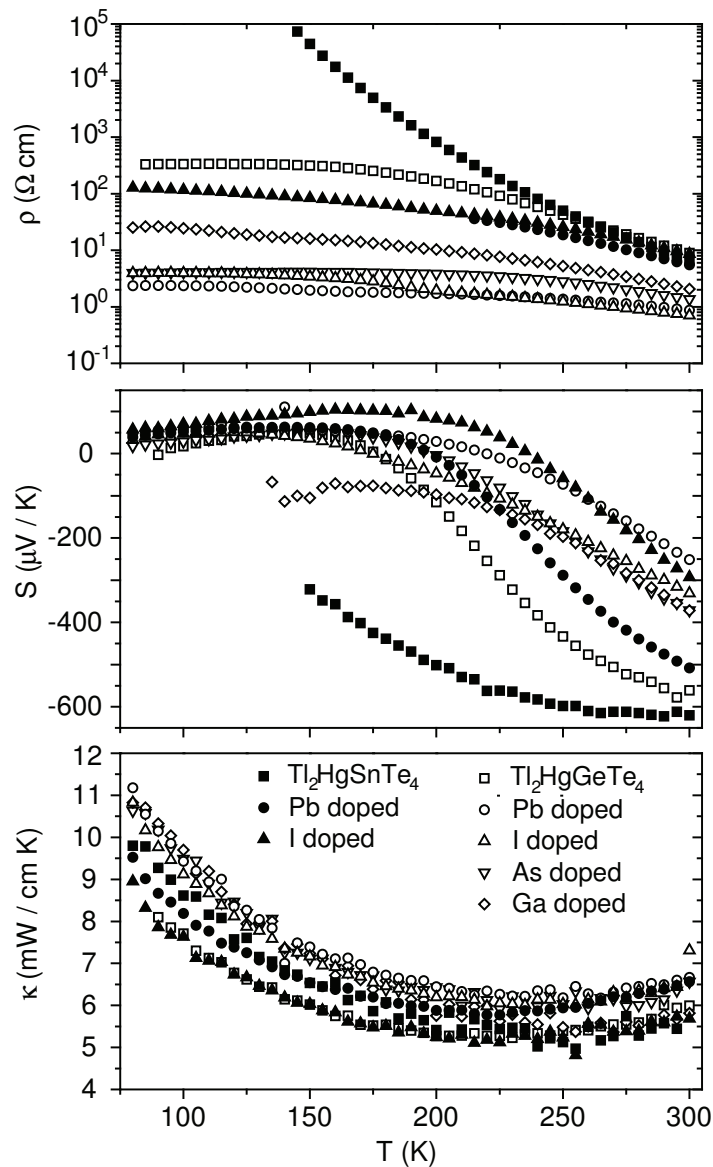


Figure 4.14: The measured resistivity (ρ), thermopower (S) and thermal conductivity (κ) of doped $\text{Tl}_2\text{HgGeTe}_4$ and $\text{Tl}_2\text{HgSnTe}_4$. Data for the undoped compounds are shown for comparison. Based on measurements of reference materials and on estimated errors in geometrical measurements, the uncertainty of the ρ and S measurements is estimated to be about 5%, and the uncertainty of the κ measurements is estimated to be about 15%.

4.6 Resistivity and Magnetization: $\text{Tl}_2\text{MnXTe}_4$ X=Ge, Sn

The measured magnetic susceptibility per mol of Mn for $\text{Tl}_2\text{MnGeTe}_4$, measured in an applied field of 2 T and corrected for the diamagnetic response of the sample holder, is shown in Figure 4.15. The measurements were made on 7.3 mg of powder ground from single crystals extracted from the polycrystalline reaction product. Powder X-ray diffraction confirmed that the resulting powder was single phase. This compound shows Curie-Weiss type paramagnetic behavior, with evidence of an antiferromagnetic transition visible at the lowest temperatures investigated (Figure 4.15). We are unsure of the origin of the small discontinuity in the data at 350 K, but suspect that it may be due to movement of the sample position within the field. We also note that a field sweep at 300 K showed the sample to be paramagnetic at this temperature, with no sign of saturation up to 5 T. Fits to the paramagnetic part of the magnetic data below 350 K in Figure 4.15 were performed using Equation 9.3. [24]

$$\chi_{mol} = \frac{C}{T - \theta}, \quad \mu_{eff} = \sqrt{\frac{3k_B C}{N_A}} \quad (4.1)$$

Here C is the molar Curie constant, θ is the paramagnetic Curie temperature, k_B is the Boltzmann constant, and N_A is Avogadro's number. Fits suggest a value for θ of ~ -120 K. The negative value of θ shows this compound to be an antiferromagnet. The model gives an effective moment for Mn of $\mu_{eff} = 5.2 \mu_B$ where μ_B is the Bohr magneton. The effective moment is in only rough agreement with the value of $5.9 \mu_B$ expected for Mn^{2+} [24]. However, Equation 9.3 is expected to be valid only for temperatures well above θ , and we are fitting data only up to $T \sim 3\theta$ [24]. This may, in part, account for the disagreement. Although a small difference exists between the expected and measured moments, the data is clearly consistent with localized Mn 3d electrons.

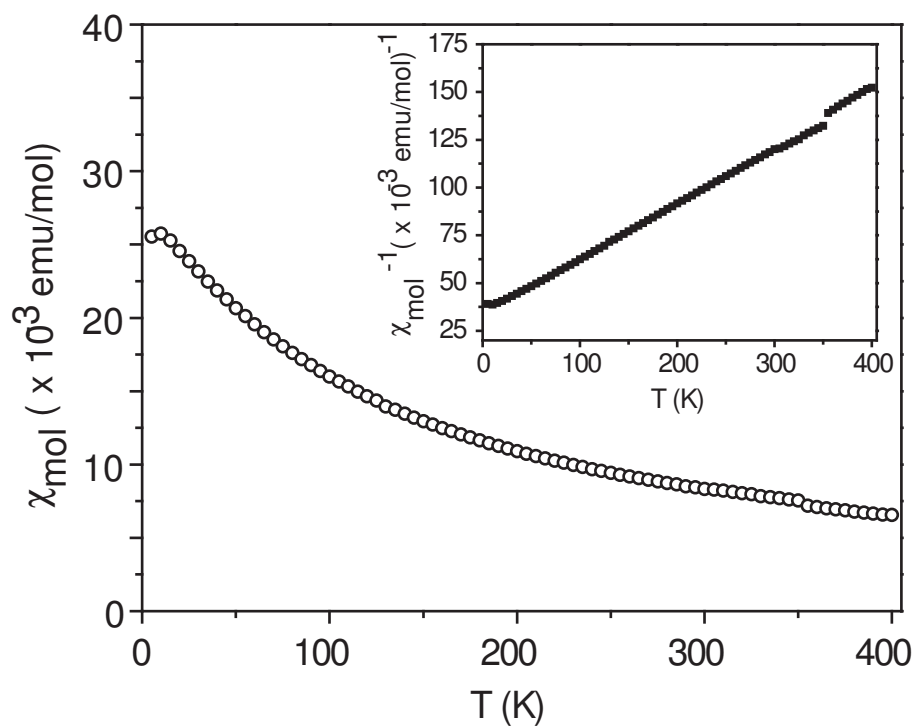


Figure 4.15: The measured temperature dependence of the molar magnetic susceptibility χ_{mol} and inverse molar magnetic susceptibility (inset) of $\text{Tl}_2\text{MnGeTe}_4$.

In addition, the resistivities of the Mn compounds, measured on single crystals at room temperature, are high: 4 k Ω cm for Tl₂MnGeTe₄ and 5 k Ω cm for Tl₂MnSnTe₄. Thus, the measured properties, magnetic and electrical, show the Mn compounds to be Mott insulators, in agreement with the spin-polarized calculations.

4.7 Conclusions

We have presented the synthesis, crystal structure and electronic structure of the six new quaternary Tl tellurides Tl₂AXTe₄ (A=Cd, Hg, Mn; X=Ge, Sn). These compounds are the first examples of a new variation on the TlSe structure type, with 1-D chains of alternating A and X centered tetrahedra which share edges. LAPW band structure calculations predict the Cd compounds to be semiconductors with a small positive gap, the Hg compounds to be semimetals with a small negative gap. Spin polarized calculations, as well as resistivity and magnetic susceptibility measurements, show the Mn compounds to be Mott insulators, due to the narrow, half-filled 3d bands of Mn²⁺.

We have also reported the measured TE properties of the Cd and Hg compounds. These were shown to be small band gap semiconductors, consistent with the DFT calculations which are known to underestimate band gaps. At room temperature, the compounds also exhibited high thermopower and very low thermal conductivity. However, the electrical resistivities of the samples were too high for TE applications. Our initial investigation into the doping behavior of these compounds produced little improvement in the overall TE performance. The high measured resistivities could be attributed to low carrier concentration due to dopant compensation, or grain boundary scattering in the polycrystalline samples.

REFERENCES

- [1] M. A. McGuire, T. K. Reynolds, and F. J. DiSalvo, *Chem. Mater.* **17**, 2875 (2005).
- [2] SMART and SAINT: Data collection and processing software for the SMART system, Bruker Analytical X-ray Instruments, Inc., Madison, WI, 1995.
- [3] SADABS program for absorption correction, G.M. Sheldrick for Bruker Analytical X-ray Instruments, Inc., Madison, WI, 2000.
- [4] XPREP program for determination of space groups, Bruker Analytical X-ray Instruments, Inc., Madison, WI, 2000.
- [5] L. Farrugia, *J. Appl. Cryst.* **32**, 837 (1999).
- [6] P.-E. Werner, L. Eriksson, and M. Westdahl, *J. Appl. Crystallogr.* **18**, 367 (1985).
- [7] T. K. Reynolds, M. A. McGuire, and F. J. DiSalvo, *J. Solid State Chem.* **177**, 3038 (2004).
- [8] M. Hanais, A. N. Anagnostopoulos, K. Kambas, and J. Spyridelis, *Phys. Rev. B* **43**, 4135 (1991).
- [9] M. P. Hanais and A. N. Anagnostopolous, *Phys. Rev. B* **47**, 4261 (1993).
- [10] W. Kohn and L. Sham, *Phys. Rev.* **140**, A1133 (1965).
- [11] J. P. Perdew, K. Burke, and M. Erzenhoff, *Phys. Rev. Lett.* **77**, 3865 (1996).
- [12] J. A. Ketelaar, W. H. t'Hart, M. Moerel, and D. Polder, *Z. Kristallogr.* **A101**, 396 (1939).
- [13] M. K. Rabadanov, i. A. Verin, Y. M. Ivanov, and V. I. Simonov, *Kristallografiya* **46**, 703 (2001).
- [14] A. Werner, H. D. Hochneimer, K. Stroessner, and A. Jayaraman, *Phys. Rev. B* **28**, 3330 (1983).
- [15] W. Bronger and H. Balk-Hardtdegen, *Z. Anorg. Allg. Chem.* **574**, 99 (1989).
- [16] R. E. Marsh, *J. Solid State Chem.* **87**, 467 (1990).
- [17] V. Agafonov et al., *Acta Cryst.* **C47**, 850 (1991).
- [18] D. Muller, G. Eulenberger, and H. Hahn, *Z. Anorg. Allg. Chem.* **398**, 207 (1973).

- [19] C. Zimmerman and S. Dehnen, *Z. Anorg. Allg. Chem.* **629**, 1553 (2003).
- [20] J. Li, H.-Y. Guo, and D. M. Proserpio, *J. Solid State Chem.* **117**, 247 (1995).
- [21] Y.-C. H. S.-J. Hwu, *Acta Cryst.* **C49**, 1588 (1993).
- [22] K. Okazaki et al., *Phys. Rev. B* **64**, 045210 (2001).
- [23] W. Yim and F. D. Rosi, *Solid-State Electron.* **15**, 1121 (1972).
- [24] J. S. Smart, *Effective Field Theories of Magnetism*, Saunders Company, 1st edition, 1966.

Chapter 5

Crystal Structure, Electronic Structure, and Thermoelectric Properties of AuTlSb: a New Pyrite Superstructure

In this Chapter, we present the structure and properties of the new ternary compound AuTlSb. This compound was discovered by Dr. Thomas K. Reynolds. In his dissertation, he presented only the crystal structure [1]. However, Dr. Reynolds did not identify the relationship between this compound's structure and the pyrite structure-type. Therefore, the current work includes a detailed description of the structure, since it is significantly different than the discussion in Dr. Reynolds' dissertation. This Chapter is adapted from a paper that has been accepted for publication in *Journal of Alloys and Compounds* with permission from Elsevier. *

5.1 Introduction

We recently reported that the structure of CrAuTe₄ can be derived from that of AuTe₂ by replacing half of the Au atoms with Cr [2]. Like CrAuTe₄, the AuTlSb structure presented in this work can also be derived from that of a known binary Au containing compound. In this case, one half of the Sb atoms in AuSb₂ are replaced by Tl. In both CrAuTe₄ and AuTlSb the substitutions occur in an ordered fashion, resulting in true ternary compounds. AuSb₂ forms the pyrite structure, with Au coordinated to Sb-Sb dimers. AuTlSb crystallizes in a new structure type, due to ordering of Sb-Sb and Tl-Tl dimers. There are no com-

*M. A. McGuire, T. K. Reynolds, and F. J. DiSalvo, *J. Alloys Compds.*, in press.

pounds isostructural to AuTlSb listed in the current version (1.3.3, 2005-1) of the Inorganic Crystal Structure Database (ICSD). Although there are several known inorganic compounds which contain polyanionic Tl clusters [3, 4], we know of only one other material, Na₆TlSb₄ [5], which contains Tl-Tl dimers like those found in AuTlSb.

In addition to the synthesis and crystal structure of AuTlSb, we report in this paper the calculated (extended Hückel tight binding) electronic structure and bonding analysis for both AuTlSb and AuSb₂. We also present the measured electrical conductivity and thermopower of AuTlSb.

5.2 Experimental Details

This compound was discovered in an attempt to make the Tl analog of the known compound K₃Au₃Sb₂ [6]. Tl (rod, Alfa Aesar, 99.9%) Au (splatters, Cerac, 99.999%) and Sb (shot, Cerac, 99.999%) were reacted in a 3:3:2 ratio in an evacuated, carbon-coated, silica tube at 700 °C for 100 hours. The furnace was then turned off and allowed to cool to room temperature. The reaction product contained irregularly shaped, silver colored crystals of AuTlSb, which were used for single crystal X-ray diffraction. Attempts to make this compound as a single phase from a 1:1:1 reaction mixture at 700 °C produced a multi-phase product containing some AuTlSb, but with AuSb₂ as the majority phase. Other unidentified phases were also present, according to powder X-ray diffraction. Initial attempts to make AuTlSb from a 1:1:1 mixture at a lower temperature (350 °C) were also unsuccessful. Since we were able to obtain crystals large enough for characterization from the 3:3:2 mixture, we did not further pursue the optimization of the synthesis conditions. The crystals used for property measurements

were produced by reacting a 3:3:2 mixture at 700 °C for 100 hours and then cooling from 700 °C to 200 °C over the course of 100 hours.

Energy dispersive electron microprobe analysis of the crystals produced by the reactions described above were performed on a JEOL 8900R electron microprobe using an accelerating voltage of 15 kV and a current of approximately 20 nA. Semi-quantitative analysis of the data gave an average stoichiometry of $\text{AuTl}_{0.9}\text{Sb}_{1.1}$, well within the expected range for a 1:1:1 stoichiometry with standardless measurements. Since the M-lines of Au and Tl overlap significantly in energy dispersive spectra, wavelength dispersive measurements were used to confirm the presence of both elements in the crystals. Microprobe analysis was also used to confirm that the crystals used for electrical resistivity and thermopower measurements were AuTlSb .

For single crystal X-ray diffraction, a crystal of AuTlSb was mounted in poly(butenes) oil and bathed in a cold nitrogen stream (175 ± 5 K) on a Bruker SMART CCD diffractometer. The program SMART was used to collect the data and the program SAINT was used to integrate the data and refine the unit cell based on strong reflections [7]. Absorption corrections were made with SADABS [8], and the space group was determined by XPREP [9]. Crystal structure solutions and refinements were carried out using SHELXS97 and SHELXL97 within the WingX program suite [10].

Two possible space groups were identified by XPREP, $\text{Pna}2_1$ (non-centrosymmetric) and Pnam (centrosymmetric). Attempts to solve the structure in the centrosymmetric space group failed, and E-statistics suggested strongly that the structure was non-centrosymmetric ($|E^2 - 1|$ tests returned 0.723, where 0.968 is expected for centrosymmetric and 0.736 is expected for non-centrosymmetric). The structure was subsequently solved in $\text{Pna}2_1$. Structure solution by direct methods identified six atoms in the asymmetric unit, two of

each element. The first refinement cycle gave $R_1=0.06$ and $wR_2=0.15$, confirming that the model was correct.

Since the scattering powers of Au and Tl are similar, it is impossible to distinguish them based solely on the diffraction data. However, the refined displacement parameters confirmed that the two Sb sites had been correctly assigned, leaving four sites (M1, M2, M3, and M4) for Tl and Au. Some attention must be given to how the occupancies of these four sites were assigned.

Examination of coordination environments, which will be discussed in greater detail below, revealed that M1 and M2 were each approximately 2.7 Å from Sb atoms. This distance is typical for a Au-Sb bond, which is 2.76 Å in AuSb₂ [11], and too short for a Tl-Sb contact, which is about 3.3 Å in Tl₇Sb₂ [12]. M1 and M2 were therefore identified as Au.

The suggested 1:1:1 stoichiometry (from microprobe measurements) then implied that M3 and M4 should be assigned as Tl. These two sites are 3.15 Å apart, which is consistent with a Tl-Tl single bond (*vide infra*). In addition, they are each 2.9-3.0 Å from three neighboring Au atoms. This is consistent with Au-Tl distances reported in the literature (*vide infra*). However, these M3/M4-Au distances are also similar to the Au-Au distance seen in Au metal (2.88 Å) [13]. Thus, it is possible that M3 and M4 may contain a mixture of Tl and Au. However, one might expect any significant occupation of these sites by Au to lead to shorter M3-M4 distances than those observed here. Based on these observations, and the 1:1:1 stoichiometry suggested by microprobe measurements, we believe that M3 and M4 can be identified as Tl with some confidence. However, the possibility of some Au mixing onto these sites cannot be excluded. Refinements allowing a mixture of Au and Tl on the M sites did not converge.

Once the Tl and Au sites were assigned, refinement of anisotropic displacement parameters for all atoms reduced the R values to $R_1=0.04$ and

$wR_2=0.10$. SHELXL suggested that an extinction parameter was needed, and the inclusion of this parameter and the suggested weighting scheme further improved the R values to $R_1=0.03$ and $wR_2=0.07$. The five highest difference peaks (2.0-2.8 $e\text{\AA}^{-3}$) are all less than 0.9 \AA from Au, Tl, or Sb atoms, and are thus attributed to truncation of the X-ray data, and not to unidentified atom sites. The final results of the structure refinement are reported in Table 5.1. Refined atomic positions and anisotropic displacement parameters are given in Tables 5.2 and 5.3, respectively.

Electrical resistivity and thermopower measurements were performed on crystals of AuTlSb using a home built apparatus that has been described elsewhere [2]. For the resistivity measurement, a bar shaped crystal of approximately triangular cross section was mounted on the sample holder using Apiezon N-grease. Electrical contacts were made by attaching four gold wires ($d = 0.05$ mm) to the sample using a conducting silver paste (DuPont Conductor Composition 4922N). For the thermopower measurement, an irregularly shaped crystal was attached to small piece of glass using a quick-set epoxy. A temperature gradient was imposed on the glass by supplying power to a resistor attached to one end, while the other end was fixed to the measurement stage. Thermocouples were attached to each end of the sample using silver epoxy (Epotek H20E), and used to measure the temperature difference and voltage difference across the sample as the resistor was heating. The slope of the linear fit to V_{sample} vs. T_{sample} , corrected for the contribution from the chromel wires used to measure the voltage, determines the thermopower S . A maximum temperature difference of about 2 K was used to measure S at each base temperature. Due to difficulty in accurately measuring the geometrical factors, we estimate the absolute uncertainty in the resistivity measurement to be $\pm 20\%$. Based upon test measurements of known

Table 5.1: Single crystal refinement data for AuTlSb.

Empirical formula	AuTlSb
Temperature	175(5) K
Wavelength	0.71073 Å
Crystal system	Orthorhombic
Space Group	Pna2 ₁
Unit cell dimensions	a = 6.5507(8) Å b = 14.2871(18) Å c = 6.5254(9) Å
Volume	610.72(14) Å ³
Absorption Correction	SADABS (based on equivalents)
Color	Black
Z	8
Calculated density	11.38 g/cm ³
Absorption coefficient	109.013 mm ⁻¹
θ range	2.85 ° to 26.37 °
Reflections collected/unique	1713 / 909 [R(int) = 0.0496]
Completeness to $\theta=26.37$ °	96.5 %
Refinement method	Full-matrix least-squares on F ²
Data/restraints/parameters	909 / 1 / 56
Goodness-of-fit on F ²	1.078
Final R indices (I > 2 σ (I))	R ₁ = 0.0321, wR ₂ = 0.0738
R indices (all data)	R ₁ = 0.0349, wR ₂ = 0.0748
Absolute structure parameter	0.017(18)
Extinction coefficient	0.00184(13)
Largest diff. peak and hole	2.80 and -1.80 eÅ ⁻³

$$R_1 = \frac{\sum ||F_o| - |F_c||}{\sum |F_o|} \quad wR_2 = \left[\frac{\sum w(F_o^2 - F_c^2)^2}{\sum w(F_o^2)^2} \right]^{\frac{1}{2}}$$

$$w^{-1} = [\sigma(F_o^2) + (aP)^2 + bP] \quad \text{where } P = [\max(F_o^2, 0) + 2F_c^2] / 3$$

Table 5.2: Atomic coordinates and equivalent isotropic displacement parameters (\AA^2) for AuTlSb. U_{eq} is defined as one third of the trace of the orthogonalized U_{ij} tensor.

Atom	x	y	z	U_{eq}
Au(1)	0.0341(2)	0.3901(1)	0.4765(2)	0.025(1)
Au(2)	0.0360(1)	0.1405(1)	0.0000(2)	0.024(1)
Tl(1)	0.1240(2)	0.0344(1)	0.3648(2)	0.028(1)
Tl(2)	0.4172(2)	0.2959(1)	0.5913(2)	0.028(1)
Sb(1)	0.1072(2)	0.5711(1)	0.3569(4)	0.023(1)
Sb(2)	0.1511(3)	0.3185(1)	0.1118(3)	0.024(1)

Table 5.3: The anisotropic displacement parameters (\AA^2) for the compound AuTlSb. The exponent of the anisotropic displacement factor is of the form: $-2\pi^2(h^2a^{*2}U_{11}+\dots+2hka^*b^*U_{12})$.

Atom	U_{11}	U_{22}	U_{33}	U_{23}	U_{13}	U_{12}
Au(1)	0.022(1)	0.023(1)	0.029(1)	-0.001(1)	0.001(1)	0.001(1)
Au(2)	0.018(1)	0.024(1)	0.031(1)	0.000(1)	-0.001(1)	0.000(1)
Tl(1)	0.024(1)	0.027(1)	0.034(1)	0.003(1)	-0.002(1)	-0.002(1)
Tl(2)	0.023(1)	0.026(1)	0.036(1)	-0.001(1)	-0.002(1)	0.003(1)
Sb(1)	0.017(1)	0.024(1)	0.028(1)	0.000(1)	0.000(1)	-0.002(1)
Sb(2)	0.019(1)	0.022(1)	0.031(1)	-0.002(1)	0.000(1)	-0.001(1)

low thermopower materials, we estimate the uncertainty in our S measurements to be about $\pm 1 \mu\text{V}/\text{K}$.

Extended Hückel tight binding electronic structure calculations were carried out using the program YAeHMOP [14]. The density of states and overlap populations were calculated using 1000 k-points. The default parameters were used for all atoms: (H_{ii} (eV) and ζ for s and p states, H_{ii} (eV), ζ_1 , c_1 , ζ_2 , c_2 for d states) Tl 6s, -11.6, 2.3; Tl 6p, -5.8, 1.6; Au 6s, -10.92, 2.602; Au 6p, -5.55, 2.584; Au 5d, -15.07, 0.6442, 6.1630, 0.5356, 2.7940; Sb 5s, -18.8, 2.323; Sb 5p 11.7, 1.999. The density of states (DOS) are reported per eV per unit cell, so that integration of the DOS curves up to the Fermi level gives the total number of electrons per unit cell.

5.3 Crystal Structure

The crystal structure of AuTlSb can be viewed as an ordered superstructure of AuSb₂, and views of both structures, emphasizing different structural aspects, are shown in Figures 5.1 and 5.2. We begin here by describing briefly the AuSb₂ structure, and then discuss how the AuTlSb structure is derived from it.

AuSb₂ forms the pyrite structure type, space group $\text{Pa}\bar{3}$, with lattice constant 6.658 Å [11]. The structure is composed of a three dimensional network of corner-sharing Au centered octahedra with Sb atoms at the vertices. Sb-Sb dimers with an interatomic distance of 2.86 Å are formed between Sb atoms on neighboring octahedra. The AuTlSb structure can be derived by doubling the AuSb₂ unit cell along one direction and replacing one half of the Sb-Sb pairs with Tl-Tl pairs. Since the pyrite structure ($\text{Pa}\bar{3}$) does not have a four-fold axis, doubling the cell reduces the symmetry to orthorhombic, and AuTlSb crystallizes in space group $\text{Pna}2_1$. In Figure 5.1, the network of corner sharing Au centered octahedra are

emphasized, while Figure 5.2 emphasizes the Sb-Sb and Tl-Tl dimers. The way in which the dimers are ordered along the b-axis in AuTlSb is responsible for the doubling of the AuSb₂ unit cell in this direction.

The coordination environments of Au(1) and Au(2) are shown in Figure 5.3. Each Au is bonded to three Tl atoms and three Sb atoms. The Au-Sb and Au-Tl distances are listed in Table 5.4, and are similar to those found in the literature: Au-Sb = 2.76 Å in AuSb₂ [11], Au-Tl = 2.87-3.25 Å in Au₂TlP₂ [15], and Au-Tl = 2.80-3.01 Å in Ba₂AuTl₇ [16]. Since the Au-Sb bonds are shorter than Au-Tl bonds, the Au centered octahedra are distorted significantly (Figure 5.3).

The interatomic distance in the Sb-Sb dimers found in AuTlSb is 2.848(3) Å. This is close to that found in AuSb₂ (2.86 Å) [11], and to the Sb-Sb distance in elemental Sb (2.91 Å) [17]. Similar distances are found in the Sb-Sb dimers in CdSb (2.81 Å) [18], NiSb₂ (2.86 Å) [19], and ZrSb₂ (2.88 Å) [20].

The Tl-Tl distance in the dimers in AuTlSb is 3.1463(17) Å. The next closest Tl-Tl contact is 3.5277(9) Å, longer than those found in Tl metal (3.41 - 3.46 Å) [21]. The only other example of a Tl-Tl dimer that we have found in the literature occurs in the compound Na₆TlSb₄, in which the Tl-Tl distance is 2.95 Å [5]. Similar Tl-Tl distances are also seen in the zigzag Tl chains in BaTl₂ (3.13-3.38 Å) [22], and in the 3-dimensional Tl-Au network in Ba₂AuTl₇ (3.03-3.51 Å) [16].

Calculated bond valences [23] for the Tl-Tl and Sb-Sb dimers in AuTlSb are 1.27 and 0.92 respectively, showing each to be nearly a single bond. For comparison, the bond valence for the Sb-Sb dimer in AuSb₂ is 0.90. The bonding in these two compounds will be explored further below.

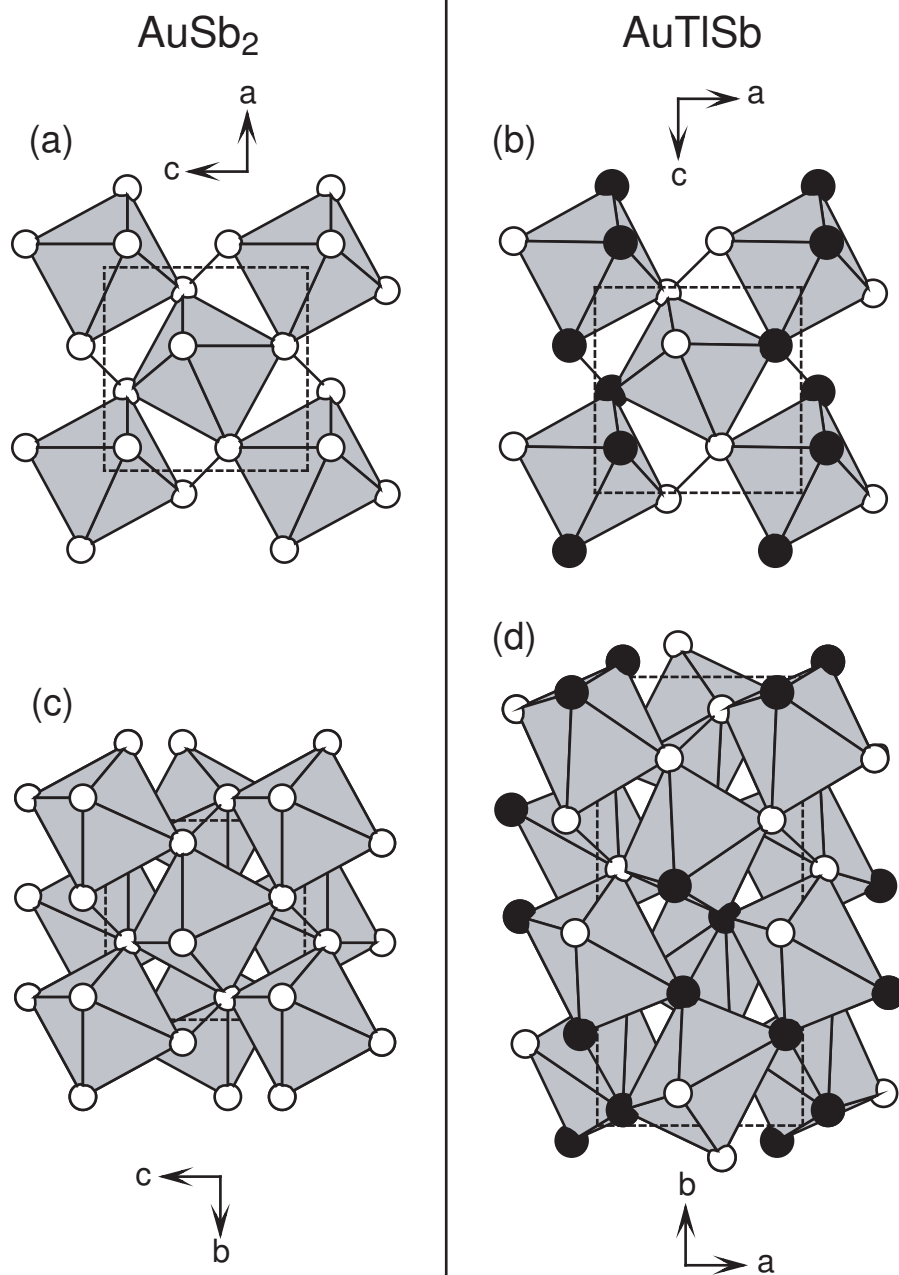


Figure 5.1: The crystal structures of AuSb_2 and AuTlSb . A single layer of octahedra is shown in (a) and (b). The stacking of these layers is shown in (c) and (d). Au is at the centers of the grey octahedra, Sb is shown as white circles and Tl as black circles. Dotted lines represent the unit cell edges. Bold lines show Sb-Sb and Tl-Tl bonds.

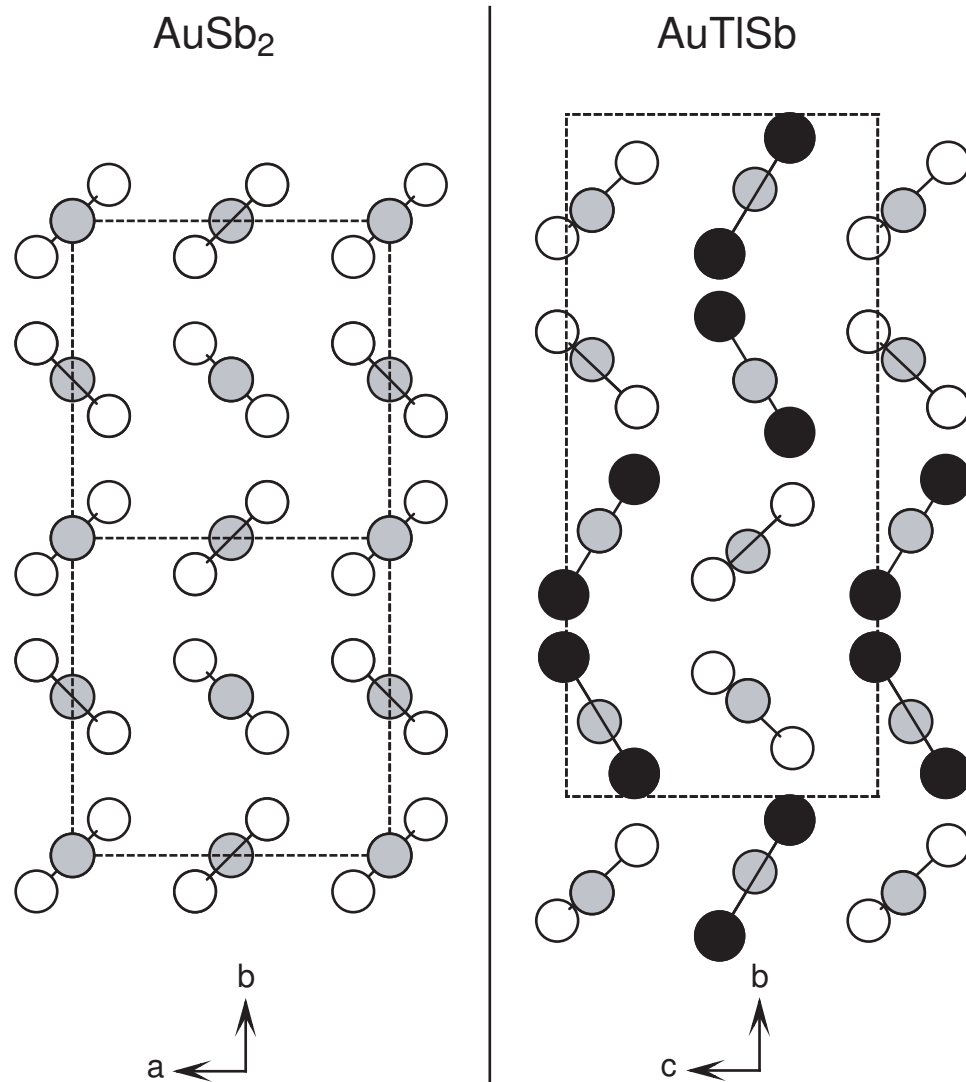


Figure 5.2: Views of the crystal structures of AuSb_2 and AuTlSb emphasizing the arrangement of the Sb-Sb and Tl-Tl dimers. Au is grey, Sb white, and Tl black. The dotted lines show the unit cell edges.

Table 5.4: Interatomic distances and average COHP values in AuTlSb and AuSb₂.

AuTlSb	distance (Å)	avg. COHP (eV)
Sb(1)-Sb(2)	2.848(3)	-14.04
Tl(1)-Tl(2)	3.1463(17)	-7.40
Au(1)-Sb(1)	2.706(3)	-8.84
	2.743(2)	-7.70
Au(1)-Sb(2)	2.701(3)	-9.00
Au(2)-Sb(1)	2.706(2)	-8.92
Au(2)-Sb(2)	2.751(2)	-8.06
	2.689(2)	-9.25
Au(1)-Tl(1)	2.9847(15)	-1.95
Au(1)-Tl(2)	2.8647(16)	-2.63
	2.9454(15)	-2.34
Au(2)-Tl(1)	2.8507(15)	-2.66
	2.8802(19)	-2.63
Au(2)-Tl(2)	2.9230(19)	-2.38
AuSb₂	distance (Å)	avg. COHP (eV)
Au(1)-Sb(1)	2.762	-7.26
Sb(1)-Sb(1)	2.860	-14.08

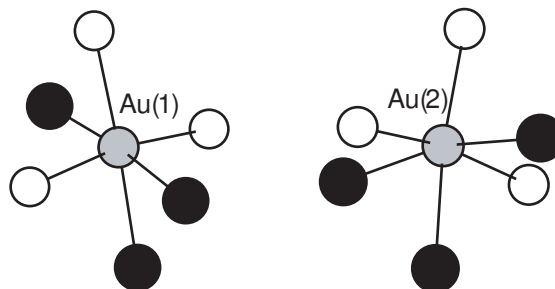


Figure 5.3: The coordination environments of the Au atoms (grey circles) in AuTlSb. Sb is white and Tl is black.

5.4 Electronic Structure and Bonding

Figure 5.4 shows the calculated band structure, density of states (DOS), and partial densities of states (PDOS), for AuTlSb. For comparison, Figure 5.5 shows the results of similar calculations on the parent structure AuSb₂. Both compounds are predicted to be metallic by these calculations, in agreement with experimental results (*vide infra*).

Although the calculated DOS for these two compounds is qualitatively similar near and below the Fermi level, there are significant differences between the calculated crystal orbital overlap populations (COOP), shown in Figure 5.6 and Figure 5.7 for AuTlSb and AuSb₂, respectively. Figure 5.7 shows that in AuSb₂ the Fermi level is situated such that some Au-Sb antibonding states are filled. Thus, the replacement of Sb by Tl (which has fewer valence electrons), should, in the rigid band approximation, stabilize the Au-Sb interactions. Indeed, Figure 5.6 shows that the Au-Sb interactions are optimized in AuTlSb. There is very little Sb-Sb interaction at and just below the Fermi level in AuSb₂. Thus it is expected that replacing Sb with Tl should have little influence on these interactions. However, it is not clear from the COOP curves how the Sb→Tl substitution affects the Sb-Sb interactions. The Sb-Sb curves in Figures 5.6 and 5.7 are qualitatively different near the Fermi level. This is due to a significant change in the

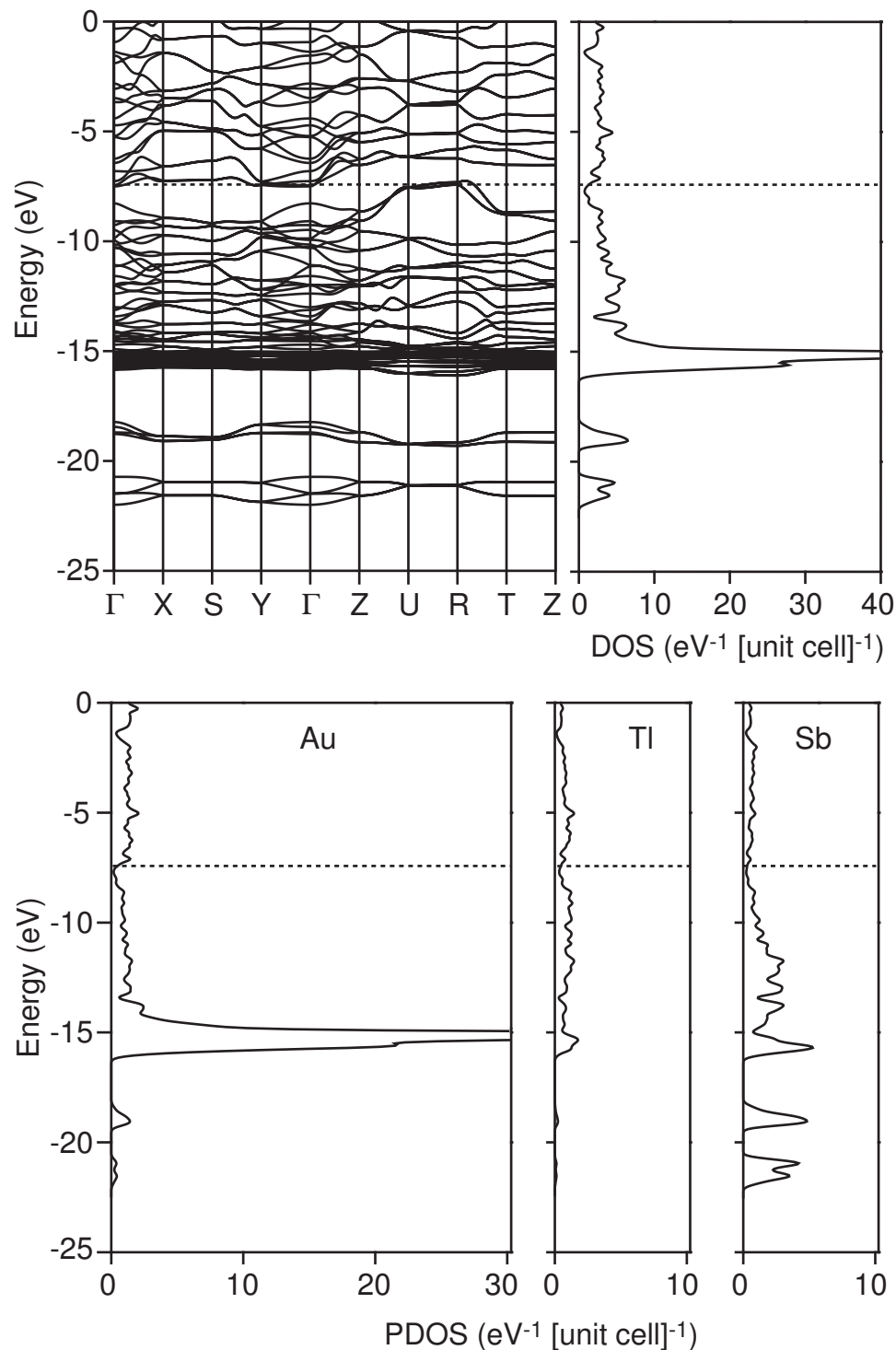


Figure 5.4: The calculated extended Hückel electronic structure of AuTiSb. The top two panels show the band structure and the total density of states (DOS) per unit cell. The bottom panels show the projected density of states (PDOS) for each element. The peak near -15 eV (the Au 5d bands) is truncated for clarity, and extends to approximately 75 on the horizontal axis.

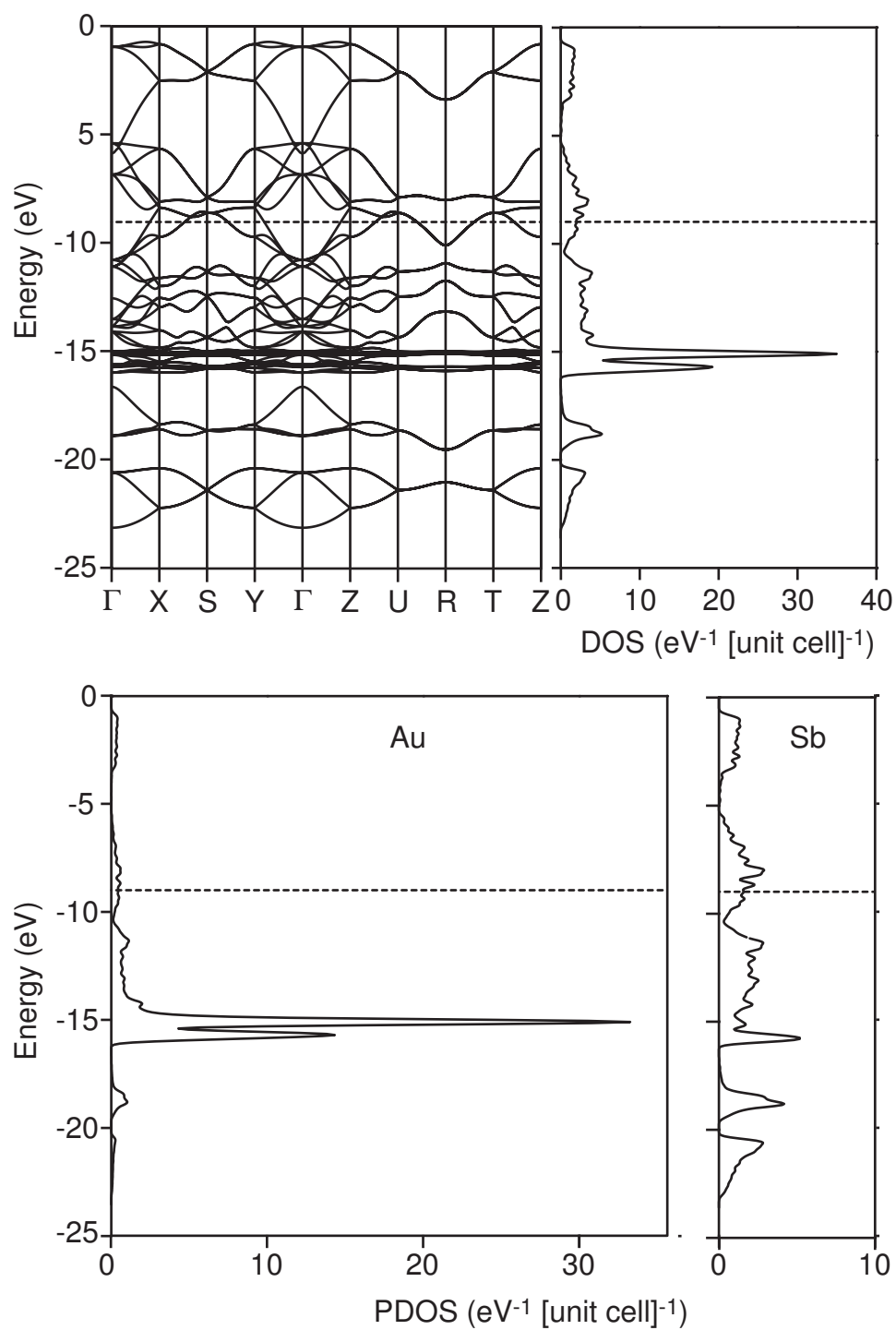


Figure 5.5: The calculated extended Hückel electronic structure of AuSb₂. The top two panels show the band structure and the total density of states (DOS) per unit cell. The bottom panels show the projected density of states (PDOS) for each element.

band structure that results when Tl is substituted for Sb (i.e. the failure of the rigid band model). However, absolute measures of the strengths of interactions can be obtained through crystal orbital Hamilton population (COHP) analysis. The average COHPs for each type of interaction in AuTlSb and AuSb₂ are listed in Table 5.4. These data show that the Sb-Sb interactions in AuTlSb are indeed similar in strength to those in AuSb₂. The average COHPs also indicate that the Au-Sb bonding is increased by the Sb→Tl substitution, in agreement with the above analysis of the COOP curves. Finally, the COOP curves (Figures 5.6 and 5.7) and the average COHP data (Table 5.4) show that there is significant Tl-Tl bonding in AuTlSb, and that the Au-Tl interactions are relatively weak.

Weak Au-Tl interactions suggest that it may be possible to describe this compound as a Zintl phase, with positively charged Tl donating electrons to a negatively charged Au-Sb framework. Indeed, the net charges on Tl(1) and Tl(2) determined from the extended Hückel calculations are +0.95 and +0.91, respectively. This is close to the normal valence of +1 for Tl. One could then assign oxidation states as (Au¹⁺)₂(Tl¹⁺)₂[Sb₂]⁴⁻. However, since Au is the most electronegative element in the compound, this assignment is questionable. Indeed, the extended Hückel calculations give a net charge of -0.56 and -0.63 for the Au atoms, and for the Sb atoms -0.33 and -0.35. This suggests that Tl reduces both Au and Sb in AuTlSb. In fact, the calculated net charges on Au and Sb in AuTlSb are reduced beyond the values calculated for AuSb₂ of -0.32 and +0.16, respectively. The difficulty in assigning formal oxidation states suggests that AuTlSb should be metallic. This is consistent with non-zero DOS at the Fermi level (Figure 5.4) and the transport measurements reported below.

We now return to the COOP curves for AuSb₂ shown in Figure 5.7. Inspection of these data and the DOS (Figure 5.5) shows that the bonding in AuSb₂ is maximized when $E_{Fermi} = -10.5$ eV, at the pseudogap in the DOS. This Fermi level

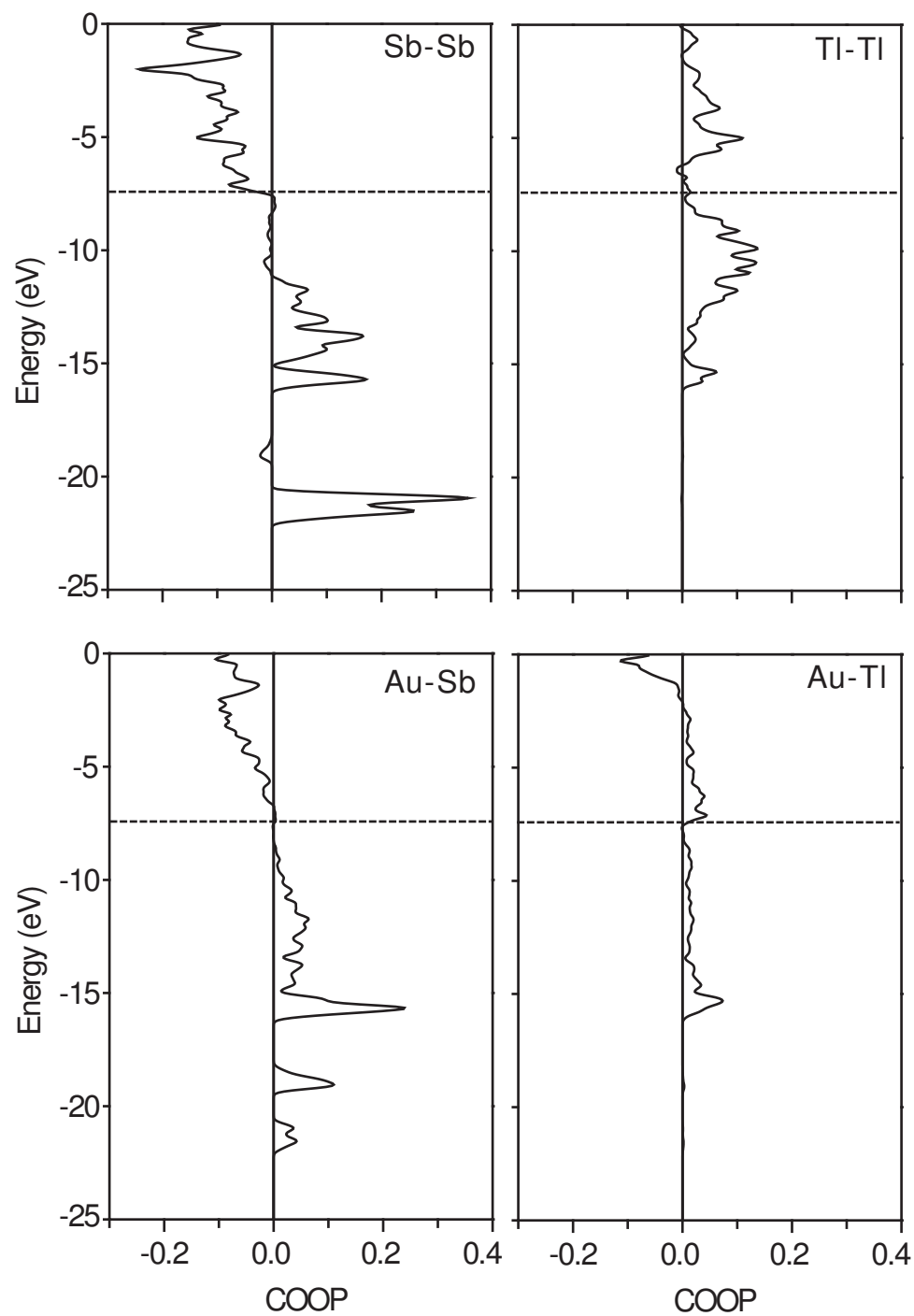


Figure 5.6: The calculated crystal orbital overlap populations (COOP) for the Sb-Sb, Tl-Tl, Au-Sb, and Au-Tl interactions in AuTlSb.

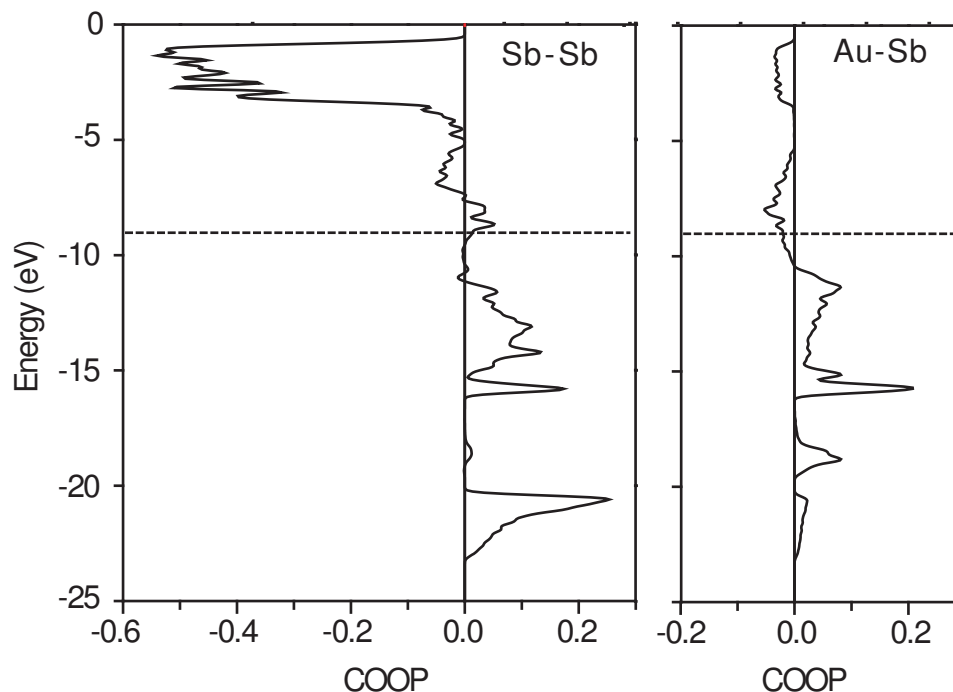


Figure 5.7: The calculated crystal orbital overlap populations (COOP) for the Sb-Sb and Au-Sb interactions in AuSb₂.

corresponds to 80 valence electrons per unit cell. AuSb₂ has four Au atoms and eight Sb atoms per primitive cubic unit cell, giving a total of 84 valence electrons. So, in the rigid band approximation, replacing one out of every four Sb atoms with Tl should optimize the interactions. This corresponds to the stoichiometry “Au₂TlSb₃”. However, Figure 5.6 shows that Au-Sb and Sb-Sb bonding is optimized in AuTlSb, which has one out of every two Sb atoms replaced by Tl. The rigid band approximation fails in this case, due to the dissimilar orbital parameters of Tl and Sb, and the differences in the crystal structures of the two compounds. Indeed, as noted above, the extended Hückel band structures of AuSb₂ and AuTlSb (Figures 5.4 and 5.5) are significantly different.

Since our calculations suggest the bonding in AuSb₂ can be further stabilized by decreasing the valence electron concentration, we have performed preliminary investigations into the substitution of In or Sn for Sb in this compound.

Attempts to make the In analog of AuTlSb produced, according to microprobe analysis, a mixture consisting primarily of Sb and a binary Au-In compound with an Au:In ratio of about 1:1. Most of the reflections observed by PXRD could be attributed to elemental Sb and the triclinic binary compound AuIn. However, a few peaks remain unidentified. Similar investigations with Sn showed that some Sn can be incorporated into the pyrite AuSb₂ structure. A loading of composition Au:Sn:Sb 1:1:1 produced a mixture of primarily two Au-Sn-Sb phases of approximate compositions 3:3:4 and 3:5:2. A few grains containing only Sn and Sb were also present. PXRD suggested that a large portion of the product forms the pyrite structure type with a unit cell ($V = 290.6 \text{ \AA}^3$) smaller than that of AuSb₂ ($V = 295.3 \text{ \AA}^3$). These results suggest that further investigation of the Au-Sn-Sb system is warranted.

5.5 Thermopower and Electrical Resistivity

The results of the resistivity ρ and thermopower S measurements on AuTlSb are shown in Figure 7.3. The nearly linear temperature dependence of ρ and S , and their small values, show this compound to be metallic, with conduction dominated by holes ($S > 0$) over most of the temperature range. The metallic behavior is in agreement with the electronic structure calculations described above (Figure 5.4). Similar measurements have shown AuSb₂ also to be metallic [24], as predicted by our calculations (Figure 5.5). For comparison, the reported thermopower of AuSb₂ is near $-0.5 \mu\text{V}/\text{K}$ over the temperature range investigated in this study, indicating n-type behavior. The reported resistivity increased linearly with increasing temperature from about $5 \mu\Omega\text{cm}$ to about $25 \mu\Omega\text{cm}$.

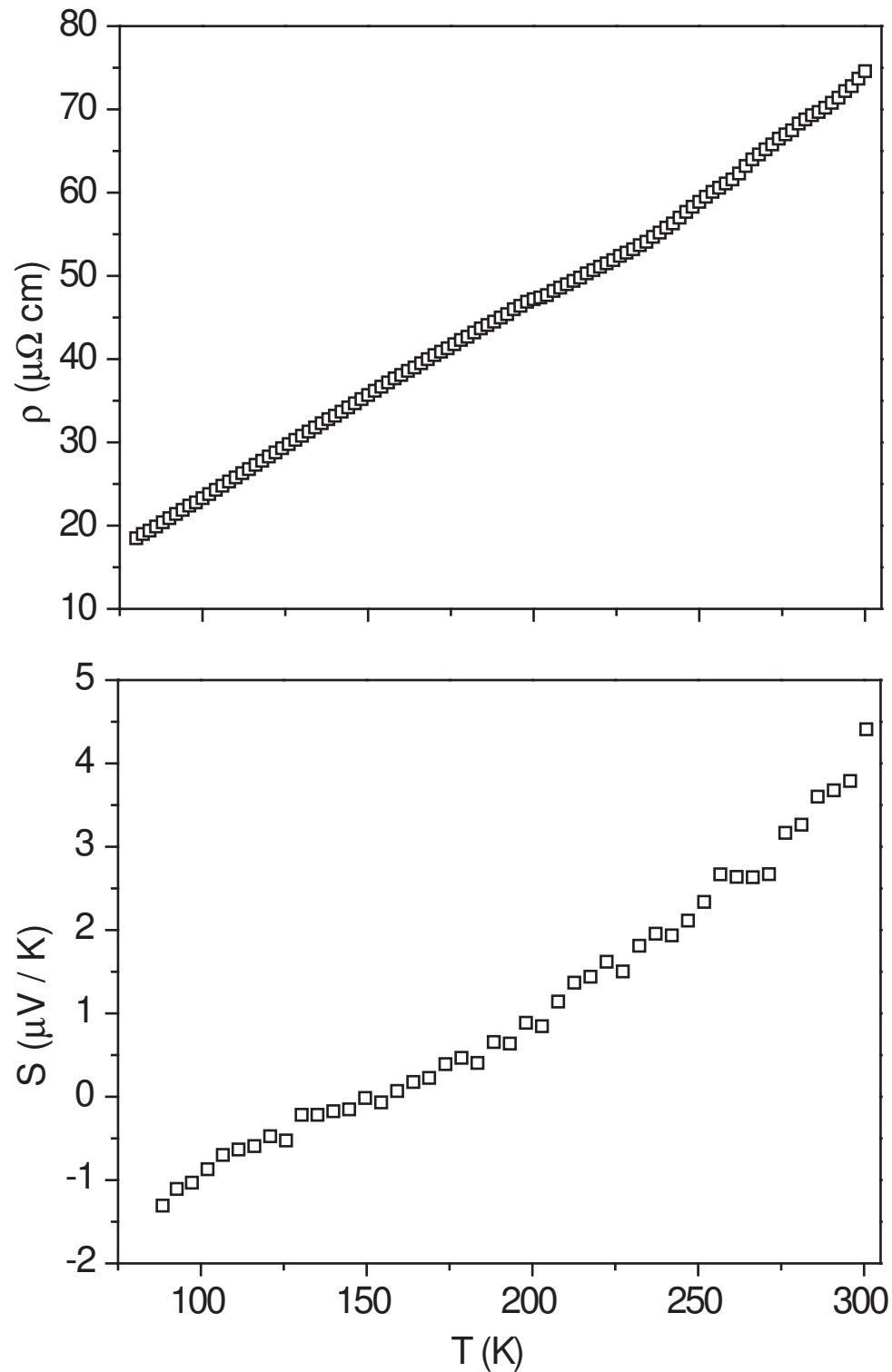


Figure 5.8: The measured electrical resistivity ρ and thermopower S of AuTiSb from 80 K to 300 K. The estimated uncertainty of these measurements is about 20% for ρ and about $\pm 1 \mu\text{V/K}$ for S (see text for details).

A subtle, but reproducible, “dip” is seen in the resistivity data (Figure 7.3) between 200 K and 275 K. We are unsure of the origin of this behavior. It could be a signature of a structural phase transition; however, we note that single crystal X-ray diffraction experiments showed that the AuTlSb unit cell is orthorhombic at room temperature, as well as at 175 K.

Since we were unable to prepare AuTlSb as a single phase bulk sample, thermal conductivity measurements were precluded. However, due to the very heavy atoms which make up this compound, we expect low lattice thermal conductivity. In any case, the thermopower is too low, and the electronic thermal conductivity κ_{el} (which is related to the electrical conductivity ρ through the Wiedemann-Franz law [25], $\kappa_{el}=L_0T\rho$ with $L_0=2.4\times 10^{-8}$ W Ω /K²) is too high, $\kappa_{el}(300\text{K})\approx 100$ mW/cmK, for TE applications.

5.6 Conclusions

The new ternary compound AuTlSb has been synthesized and characterized by X-ray structure determination, electronic structure calculations, and physical property measurements. This material crystallizes in a new structure type, which can be viewed as an ordered superstructure of the AuSb₂ (pyrite) structure, and contains singly bonded Tl-Tl dimers. Extended Hückel tight binding calculations predict that AuTlSb, like AuSb₂, is metallic. This is confirmed by temperature dependent electrical resistivity and thermopower measurements. As is true for most metallic materials, the thermopower is too low, and the electronic contribution to the thermal conductivity is too high, for AuTlSb to be utilized effectively for TE conversion. Attempts to make the In analog of AuTlSb were not successful. However, evidence for a pyrite type structure with some Sb replaced by Sn was seen.

REFERENCES

- [1] T. K. Reynolds, *Design, Synthesis, and Characterization of New Materials for Thermoelectric Applications*, PhD thesis, Cornell University, 2003.
- [2] T. K. Reynolds, M. A. McGuire, and F. J. DiSalvo, *J. Solid State Chem.* **177**, 3038 (2004).
- [3] S. Kaskel and J. D. Corbett, *Inorg. Chem.* **39**, 3086 (2000).
- [4] Z.-C. Dong and J. D. Corbett, *J. Am. Chem. Soc.* **117**, 6447 (1995).
- [5] B. Li, L. Chi, and J. D. Corbett, *Inorg. Chem.* **42**, 3036 (2003).
- [6] J. Mueller and U. Zachwieja, *Z. Anorg. Allg. Chem.* **662**, 635 (1996).
- [7] SMART and SAINT: Data collection and processing software for the SMART system, Bruker Analytical X-ray Instruments, Inc., Madison, WI, 1995.
- [8] SADABS program for absorption correction, G.M. Sheldrick for Bruker Analytical X-ray Instruments, Inc., Madison, WI, 2000.
- [9] XPREP program for determination of space groups, Bruker Analytical X-ray Instruments, Inc., Madison, WI, 2000.
- [10] L. Farrugia, *J. Appl. Cryst.* **32**, 837 (1999).
- [11] S. Furuseth, K. Selte, and A. Kjekshusa, *Acta. Chem. Scandinavica* **19**, 735 (1965).
- [12] R. Shockhuizen, C. Chieh, and W. B. Pearson, *Can. J. Phys.* **55**, 472 (1973).
- [13] E. A. Owen and E. L. Yates, *Phil. Mag.* **15**, 472 (1933).
- [14] YAeHMOP (Version 3.0), G. Landrum, <http://yaehmop.sourceforge.net>, 1999.
- [15] M. Eschen and W. Jeitschko, *J. Solid State Chem.* **165**, 238 (2002).
- [16] S.-F. Liu and J. D. Corbett, *Inorg. Chem.* **43**, 2471 (2003).
- [17] C. S. Barrett, P. Cucka, and K. Haefner, *Acta Cryst.* **16**, 451 (1963).
- [18] K. E. Almin, *Acta Chem. Scandinavica* **2**, 400 (1948).
- [19] H. Holseth and A. Kjekshus, *Acta Chem. Scandinavica* **22**, 3284 (1968).
- [20] A. Kjekshus, *Acta Chem. Scandinavica* **5**, 64 (1972).
- [21] H. Lipso and A. R. Stokes, *Nature* **148**, 437 (1941).

- [22] A. Iandelli, *Z. Anorg. Allg. Chem.* **330**, 221 (1964).
- [23] M. O'Keeffe and N. Brese, *J. Am. Chem. Soc.* **113**, 3226 (1991).
- [24] W. B. Pearson, *Can. J. Phys.* **42**, 519 (1964).
- [25] N. W. Ashcroft and N. D. Mermin, *Solid State Physics*, Saunders College, 1st edition, 1976.

Chapter 6

Chevrel Phase Thermoelectric Materials

In 1971, R. Chevrel, M. Sergent, and J. Prignet reported the preparation of a series of ternary molybdenum sulfides of the form $M_xMo_nS_{n+1}$ where $M = Ag, Sn, Ca, Sr, Pb, Ba, Ni, Co, Fe, Cr, Mn, Cu, Mg, Zn, Cd$, and $2 \leq n \leq 6$ [1]. These materials have since been termed “Chevrel phases”. The first occurrence of the name Chevrel phase seems to have been in 1976. Soon after their discovery, superconductivity was observed in this class of compounds in 1972 [2]. Most Chevrel phase publications were produced in the 1980s, primarily motivated by the high superconducting transition temperatures (up to 15 K in $PbMo_6S_8$), high superconducting critical fields (up to 60 T in $PbMo_6S_8$), and coexistence of superconductivity and long range magnetic order (in rare earth containing Chevrel phases). Reviews of the structural and superconducting properties of these compounds were published in 1982 [3, 4].

Interest in Chevrel phases as TE materials began in 1997-1998, when promising TE properties were observed in the semiconducting phase $Mo_2Re_4Se_8$ by Caillat and Fleurial [5]. In this Chapter, we will discuss the structure and composition of Chevrel phases, their electronic structure and what is known about their TE properties. We will then present some of the work that has been performed at Cornell on Chevrel phase high temperature thermoelectric materials.

6.1 Structure and Chemistry of Chevrel Phases

The Chevrel phase structure shows remarkable versatility regarding chemical substitutions and intercalations. Some of the many known Chevrel phase compositions will be reviewed here. Consideration will be limited those

phases based on the pseudo-cubic M_6Q_8 cluster. This cluster is made up of an octahedral M_6 unit which is face capped by eight Q atoms. It can also be viewed as an Q_8 cube with M atoms on each of the six faces. Views of the M_6Q_8 cluster are shown in Figure 6.1. In extended Chevrel phase structures the cluster does not have cubic symmetry, but is trigonally distorted, stretched or compressed along the 3-fold axis of the cube. The cluster can then be viewed as a stack of two M_3Q_3 triangular units capped by Q atoms. This is also shown in Figure 6.1. More than two M_3Q_3 can occur in the stacks, giving clusters like M_9Q_{11} . Compounds containing such clusters will not be considered here.

Before discussing the multitude of compositions which adopt the M_6Q_8 based Chevrel phase structure, we will describe briefly the common framework made up of the clusters through intercluster bonding. These compounds usually crystallize in the rhombohedral space group $R\bar{3}$, however in some instances the symmetry is reduced to triclinic ($P\bar{1}$). Typical rhombohedral unit cell parameters are $a_R \approx 7 \text{ \AA}$ and $\alpha_R \approx 90^\circ$. Each unit cell contains one M_6Q_8 cluster. Each cluster is rotated about its 3-fold axis (which it shares with the unit cell) by about 20° . This rotation allows six of the Q atoms on one cluster to bond to M atoms of clusters in neighboring unit cells. The rotation of the cluster relative to the unit cell, and the resulting 3-D network is shown in Figure 6.2.

The manner in which the cluster units pack leaves large, interconnected cavities or channels throughout the structure. Often the literature refers to these as cavities 1, 2, and 3. They are shown in Figure 6.3. Cavity 1 is the largest and is centered at the unit cell origin. It is surrounded by eight Q atoms one from the corner of each of the eight neighboring clusters. Large atoms like Pb often occupy cavity 1, or sometimes disordered arrangements of small cations like Cu. Cavity 2 is smaller than cavity 1, and is located between the edges of four neighboring clusters. It is also surrounded by eight Q atoms, two from each

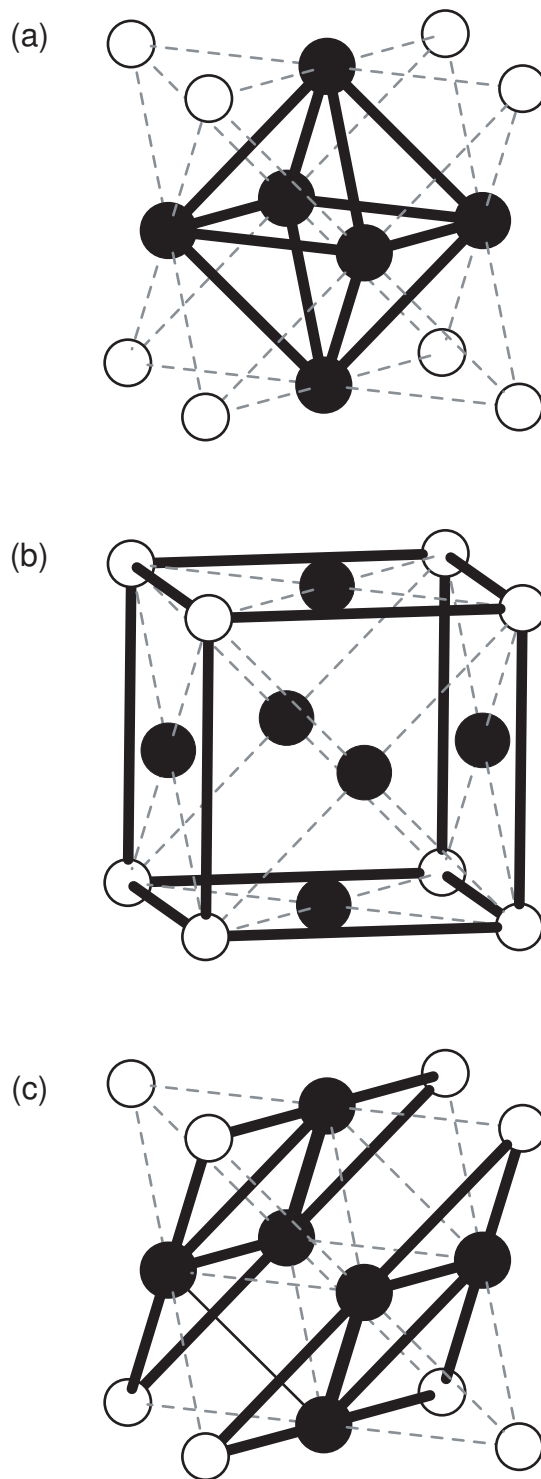


Figure 6.1: Three views of the M_6Q_8 cluster. M is shown as black circles and Q as white circles. In (a) the M_6 octahedron face capped by Q is emphasized. In (b) the Q_8 cube with M on the faces is emphasized. In (c) the cluster is viewed as a stack of M_3Q_3 triangles capped by Q atoms.

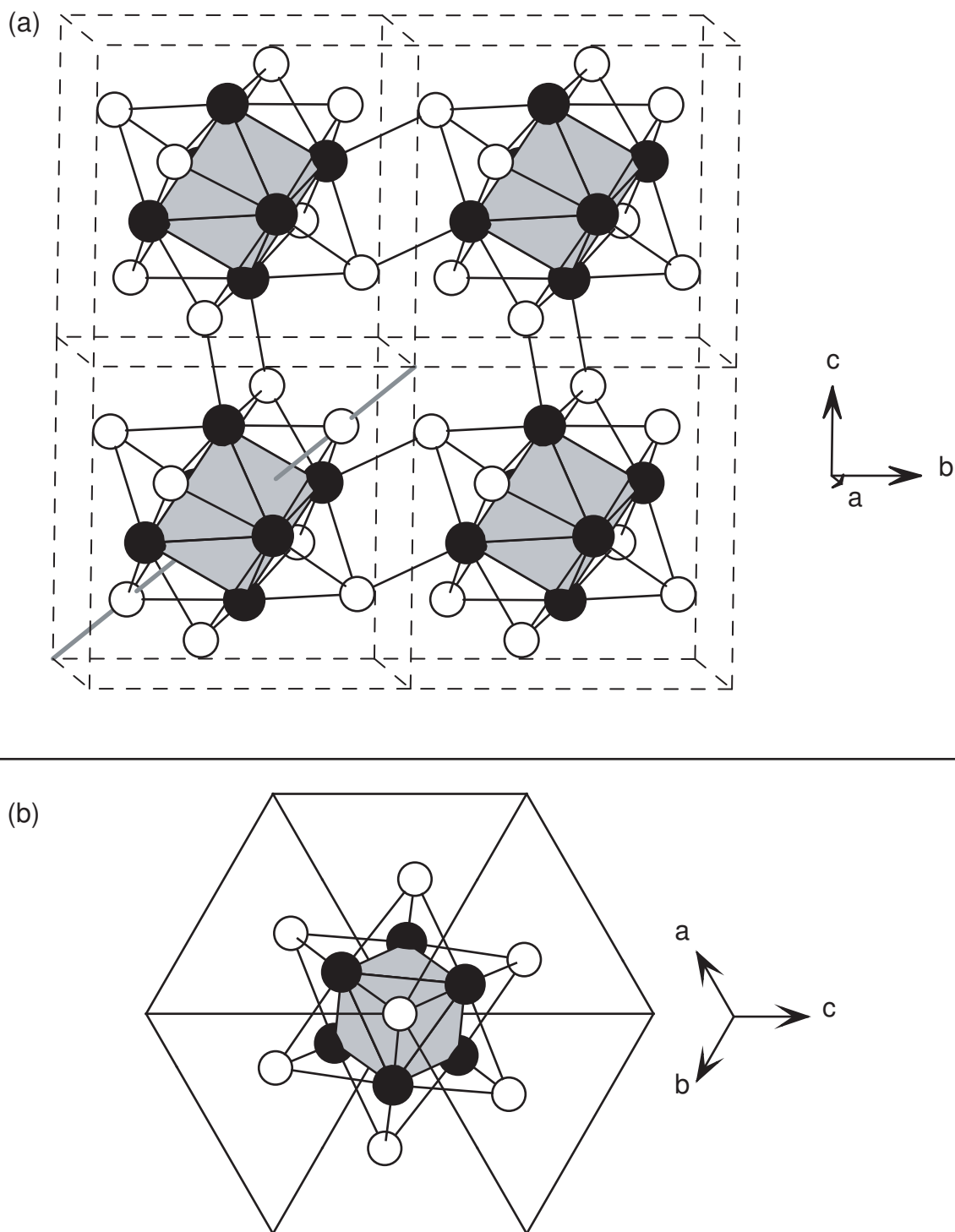


Figure 6.2: (a) A portion of the network made up by intercluster M–Q bonding in Chevrel phases. The dashed lines are the unit cell edges, M is black, and Q is white. In one unit cell, the 3-fold axis is shown as a grey line. (b) A view down the 3-fold axis of a unit cell, showing the rotation of the M_6Q_8 cluster.

of the four clusters. Small cations often reside in cavity 2, like Ti, Ni, and other 3d transition elements. Cavity 3 is the smallest cavity, and probably shouldn't be considered a cavity at all, since no atoms are known to reside there. It is the space between the faces of two neighboring clusters, made up of eight Q atoms, four from each cluster. There are two M–Q bonds that pass through cavity 3 (6.3), which is probably why no intercalant atoms inhabit it.

6.1.1 Mo_6Q_8 compounds (Q = S, Se, Te)

The binary compounds Mo_6S_8 , Mo_6Se_8 , and Mo_6Te_8 are all known to exist. Solid solutions between them are also known. The most interesting feature of these compounds is the self-intercalation of Mo into the cavities. This has been well documented by Belin et al. in the sulfide-selenide solid solution series [6, 7]. They found that there are three types of $\text{Mo}_6\text{Se}_{8-x}\text{S}_x$ compounds (abbreviated Mo_6Q_8 here for brevity): the high temperature or HT-phases and the α - and β -phases. We will describe each of these phase here, but will not give detailed discussions of their structures.

The HT series are made by reacting $(6)\text{Mo} + (8-x)\text{Se} + (x)\text{S}$ at high temperature (around 1200 °C). The product of this reaction contains HT- Mo_6Q_8 and MoSe_2 . The authors found that the HT-phases have Mo (up to about one atom per unit cell) intercalated into the cavities of the Mo_6Q_8 framework, and thus explained the formation of the Mo-poorer second phase MoQ_2 . The same reactions with a slight excess of Mo (0.3 excess Mo per formula unit) gave single phase HT- Mo_6Q_8 . Single crystal studies showed that the “self-intercalated” Mo resides in cavity 2.

The α -phases are “pure” Mo_6Q_8 with no intercalated Mo. These are obtained by first forming a filled phase like $\text{Cu}_2\text{Mo}_6\text{Q}_8$ and then removing the guest

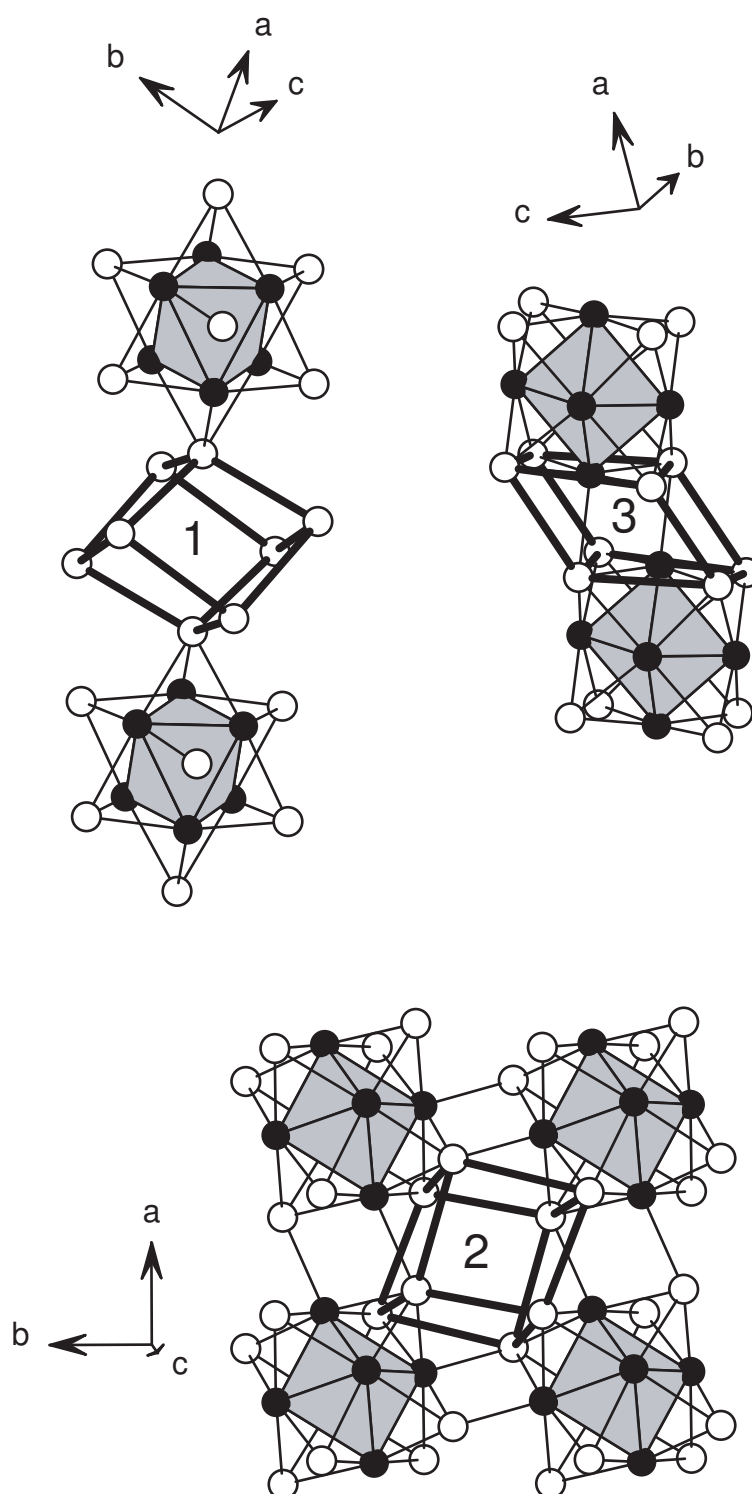


Figure 6.3: The three cavities in the Chevrel phase structure. M is black and Q is white. Bold lines outline the cavities and do not represent bonds.

atoms. Deintercalation of Cu can be achieved by reaction with Iodine dissolved in acetonitrile [8]. Iodine reacts with Cu ions at the surface of the material and forms CuI which is soluble in acetonitrile. The mobility of Cu ions in the Chevrel phases allows this reaction to readily occur to completion at room temperature. The α -phase is metastable.

Finally, the β -phases are obtained by heating the α -phases to intermediate temperatures (400–800°C). Like the HT-phase, the β phase has Mo intercalated into the cavities, and the transformation is from the α -phase to the β -phase plus MoQ₂. In these compounds, the self-intercalated Mo atoms are disordered over a set of six sites which form an octahedron inside of cavity 1.

These three Mo₆Q₈ phases can be distinguished by comparison of unit cell parameters. In particular, the rhombohedral angle is quite sensitive to the presence and location of intercalant atoms. The end members Mo₆Se₈ and Mo₆S₈, and the telluride analogue Mo₆Te₈ behave somewhat differently. There is no mention of Mo self-intercalation into Mo₆Te₈. In fact, this material can be made from the elements as a single phase by heating at 1000 °C. This is in contrast to Mo₆Se₈, which, when made from the elements by heating at high temperature, forms a HT phase plus MoSe₂. The sulfide compound can not be made in any form by reaction of the elements. The reason for these differences may lie in the electronegativity of the anions and the stability of the Mo₆ octahedron. The electronegativity of the Q atom will determine the oxidation state of the Mo atoms in the cluster. For example, in the limit of very high electronegativity, the charge on the Q atom will be its formal charge of -2. This gives each Mo atom in the cluster a charge of +2.67. As the Q atoms become less electronegative, their valence state becomes Q^{-2+ δ} , and they withdraw fewer electrons from the cluster core. This lowers the charge on the Mo ions. It may be that there is a maximum Mo valence state for which the cluster is stable. The least electronegative Q, Te, may with-

draw few enough electrons to allow a stable Mo_6 cluster to form, while the more electronegative Se withdraws too many, which can be compensated by the self-intercalation of some Mo cations into the channels. The most electronegative Q, S, may withdraw enough electrons from the cluster core to require a significant amount of intercalant to be added to stabilize the phase.

It has become clear in the discussion of the “unfilled” phases above that the filling of the cavities by intercalant atoms is an important part of Chevrel phase chemistry. Next we will review some of the wide variety of intercalated compositions that have been realized in these compounds.

6.1.2 Filled compounds of the type $\text{A}_x\text{Mo}_6\text{Q}_8$

Figure 6.4 shows the elements which are known to occupy the cavities in Chevrel phases described above. This list was compiled using the Inorganic Crystal Structure Database (ICSD) and by searching the literature using Scifinder Scholar. Some of these are known only for either $\text{Q} = \text{S}$ or $\text{Q} = \text{Se}$, and some are known for both. The number of A atoms per unit cell varies with different elements. Large A (like Pb) sit at the unit cell origin, and the maximum filling is one per unit cell. Often fillings of less than one are seen. When the A atoms are small (like Cu), they often occupy disordered sites surrounding the unit cell origin, and filling fractions in excess of one are common. For example, it is possible to add up to four Li or Cu atoms per unit cell [9, 10]. In some cases, particularly when the A atom is a transition metal that occupies cavity 2, the symmetry of the structure is decreased from rhombohedral to triclinic (space group $\text{P}\bar{1}$) [3]. This is due to ordering of the A atoms in the cavities. Examples of three different A atom positions are illustrated in Figure 6.5.

H																	He
Li	Be											B	C	N	O	F	Ne
Na	Mg											Al	Si	P	S	Cl	Ar
K	Ca	Sc	Ti	V	Cr	Mn	Fe	Co	Ni	Cu	Zn	Ga	Ge	As	Se	Br	Kr
Rb	Sr	Y	Zr	Nb	Mo	Tc	Ru	Rh	Pd	Ag	Cd	In	Sn	Sb	Te	I	Xe
Cs	Ba	La	Hf	Ta	W	Re	Os	Ir	Pt	Au	Hg	Tl	Pb	Bi	Po	At	Rn
Fr	Ra	Ac															

Ce	Pr	Nd	Pm	Sm	Eu	Gd	Tb	Dy	Ho	Er	Tm	Yb	Lu
Th	Pa	U	Np	Pu	Am	Cm	Bk	Cf	Es	Fm	Md	No	Lr

Figure 6.4: The periodic table. Shaded boxes represent elements that are known to occupy the cavities in Chevrel phases. Light grey elements occupy the site at the origin in cavity 1, medium grey elements occupy disordered sites around the origin in cavity 1, and dark grey elements occupy disordered sites in cavity 2.

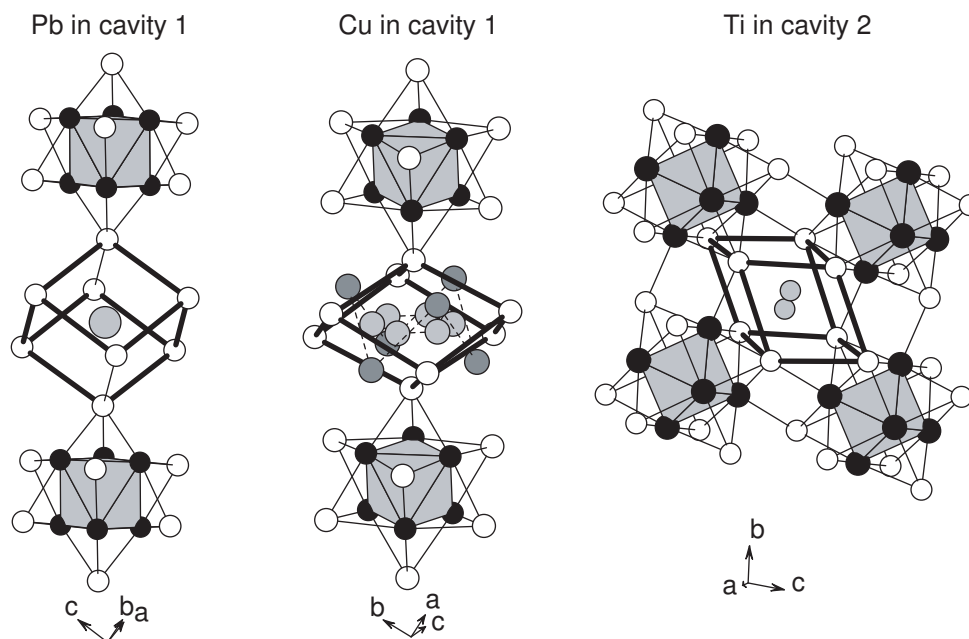


Figure 6.5: Three examples of different locations of the filling atom A in Chevrel phases. The Pb and Cu case retain rhombohedral symmetry, while the Ti compound is triclinic. Bold and dotted lines which outline the cavities and connect the Cu atoms in the inner (light grey) and outer (medium grey) rings are there just to highlight structural features, and do not necessarily represent chemical bonds.

To synthesize filled Chevrel phases, the filling element can sometimes be added directly to the reaction mixture. Alternatively, lower temperature techniques are also used. Elements with higher vapor pressures, like the low melting elements In, Tl, and Hg, can be added by mixing them with the unfilled Chevrel phase and heating at intermediate temperatures (near 500 °C) [11]. In addition, several groups have used electrochemical cells for intercalating various filling atoms into these compounds (including Li [9, 12, 13, 14], Mg [9], Na [15], Zn [15], Cd [15], Cu [13, 10]). We have developed another low temperature method, which will be described in a later Chapter. As mentioned above, filled phases are often synthesized at high temperature and then used to obtain unfilled (α -phase) Mo_6Q_8 through deintercalation.

The versatility of the Chevrel phase structure is demonstrated by the variety of filling atoms shown in Figure 6.4. The solid state chemistry of these materials is made even richer by the possibility of substitutions of other elements for Mo in the cluster core. These types of materials will be reviewed briefly next.

6.1.3 Cluster core substitutions: $\text{Mo}_{6-x}\text{M}_x\text{Q}_8$

Substitution of other transition metals for Mo in the cluster core have been observed in the sulfide, selenide, and telluride Chevrel phases. Elements for which mixed metal clusters (with Mo) are known include Ru, Re, and Rh [16, 17]. The structure retains its rhombohedral symmetry when these substitution are made. Since there is only one cluster metal crystallographic site (Wyckoff position 6f), this means that the mixing is random. Any ordering on the cluster metal sites would lower the symmetry of the cluster and the crystal. The maximum number of Mo atoms that have been replaced on each cluster are 1.33 for Rh, 2 for Ru, and 4 for Re. We will see later when discussing the electronic struc-

ture of Chevrel phases that the origin of these limits is electronic in nature. Other than work done recently in the DiSalvo group, there has been little study of compounds that have both filling atoms and mixed metal clusters. The only reference to these types of compounds found in the literature is a study of Li insertion in to partially Ru substituted compounds [18].

6.1.4 Substitutions on the Q sites: $\text{Mo}_6\text{Q}_{8-y}\text{X}_y$

Several researchers have studied the substitution of other elements for S, Se, or Te in Chevrel phases, in particular halogens and oxygen. There are two crystallographically distinct Q sites, one at 2c and one at 6f, so ordering of substituted atoms may occur and in fact has been observed. For example, the compounds $\text{Mo}_6\text{S}_6\text{Y}_2$ exist for $\text{Y} = \text{Br}$ and I [4]. In these two materials, the halogen atoms occupy the two 2c sites (on the 3-fold axis) and S occupies the six 6f sites. Partial filling of these halogen substituted phases has also been demonstrated, in particular with Cu [4].

Oxygen can replace some of the Q atoms in Chevrel phases [19, 20, 21], and is probably always present to some degree in samples synthesized in silica tubes at high temperature. At 1200 °C the vapor pressure of the gaseous species SiO and O_2 over silica is expected to be on the order of 10^{-6} torr [22].

6.2 Chevrel phase compounds as thermoelectric materials

Work on Chevrel phases in the DiSalvo group at Cornell has been focussed mainly on their use as TE materials. Here we will review what is known regarding Chevrel phase TE materials, both theoretical and experimental.

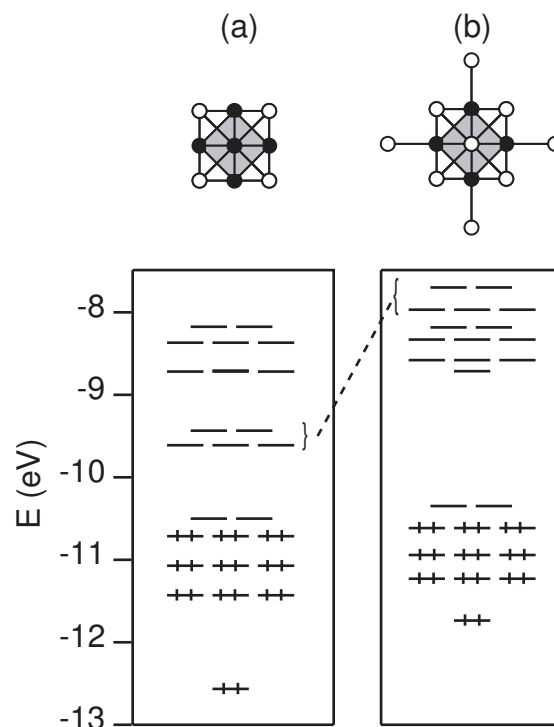


Figure 6.6: The calculated MO's for (a) a neutral Mo_6Se_8 cluster and (b) the same cluster with capping Se atoms. Note the large HOMO–LUMO gap for the cluster of charge -4 in (b).

6.2.1 Electronic structure of Chevrel phases

The compounds Mo_6Q_8 ($\text{Q} = \text{S}, \text{Se}, \text{Te}$) are metallic, while the compounds $\text{Mo}_4\text{Ru}_2\text{Se}_8$, $\text{Mo}_2\text{Re}_4\text{Se}_8$, and $\text{Mo}_2\text{Re}_4\text{S}_8$ are semiconductors. The extra valence electrons of Ru and Re fill the M_6Q_8 conduction band up to a gap in the density of states. It has been demonstrated by Hughbanks and Hoffmann that the origin of this gap can be traced back to the molecular orbitals (MO's) of the Mo_6Q_8 cluster unit [23].

The MO's calculated for a neutral Mo_6Se_8 cluster are shown in Figure 8.9. These were calculated using the program YAeHMOP [24]. Also shown is how the MO's change when the Mo atoms are capped by six Se atoms (as in the extended structure, where the clusters rotate to form bonds between their Mo atoms and Se

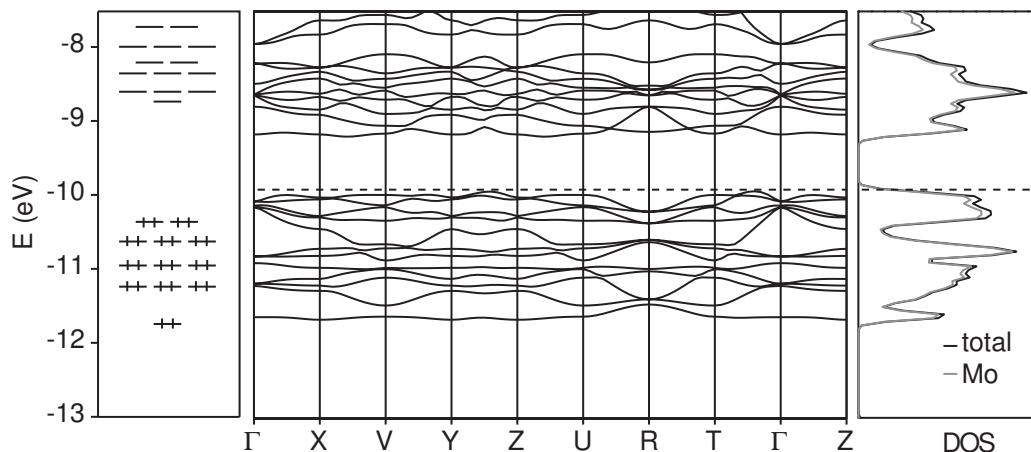


Figure 6.7: The calculated (extended Hückel) band structure and relative density of states (DOS) for Mo_6Se_8 . The dashed line shows the Fermi level for the 4-cluster.

atoms on neighboring clusters). A large gap between the highest occupied MO (HOMO) and the lowest unoccupied MO (LUMO) exists for the cluster of charge -4 (Figure 8.9. It is this HOMO–LUMO gap that evolves into the band gap of the extended structure. Figure 6.7 shows the extended Hückel band structure and density of states (DOS) for the Chevrel phase Mo_6Se_8 . Both the total DOS and the Mo projection are shown. Note the the states around the gap are primarily Mo-4d based. The dashed line shows the Fermi level for the case in which four electrons have been added to each neutral unit cell. The semiconducting Chevrel phases listed above each have four more valence electrons than Mo_6Se_8 , consistent with these calculations which show the presence of a band gap at the Fermi level for this case.

Several authors have used density functional theory (DFT) to calculate the band structure for filled Chevrel phases, usually with TE applications in mind. It has been noted that filling atoms and cluster core substitutions can significantly change the band structure near the Fermi surface [25], but the gap above

Mo-4d states remains. These calculations predict $\text{Cu}_4\text{Mo}_6\text{Se}_8$, $\text{Li}_4\text{Mo}_6\text{Se}_8$, and $\text{Zn}_2\text{Mo}_6\text{Se}_8$ to be semiconductors [25, 26].

It is often useful to refer to the number of valence electrons in these compounds. The importance of this information is demonstrated by the evolution of these materials from metals (often superconductors) to semiconductors as this number increases. This is sometimes referred to in the literature as the “valence electron count” or “valence electron concentration” abbreviated VEC, and is defined in different ways. Some authors refer to the total number of valence electrons per cluster. For the neutral cluster this is 20, since each of the six Mo brings along six valence electron and the eight formally 2- Q’s extracts a total of 16. Sometimes it is only the number of electrons beyond this neutral case that is quoted, i.e. the number of “extra” electrons. In addition, sometimes the total number of valence electrons is quoted per Mo atom, giving 3.33 for the neutral cluster. Since the conduction bands of Mo_6Q_8 have room for four more electrons, the ranges for these values are: 20–24 valence electrons per cluster, 0–4 extra valence electrons per cluster, and 3.33–4 valence electrons per Mo. The value that these numbers take for a particular Chevrel phases depends on the number of filling atoms and their valence states (how many electrons they each give to the cluster), and the number of substituted cluster core atoms and how many valence electrons they have. Here we will use VEC to refer to the number of valence electrons per octahedral metal cluster, for example 20 for Mo_6Se_8 , 22 for PbMo_6Se_8 , and 24 for $\text{Mo}_4\text{Ru}_2\text{Se}_8$.

6.2.2 Thermoelectric properties of Chevrel phase compounds

Most of the experimental investigations of the TE properties of Chevrel phases have been carried out by Caillat, Fluerial, and Snyder at NASA’s Jet

Propulsion Laboratory (JPL). One exception is Kurosaki et al. who investigated solid solutions of Mo_6Te_8 and Mo_6S_8 , and found them to be metallic with low thermopower, as expected [27]. The JPL group has identified several interesting Chevrel phase TE materials, including Mo_6Se_8 filled with Ti and Cu [28], and $\text{Mo}_2\text{Re}_4\text{Se}_8$ [5]. Their motivation for studying these compounds is from a need for new p-type TE materials for use at high temperatures in radioisotope TE generators (RTG's) used by NASA to power space probes. Their work is summarized in Ref. [28], and will be reviewed here.

In this paper, the properties of phases filled with Fe, Cu, and Ti reported, and compared to those of unfilled Mo_6Se_8 and the previously reported data for $\text{Mo}_2\text{Re}_4\text{Se}_8$ [5]. The samples were made by mixing the elements in a ball mill and then reacting them in silica tubes at 1200 °C for two days, with two subsequent grinding and anneals under the same conditions. The samples were then hot-pressed at 850-1000 °C and 20,000 psi for two hours under argon. The target compositions were the VEC = 24 compounds “ $\text{Cu}_4\text{Mo}_6\text{Se}_8$ ”, “ $\text{Cu}_2\text{FeMo}_6\text{Se}_8$ ”, and “ TiMo_6Se_8 ”, assuming valence states of Cu^{1+} , Fe^{2+} , and Ti^{4+} . The sample compositions were measured by electron microprobe analysis, giving $\text{Cu}_{3.1}\text{Mo}_6\text{Se}_8$ (VEC = 23.1), $\text{Cu}_{1.38}\text{Fe}_{0.66}\text{Mo}_6\text{Se}_8$ (VEC = 22.7), and $\text{Ti}_{0.9}\text{Mo}_6\text{Se}_8$ (VEC = 23.6). Accordingly, the Cu and Cu/Fe filled samples showed semimetallic behavior with carrier concentrations $n \approx 9 \times 10^{21} / \text{cm}^3$. Interestingly, the Ti filled phase ($n = 2 \times 10^{21} / \text{cm}^3$) showed semiconducting behavior (ρ decreased as T increased), even though it was not fully filled. The measured TE properties are shown in Figure 6.8.

The unfilled phase Mo_6Se_8 has properties expected for poor metals or semimetals: low S and moderately low ρ . It has intermediate thermal conductivity. It is about 5 times that of state of the art TE materials, and about half that

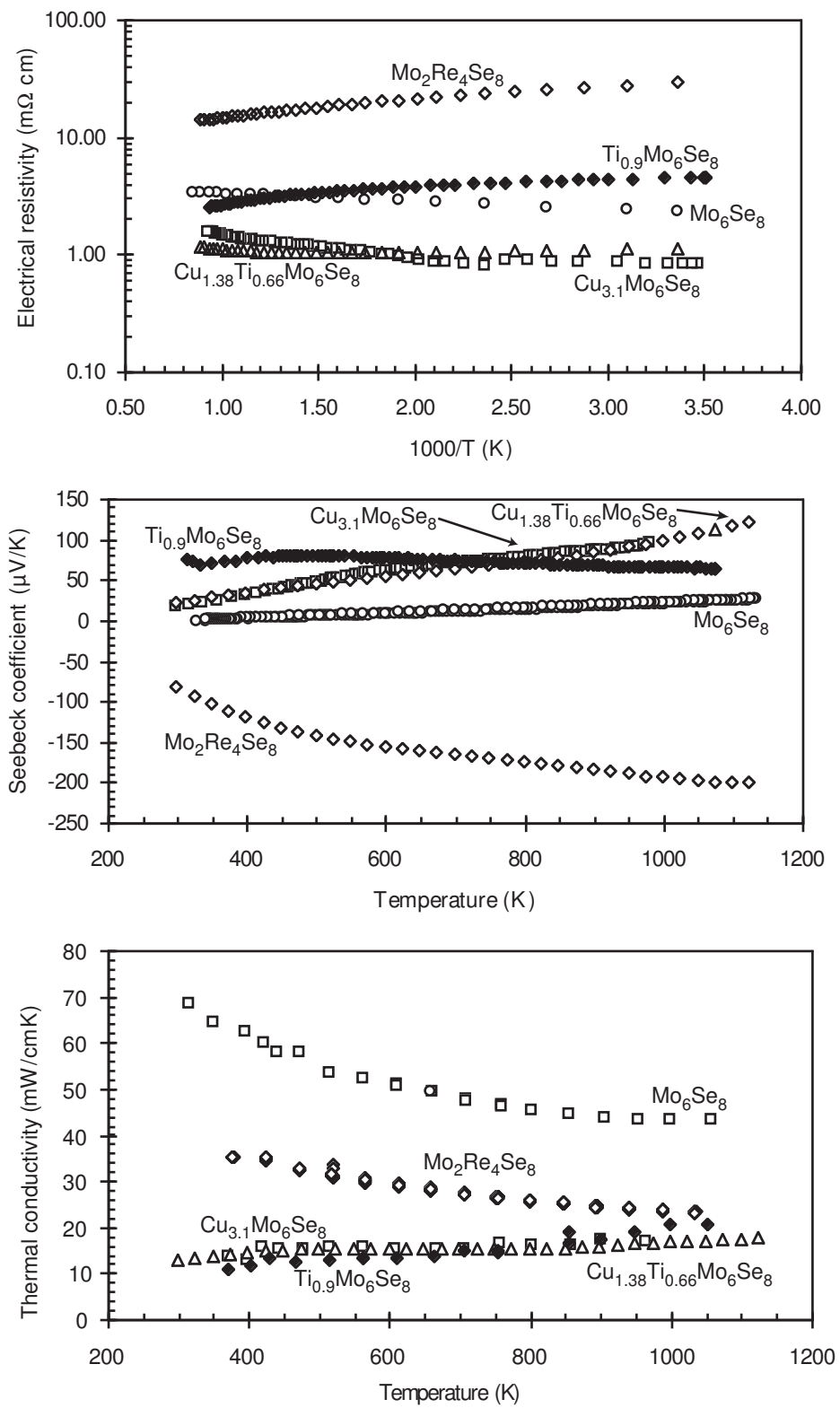


Figure 6.8: The measured TE properties of several Chevrel phases. From Ref. [28].

of stainless steel. Fillings and substitutions are seen to have significant effects on the TE properties. We will first discuss the Seebeck coefficient S .

As expected, S is enhanced as the conduction band is filled and the carrier concentration decreased. Like Mo_6Se_8 , the partially-filled phases have positive S , due to holes left in the conduction band by the incomplete filling. In the Re substituted phase S is negative, indicating conduction by electrons. Either this phase is slightly over-filled ($\text{VEC} > 24$) or it is filled ($\text{VEC} = 24$) and the mobility of the states above the gap is greater than those below the gap, allowing the electrons excited across the gap to dominate the conduction. The carrier concentration in this phase at room temperature was measured to be on the order of $10^{21}/\text{cm}^3$. This is probably too high to be due to intrinsic activation, and suggests over-filling. Unfortunately, the exact composition of this material is not clear [5].

The variation of the resistivity ρ between these compounds is interesting. However, since the band structure near the Fermi surface is sensitive to the composition, it is difficult to explain the observations. The Cu and Cu/Fe filled samples behave like semimetals or heavily doped semiconductors, with ρ increasing with increasing T . The values are also lower than those of Mo_6Se_8 . The Ti filled phase and the Re substituted phase, with higher VEC's than the others, show activated behavior, with ρ decreasing as T increases.

The thermal conductivity κ behaves as expected in this series of materials. The disorder introduced by these modifications decrease κ from that observed in Mo_6Se_8 . The data suggest that filling atoms, which due to their large measured atomic displacement parameters and multiple closely-spaced crystallographic positions may behave like rattlers, are more effective at scattering phonons than the alloy scattering in $\text{Mo}_2\text{Re}_4\text{Se}_8$. At room temperature the partially-filled phases have κ values close to those of Bi_2Te_3 alloys.

Of these materials, $\text{Cu}_{3.1}\text{Mo}_6\text{Se}_8$ and $\text{Cu}_{1.38}\text{Fe}_{0.66}\text{Mo}_6\text{Se}_8$ have the best combination of transport properties for TE applications. However, the Cu/Fe data have proven difficult to reproduce [29]. Thus, $\text{Cu}_{3.1}\text{Mo}_6\text{Se}_8$ is considered the best Chevrel phase TE material known. In the next section we will see how this compound compares to other state of the art TE materials.

6.2.3 Comparison of $\text{Cu}_{3.1}\text{Mo}_6\text{Se}_8$ with other thermoelectric materials

Snyder and coworker at JPL construct segmented TE generators and thus have compiled properties measurements from the best high temperature materials. Most of these were summarized in Ref. [30]. Values of ZT and the compatibility factor s reported in that work are shown in Figure 6.9. We recall here the definition of these two important TE parameters and their dependence on the material's resistivity ρ , thermal conductivity κ and Seebeck coefficient S .

$$ZT = \frac{S^2 T}{\rho \kappa} \quad (6.1)$$

$$s = \frac{\sqrt{1 + ZT} - 1}{ST} \quad (6.2)$$

The data in Figure 6.9 show that the ZT of $\text{Cu}_{3.1}\text{Mo}_6\text{Se}_8$ (often referred to as $\text{Cu}_4\text{Mo}_6\text{Se}_8$ in the literature) is comparable to that of $\text{Si}_{0.7}\text{Ge}_{0.3}$ alloys. In addition, the Chevrel phase has is by far more compatible than $\text{Si}_{0.7}\text{Ge}_{0.3}$ with other materials, like TAGS and the skutterudites. The authors calculated that, due of the mismatched s values, adding $\text{Si}_{0.7}\text{Ge}_{0.3}$ as the highest temperature segment of the p-type leg of a TE generator results in an overall *decrease* in efficiency of 0.5%. However, using the more compatible Chevrel phase *increases* the efficiency by 1.0%.

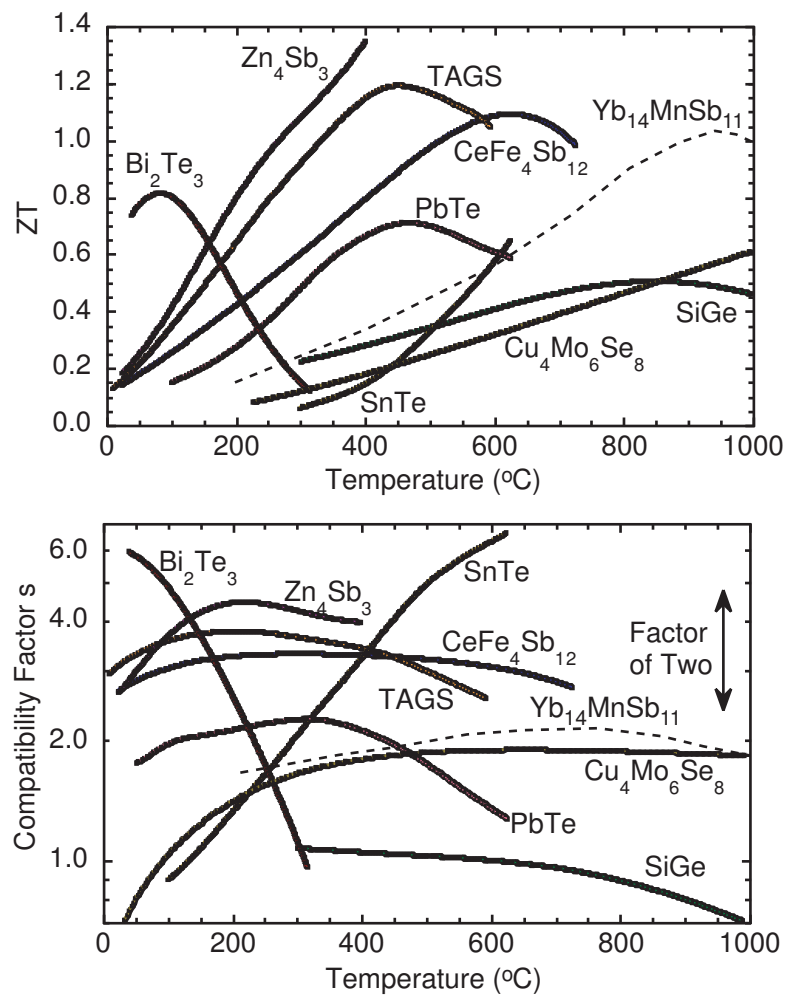


Figure 6.9: The figure of merit ZT and compatibility factor s for good high temperature TE materials, as reported in Ref. [30]

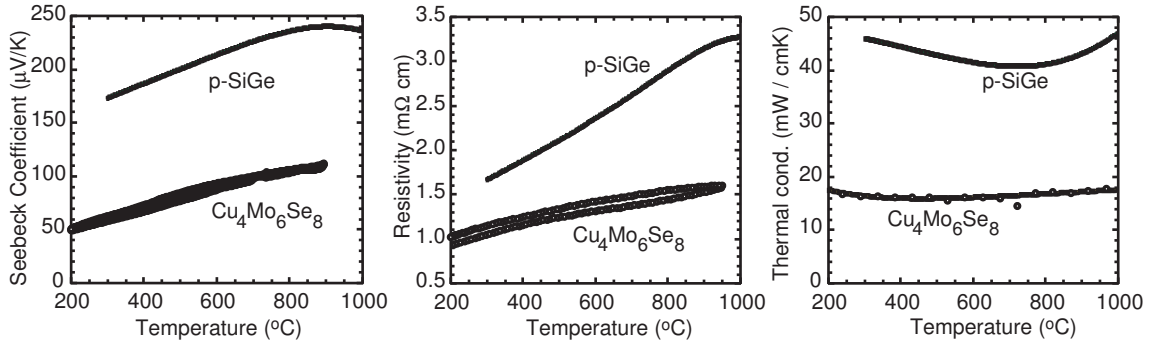


Figure 6.10: Measured TE properties of $\text{Si}_{0.7}\text{Ge}_{0.3}$ and $\text{Cu}_{3.1}\text{Mo}_6\text{Se}_8$ from Ref. [30].

The reason that $\text{Si}_{0.7}\text{Ge}_{0.3}$ and $\text{Cu}_{3.1}\text{Mo}_6\text{Se}_8$ have such different compatibility factors but similar ZT values is shown in Figure 6.10, also taken from Ref. [30]. $\text{Si}_{0.7}\text{Ge}_{0.3}$ achieves high ZT by having high S with only moderately low ρ and κ , while $\text{Cu}_{3.1}\text{Mo}_6\text{Se}_8$ realizes a similar ZT with lower S, ρ , and κ . Since the compatibility factor depends on ZT and S, these two materials have different compatibilities.

Finally, we note here that it has recently been reported that the Zintl phase $\text{Yb}_{14}\text{MnSb}_{11}$ shows great promise as a high temperature p-type TE material [31]. This compound is as compatible with the lower temperature materials as $\text{Cu}_{3.1}\text{Mo}_6\text{Se}_8$, and has significantly higher ZT values (in excess of 1 at 1200 K). Data for this Zintl phase are also shown in Figure 6.9.

6.3 Chevrel phase work at Cornell University

We have seen that Chevrel phase materials show promise as high temperature TE materials. However, there are improvements that must be made if these compounds are to be used in actual devices. In particular, higher ZT values are expected if the carrier concentration can be lowered. Good TE materials have carrier densities on the order of $10^{19} - 10^{20}/\text{cm}^3$, while the Chevrel phases

studied to date have carrier densities one to three orders of magnitude greater than this. Another concern is the stability of these compounds under operating conditions, especially those filled with Cu ions, which are known to be mobile and may migrate and degrade the performance of the device under the influence of a large temperature gradient over long times. Our work at Cornell has been directing toward synthesizing compound with lower carrier densities, by using low temperature methods to try to increase the Cu filling fraction in Mo_6Se_8 and by using a combination of both filling atoms and cluster core substitutions in the same material. Since filling atoms seem to be need to achieve low thermal conductivity, but “complete” filling of the conduction band (i.e. semiconductivity) is more commonly seen with substituted compounds, we believe that a partially-substituted, partially-filled material may be the best way to realize the combination of properties needed for high efficiency TE materials. We have also studied filling atoms other than Cu, since the stability of the Cu phases are a concern.

In this Section we will recall briefly some previously reported work from our group, and then discuss results from our investigation into the Ti filling of Mo_6Se_8 . Our results regarding Ti filled Mo_5RuSe_8 and Cu filled Mo_6Se_8 have been prepared as self-contained manuscripts for publication, and therefore will be presented as separate Chapters following this one.

6.3.1 Previously reported work

A former DiSalvo group student, Anneliese M. Schmidt, synthesized many partially-substituted, partially-filled compounds. The results of these studies can be found in her Masters Thesis. The addition of Zn, Cd, Sn, and Pb to Mo_5RuSe_8 was studied. The resulting compounds have high VEC (23.8–24), but are not stable above about 500 °C. This precluded hot-press treatment, so no TE

properties were measured. In addition, two series of alloys of partially Cu filled Mo_6Se_8 and $\text{Mo}_4\text{Ru}_2\text{Se}_8$ were synthesized, and their high temperature TE properties were measured. Many of these compounds had thermopowers exceeding that of $\text{Cu}_{3.1}\text{Mo}_6\text{Se}_8$, but their resistivities were also higher. The maximum ZT observed in these series was about 0.37 at 1000 °C, lower than that of $\text{Cu}_{3.1}\text{Mo}_6\text{Se}_8$ at the same temperature (ZT = 0.43).

6.3.2 Ti filled Chevrel phases

$\text{Ti}_{0.9}\text{Mo}_6\text{Se}_8$ is the only filled Chevrel phase that has shown semiconducting properties [28]. As expected, this material has high S but also high ρ . The thermopower peaks at about 150 °C. It would be of interest to modify this phase to decrease ρ and move the thermopower peak to higher temperatures. An obvious tuning parameter is the Ti concentration. Lowering the Ti content should lower ρ by increasing the number of holes, but the influence it might have on the thermopower peak, which is related to the band gap, is less clear. Ti-3d bands are expected to be positioned just above the gap [26], and through interaction with Mo-4d/Se-4p band may decrease the band gap by pushing down the bands above the gap. Lower band gaps allow S degrading intrinsic conduction at lower temperatures. Tuning the Ti concentration may then be a way to tune the gap, and therefore the temperature at which S peaks. To investigate how the Ti concentration affects the TE properties, we synthesized samples with nominal compositions $\text{Ti}_x\text{Mo}_6\text{Se}_8$ for $0 \leq x \leq 1.1$.

6.3.3 Synthesis of $\text{Ti}_x\text{Mo}_6\text{Se}_8$

Stoichiometric mixtures of Ti and previously synthesized Mo_6Se_8 were prepared for $x = 0.2, 0.4, 0.6, 0.8, 1.0$. The mixtures were pressed into 1/2 inch

diameter pellets and heated at 1200 °C for 60 hours in sealed evacuated silica tubes. The Mo_6Se_8 starting material was made from the elements sealed in evacuated silica tubes and reacted at 400 °C for one day, then 1100 °C for two days, and finally 1200 °C for 60 hours. Samples with $x = 0.7, 0.9, 1.1$ (each about 2g total mass) were made by reacting stoichiometric mixtures of the elements in evacuated silica tubes at 400 °C for one day, then 1100 °C for two days, pressing the products into pellets, and annealing the pellets at 1200 °C for 72 hours. The total mass of each Ti containing sample was about 2g. Ti and Se were used as received; however, the Mo powder was reduced in forming gas at 1000 °C overnight. The tubes were loaded in air, immediately after the reduction of the Mo powder. For heating at 1200 °C the silica tubes were “double-sealed” inside larger diameter silica jackets.

6.3.4 Structure and composition of $\text{Ti}_x\text{Mo}_6\text{Se}_8$

Powder X-ray diffraction (PXRD) patterns were recorded for each sample. These are shown in Figure 6.11. For $0.2 \leq x \leq 0.6$, the patterns show that the product has rhombohedral symmetry, similar to unfilled Mo_6Se_8 ($x = 0$). In fact, no discernable difference is seen between the unit cell volumes for $x = 0$ and $x = 0.6$ determined by indexing the observed diffraction peaks. A plot of indexed unit cell volume versus nominal composition is also shown in Figure 6.11. For $0.8 \leq x \leq 1.1$, triclinic unit cells are observed, similar to that found by single crystal structure refinement of $\text{Ti}_{0.88}\text{Mo}_6\text{Se}_8$ [32]. The indexed unit cell volumes for these samples are close to that of $\text{Ti}_{0.88}\text{Mo}_6\text{Se}_8$. For $x = 0.7$, a mixture of these two phases (rhombohedral and triclinic) was observed. This material was annealed two more times at 1200 °C, each for 60 hours, however the PXRD pattern did not change. In some cases peaks attributed to an MoSe_2 impurity are seen, and

are labeled by small arrows in Figure 6.11. Although, as discussed below, Ti containing impurities were identified by electron microprobe measurements, no reflections from Ti containing impurities are seen in the PXRD data. However, the detection limit for PXRD is typically on the order of 1% by weight, and the most Ti rich loading in this series contained only about 4% Ti by weight. It is not surprising that impurities at this level are missed.

The samples were sent to Franck Gascoin at JPL for hot-pressing and TE properties measurements. The results of the measurements will be discussed below. The samples were then shipped back to Cornell for quantitative microprobe measurements. Microprobe measurements were carried out on polished (final step with 1 μm diamond) samples that had been coated with about 250 Å of carbon in an evaporating chamber. This coating was applied to be consistent with the standards, which were also coated with carbon to eliminate charging of the Se standard which had been embedded in non-conducting epoxy. The measured Ti concentrations are shown in Table 6.1. Also listed are the estimated purities of the samples based on observations in composition mode, and the impurities which were identified. In what follows, these samples will often be referred to by their nominal compositions by quoting the value of x using in the loading, for example “ $x = 1.0$ ”. When referring to the average measured compositions, the chemical formula will be written out explicitly, for example “ $\text{Ti}_{0.95}\text{Mo}_6\text{Se}_8$ ”.

As expected based on the PXRD results, the microprobe measurements show that the very little Ti was incorporated into the $x = 0.4$ compound, while for $x \geq 0.8$ the measured compositions are similar to the loadings. However, even in the Ti rich samples the measured x is lower than the loaded x , probably due to the formation of Ti containing impurity phases. As noted before, it is not surprising that some oxygen containing impurities are formed in silica tubes at 1200 °C. It is interesting to note that the $x = 1.0$ sample has the highest measured Ti filling frac-

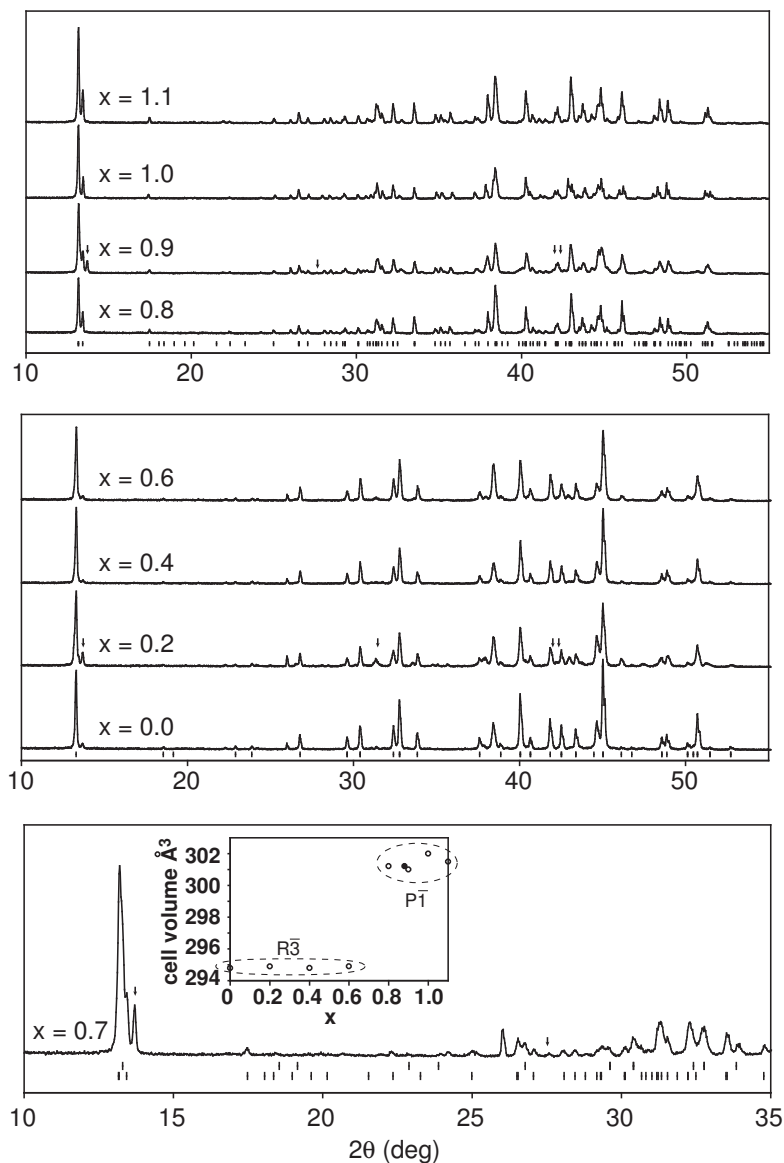


Figure 6.11: Measured powder X-ray diffraction patterns from $\text{Ti}_x\text{Mo}_6\text{Se}_8$ samples, labeled by the nominal value of x . For $x \leq 0.6$, the tick marks locate calculated reflections from the Mo_6Se_8 structure. For $x \geq 0.8$, the ticks locate reflections predicted for the known triclinic Ti filled Chevrel phase structure. Both sets of reflections are marked for $x = 0.7$. Arrows indicate predicted reflections from the MoSe_2 impurity phase. The inset shows indexed unit cell volumes (filled circle is the literature value for $\text{Ti}_{0.88}\text{Mo}_6\text{Se}_8$ [32]).

Table 6.1: Measured compositions, estimated purities, and observed impurities based on quantitative microprobe measurements for $\text{Ti}_x\text{Mo}_6\text{Se}_8$.

x nom	x avg	x min	x max	% Chevrel	impurities
0.4	0.09	0.06	0.12	95	TiO_2
0.7	0.47	0.42	0.61	90	$\text{TiO}_2, \text{MoSe}_2$
0.8	0.70	0.65	0.76	95	TiSe_2
0.9	0.79	0.70	0.86	90	$\text{TiO}_2, \text{MoSe}_2$
1.0	0.95	0.92	0.99	95	$\text{TiO}_2, \text{TiSe}_2$
1.1	0.79	0.73	0.91	90	TiO_2

tion that has been observed to date ($\text{Ti}_{0.95}\text{Mo}_6\text{Se}_8$). Previous investigators found a maximum of $\text{Ti}_{0.88-0.90}\text{Mo}_6\text{Se}_8$ [29]. The consequences of this high filling fraction are seen in the TE properties measurements presented below.

6.3.5 TE properties of $\text{Ti}_x\text{Mo}_6\text{Se}_8$

The measured TE properties of this series of samples is shown in Figure 6.12. The plots are labeled by the nominal compositions of the samples. The measurements were performed by Franck Gascoin at JPL, and data from two of their Chevrel phase samples (unfilled Mo_6Se_8 and $\text{Ti}_{0.9}\text{Mo}_6\text{Se}_8$ [28]) are shown for comparison. Data are only shown up to 600 °C, since above this temperature the Seebeck coefficient showed a rapid increase, an artifact of the measurement apparatus.

Of the samples described above, Seebeck coefficient (S) measurements were performed for $x = 0.2, 0.4, 0.6, 0.8, 0.9, 1.0, 1.1$. No measurements were made on the two-phase $x = 0.7$ sample. For $x < 0.8$, the measured S matches closely that for unfilled Mo_6Se_8 . This is consistent with the PXRD and microprobe re-

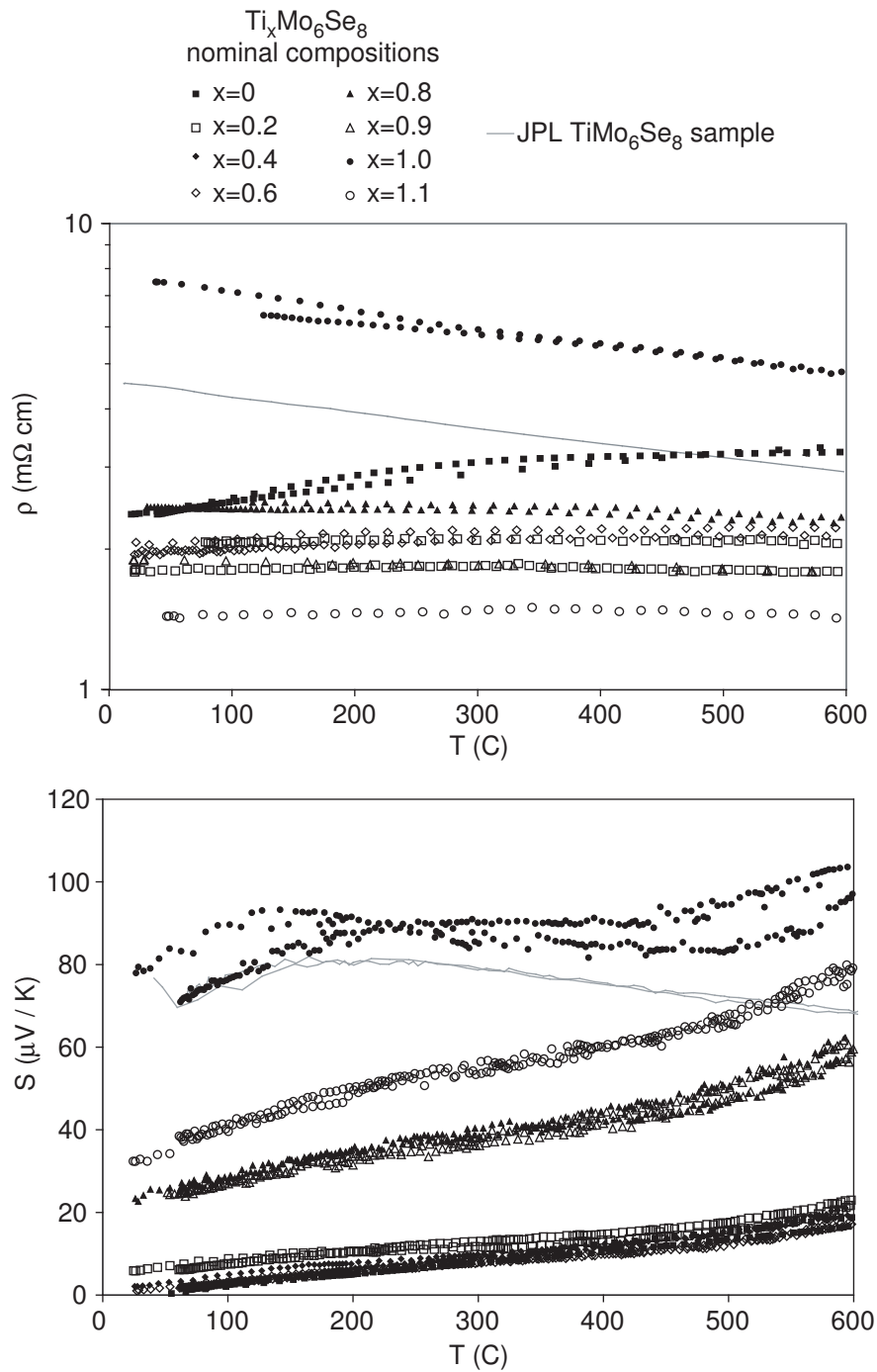


Figure 6.12: Measured thermoelectric properties of $\text{Ti}_x\text{Mo}_6\text{Se}_8$ samples labeled by their nominal compositions. Data from $\text{Ti}_{0.9}\text{Mo}_6\text{Se}_8$ made at JPL and reported in Ref. [28] are shown for comparison. The uncertainty associated with these measurements is about $\pm 3\%$ for the S and about $\pm 1\%$ for ρ .

sults given above, which suggested that there was little Ti incorporated into the Chevrel phase component of these materials. Compared to the unfilled phase, the $x = 0.8$ and $x = 0.9$ samples show a similar temperature dependence but significantly larger values of S . This is expected as the number of charge carriers is decreased due to the partial filling of the cavities with Ti^{4+} ions. Interestingly, there is little difference in S between these two samples, even though their measured Ti content differs ($\text{Ti}_{0.7}\text{Mo}_6\text{Se}_8$ and $\text{Ti}_{0.8}\text{Mo}_6\text{Se}_8$). The Seebeck coefficient for the $x = 1.0$ sample is higher still, and peaks at around 100°C . This is similar to the behavior observed in the JPL $\text{Ti}_{0.9}\text{Mo}_6\text{Se}_8$ material. However, S is larger in $x = 1.0$ than in the JPL sample, consistent with the higher measured Ti content ($\text{Ti}_{0.95}\text{Mo}_6\text{Se}_8$). Finally, the $x = 1.1$ sample has a measured S between those of the $x = 0.8, 0.9$ and $x = 1.0$. This observation is likely to be related to impurities formed by the excess Ti.

Electrical resistivity (ρ) measurements were carried out on the samples with $x = 0.2, 0.6, 0.8, 0.9, 1.0, 1.1$. (Figure 6.12). The partially filled samples have ρ values lower than that of Mo_6Se_8 , contrary to what would be expected if the Ti filling only decreased the carrier concentration. This shows that the effects of the filling atoms on the carrier mobility are also important. The nearly fully filled phase ($x = 1.0$) has the highest measured resistivity, as expected.

The thermal conductivity of the $x = 1.0$ sample was also measured. The measured data are shown in 6.13. As in other filled Chevrel phases, κ was low and increased slowly with temperature. The measurements agree well with those reported for $\text{Ti}_{0.9}\text{Mo}_6\text{Se}_8$ [28]

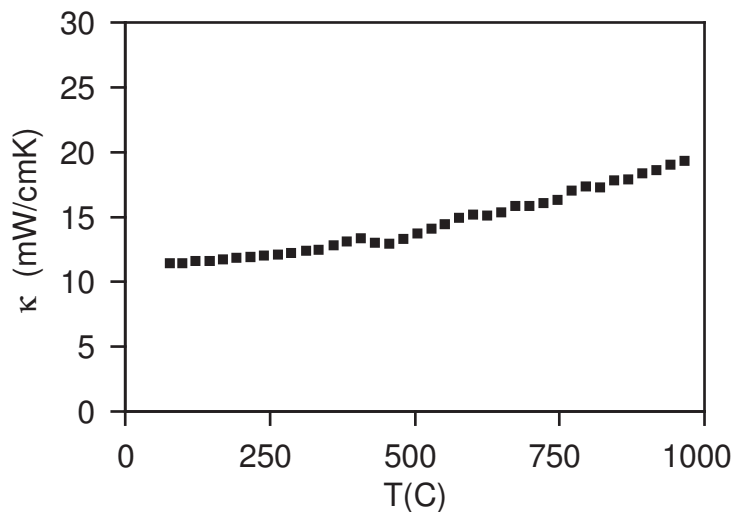


Figure 6.13: Measured thermal conductivity of $\text{Ti}_{0.95}\text{Mo}_6\text{Se}_8$. The estimated uncertainty of these measurements is about $\pm 10\%$.

6.3.6 Discussion and Conclusions

These experiments demonstrate the ability to tune the TE properties of Ti filled Chevrel phases by variation of the Ti content. Due to the rapid decrease in S as the Ti filling fraction is lowered, the best performance occurs for the highest Ti content ($\text{Ti}_{\sim 1}\text{Mo}_6\text{Se}_8$), and no significant improvements were observed in this investigation. The most interesting results from these studies are (1) the highest observed filling fraction in $\text{Ti}_{0.95}\text{Mo}_6\text{Se}_8$ ($\text{VEC} = 23.8$) and corresponding increase in S and ρ , and (2) the structural and compositional discontinuities observed near $x = 0.7$. The latter is especially peculiar, and will be considered further here.

The symmetry and unit cell volumes determined by powder X-ray diffraction data are unambiguous. For loadings with $x < 0.7$ the Chevrel phase is rhombohedral, and the cell volume does not depend on x and is equal that of Mo_6Se_8 . For loadings with $x > 0.7$ the structure is triclinic, with a cell volume significantly larger than the unfilled phase, and close to that obtained by single crystal X-ray structure determination for $\text{Ti}_{0.88}\text{Mo}_6\text{Se}_8$. These observations, and the measured

microprobe compositions, suggest that the minimum Ti filling fraction possible in Mo_6Se_8 is near 0.7. It is not surprising that there is not a complete solid solution between Mo_6Se_8 and “ TiMo_6Se_8 ” since the end members crystallize in different space groups. The PXRD and microprobe observations for the $x = 0.7$ loading can then be explained as follows. Some Ti is effectively removed from the mixture by the formation of impurities, leading to a mixed phase sample with rhombohedral and triclinic Chevrel phase components, as observed by PXRD. Phase separation over length scales similar or smaller than the beam diameter may account for the relatively high variability and intermediate average value of the measured Ti filling fraction (Table 6.1). However, one would then expect to see this two phase region extend all the way down to $x = 0$, with the fraction of the triclinic phase diminishing toward zero as $x \rightarrow 0$. This is not the case. No evidence of the triclinic phase is seen for $x < 0.7$, with the possible exception of $x = 0.2$. Close inspection of this pattern (Figure 6.11) reveals a few peaks and shoulders, not seen for $x = 0, 0.4, 0.6$, that might be attributed to the presence of a small amount of the triclinic phase. Clearly the observed behavior cannot be accounted for without consideration of impurity phases identified by microprobe analysis. The competition for the Ti between the Chevrel phase and Ti containing secondary phases, TiSe_2 and TiO_2 , may be responsible for the suppression of the triclinic phase at lower Ti loadings.

Better control over the compositions of the products of reactions like the ones presented here may be afforded by more careful exclusion of oxygen. This could be accomplished by mixing and loading the samples in an inert atmosphere, using oxygen free Ti (filed from a Ti rod in a dry box, for example), and carrying out the reaction in sealed Mo tubes instead of SiO_2 . However, due to the absence of enhanced TE properties, further examination of this system was not pursued.

REFERENCES

- [1] R. Chevrel, M. Sergent, and J. Prignet, *J. Solid State Chem.* **3**, 315 (1971).
- [2] B. Matthias, M. Marezio, E. Corenzwit, A. Cooper, and H. Barz, *Science* **175**, 1465 (1972).
- [3] O. Fischer and M. Maple, *Topics in Current Physics Vol. 32: Superconductivity in Ternary Compounds I*, Springer-Verlag, 1982.
- [4] M. Maple and O. Fischer, *Topics in Current Physics Vol. 34: Superconductivity in Ternary Compounds II*, Springer-Verlag, 1982.
- [5] T. Caillat and J.-P. Fleurial, *J. Phys. Chem. Solids* **59**, 1139 (1998).
- [6] S. Belin, R. Chevrel, and M. Sergent, *J. Solid State Chem.* **145**, 159 (1999).
- [7] S. Belin, L. Burel, R. Chevrel, and M. Sergent, *Mater. Res. Bull.* **35**, 151 (2000).
- [8] J. Tarascon, J. Waszczak, G. Hull Jr., F. DiSalvo, and L. Blitzer, *Solid State Comm.* **47**, 973 (1983).
- [9] J. Dahn, W. McKinnon, and S. Coleman, *Phys. Rev. B* **31**, 484 (1985).
- [10] C. Fischer, E. Gocke, U. Stege, and R. Schoellhorn, *J. Solid State Chem.* **102**, 54 (1993).
- [11] J. Tarascon, F. DiSalvo, J. Waszczak, and G. Hull Jr., *Phys. Rev. B* **34**, 7342 (1986).
- [12] M. Levi et al., *J. Electroanalytical Chem.* **569**, 211 (2004).
- [13] L. Selwyn and W. McKinnon, *J. Phys. C: Solid State Phys.* **21**, 1905 (1988).
- [14] L. ter Haar, F. DiSalvo, and J. Tarascon, *Phys. Rev. B* **34**, 7342 (1986).
- [15] E. Gocke, W. Schramm, P. Dolscheid, and R. Shoellhorn, *J. Solid State Chem.* **70**, 71 (1987).
- [16] A. Perrin, R. Chevrel, M. Sergent, and O. Fischer, *J. Solid State Chem.* **33**, 43 (1980).
- [17] A. Perrin, M. Sergent, and O. Fischer, *Mat. Res. Bul.* **13**, 259 (1978).
- [18] L. Selwyn and W. McKinnon, *J. Phys. C: Solid State Phys.* **20**, 5105 (1987).
- [19] D. Hinks, J. Jorgensen, and H.-C. Li, *Phys. Rev. Lett.* **51**, 1911 (1983).
- [20] R. Cerny, K. Yvon, M. Wakihara, and P. Fischer, *J. Alloys Compd.* **209**, L29 (1994).

- [21] C. Chang, Y. Tao, J. Swinnea, and H. Steinfink, *Acta Crystallogr.* **C43**, 1461 (1987).
- [22] H. Schick, *Chem. Rev.* **60**, 331 (1960).
- [23] T. Hughbanks and R. Hoffmann, *J. Am. Chem. Soc.* **105**, 1150 (1983).
- [24] YAeHMOP (Version 3.0), G. Landrum, <http://yaehmop.sourceforge.net>, 1999.
- [25] R. Nunes, I. Mazin, and D. Singh, *Phys. Rev. B* **59**, 7969 (1999).
- [26] C. Roche et al., *J. Phys.: Condens. Matter* **10**, L333 (1998).
- [27] K. Kurosaki, A. Kosuga, and S. Yamanaka, *J. Alloys Comp.* **351**, 208 (2003).
- [28] T. Caillat, J.-P. Fleurial, and G. Snyder, *Solid State Sciences* **1**, 535 (1999).
- [29] G.J. Snyder, Personal communication, 2005.
- [30] G. Snyder and T. Caillat, *MRS Proceedings* **793**, 37 (2004).
- [31] S. Brown, S. Kauzlarich, F. Gascoin, and G. Snyder, *Chem. Mater.* **18**, 1873 (2006).
- [32] A. Moncour-Billah and R. Chevrel, *J. Solid State Chem.* **170**, 281 (2003).

Chapter 7

Thermoelectric and structural properties of a new Chevrel phase: $\text{Ti}_{0.3}\text{Mo}_5\text{RuSe}_8$

In this Chapter, we report the synthesis and properties of a new filled, mixed-metal cluster Chevrel phase. This Chapter is adapted from a paper that has been published in *Journal of Solid State Chemistry* with permission from Elsevier. *

7.1 Introduction

As noted in the previous Chapter, much of the Chevrel phase work at Cornell has been focused on the synthesis of compounds that incorporate both filling atoms and cluster core substitutions. The hope is that by using this combination of approaches we can produce materials with lower carrier concentrations, and therefore enhanced TE properties. Ti was chosen as a filling atom, since the stability of Cu filled phases is of concern due to the high mobility of Cu^{1+} ions. Ru was chosen to substitute for Mo, since researchers at JPL were primarily investigating Re substituted materials. The VEC = 24 phase “ $\text{Ti}_{0.5}\text{Mo}_5\text{RuSe}_8$ ” was targeted for synthesis.

Here we report the results of this synthetic effort, which produced the compound $\text{Ti}_{0.3}\text{Mo}_5\text{RuSe}_8$. The composition was determined by quantitative microprobe analysis. Rietveld analysis was applied to the measured powder X-ray diffraction pattern, and allowed the refinement of the Mo_5RuSe_8 framework in this material. The Ti atoms could not be located by this method. To investigate

*M. A. McGuire, A. M. Schmidt, F. Gascoin, G. J. Snyder and F. J. DiSalvo, *J. Solid State Chem.* **179**, 2158 (2006).

the effects that the Ti had on the Chevrel framework, the structure of the unfilled phase Mo_5RuSe_8 was also refined. Comparison of the two structures shows the influence of the Ti atoms on the unit cell size and the bond lengths in the Mo_5RuSe_8 framework. High temperature TE properties measurements were carried out at JPL on a hot-pressed sample of this material. The results are reported here and compared to those of related compounds. The combination of filling and substitutions is seen to lead to better TE performance than either only filling with Ti or only substituting Ru.

7.2 Experimental

7.2.1 Synthesis Methods

Mo_5RuSe_8 was obtained by deintercalation of $\text{CuMo}_5\text{RuSe}_8$, which had been made by reacting a mixture of stoichiometric amounts of the elements in sealed, evacuated, silica tubes. The mixture was first reacted at 400 °C for one day, mixed by shaking the unopened tube, and then heated at 1100 °C for two days. The product was ground, pressed into a pellet, and then annealed twice for three days each at 1200 °C. The sample was reground and pressed into a pellet between the two anneals. For annealing at 1200 °C, the sample was sealed in a silica tube which was then sealed in a second, larger diameter silica tube. The deintercalation was carried out by reacting $\text{CuMo}_5\text{RuSe}_8$ with iodine dissolved in acetonitrile [1]. We produce Mo_5RuSe_8 through this deintercalation method because we have found that the amount of the MoSe_2 impurity in the final product is lower than when Mo_5RuSe_8 is synthesized directly from the elements. This may be due to Mo self-intercalation, to which similar behavior has been attributed in $\text{Mo}_6\text{S}_{8-x}\text{Se}_x$ [2, 3].

The deintercalation product was then used for powder X-ray diffraction studies, and as a starting material for synthesis of the Ti filled phase. Since one half of a Ti^{4+} ion per Mo_5RuSe_8 cluster would be needed to give a VEC of 24 per cluster, the target stoichiometry of the Ti filled phase was $\text{Ti}_{0.5}\text{Mo}_5\text{RuSe}_8$. A 1:2 molar ratio of Ti powder and Mo_5RuSe_8 was pressed into a pellet, sealed in an evacuated silica tube, and heated at 1100 °C for 48 hours. The product was ground thoroughly, pressed into a pellet, and sealed in a silica tube. This tube was then sealed under vacuum in a second silica tube, and heated at 1200 °C for 48 hours. The resulting product was then used for X-ray diffraction studies, electron microprobe analysis, and high temperature thermoelectric properties measurements.

7.2.2 Powder X-ray Diffraction

Powder X-ray diffraction patterns were recorded with a Scintag 2000 theta-theta diffractometer, using $\text{Cu-K}\alpha$ radiation. Rietveld analysis was carried out using the program FULLPROF [4]. Data used for Rietveld analysis were collected in step mode, with a counting time of 6 seconds per 0.2 degree step, using an internal Si standard. In each case, three phases were refined: the Chevrel phase, the internal Si standard, and the MoSe_2 impurity. Refined parameters include: zero offset, asymmetry, background polynomials, scale factors, peak shapes, half-width parameters, lattice constants, displacement parameters, atomic coordinates, and preferred orientation (for MoSe_2 only). The Mo:Ru ratio was fixed at 5:1 in the refinements. Due to weak reflections ($\sim 1\%$ of the height of the strongest Chevrel phase reflection) from unidentified impurities, two small regions (each about one degree wide) were excluded from the refinement for Mo_5RuSe_8 .

7.2.3 Microprobe Analysis

Electron microprobe analysis of the Ti filled phase was performed on a piece broken away from the pellet after the 1200 °C anneal. The sample was mounted in conducting epoxy, polished using 1200 grit SiC paper followed by a 1 mm diamond suspension on a Struers Rotopol Rotoforce polishing system. Approximately 250 Å of carbon was evaporated onto the surface after polishing. Quantitative analyses of wavelength dispersive spectra were performed using pure elemental standards prepared in a similar fashion. Measurements were carried out in a Jeol 8900 electron microprobe, operating at 15 kV and ~20 nA. Data were collected on grains which were at least 5 μm in size.

7.2.4 Property Measurements

To prepare dense samples for property measurements, a finely ground polycrystalline powder of $\text{Ti}_{0.3}\text{Mo}_5\text{RuSe}_8$ was pressed at 1223 K at a pressure of about 20,000 psi and for 1.5 hours under argon atmosphere in high-density graphite dies (POCO HPD-1). The measured density of the resulting pellet was about 95 % of the theoretical density. Van der Pauw resistivity measurements were performed on 1 mm thick slice of the pellet using a current of 100 mA in a special high-temperature apparatus [5]. The thermopower measurement was performed on the remaining cylinder using a high temperature light pulse technique [6]. The measurements were performed as a function of temperature from room temperature to about 1200 K.

7.3 Measured Compositions

Electron microprobe analysis showed that in addition to the Chevrel phase, small amounts of MoSe_2 , TiSe_2 , and TiO_x were also present in the sample. Based on observations made in composition mode, it is estimated that the sample was approximately 90-95 % Chevrel phase. Composition data from ten different Chevrel phase grains were normalized to give a total of six cluster metal atoms (Mo + Ru) per formula unit, and then averaged. The uncertainty on the average composition was estimated as the standard deviation of the normalized measurements. This analysis gave an average composition (with estimated uncertainties in parentheses) of $\text{Ti}_{0.28(2)}\text{Mo}_{5.08(2)}\text{Ru}_{0.92(2)}\text{Se}_{7.81(19)}$.

Clearly, not all of the Ti was incorporated into the Chevrel phase. This is consistent with the observation of Ti containing impurities (TiSe_2 and TiO_x) in the sample. We are unsure of the origin of the discrepancy between the measured Mo:Ru ratio and the expected ratio of 5:1. It may be a systematic error associated with the microprobe analysis, or signify the presence of an undetected Ru containing phase in the sample. We attribute the low Se content to a small amount of oxygen for selenium substitution, which has been observed in several Chevrel phases [7, 8, 9], and is likely to occur in silica tubes at 1200 °C since the vapor pressures of SiO and O_2 are expected to be on the order of 10^{-6} torr [10]. Low Se content could also be caused by Se vacancies, which have been observed in Chevrel phases. Selenium vacancies could be related to the incomplete filling observed in many Chevrel phase compounds, since fewer additional electrons would be needed to reach a semiconducting state.

7.4 Refined Crystal Structures of Mo_5RuSe_8 and $\text{Ti}_{0.3}\text{Mo}_5\text{RuSe}_8$

The powder X-ray diffraction results for both Mo_5RuSe_8 and $\text{Ti}_{0.3}\text{Mo}_5\text{RuSe}_8$ are shown in Figure 7.1. Both compounds adopt the classic Chevrel phase structure (space group $R\bar{3}$). Agreement factors and refined unit cell parameters for the Chevrel phases are shown in Table 7.1. The unit cell parameters for the Chevrel phases are shown in Table 7.1. The unit cell parameters for Mo_5RuSe_8 in Table 7.1 agree well with those reported by in the literature ($a = 9.638 \text{ \AA}$, $c = 10.971 \text{ \AA}$) [11]. Atomic positions (in the hexagonal setting) are listed in Table 7.2. The Mo/Ru site and the site occupied by Se(1) are at Wyckoff positions 6f (x, y, z), while Se(2) is at Wyckoff position 2c ($0, 0, z$). The low level of incorporation of Ti, the possibility that it partially occupies several different sites, and its relatively low scattering power, precluded the determination of the Ti positions from the present data. Many different locations have been observed for transition metals in the cavities of Chevrel phase structures [12, 13, 14]. In each case the transition metal atoms are disordered over several positions within the unit cell. Such disorder would further dilute the already small scattering power of the Ti atoms, adding to the difficulty in locating the Ti using powder X-ray diffraction methods. Only the Mo_5RuSe_8 framework has been refined for the Ti filled phase, which may be partly responsible for the somewhat higher R-factors when compared to Mo_5RuSe_8 .

Although the Ti atoms could not be located using the X-ray diffraction data, evidence of its incorporation is seen. The primitive unit cell volume of the Ti filled phase is 2.05 \AA^3 larger than that of the unfilled phase. This corresponds to an increase of 6.8 \AA^3 per Ti atom. This increase is similar to the behavior seen in $\text{Ti}_{0.88}\text{Mo}_6\text{Se}_8$ (with a slightly distorted triclinic Chevrel phase structure [13]) in which the volume increases by 7.3 \AA^3 per Ti atom over that of Mo_6Se_8 [15].

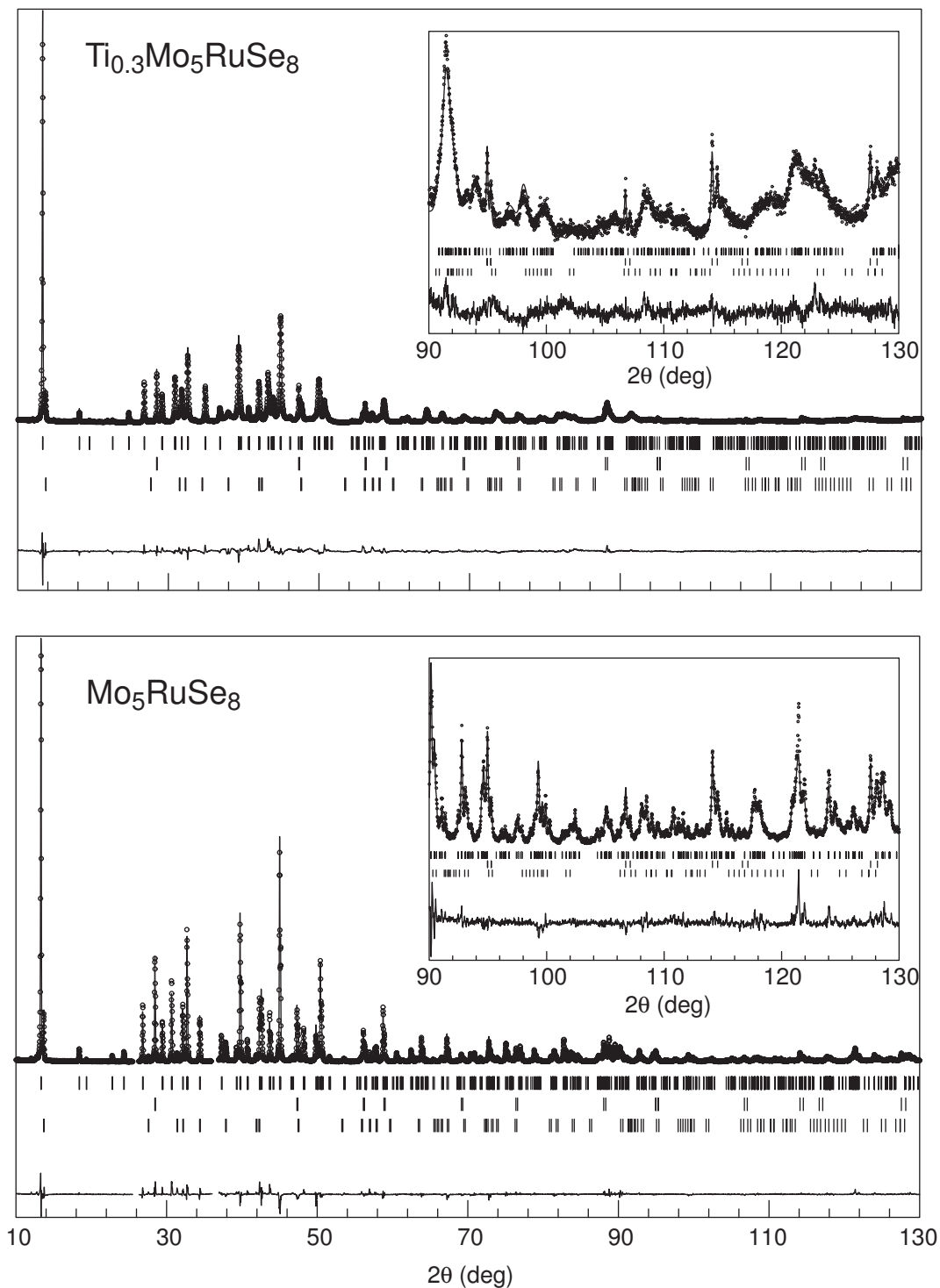


Figure 7.1: Results from the Rietveld refinements for Mo_5RuSe_8 and $\text{Ti}_{0.3}\text{Mo}_5\text{RuSe}_8$, including expanded views of the high angle data, showing the measured data (circles) and calculated data (solid line). The difference curves are shown at the bottoms, and the tick marks indicate the position of the Bragg peaks for the Chevrel phases, Si, and MoSe_2 , from top to bottom.

Table 7.1: Refinement Agreement Factors and Refined Unit Cell Parameters for Mo_5RuSe_8 and $\text{Ti}_{0.3}\text{Mo}_5\text{RuSe}_8$

	Mo_5RuSe_8	$\text{Ti}_{0.3}\text{Mo}_5\text{RuSe}_8$
a_H (Å)	9.63994(8)	9.75430(25)
c_H (Å)	10.97191(11)	10.79064(40)
V_H (Å ³)	883.001(13)	889.140(46)
R_p	8.04	10.4
R_{wp}	10.5	14.2
S	2.93	3.59
R_{Bragg} (Chevrel)	6.40	6.11

$$R_p = 100 \sum |y_{obs} - y_{calc}| / \sum |y_{obs}|;$$

$$R_{wp} = [100 \sum w |y_{obs} - y_{calc}|^2 / \sum w y_{obs}^2]^{1/2};$$

$$R_{Bragg} = 100 \sum_k |I_k - I_{calc,k}| / \sum |I_k|;$$

$$S = R_{wp} / R_{exp}; w = 1/\sigma^2;$$

$$R_{exp} = 100 [N - P / \sum w y_{obs}^2]^{1/2};$$

$N - P$ is the number of degrees of freedom.

Table 7.2: Refined fractional coordinates in the hexagonal setting for Mo_5RuSe_8 and $\text{Ti}_{0.3}\text{Mo}_5\text{RuSe}_8$

	Mo_5RuSe_8	$\text{Ti}_{0.3}\text{Mo}_5\text{RuSe}_8$
Mo/Ru		
x	0.01723(16)	0.01885(25)
y	0.16789(15)	0.16703(19)
z	0.39575(13)	0.39651(20)
Se(1)		
x	0.32335(21)	0.32349(30)
y	0.28474(18)	0.28353(28)
z	0.41394(15)	0.40874(30)
Se(2)		
z	0.21499(26)	0.20900(42)

The effects of the Ti on the interatomic distances in the Chevrel phase framework (Figure 7.2) are also apparent. These distances are listed in Table 7.3. There are two metal-metal distances in the Chevrel phase cluster, d_1 (roughly parallel to the hexagonal c-axis) and d_2 (roughly perpendicular to the hexagonal c-axis). In going from Mo_5RuSe_8 to $\text{Ti}_{0.3}\text{Mo}_5\text{RuSe}_8$, d_1 increases, while d_2 decreases. It is usually the case for Chevrel phase sulfides and selenides that, as electrons are added to cluster (filling metal-metal bonding states and approaching a VEC of 24), the intra-cluster bonds become shorter and its shape becomes more regular [16]. The behavior observed here in $\text{Ti}_{0.3}\text{Mo}_5\text{RuSe}_8$ is consistent with these general rules. The average intracuster metal-metal distance decreases upon addition of Ti, from 2.715 Å to 2.697 Å. The cluster also become more regular; the difference between d_2 and d_1 decreases from 0.088 Å to 0.039 Å. It is also clear from Table 7.3 that the intercluster Mo/Ru-Se distances are increased by the addition of Ti. This is consistent with previous observation of the effect reducing the Mo cluster core (through the introduction of filling atoms) on these distances [16]].

Table 7.3: Interatomic distances (Å) in Mo_5RuSe_8 and $\text{Ti}_{0.3}\text{Mo}_5\text{RuSe}_8$ (M = Mo/Ru).

	Mo_5RuSe_8	$\text{Ti}_{0.3}\text{Mo}_5\text{RuSe}_8$
M-M (d_1)	2.671(1)	2.677(2)
M-M (d_2)	2.759(2)	2.716(3)
M-Se (intracuster)	2.512(3)	2.545(4)
	2.518(2)	2.546(4)
	2.537(2)	2.568(4)
	2.587(2)	2.601(4)
M-Se (intercluster)	2.621(2)	2.621(4)

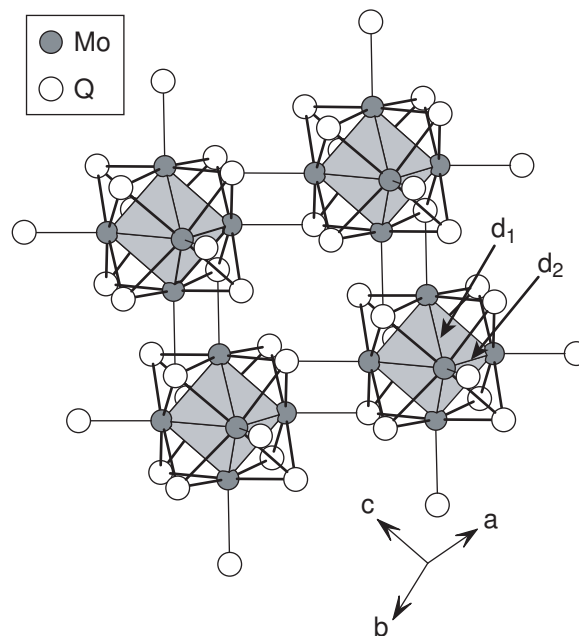


Figure 7.2: A view of the Chevrel phase structure, showing how the Mo_6Q_8 are interconnected into a three dimensional network. The hexagonal unit cell axes and the two unique metal metal bonds d_1 and d_2 are labeled.

7.5 Thermoelectric Properties of $\text{Ti}_{0.3}\text{Mo}_5\text{RuSe}_8$

Figure 7.3 shows the measured electrical resistivity and thermopower of $\text{Ti}_{0.3}\text{Mo}_5\text{RuSe}_8$, and the thermoelectric power factor calculated from these measurements. The power factor (PF) is defined as $\text{PF} = S^2/\rho$, and is thus closely related to Z . The thermal hysteresis in the measured thermopower is likely due to surface oxidation of the sample during the measurement, or degradation of the electrical contacts. In calculating PF the data taken on warming were used.

The measured resistivity of $\text{Ti}_{0.3}\text{Mo}_5\text{RuSe}_8$ increases slowly with temperature up to about 1000 K, at which point it begins to decline. The thermopower is positive indicating conduction dominated by holes, and achieves a maximum value at about the same temperature as the resistivity. This behavior suggests that $\text{Ti}_{0.3}\text{Mo}_5\text{RuSe}_8$ may be described as a heavily doped semiconductor, with the de-

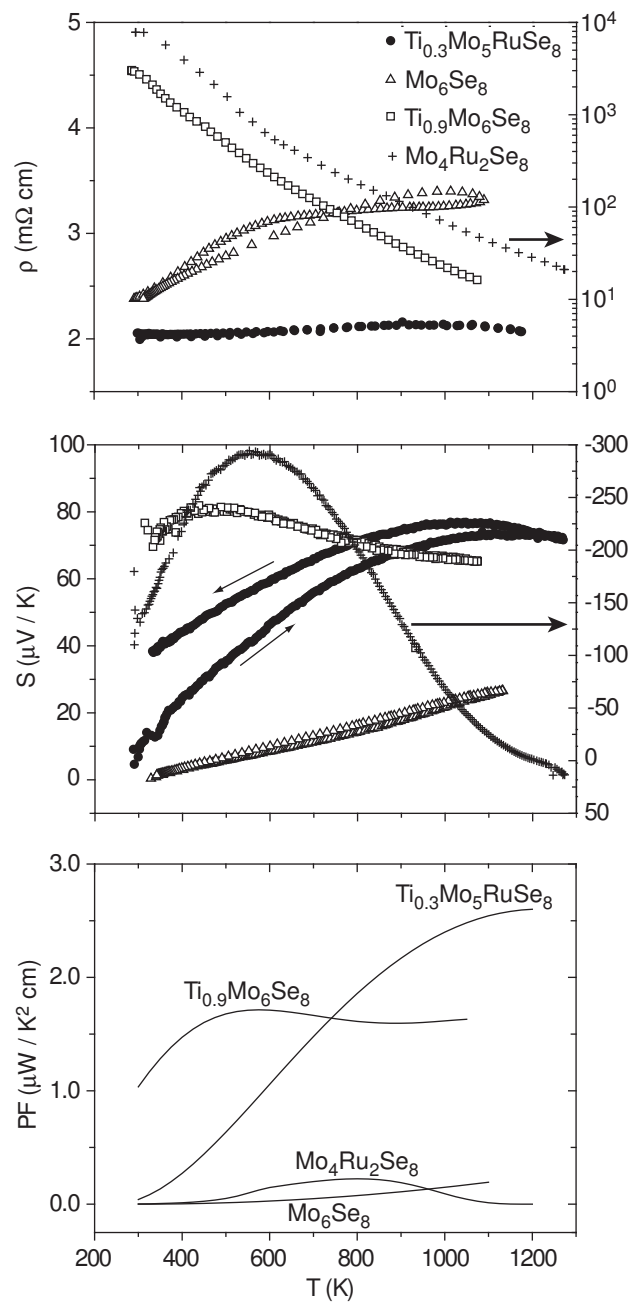


Figure 7.3: The resistivity (ρ), thermopower (S) and power factor (PF) of $Ti_{0.3}Mo_5RuSe_8$, along with data from Mo_6Se_8 [17], $Ti_{0.9}Mo_6Se_8$ [17], and $Mo_4Ru_2Se_8$ [18] for comparison. Note the different scales (at right) for the resistivity and thermopower of $Mo_4Ru_2Se_8$. The uncertainty associated with these measurements is about $\pm 3\%$ for the S and about $\pm 1\%$ for ρ .

cline in resistivity and thermopower seen at the highest temperatures attributed to the onset of intrinsic behavior. For comparison, data for some other Chevrel phase materials are also included in the plots. These include: the unfilled compound Mo_6Se_8 , the unfilled mixed Mo/Ru cluster compound $\text{Mo}_4\text{Ru}_2\text{Se}_8$, and the Ti filled pure Mo cluster compound $\text{Ti}_{0.9}\text{Mo}_6\text{Se}_8$. When compared to the parent compound Mo_6Se_8 , the influence of fillings and cluster core substitutions (both increasing the VEC) on the TE properties are apparent in Figure 7.3. Inspection of the PF plot also shows that the combination of filling and substitutions used in $\text{Ti}_{0.3}\text{Mo}_5\text{RuSe}_8$ is more effective than just filling with Ti ($\text{Ti}_{0.9}\text{Mo}_6\text{Se}_8$) or just substituting Ru ($\text{Mo}_4\text{Ru}_2\text{Se}_8$). However, this material does not perform as well as $\text{Cu}_{3.1}\text{Mo}_6\text{Se}_8$, which has $\text{PF} \approx 6 \mu\text{W}/\text{K}^2\text{cm}$ at 1000 K [17].

Goldsmid and Sharp have shown that the band gap of a material can be estimated from the maximum in the S vs. T plot [19]. They derived the expression $E_{gap} \approx 2S_{max}T$, where T is the temperature at which the maximum thermopower S_{max} is realized. They note that this method typically gives errors of about 5–20%. Applying this equation to the data presented in Figure 7.3 gives an estimated band gap of 0.16 eV for $\text{Ti}_{0.3}\text{Mo}_5\text{RuSe}_8$, 0.32 eV for $\text{Mo}_4\text{Ru}_2\text{Se}_8$, and 0.08 eV for $\text{Ti}_{0.9}\text{Mo}_6\text{Se}_8$. It is not surprising that the gap of $\text{Ti}_{0.3}\text{Mo}_5\text{RuSe}_8$ lies between those of the fully Ru substituted phase $\text{Mo}_4\text{Ru}_2\text{Se}_8$ and the Ti-filled phase $\text{Ti}_{0.9}\text{Mo}_6\text{Se}_8$. The variation in band gaps show that these fillings and substitution do more than simply add electrons to the cluster-metal d orbital based conduction band, but in fact alter the band structure near the Fermi level.

7.6 Conclusions

The new Chevrel phase $\text{Ti}_{0.3}\text{Mo}_5\text{RuSe}_8$, incorporating both filling atoms and cluster core substitutions, has been synthesized, and the structure of its

Mo_5RuSe_8 framework refined. Although the location of the Ti atoms could not be determined from the powder X-ray diffraction data, its influence on the Chevrel phase framework was observed. This was made possible by the Rietveld refinement of the structure of the unfilled phase Mo_5RuSe_8 . The observed changes in the M-M distances in the octahedral cluster core and the M-Se distances in the M_6Se_8 unit caused by the Ti filling follow the general trends that have been previously observed in Chevrel phase compounds. The measured thermoelectric properties of $\text{Ti}_{0.3}\text{Mo}_5\text{RuSe}_8$ show it to behave like a heavily doped semiconductor, and a band gap of 0.16 eV was estimated from the thermopower data. Although its high temperature thermoelectric properties are not as good as those of the best Chevrel phase thermoelectric material ($\text{Cu}_{3.1}\text{Mo}_6\text{Se}_8$), it does outperform both $\text{Ti}_{0.9}\text{Mo}_6\text{Se}_8$ and $\text{Mo}_4\text{Ru}_2\text{Se}_8$. This demonstrates how a combination of both filling and cluster core substitutions can lead to improved thermoelectric materials.

REFERENCES

- [1] J. Tarascon, J. Waszczak, G. Hull, F. DiSalvo, and L. Blitzer, *Solid State Comm.* **47**, 973 (1983).
- [2] S. Belin, R. Chevrel, and M. Sergent, *J. Solid State Chem.* **145**, 159 (1999).
- [3] S. Belin, L. Burel, R. Chevrel, and M. Sergent, *Mater. Res. Bull.* **35**, 151 (2000).
- [4] FULLPROF.2k version 3.30, J. Rodriguez-Carvajal, ILL (unpublished), June 2005.
- [5] J. McCormack and J.-P. Fleurial, *Mater. Res. Soc. Symp. Proc.* **234**, 135 (1991).
- [6] C. Wood, D. Zoltan, and G. Stapfer, *Rev. Sci. Instrum.* **56**, 719 (1985).
- [7] R. Cerny, K. Yvon, M. Wakihara, and P. Fischer, *J. Alloys Compd.* **209**, L29 (1994).
- [8] C. Chang, Y. Tao, J. Swinnea, and H. Steinfink, *Acta Crystallogr.* **C43**, 1461 (1987).
- [9] D. Hinks, J. Jorgensen, and H.-C. Li, *Phys. Rev. Lett.* **51**, 1911 (1983).
- [10] H. Schick, *Chem. Rev.* **60**, 331 (1960).
- [11] L. S. Selwyn and W. McKinnon, *J. Phys. C: Solid State Phys.* **20**, 5105 (1987).
- [12] O. Fischer and M. Maple, *Topics in Current Physics: Superconductivity in Ternary Compounds I*, Springer-Verlag, 1982.
- [13] A. Moncour-Billah and R. Chevrel, *J. Solid State Chem.* **170**, 281 (2003).
- [14] S. Belin, R. Chevrel, and M. Sergent, *J. Solid State Chem.* **155**, 250 (2000).
- [15] O. Bars, J. Guillevic, and D. Grandjean, *J. Solid State Chem.* **6**, 48 (1973).
- [16] F. Berry and C. Gibbs, *J. Solid State Chem.* **109**, 22 (1994).
- [17] T. Caillat, J.-P. Fleurial, and G. Snyder, *Solid State Sciences* **1**, 535 (1999).
- [18] A. Schmidt, M. McGuire, F. Gascoin, G. Snyder, and F. DiSalvo, to be submitted to *J. Solid State Chem.* (2006).
- [19] H. Goldsmid and J. Sharp, *J. Electron. Mater.* **28**, 869 (1999).

Chapter 8

$\text{Cu}_4\text{Mo}_6\text{Se}_8$: Synthesis, Crystal Structure, and Electronic Structure of a New Chevrel Phase Structure-Type

In this Chapter, we report the discovery and analysis of a new Chevrel phase structure. The discovery was made during our study of the intercalation of Cu into Chevrel phases at room temperature. This Chapter is adapted from a paper that has been published in *Inorganic Chemistry*. *

8.1 Introduction

Although not semiconducting, the copper-filled compound $\text{Cu}_{3.1}\text{Mo}_6\text{Se}_8$ shows the best TE performance at high temperature of any Chevrel phase studied to date [1]. Efforts to improve this material by increasing the Cu concentration have not been successful. This is not true for the sulfides, and $\text{Cu}_4\text{Mo}_6\text{S}_8$ has been synthesized by the electrochemical intercalation of Cu [2]. One reason for the limited Cu content seen in the Se compounds may be the high temperatures ($> 1100^\circ\text{C}$) at which these materials are typically prepared. This led us to investigate lower temperature routes toward Cu filled Mo_6Se_8 .

There have been numerous investigations of the addition of guest atoms to these materials near room temperature. Electrochemical cells have been used to intercalate Li, Mg, Na, Zn, Cd and Cu into Chevrel phase sulfides and selenides [3, 4, 5]. One study by Selwyn and McKinnon investigated the intercalation of

*Reproduced in part with permission from M. A. McGuire, C. Ranjan, and F. J. DiSalvo, *Inorg. Chem.* **45**, 2718 (2006). Copyright 2006 American Chemical Society.

Li into already partially filled $\text{Cu}_y\text{Mo}_6\text{Se}_8$ ($0 < y < 2.5$) [6]. They found, in addition to a series of Li/Cu filled phases, an unidentified Cu rich phase. They also showed that this phase could be produced by the intercalation of Cu into $\text{Cu}_y\text{Mo}_6\text{Se}_8$, proving that no Li was incorporated into the structure. The authors were unable to prepare the copper-rich compound as a single phase ($\text{Cu}_{1.7}\text{Mo}_6\text{Se}_8$ was always present as an impurity), and were unable to index the observed powder X-ray diffraction peaks. In this paper, we report the crystal structure of this copper-rich Chevrel phase.

Unlike many previous authors' work, our low temperature studies were not performed in an electrochemical cell, but in a specially designed apparatus described below. We characterized the products of our reactions using powder X-ray diffraction, quantitative electron microprobe analysis, and single crystal X-ray diffraction. We determined the composition of this phase to be $\text{Cu}_4\text{Mo}_6\text{Se}_8$. This compound adopts a new structure type, and represents the first example of an extended structure with Chevrel-like Mo_6Se_8 layers that are not joined to each other through Mo-Se bonding. The only interlayer connections are through Cu-Se bonding. This results in two Mo atoms on each cluster having square planar Se coordination, while the other four have the usual square pyramidal coordination. In addition to the synthesis and crystal structure of $\text{Cu}_4\text{Mo}_6\text{Se}_8$ we discuss the electronic consequences of the separation of the Mo_6Se_8 layers.

8.2 Experimental

8.2.1 Synthesis Methods

Mo_6S_8 and Mo_6Se_8 can not be prepared directly from the elements [7], so the starting materials used in our intercalation studies for the sulfide and selenide systems were $\text{Cu}_2\text{Mo}_6\text{Q}_8$ ($\text{Q} = \text{S}, \text{Se}$). For the telluride system, Mo_6Te_8 was used,

since it can be produced by direct reaction of Mo and Te. These starting compounds were synthesized from the elements: Cu (Fisher, electrolytic powder), Mo (Aldrich, 99.9%, -100 mesh), S (Cominco, 99.99%), Se (unspecified source, 99.999%), Te (Johnson Matthey, 99.9999%). The Mo (Cu) powder was reduced in forming gas at 1000 °C (300 °C) for about 24 (3) hours, and subsequently stored and handled inside an argon filled glove box. The S, Se, and Te were used as received. Stoichiometric mixtures (typically 2-3 g total) were sealed in evacuated silica tubes and heated over one day to 400 °C and held at this temperature for one day. The tubes were then shaken to mix the reaction products, but not opened. The tubes were then heated to various temperatures, from 900 °C to 1200 °C, held there for three days, and then cooled naturally to room temperature with the furnace power off. The resulting powdered products were almost single phase $\text{Cu}_2\text{Mo}_6\text{Q}_8$ or Mo_6Te_8 with lattice constants matching closely those reported in the literature [8]. A small amount ($\sim 5\%$) of MoQ_2 impurity was present in some samples.

It is common to prepare partially Cu-filled Chevrel phases and then remove the Cu to obtain unfilled Mo_6Q_8 , which cannot be prepared from the elements for $\text{Q} = \text{S}, \text{Se}$, as noted above. One way in which this is done is through reaction with iodine dissolved in acetonitrile (AN) [9]. The Chevrel phase is oxidized by the I_2 in solution and forms CuI , which is soluble in AN (3.4 wt. % [10]).

As a means for adding Cu to the Chevrel phase, we essentially performed this reaction in reverse. Copper was intercalated through CuI dissolved in AN from an excess supply of elemental Cu in electrical contact with the Chevrel phase. In the presence of excess Cu, this reaction should proceed until it is no longer energetically favorable to add more Cu to the Chevrel phase (assuming that the diffusion rate of Cu in the Chevrel phase remains large enough). A spe-

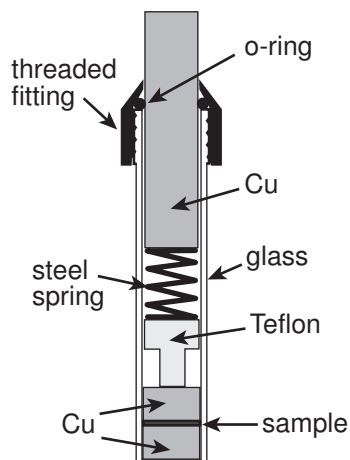


Figure 8.1: A drawing of the apparatus used for the room temperature intercalation studies. The outer diameter of the glass tube is approximately 19 mm.

cial device was constructed for this reaction, designed to ensure the required electrical contact between the Cu reservoir and the sample.

Our Cu intercalation apparatus is shown in Figure 8.1. It consists of a glass tube which is threaded on one end and sealed with a flat glass plate on the other. The glass plate is held in place with Torr-Seal epoxy. The sample (typically 200 - 500 mg) is placed between two accurately weighed cylindrical copper blocks, machined from oxygen-free high conductivity copper rod to fit snugly inside the glass tube, in the bottom of the apparatus. The faces of the copper blocks are cleaned with 1200 grit SiC paper before each run. A solution of CuI in AN (about 2 % by weight) is added so that the sample and Cu blocks are immersed. A copper rod and steel spring are used to apply pressure to the sample, ensuring good electrical contact between the powder grains and the copper, and the o-ring seal is tightened to maintain the pressure. A Teflon spacer is used to keep the steel spring out of the CuI/AN solution.

The intercalation experiments were carried out inside an argon filled glove box. The reactions were allowed to proceed for various lengths of time, from two

hours up to ten days. The apparatus was then removed from the glove box and opened. The product was removed, filtered and rinsed with AN in air.

8.2.2 Characterization Techniques

Powder X-ray diffraction (PXRD) patterns were collected on a Scintag 2000 theta-theta diffractometer using Cu-K α radiation. Quantitative electron microprobe analysis was performed using a JEOL 8900 Superprobe operating at 15 kV and approximately 20 nA. Measurements were carried out in wavelength dispersive mode, using pure elemental Cu, Mo, and Se as standards. The powdered samples were embedded in electrically conducting epoxy mounts, and then polished using 1200 grit SiC paper followed by a 1 micron diamond suspension on a Struers Rotopol/Rotoforce polishing system. The samples and standards were coated with approximately 250 Å of carbon prior to analysis. Single crystal X-ray diffraction data were collected on a Bruker APEX diffractometer. The data were collected using the program APEX and integrated with SAINT-Plus [11]. Absorption corrections and space group determinations were performed using SADABS [12] and XPREP [13], respectively. SHELXS and SHELXL were used for the crystal structure solution (direct methods) and refinement (full-matrix least-squares on F^2), within the WinGX program suite [14]. Scattering factors for all atoms were taken from the International Tables Vol C, Tables 4.2.6.8 and 6.1.1.4. Magnetic susceptibility measurements were performed using a Quantum Design MPMS.

8.2.3 Electronic Structure Calculations

Extended Hückel molecular orbital and electronic band structure calculations were carried out using YAeHMOP [15]. The default parameters were used

for all orbitals in the calculations: H_{ii} (eV) and ζ for s and p states, H_{ii} (eV), ζ_1 , c_1 , ζ_2 , c_2 for d states: Mo 5s, -8.34, 1.96; Mo 5p, -5.24, 1.9; Mo 4d, -10.5, 0.5899, 4.54, 0.5899, 1.9; Cu 4s, -11.4, 2.2; Cu 4p, -6.06, 2.2; Cu 3d, -14.0, 0.5933, 5.95, 0.5744, 2.3; Se 4s, -20.5, 2.44; Se 4p 14.4, 2.07.

GGA-PW91 [16, 17], DFT based periodic calculations were carried out in a PAW [18, 19], basis using the VASP [20] package. The plane wave cut off energy was fixed at 500 eV. A $6 \times 6 \times 6$ Monkhorst Pack [21] grid of K points was used. The optimized geometry used to calculate the band structure and density of states varied less than 3 % from the experimental values (optimized lattice parameters: $a = 6.89 \text{ \AA}$, $b = 6.92 \text{ \AA}$, $c = 8.03 \text{ \AA}$, $\alpha = 71.52^\circ$, $\beta = 72.64^\circ$, $\gamma = 84.83^\circ$). The Wigner Seitz radii used to calculate projected densities of states were 1.455 \AA for Mo, 1.312 \AA for Cu and 1.164 \AA for Se. All electronic iterations were converged within 10^{-4} eV. The density of states (DOS) are reported as number of states per eV per unit cell, so that integration of the DOS curves up to the Fermi level gives the total number of electrons in the unit cell.

8.3 Results of Intercalation Studies

8.3.1 $\text{Cu}_x\text{Mo}_6\text{S}_8$

The Chevrel phase sulfide system $\text{Cu}_x\text{Mo}_6\text{S}_8$ has been extensively studied. Of particular relevance to the current work are the results from in situ X-ray studies during the formation of these phases via electron/ion transfer [2]. These authors were able to synthesize samples with $1 \leq x \leq 4$ by electrochemical reactions. Before discussing the selenides, the main focus of our work, we briefly report here the results of the intercalation of the sulfide $\text{Cu}_2\text{Mo}_6\text{S}_8$ in our apparatus.

$\text{Cu}_2\text{Mo}_6\text{S}_8$ was synthesized as described above, with the final heating at 1100 °C. PXRD of the resulting powder showed it to be essentially single-phase, with one small peak attributed to highly oriented MoS_2 . The powder pattern was indexed with the program TREOR [22], which gave a hexagonal unit cell volume of 819.9 \AA^3 , in good agreement with previous work, which found $V = 818.3 \text{ \AA}^3$ for $x = 1.88$ [2]. This material was then intercalated in our apparatus for one day, and then removed and analyzed by PXRD. This product was then put back into the apparatus and intercalated for one more day. Measurement of the mass loss of the Cu blocks suggested an average stoichiometry of $\text{Cu}_{3.6}\text{Mo}_6\text{S}_8$ after the first intercalation run, and $\text{Cu}_{3.7}\text{Mo}_6\text{S}_8$ after the second run. The hexagonal unit cell volume determined by PXRD after the first run was 849.6 \AA^3 , and after the second run 850.4 \AA^3 . These are in good agreement with the previous study, which found $V = 849.9 \text{ \AA}^3$ for $x = 3.6$ [2]. This shows that the mass loss of the Cu reservoirs is a reliable way to determine the final stoichiometry of the intercalated compound. The same authors found that the maximum Cu content realized by high temperature reactions with subsequent slow cooling was $x = 3.66$, suggesting that phases prepared at room temperature by electrochemical reaction with $3.66 \leq x \leq 4$ are metastable. Thus, it is not surprising that our intercalation, which should stop at the thermodynamic limit of x , produced $\text{Cu}_{3.7}\text{Mo}_6\text{S}_8$.

8.3.2 $\text{Cu}_x\text{Mo}_6\text{Se}_8$

Results similar to those observed in the sulfide system were seen when $\text{Cu}_2\text{Mo}_6\text{Se}_8$ which was synthesized at 900 °C was intercalated in our apparatus. This material was intercalated for 2.5 days and then analyzed by PXRD. The product was then placed back into the apparatus and further intercalated for 3 days. After analysis of the product of the second run, a third intercalation was per-

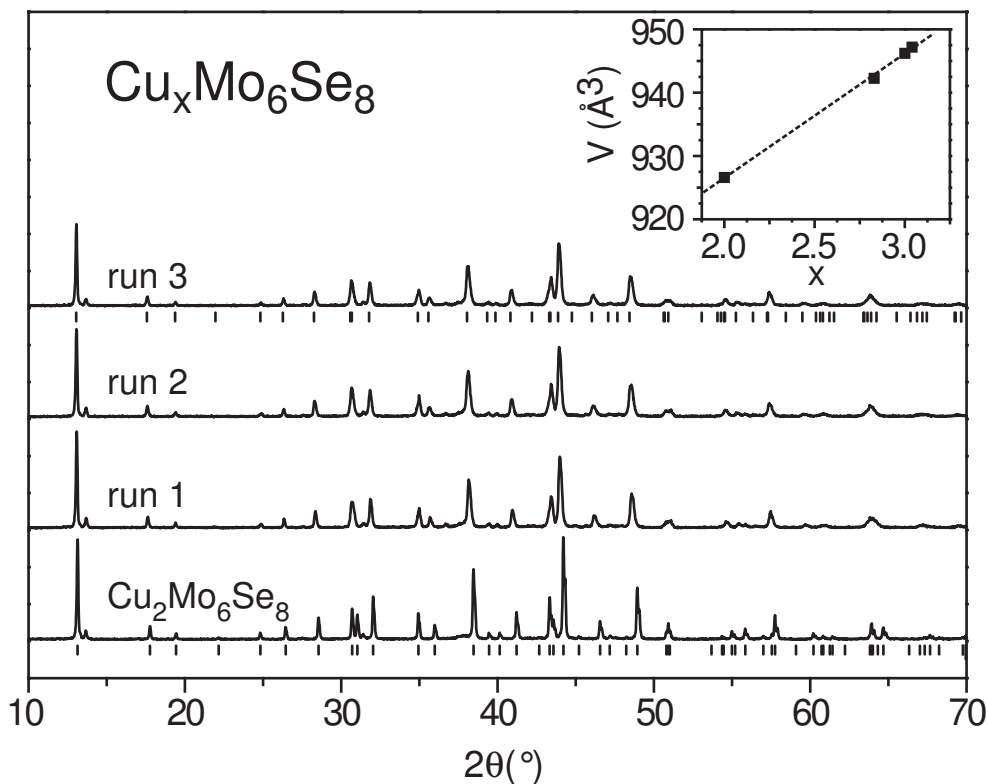


Figure 8.2: PXRD patterns for products of the intercalation of $\text{Cu}_2\text{Mo}_6\text{Se}_8$ made at 900°C . Tick marks locate the calculated peak positions for the indexed $R\bar{3}$ Chevrel phase unit cells for the starting material and for the final product. The inset shows the hexagonal unit cell volume versus composition.

formed. The PXRD patterns for the starting material and for the product after each intercalation is shown in Figure 8.2. The inset shows the indexed unit cell volume versus x determined by mass loss from the Cu blocks. The final product was $\text{Cu}_{3.04}\text{Mo}_6\text{Se}_8$, close to the maximum Cu content ($x=3.1$) that has been achieved through high temperature synthesis [1].

More interesting results were produced when the starting material was synthesized at higher temperature. $\text{Cu}_2\text{Mo}_6\text{Se}_8$ was made as described in the Experimental section, with the second heating carried out at 1100°C . This material was then heated for two days at 1200°C in a sealed evacuated silica tube. The behavior of the resulting material upon intercalation was dramatically different

than that described above for $\text{Cu}_2\text{Mo}_6\text{Se}_8$ made at $900\text{ }^\circ\text{C}$. The PXRD patterns of the starting material and the intercalation product are shown in Figure 8.3. Upon intercalation a second phase is formed, but with a significant amount of rhombohedral $\text{Cu}_x\text{Mo}_6\text{Se}_8$ still present. It is interesting to note that upon deintercalation of Cu, the mixed phase intercalation product is transformed completely into single phase Mo_6Se_8 (Figure 8.3). This shows that the transformation between rhombohedral $\text{Cu}_x\text{Mo}_6\text{Se}_8$ and the new phase at room temperature is reversible with respect to the addition/removal of Cu. Based on the reported Bragg peaks of the Cu rich phase reported by Selwyn and McKinnon [6], we believe that this is the same material they first observed. Microprobe analysis of the intercalation product showed that all of the crystallites had the stoichiometry $\text{Cu}_x\text{Mo}_6\text{Se}_8$. The average measured Cu content ($x=3.2$) was close to that determined by the Cu mass loss ($x=3.1$). However the grains could be divided in to two groups based on the value of x . One group had $x \approx 2.5$ while the second had $x \approx 4$. Thus, we conclude that the rhombohedral phase is $\text{Cu}_{2.5}\text{Mo}_6\text{Se}_8$, and the new phase is $\text{Cu}_{\sim 4}\text{Mo}_6\text{Se}_8$.

Repeated intercalations of these two-phase products did not significantly increase the fraction of $\text{Cu}_4\text{Mo}_6\text{Se}_8$, but led only to a gradual increase in the Cu content of the rhombohedral phase. This suggests that only certain crystallites in the starting material are capable of transforming into $\text{Cu}_4\text{Mo}_6\text{Se}_8$. Since this phase only forms from starting materials that have been annealed at higher temperatures, we believe that defects or impurities are important in allowing the transformation to occur. It has been shown that the high temperature synthesis ($\sim 1200\text{ }^\circ\text{C}$) of $\text{Mo}_6\text{Se}_{8-x}\text{S}_x$ can lead to the self-intercalation of Mo into the cavities [23, 24]. In addition, several authors have studied the substitution of O for S in Chevrel phases sulfides [25, 26, 27]. In these studies oxygen was intentionally added to the starting mixture in the form of binary metal oxides. X-ray and

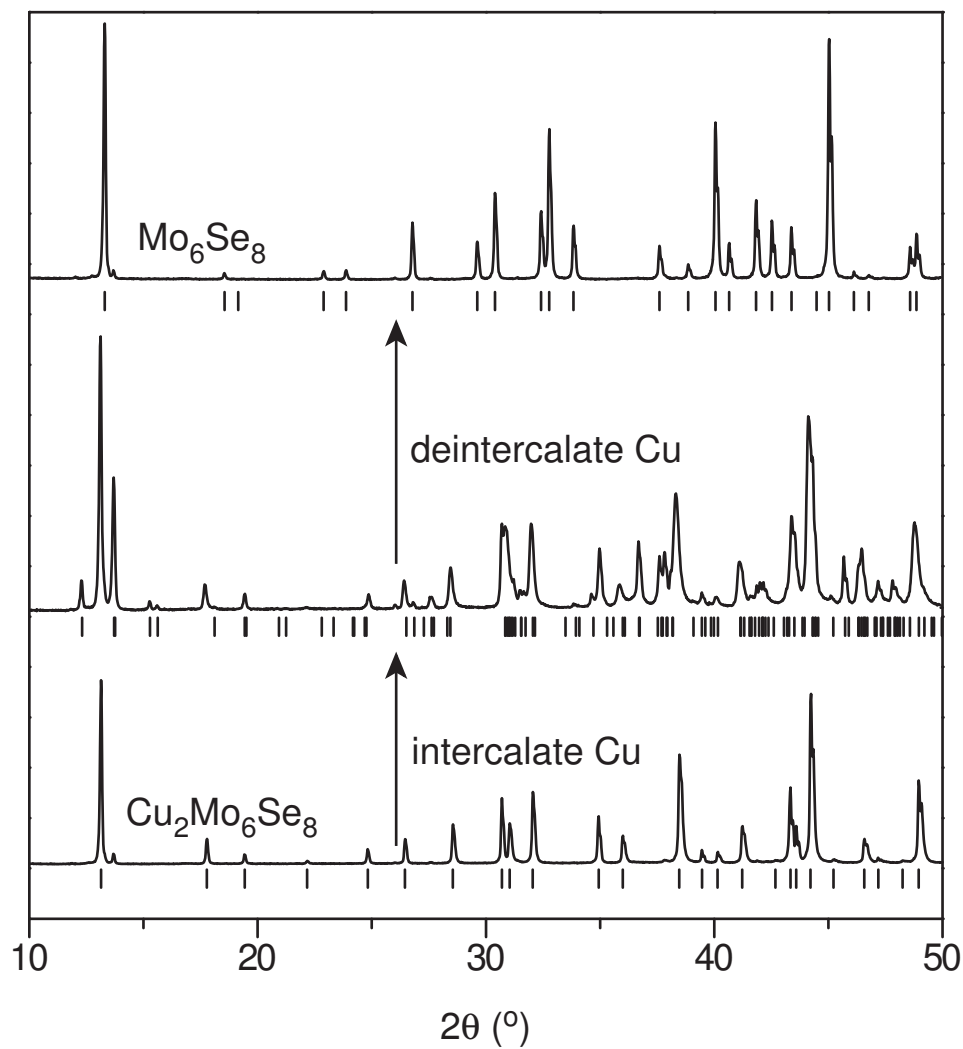


Figure 8.3: PXR D patterns showing the effect of Cu intercalation into $\text{Cu}_2\text{Mo}_6\text{Se}_8$ which was annealed at 1200°C , and the subsequent deintercalation of Cu from the intercalation product. Tick marks indicate the calculated peak positions for rhombohedral Chevrel phase unit cells in the lower and upper patterns, and the new phase $\text{Cu}_4\text{Mo}_6\text{Se}_8$ in the middle pattern.

neutron diffraction structure refinements indicated that the products had compositions near $M_x\text{Mo}_6\text{Se}_{7.8}\text{O}_{0.2}$, with $M = \text{Cu}, \text{Sn},$ and Pb . However, even with oxygen free starting materials, it is possible that some oxygen may enter the samples via the low pressure gaseous species SiO and O_2 present inside the silica tubes at high temperatures. Partial pressures of SiO and O_2 over silica near 1200°C are expected to be on the order of 10^{-6} torr [28]. We have also observed the formation of significant amounts of triclinic $\text{Cu}_4\text{Mo}_6\text{Se}_8$ from the reaction of $4\text{Cu} + 6\text{Mo} + 8\text{Se}$ at 1100°C when the starting materials (Cu and Mo) were not first reduced in forming gas. The same reaction using reduced metals showed no evidence of the triclinic phase. This supports the hypothesis that the presence of defects or impurities is important for the formation of $\text{Cu}_4\text{Mo}_6\text{Se}_8$.

8.3.3 $\text{Cu}_x\text{Mo}_6\text{Te}_8$

Chevrel phase tellurides are not likely to be promising high temperature thermoelectric materials, partly due to their lower decomposition temperatures. However, we performed preliminary studies of Cu intercalation into Mo_6Te_8 , with the aim of determining whether a Te analogue of triclinic $\text{Cu}_4\text{Mo}_6\text{Se}_8$ exists. Our room temperature intercalation of Mo_6Te_8 (which was made from the elements at 1000°C) produced a material with average composition $\text{Cu}_{1.8}\text{Mo}_6\text{Te}_8$ which had a powder pattern similar to that seen for the slightly distorted triclinic phases like $\text{Ti}_{0.88}\text{Mo}_6\text{Se}_8$. However, the PXRD pattern of the product of the reaction $4\text{Cu} + \text{Mo}_6\text{Te}_8$ at 400°C showed evidence of a $\text{Cu}_x\text{Mo}_6\text{Te}_8$ phase isostructural to triclinic $\text{Cu}_4\text{Mo}_6\text{Se}_8$.

8.3.4 Stability of $\text{Cu}_x\text{Mo}_6\text{Q}_8$ ($\text{Q} = \text{S}, \text{Se}$) in Air

Before proceeding to discuss the crystal structure and electronic structure of $\text{Cu}_4\text{Mo}_6\text{Se}_8$ in detail, we will note here briefly some observations that we have made about the stability of rhombohedral Cu filled Chevrel phases. We have found, based on PXRD studies, that when left in air over the course of several months the unit cell volumes of $\text{Cu}_x\text{Mo}_6\text{Se}_8$ samples decrease significantly. We attribute this to loss of Cu from the Chevrel phase structure, probably through reaction with oxygen at the surface of the grains. This reaction, as in removing Cu with I_2 in AN, occurs because of the high diffusion rate of the Cu in the bulk Chevrel phase. In addition, in some cases the PXRD peaks were broadened, with tails extending toward higher angle. For example, based on a comparison of powder patterns, the $\text{Cu}_{3.04}\text{Mo}_6\text{Se}_8$ intercalation product described above transformed into $\text{Cu}_{\sim 2}\text{Mo}_6\text{Se}_8$ over the course of five months. The $\text{Cu}_2\text{Mo}_6\text{Se}_8$ (synthesized at 900 °C) used as a starting material for the intercalations also showed significant peak broadening and shifts and toward lower Cu content after storage in air for about six months. However, no change was seen in the sulfide intercalation product $\text{Cu}_{3.7}\text{Mo}_6\text{S}_8$ upon exposure to air for ten months. Finally, we note that when a mixed phase intercalation product containing rhombohedral $\text{Cu}_{2.5}\text{Mo}_6\text{Se}_8$ and triclinic $\text{Cu}_4\text{Mo}_6\text{Se}_8$ was left in air for six months, Cu loss from the rhombohedral phase was observed, while the positions and widths of PXRD peaks corresponding to $\text{Cu}_4\text{Mo}_6\text{Se}_8$ did not perceptibly change. At present, it is not clear why the "stability" of these different compounds is different.

8.4 Crystal Structure of $\text{Cu}_4\text{Mo}_6\text{Se}_8$

Small crystallites were extracted from the two-phase intercalation product and used for single crystal diffraction studies. While the first crystal selected in-

dexed to a rhombohedral unit cell consistent with $\text{Cu}_{2.5}\text{Mo}_6\text{Se}_8$, the second gave a triclinic cell ($R_{int} = 0.0413$) which matched well with the observed PXRD pattern (see Figure 8.3). The results of the structure refinement from data collected using this crystal are listed in Table 8.1. Refined atom positions and displacement parameters are listed in Tables 8.2 and 8.3. In the reported data, all atomic sites are refined fully occupied. When allowed to refine freely, the occupancy of Cu(1) and Cu(2) refine to 0.987(5) and 0.985(5), respectively, giving a stoichiometry of $\text{Cu}_{3.94}\text{Mo}_6\text{Se}_8$. The corresponding R values for $I > 2 \sigma(I)$ were $R_1 = 0.0331$ and $wR_2 = 0.0668$, reduced only slightly from the refinement with fully occupied Cu sites which gave $R_1 = 0.0333$ and $wR_2 = 0.0697$. The residual electron density does not suggest the presence of other atoms in this structure. All but one of the first twenty residuals peaks are close to other the atoms in the structure ($d < 2 \text{ \AA}$, and for many $d < 1.5 \text{ \AA}$). These peaks are likely due to truncation of the diffraction data at $2\theta = 55.16^\circ$. The remaining residual (2.07 e/ \AA^3) is at the special position $(0, 1/2, 1/2)$, with Se as a nearest neighbor, at a distance of 2.18 \AA . However, when an Mo, Cu, or O atom is placed at this position, the occupancy of the site refines essentially to zero (< 0.009).

The structure of this compound will be discussed here in terms of "sheets" of composition Mo_6Se_8 shown in Figure 8.4, and "columns" of composition $\text{Cu}_4\text{Mo}_6\text{Se}_8$ shown in Figure 8.5. The sheets consist of pseudo-cubic Mo_6Se_8 units connected by inter-cluster Mo-Se bonds. These same sheets are seen in the classic rhombohedral Chevrel phases. However, in the rhombohedral structures (and the slightly distorted triclinic structures) this same connectivity is also present perpendicular to the sheets, giving a 3-dimensional framework of Mo_6Se_8 units connected by inter-cluster Mo-Se bonds. In $\text{Cu}_4\text{Mo}_6\text{Se}_8$, on the other hand, a different connectivity exists between the sheets, as shown in Figure 8.5. The clusters are aligned along the c-axis face to face, with Cu atoms separating the Mo_6Se_8

Table 8.1: Single crystal refinement data for $\text{Cu}_4\text{Mo}_6\text{Se}_8$.

Empirical formula	$\text{Cu}_4\text{Mo}_6\text{Se}_8$	
Temperature	175(5) K	
Wavelength	0.71073 Å	
Crystal system	Triclinic	
Space Group	$\bar{P}1$	
Unit cell dimensions	$a = 6.7609(8)$ Å	$\alpha = 70.739(4)^\circ$
	$b = 6.8122(7)$ Å	$\beta = 72.669(4)^\circ$
	$c = 7.9355(10)$ Å	$\gamma = 84.555(5)^\circ$
Volume	$329.36(7)$ Å ³	
Absorption Correction	SADABS	
Color	Black	
Z	1	
Calculated density	7.449 g/cm ³	
Absorption coefficient	33.894 mm ⁻¹	
θ range	2.84 ° to 27.58 °	
Independent reflections	1496	[R(int) = 0.0413]
Completeness to $\theta=27.58^\circ$	98.2 %	
Data/restraints/parameters	1496 / 0 / 82	
Goodness-of-fit on F^2	0.958	
Final R indices ($I > 2\sigma(I)$)	$R_1 = 0.0333$	$wR_2 = 0.0697$
R indices (all data)	$R_1 = 0.0575$	$wR_2 = 0.0755$
Largest diff. peak and hole	2.167 and -1.406 eÅ ⁻³	

$$R_1 = \frac{\sum ||F_o| - |F_c||}{\sum |F_o|} \quad wR_2 = \left[\frac{\sum w(F_o^2 - F_c^2)^2}{\sum w(F_o^2)^2} \right]^{\frac{1}{2}}$$

$$w^{-1} = [\sigma(F_o^2) + (aP)^2 + bP] \quad \text{where } P = [\max(F_o^2, 0) + 2F_c^2] / 3$$

Table 8.2: Atomic coordinates and equivalent isotropic displacement parameters (\AA^2) for $\text{Cu}_4\text{Mo}_6\text{Se}_8$. U_{eq} is defined as one third of the trace of the orthogonalized U_{ij} tensor.

Atom	x	y	z	U_{eq}
Cu(1)	0.2111(2)	0.0299(2)	0.0709(2)	0.014(1)
Cu(2)	0.4713(2)	0.7023(2)	0.0854(2)	0.014(1)
Mo(1)	0.5075(1)	0.0125(1)	0.2581(1)	0.005(1)
Mo(2)	0.4225(1)	0.2830(1)	0.4530(1)	0.005(1)
Mo(3)	0.7834(1)	0.0780(1)	0.4123(1)	0.005(1)
Se(1)	0.1378(2)	0.1849(1)	0.7703(1)	0.006(1)
Se(2)	0.1657(2)	0.2219(1)	0.2942(1)	0.006(1)
Se(3)	0.2911(2)	0.6685(1)	0.4042(1)	0.006(1)
Se(4)	0.6997(1)	0.3679(1)	0.1314(1)	0.007(1)

Table 8.3: The anisotropic displacement parameters (\AA^2) for the compound $\text{Cu}_4\text{Mo}_6\text{Se}_8$. The exponent of the anisotropic displacement factor is of the form: $-2\pi^2(h^2a^{*2}U_{11}+\dots+2hka^*b^*U_{12})$.

Atom	U_{11}	U_{22}	U_{33}	U_{23}	U_{13}	U_{12}
Cu(1)	0.013(1)	0.022(1)	0.011(1)	-0.009(1)	-0.004(1)	0.001(1)
Cu(2)	0.021(1)	0.011(1)	0.009(1)	-0.003(1)	-0.004(1)	-0.001(1)
Mo(1)	0.005(1)	0.006(1)	0.005(1)	-0.003(1)	-0.001(1)	-0.001(1)
Mo(2)	0.005(1)	0.005(1)	0.004(1)	-0.002(1)	-0.001(1)	-0.001(1)
Mo(3)	0.005(1)	0.005(1)	0.005(1)	-0.002(1)	-0.001(1)	-0.001(1)
Se(1)	0.006(1)	0.007(1)	0.005(1)	-0.002(1)	-0.001(1)	-0.001(1)
Se(2)	0.006(1)	0.006(1)	0.005(1)	-0.002(1)	-0.001(1)	-0.001(1)
Se(3)	0.006(1)	0.005(1)	0.007(1)	-0.002(1)	-0.002(1)	-0.001(1)
Se(4)	0.006(1)	0.007(1)	0.005(1)	0.000(1)	-0.001(1)	-0.002(1)

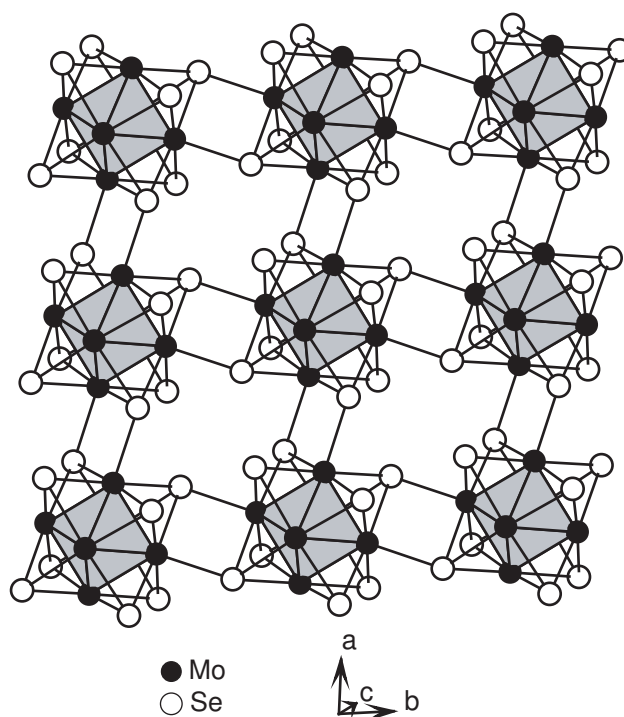


Figure 8.4: A view of the sheets of connected Mo_6Se_8 units found roughly in the ab -plane of the $\text{Cu}_4\text{Mo}_6\text{Se}_8$ structure.

units in adjacent sheets. Inter-sheet connections are made solely by Cu-Se interactions.

In $\text{Cu}_4\text{Mo}_6\text{Se}_8$, the Mo(1) atoms which are nearest the Cu atoms are in square planar coordination by Se, while Mo(2) and Mo(3) are in square pyramidal coordination due to the inter-cluster Mo-Se bonds. We will see below that the square planar coordination of Mo(1), which is not seen in classic Chevrel phase compounds, has important electronic implications. The coordination of the Mo atoms, as well as the Cu atoms which are each coordinated to three Se atoms, is shown in Figure 8.6a. The CuSe_3 units are not planar. The perpendicular distance between the Cu atom and the plane defined by the three coordinating Se atoms (Figure 8.6b) is 0.92 Å and 0.98 Å for Cu(1) and Cu(2), respectively. Linear two-

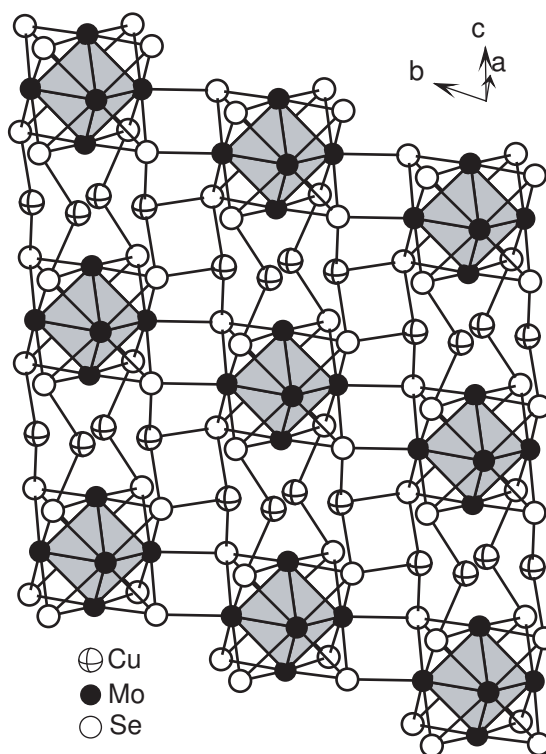


Figure 8.5: A view of the crystal structure of $\text{Cu}_4\text{Mo}_6\text{Se}_8$ showing the connection via Cu atoms of the Mo_6Se_8 sheets shown in Figure 8.4.

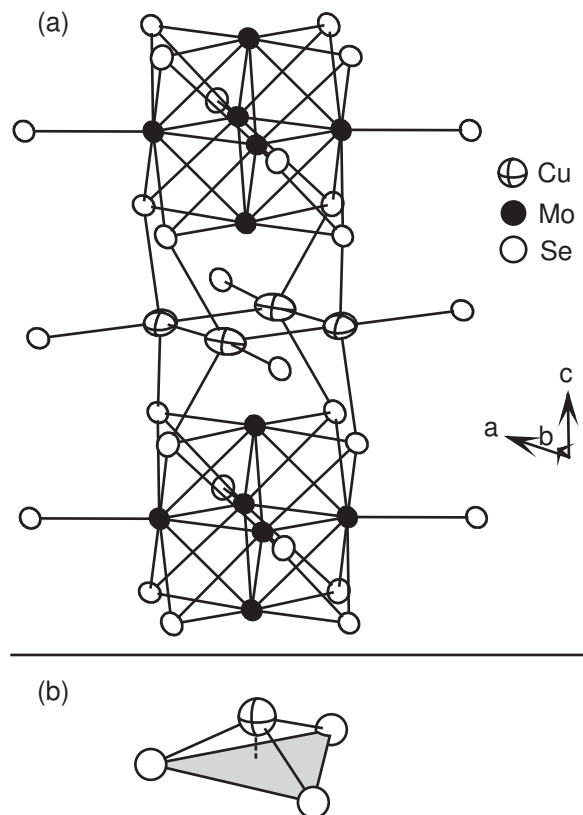


Figure 8.6: (a) A portion of the $\text{Cu}_4\text{Mo}_6\text{Se}_8$ structure showing the displacement ellipsoids (95% level) for all atoms, and the full 3-dimensional coordination of the Cu and Mo atoms. (b) The coordination of Cu by Se, emphasizing the elevation of the Cu atoms (dotted line) above the plane of the coordinating Se atoms.

fold and tetrahedral four-fold coordination are most common for Cu^{1+} , however puckered triangular units are also frequently observed (for example, $\text{Tl}_2\text{Cu}_3\text{Se}_2$ [29], TlCu_7Se_4 [30], and CsCu_5S_3 [31]).

Interatomic distances in this compound are reported in Table 8.4, where the connections between the columns in the structure are marked with asterisks. The Cu-Cu distances are significantly longer than twice the ionic radius for Cu^{1+} in four-fold coordination (0.6 Å) [32]. The intra-column Cu-Se distances are similar to those found in Cu_2Se (2.33 Å, 2.47 Å) [33], Cu_3PSe_4 (2.39 - 2.47 Å) [34], CuInSe_2 (2.43 Å) [35], and in $\text{Cu}_2\text{Mo}_6\text{Se}_8$ (2.36 - 2.58 Å) [36], while the inter-column distances are slightly longer. The Mo-Mo and Mo-Se distances in Table 8.4 are similar to those found in Mo_6Se_8 , in which the Mo-Mo distances are 2.69 - 2.84 Å, the intracluster Mo-Se distances are 2.55 - 2.59 Å, and the intercluster Mo-Se distance is 2.60 Å [37]. In $\text{Cu}_4\text{Mo}_6\text{Se}_8$ the distances among the five coordinate Mo(2) and Mo(3) atoms are not seen to be significantly different than the distances between Mo(2)/Mo(3) and the four coordinate Mo(1) atom. It does not seem that the difference in coordination significantly distorts the Mo octahedron. In fact, inspection of the distances in Table 8.4 shows that the Mo_6 octahedra in $\text{Cu}_4\text{Mo}_6\text{Se}_8$ are quite regular.

A more quantitative measure of the distortion can be gained by comparison of continuous shape measures for the Mo_6 clusters in $\text{Cu}_4\text{Mo}_6\text{Se}_8$ and in other Chevrel phases with known crystal structures [38, 39]. The continuous shape measure S is a measure of the minimum distance needed to move the vertices of a distorted polyhedron to match a given reference shape. Values of S , obtained by comparing the Mo_6 clusters found in $\text{Cu}_4\text{Mo}_6\text{Se}_8$ and all $\text{M}_x\text{Mo}_6\text{Se}_8$ Chevrel phases listed in the current version of the Inorganic Crystal Structure Database (ICSD) to a perfect octahedron, are listed in Table 8.5. These calculations were performed using the program SHAPE [40]. For a perfect, octahedral cluster, $S =$

Table 8.4: Interatomic distances (Å) in $\text{Cu}_4\text{Mo}_6\text{Se}_8$.

Mo(1)-Mo(2)	2.6958(11), 2.6372(11)
Mo(1)-Mo(3)	2.6555(12), 2.6818(12)
Mo(2)-Mo(3)	2.6814(11), 2.6751(12)
Mo(1)-Se(1)	2.6225(12)
Mo(1)-Se(2)	2.5897(12)
Mo(1)-Se(3)	2.6122(13)
Mo(1)-Se(4)	2.6029(13)
Mo(2)-Se(1)	2.5960(13)
Mo(2)-Se(2)	2.5618(13)
Mo(2)-Se(3)	2.6115(13), 2.6319(12)*
Mo(2)-Se(4)	2.5965(13)
Mo(3)-Se(1)	2.5809(12)
Mo(3)-Se(2)	2.6316(12), 2.6368(13)*
Mo(3)-Se(3)	2.5329(12)
Mo(3)-Se(4)	2.6121(12)
Cu(1)-Se(1)	2.4482(15), 2.6386(17)*
Cu(1)-Se(2)	2.4641(16)
Cu(2)-Se(3)	2.4021(16)
Cu(2)-Se(4)	2.5217(16), 2.6124(15)*
Cu(1)-Cu(2)	2.6718(19), 2.7011(17)
Mo(1)-Cu(1)	2.8013(15), 2.8201(15)
Mo(1)-Cu(2)	2.7478(15), 2.9348(15)

* denotes inter-columnar connections.

0. It is interesting to note that $\text{Li}_{3.2}\text{Mo}_6\text{Se}_8$ has $S = 0$. Table 8.5 shows that the Mo_6 cluster in $\text{Cu}_4\text{Mo}_6\text{Se}_8$ is more regular than those found in unfilled Mo_6Se_8 , and in filled Chevrel phases which undergo triclinic distortions. In fact, it is among the least distorted Mo_6 clusters found in the listed selenide Chevrel phases.

Also shown in Table 8.5 are the calculated S values for the sulfide series $\text{Cu}_x\text{Mo}_6\text{S}_8$. Inspection of these data show a smooth decrease in S from Mo_6S_8 to $\text{Cu}_{3.66}\text{Mo}_6\text{S}_8$. As x increases, the Mo_6 octahedra become more regular. This is a result the filling of Mo-Mo intracluster bonding orbitals by valence electrons donated by Cu (vide infra). For $x \geq 2.76$ in the sulfide series, the Mo_6 octahedra are more regular than that found in triclinic $\text{Cu}_4\text{Mo}_6\text{Se}_8$. This must be attributed, at least in part, to the different coordination environment of Mo(1) and the lower symmetry in $\text{Cu}_4\text{Mo}_6\text{Se}_8$.

8.5 Electronic Structure of Triclinic $\text{Cu}_4\text{Mo}_6\text{Se}_8$

The band structure of $\text{Cu}_4\text{Mo}_6\text{Se}_8$, calculated using plane-wave DFT is shown in Figure 8.7. The calculations show this compound to be a semimetal, with a single band dipping below the Fermi level at R. Figure 8.8 shows the corresponding density of states, and projected densities of states. This figure shows that the band just above the Fermi level is derived primarily from Mo orbitals, with some Se and Cu contributions. We find that, near the Fermi level, there is good agreement between the DFT results shown in Figure 8.7 and the band structure calculated at the extended Hückel level. Thus, we proceed to analyze the electronic structure of this compound using extended Hückel methods, paying particular attention to the band that lies between about -6 eV and -5.5 eV in Figure 8.7.

Table 8.5: Continuous Symmetry Measures S for the molybdenum octahedra in $\text{Cu}_4\text{Mo}_6\text{Se}_8$, all $\text{M}_x\text{Mo}_6\text{Se}_8$ Chevrel phases listed in the current version of the ICSD, and the series $\text{Cu}_x\text{Mo}_6\text{S}_8$.

$\text{Cu}_4\text{Mo}_6\text{Se}_8$	0.01117
Mo_6Se_8	0.15117
$\text{Li}_{3.2}\text{Mo}_6\text{Se}_8$	0.00000
PbMo_6Se_8	0.01030
InMo_6Se_8	0.01110
$\text{Ti}_{0.88}\text{Mo}_6\text{Se}_8$	0.05207*
FeMo_6Se_8	0.05226*
$\text{Co}_{0.54}\text{Mo}_6\text{Se}_8$	0.05752
$\text{Ni}_{0.33}\text{Mo}_6\text{Se}_8$	0.11923*
$\text{Ni}_{1.25}\text{Mo}_6\text{Se}_8$	0.07502
$\text{La}_{0.82}\text{Mo}_6\text{Se}_8$	0.01406
$\text{La}_{0.84}\text{Mo}_6\text{Se}_8$	0.01520
$\text{La}_{0.88}\text{Mo}_6\text{Se}_8$	0.01406
$\text{La}_{0.94}\text{Mo}_6\text{Se}_8$	0.01198
$\text{Ce}_{0.82}\text{Mo}_6\text{Se}_8$	0.01473
$\text{Ce}_{0.92}\text{Mo}_6\text{Se}_8$	0.01182
$\text{Pr}_{0.86}\text{Mo}_6\text{Se}_8$	0.01485
$\text{Nd}_{0.85}\text{Mo}_6\text{Se}_8$	0.01737
$\text{Sm}_{0.87}\text{Mo}_6\text{Se}_8$	0.01812
$\text{U}_{0.8}\text{Mo}_6\text{Se}_8$	0.02105
$\text{Cu}_{1.8}\text{Mo}_6\text{S}_8$	0.03343
$\text{Cu}_{2.77}\text{Mo}_6\text{S}_8$	0.00985
$\text{Cu}_{2.94}\text{Mo}_6\text{S}_8$	0.00742
$\text{Cu}_{3.66}\text{Mo}_6\text{S}_8$	0.00377

* denotes distorted, triclinic structures.

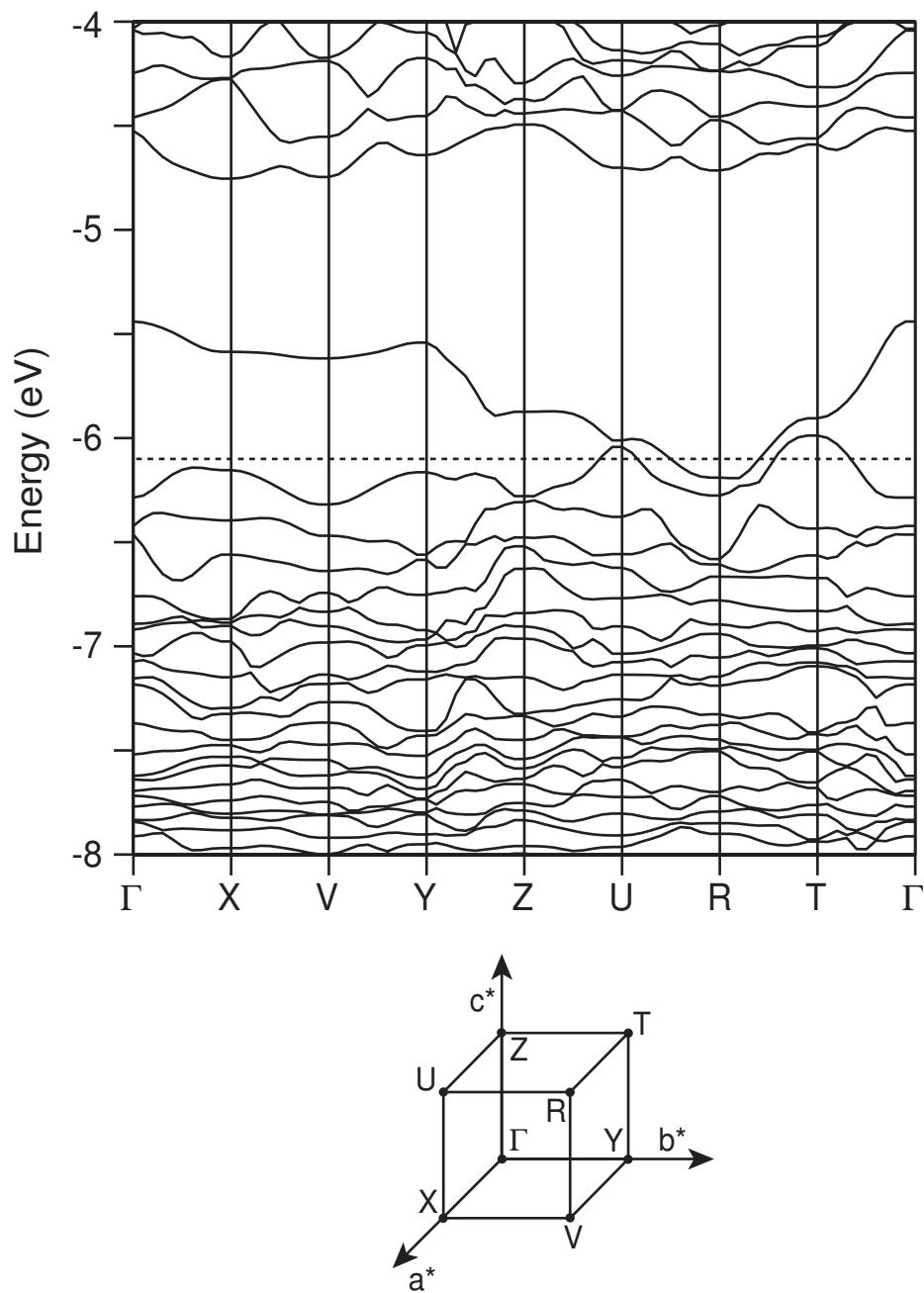


Figure 8.7: The band structure of $\text{Cu}_4\text{Mo}_6\text{Se}_8$ calculated using DFT. The dotted line represents the Fermi level. The location of the special k-points used in the band structure plot are also shown.

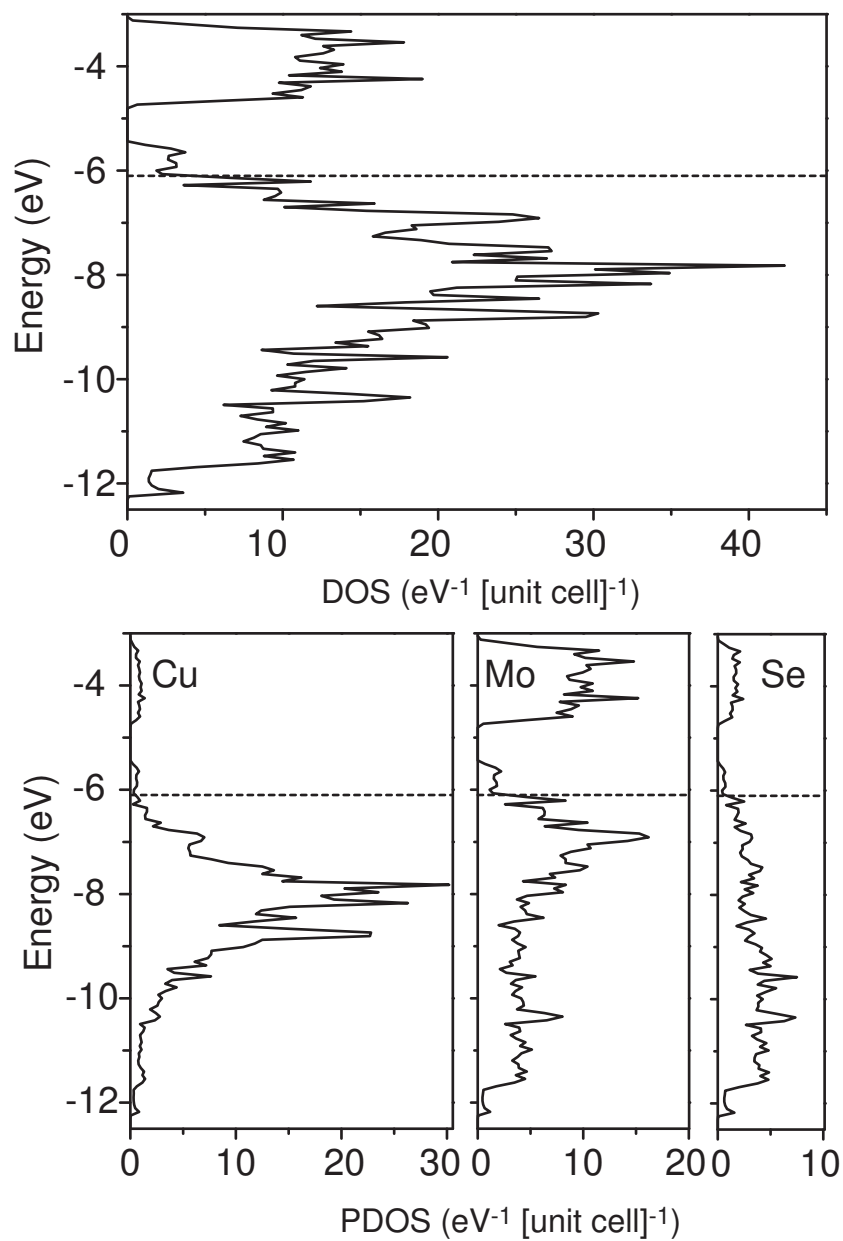


Figure 8.8: The calculated total density of states per unit cell (DOS) and partial densities of states (PDOS) for $\text{Cu}_4\text{Mo}_6\text{Se}_8$ calculated with DFT.

We begin by examining the molecular orbitals of an ideal Mo_6Se_8 cluster, that is, a perfect cube of Se atoms with Mo atoms at the centers of the six faces. A careful study of this model for the sulfide cluster, and the effect of crystallizing these clusters in the Chevrel phase motif, has been presented by Hughbanks and Hoffmann [41]. They find that the frontier orbitals are all primarily Mo 4d in character. Upon crystallization, the faces of the cube are capped by chalcogens on neighboring clusters, which pushes a set of five unoccupied orbitals up in energy. These orbitals all have large lobes directed out of the cube faces toward the capping sulfur atoms. The increase in energy of these orbitals produces a large HOMO-LUMO gap for the cluster of charge -4. This is the molecular origin of the energy gap seen in the semiconducting Chevrel phases.

We show results from a similar calculation for the neutral selenide cluster in Figure 8.9. In this figure, panel (b) shows molecular orbitals for the uncapped Mo_6Se_8 cluster, while (a) shows the results of capping each face with Se. These MO diagrams are very similar to those calculated for the sulfide cluster [41]. Panel (c) in Figure 8.9 shows the result of capping only four of the six faces of the cubic cluster. This approximates the situation found in $\text{Cu}_4\text{Mo}_6\text{Se}_8$. In this case, we see that two of the five energy levels are "left behind". These correspond to orbitals directed primarily out of the uncapped faces. Representations of these orbitals, labeled MO 1 and MO 2, are also shown in Figure 8.9(c). We will see that it is MO 1 which evolves into the band of interest in the 3 dimensional structure.

Figure 8.10 shows how the band structure of the 3 dimensional structure evolves from the MO diagram shown in Figure 8.9(c). For ease of comparison, this MO diagram is reproduced in panel (a) of Figure 8.10. Panel (b) shows the bands for a single sheet of composition Mo_6Se_8 , extracted from the structure of $\text{Cu}_4\text{Mo}_6\text{Se}_8$. As expected, band 1 and band 2, which originate from MO 1 and MO

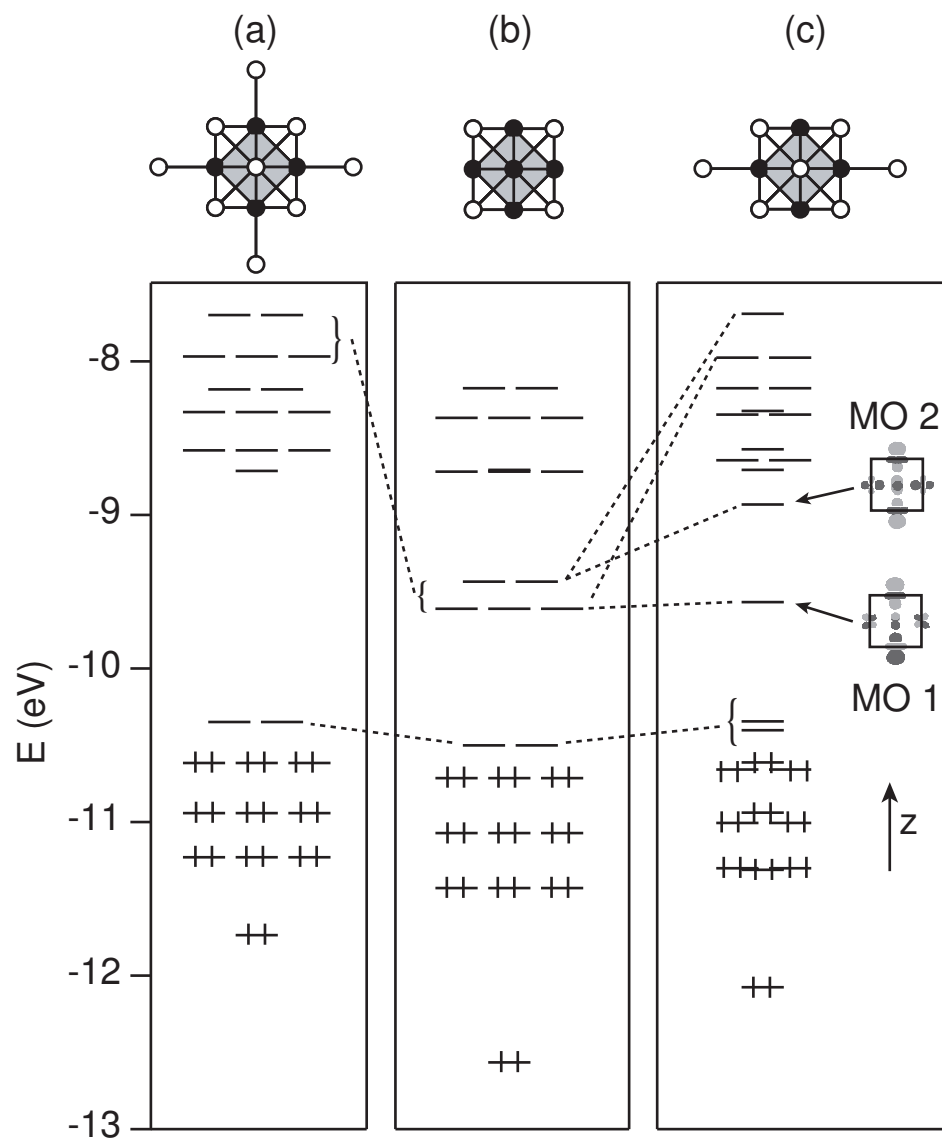


Figure 8.9: Extended Hückel molecular orbital diagrams for (a) an Mo₆Se₈ cluster with six capping Se atoms as found in classic Chevrel phases, (b) a bare Mo₆Se₈ cluster, and (c) an Mo₆Se₈ cluster with four equatorial Se ligands, as found in Cu₄Mo₆Se₈.

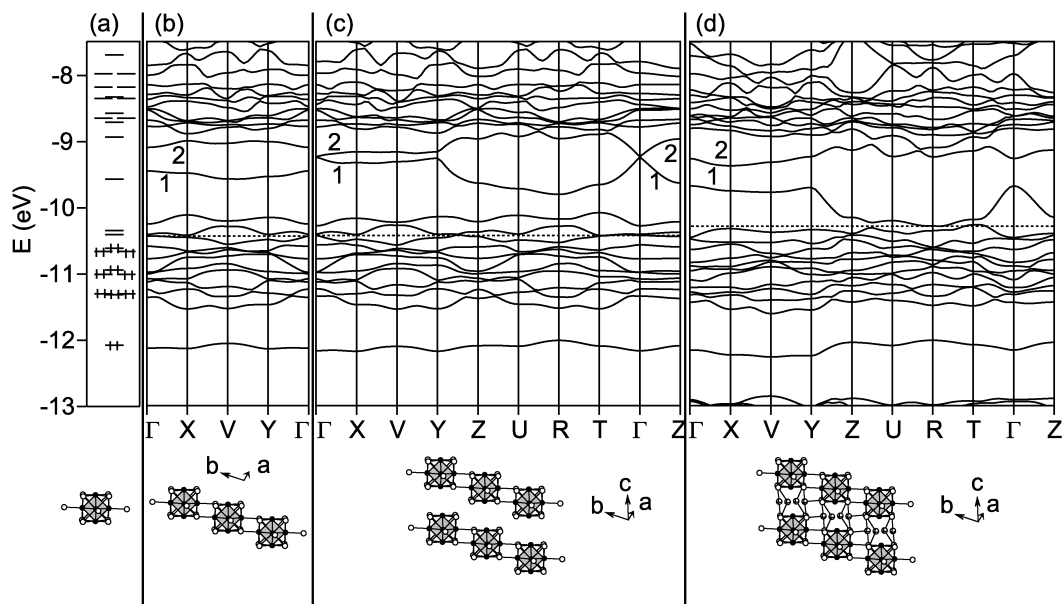


Figure 8.10: The evolution of the band structure (extended Hückel of $\text{Cu}_4\text{Mo}_6\text{Se}_8$ from (a) molecular orbitals, to (b) two dimensional sheets, to (c) stacked sheets, to (d) the full $\text{Cu}_4\text{Mo}_6\text{Se}_8$ structure.

2, show little dispersion, since these MOs are primarily directed perpendicular to the sheet.

Figure 8.10(c) shows the calculated band structure for a stack of such sheets, like that which occurs in $\text{Cu}_4\text{Mo}_6\text{Se}_8$. Here significant band dispersion is observed in band 1 and band 2, especially in directions perpendicular to the sheets. We see that band 1 runs down from Γ to Z, while band 2 runs up. This is consistent with the reflection symmetry of MO 2 (mirror plane perpendicular to the z-direction) and the reflection antisymmetry of MO 1 (Figure 8.9). We note here that the apparent degeneracy of these two bands at Γ is accidental.

Finally, Figure 8.10(d) shows the extended Hückel band structure for the full $\text{Cu}_4\text{Mo}_6\text{Se}_8$ structure. We first note the striking similarities to the band structure calculated using DFT (see Figure 8.7), especially near the Fermi level. The only difference between the crystal structures in Figure 8.10(c) and (d) is the Cu

atoms which are included in (d), but not in (c). Figure 8.10(c) shows that, in the rigid band approximation, the four electrons donated to the Mo_6Se_8 framework by four Cu^{1+} ions would produce a semiconducting compound, filling the two empty bands below band 1. However, since the Cu atoms in $\text{Cu}_4\text{Mo}_6\text{Se}_8$ are situated between the uncapped cluster faces, they interact with bands 1 and 2. This interaction lowers the energy of band 1 so that it dips below the Fermi level, making $\text{Cu}_4\text{Mo}_6\text{Se}_8$ a semimetal, not a semiconductor.

8.6 Magnetic Susceptibility Measurements

Since many metallic phases with the classical Chevrel phase structure are superconducting, magnetic susceptibility measurements were performed between 4 K and 20 K on a powder sample containing a mixture of approximately equal amounts of $\text{Cu}_{\sim 2}\text{Mo}_6\text{Se}_8$ and $\text{Cu}_4\text{Mo}_6\text{Se}_8$. The results are shown in Figure 8.11. The measurements showed only a single superconducting transition near 6 K. This is close to the previously measured T_C for $\text{Cu}_2\text{Mo}_6\text{Se}_8$ of 5.9 K [8]. At 4 K the diamagnetic susceptibility had not yet saturated, and its value suggests that about 30% (by volume) of the sample was superconducting at this temperature. These observations suggest that $\text{Cu}_4\text{Mo}_6\text{Se}_8$ is not a superconductor above 4 K.

8.7 Conclusions

In this work we have demonstrated an alternative method for intercalating Cu into Chevrel phase materials ($\text{Cu}_x\text{Mo}_6\text{Q}_8$, Q=S, Se, Te) at room temperature. This method produced maximum Cu contents in agreement with those reported for high temperature syntheses for the sulfides ($x=3.7$) and selenides ($x=3.0$). The success of this, and other intercalation methods, is dependent upon the relatively high mobility of Cu ions in the Chevrel phase structure. This ionic conduction

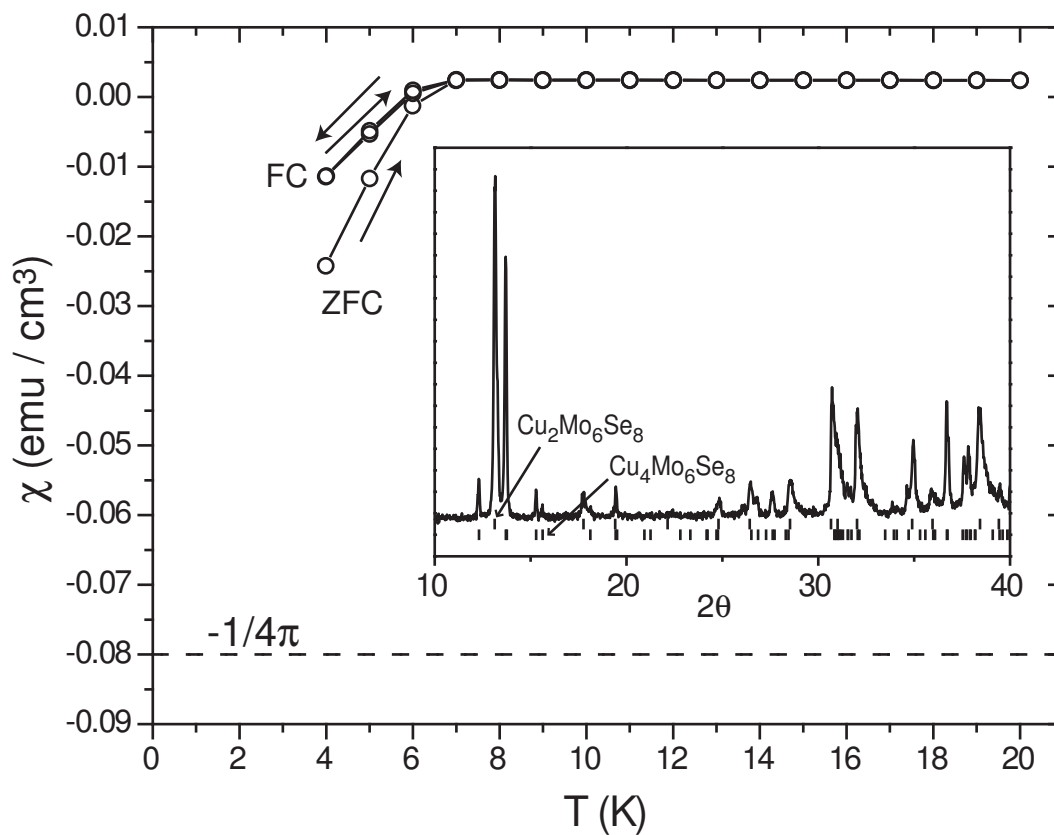


Figure 8.11: The measured magnetic susceptibility per unit volume of a mixture of $\text{Cu}_{2-2}\text{Mo}_6\text{Se}_8$ and $\text{Cu}_4\text{Mo}_6\text{Se}_8$ between 4 K and 20 K. Zero field cooled (ZFC) and field cooled (FC) data are shown. The inset shows the PXRD pattern of the sample, with ticks marking calculated peak positions for the two phases.

may limit the use of Cu filled Chevrel phases for high temperature thermoelectric power generators.

These studies also led to the identification of the new Chevrel phase polymorph $\text{Cu}_4\text{Mo}_6\text{Se}_8$, which had been previously observed only as unidentified reflections in powder diffraction studies [6]. We have reported here the structure of this phase, determined by single crystal X-ray diffraction. This structure represents the first example of extended Mo_6Se_8 sheets which are not connected to one another through Mo-Se bonding. The location of the Cu atoms, between faces of Mo_6Se_8 clusters in neighboring sheets, separates the layers along the c axis. The only connections between the layers are through Cu-Se interactions.

The separation of the Mo_6Se_8 layers and the location of the Cu atoms have interesting electronic consequences. Although $\text{Cu}_4\text{Mo}_6\text{Se}_8$ has formally 24 electrons per metal cluster, and therefore should be a semiconductor according to the usual electron counting schemes, band structure calculations predict this material to be metallic. Analysis of extended Hückel calculations show this to be due to the interaction between the Cu atoms and Mo based molecular orbital pointed toward the "missing" Se.

REFERENCES

- [1] T. Caillat, J.-P. Fleurial, and G. Snyder, *Solid State Sciences* **1**, 535 (1999).
- [2] C. Fischer, E. Gocke, U. Stege, and R. Schoellhorn, *J. Solid State Chem.* **102**, 54 (1993).
- [3] J. Dahn, W. McKinnon, and S. Coleman, *Phys. Rev. B* **31**, 484 (1985).
- [4] E. Gocke, W. Schramm, P. Dolscheid, and R. Schoellhorn, *J. Solid State Chem.* **70**, 71 (1987).
- [5] M. Levi et al., *Journal of Electroanalytical Chemistry* **569**, 211 (2004).
- [6] L. S. Selwyn and W. McKinnon, *J. Phys. C: Solid State Phys.* **21**, 1905 (1988).
- [7] S. Belin, R. Chevrel, and M. Sergent, *J. Solid State Chem.* **145**, 159 (1999).
- [8] O. Fischer and M. Maple, *Topics in Current Physics: Superconductivity in Ternary Compounds I*, Springer-Verlag, 1982.
- [9] J. Tarascon, J. Waszczak, G. Hull, F. DiSalvo, and L. Blitzer, *Solid State Comm.* **47**, 973 (1983).
- [10] G. Janz and R. Tomkins, *Nonaqueous Electrolytes Handbook II*, Academic Press, 1973.
- [11] Apex2 (version 1.22, 2004) and saint-plus (version 7.06a, 2003), Bruker Analytical X-ray Instruments, Inc., Madison, WI.
- [12] SADABS program for absorption correction, G.M. Sheldrick for Bruker Analytical X-ray Instruments, Inc., Madison, WI, 2000.
- [13] XPREP program for determination of space groups, Bruker Analytical X-ray Instruments, Inc., Madison, WI, 2000.
- [14] L. Farrugia, *J. Appl. Cryst.* **32**, 837 (1999).
- [15] YAeHMOP (Version 3.0), G. Landrum, <http://yaehmop.sourceforge.net>, 1999.
- [16] J. Perdew et al., *Phys. Rev. B* **46**, 6671 (1992).
- [17] J. Perdew et al., *Phys. Rev. B* **48**, 4978 (1993).
- [18] P. Bloechl, *Phys. Rev. B* **50**, 17953 (1994).
- [19] G. Kresse and D. Joubert, *Phys. Rev. B* **59**, 1758 (1999).
- [20] G. Kresse and J. Hafner, *Phys. Rev. B* **47**, 558 (1993).

- [21] H. J. Monkhorst and J. Pack, *Phys. Rev. B* **13**, 5188 (1976).
- [22] P.-E. Werner, L. Eriksson, and M. Westdahl, *J. Appl. Cryst.* **18**, 367 (1985).
- [23] S. Belin, R. Chevrel, and M. Sergent, *J. Solid State Chem.* **145**, 159 (1999).
- [24] S. Belin, L. Burel, R. Chevrel, and M. Sergent, *Mater. Res. Bull.* **35**, 151 (2000).
- [25] R. Cerny, K. Yvon, M. Wakihara, and P. Fischer, *J. Alloys Compd.* **209**, L29 (1994).
- [26] C. Chang, Y. Tao, J. Swinnea, and H. Steinfink, *Acta Crystallogr.* **C43**, 1461 (1987).
- [27] D. Hinks, J. Jorgensen, and H.-C. Li, *Phys. Rev. Lett.* **51**, 1911 (1983).
- [28] H. Schick, *Chem. Rev.* **60**, 331 (1960).
- [29] R. Berger and L. Erikson, *J. Less-Common Metals* **161**, 101 (1990).
- [30] L. Eriksson, P.-E. Werner, R. Berger, and A. Meerschaut, *J. Solid State Chem.* **90**, 61 (1991).
- [31] J. Hunter and W. Bronger, *Z. Anorg. Allg. Chem.* **627**, 1395 (2001).
- [32] R. Shannon, *Acta Crystallogr.* **A32**, 751 (1974).
- [33] K. Yamamoto and S. Kashida, *J. Solid State Chem.* **93**, 202 (1991).
- [34] J. Garin and E. Parthe, *Acta Crystallogr.* **B28**, 3672 (1972).
- [35] K. Knight, *Mater. Res. Bull.* **27**, 161 (1972).
- [36] E. Kaldis, *Current Topics in Materials Science vol. 3*, Elsevier, 1979.
- [37] O. Bars, J. Guillevic, and D. Grandjean, *J. Solid State Chem.* **6**, 48 (1973).
- [38] M. Pinsky and D. Avnir, *Inorg. Chem.* **37**, 5575 (1998).
- [39] H. Zabrodsky, S. Peleg, and D. Avnir, *J. Am. Chem. Soc.* **114**, 7843 (1992).
- [40] Shape v1.1a02, Continuous Shape Measures calculation, 2003.
- [41] T. Hughbanks and R. Hoffmann, *J. Am. Chem. Soc.* **105**, 1150 (1983).

Chapter 9

Miscellaneous Materials

9.1 Introduction

This Chapter reports results from investigations of several different materials. First the structural, thermoelectric, and magnetic properties of the new quaternary transition metal chalcogenide series $\text{Ni}_3\text{Cr}_2\text{P}_2\text{S}_{9-x}\text{Se}_x$ are presented. These compounds adopt a new, layered structure type and show interesting magnetic behavior. This work was a continuation of previous research carried out by Dr. Thomas K. Reynolds, Dr. Kristen M. Poduska, Dr. Kevin J. Proctor, and Dr. Christopher B. Hoffman in the DiSalvo group, searching for new high symmetry chalcogenide compounds.

Also the addition of As_2Te_3 to Bi_2Te_3 based thermoelectric alloys is reported. Interesting correlations are seen between the As_2Te_3 concentration and the thermopower and unit cell parameters. This work was initiated by and carried out in collaboration with Dr. Tom Scheidemantel in Prof. John Badding's research group at the Pennsylvania State University.

Finally, the effect of high-pressure high-temperature (HPHT) treatment of PbTe is explored. Significant differences are seen in thermoelectric properties of these materials before and after HPHT treatment. This investigation was performed in collaboration with Dr. Abds-Sami Malik at Diamond Innovations Inc., a former DiSalvo Group member. This project may continue with a future group member.

9.2 The Layered Transition Metal Chalcogenides $\text{Ni}_3\text{Cr}_2\text{P}_2\text{S}_9$ and $\text{Ni}_3\text{Cr}_2\text{P}_2\text{Se}_9$

A list of desirable materials characteristics which should lead to improved thermoelectric performance was given in Chapter 2. Several of the properties on that list were included because they lead to low lattice thermal conductivity. This is universally accepted as a requirement for thermoelectric materials, and much effort has been focused on exploring compounds with heavy elements and/or rattling atoms. Another member of this list which has received little attention from thermoelectrics researchers is high symmetry. Most of the thermoelectric materials reviewed in Chapter 1 are seen to adopt structures with high symmetry (Bi_2Te_3 alloys are rhombohedral, PbTe , $\text{Si}_x\text{Ge}_{1-x}$, Skutterudites, TAGS, and Half-Heusler compounds are all cubic). The advantage of high symmetry is recalled here through the B factor described in Chapter 2.

$$B \propto \frac{N_c \mu_x \sqrt{m_x m_y m_z}}{\kappa_L}. \quad (9.1)$$

ZT increases monotonically with B. We see that large B arises from high mobility μ and effective mass m_i and low lattice thermal conductivity κ_L . In addition, B increases as the number of degenerate conduction band minima (or valence band maxima) N_c increases. Large N_c allows the chemical potential to be close to the edge of the bands where the density of states is changing most rapidly with energy (high S) even when there is a large number of charge carriers (low ρ). This leads to high ZT.

If a conduction band minimum occurs away from a high symmetry point in k-space, the crystallographic symmetry operations of the crystal structure produce degenerate minima at symmetry equivalent positions. This can lead to large N_c , especially in high symmetry Laue groups (up to 48 for m3m). Complex crys-

tal structures may be more likely to have large N_c than simple structures, since the resulting complex band structure may be more likely to have band extrema away from high symmetry points. In addition, complex structures may have multiple non-equivalent band extrema close in energy (less than $k_B T$ apart). Such accidental degeneracy is another way to get large N_c .

One reason that this factor has not received much attention from researchers seeking new thermoelectric materials is that the prediction of the crystal structure of complex new compounds is impossible. Previous members of the DiSalvo group have investigated the possibility of forming new high symmetry phases by starting with compounds which contain high symmetry “building blocks”, like tetrahedral polyanionic units. The inclusion of such units may bias the structures of new compounds toward high symmetry. Tightly bound polyatomic units may also behave similarly to single heavy atoms which are important for low κ_L . The reader is referred to the Dissertation of Dr. Thomas K. Reynolds for further details about this project [1].

As an introduction to solid state chemistry techniques, my first task after joining the DiSalvo group was to synthesize the known compound CrPS_4 , which contains isolated tetrahedral $(\text{PS}_4)^{3-}$ units, to be used as a starting material. This was then reacted with binary sulfides of several transition metals (TM), with the goal of discovering a quaternary compounds of the type $\text{TM}_w\text{Cr}_x(\text{PS}_4)_y\text{S}_z$ with covalent transition metal-sulfur framework surrounding isolated PS_4 units. Although many transition metal (TM) sulfide systems were investigated, the only indication of the formation of a new compound was seen for $\text{TM} = \text{Ni}$.

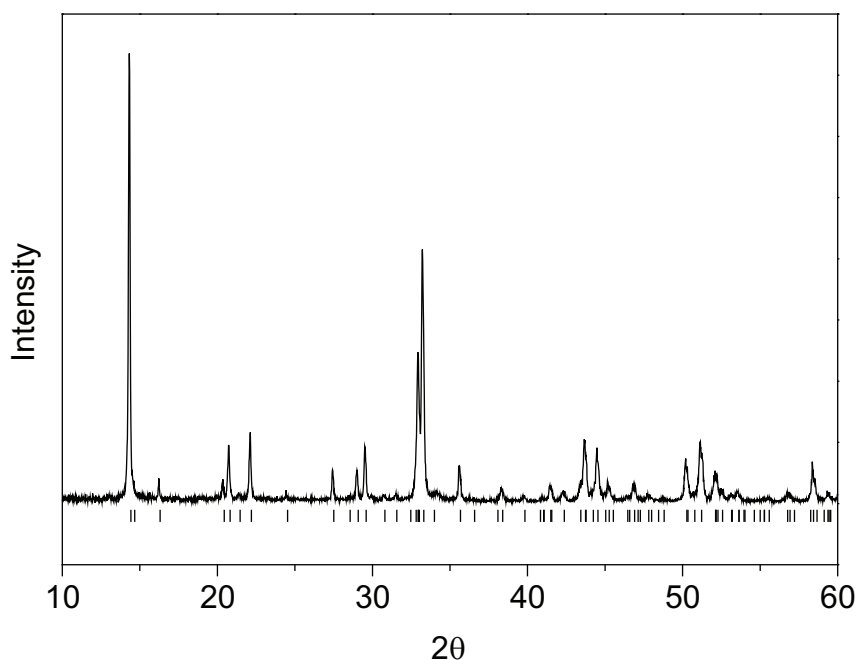


Figure 9.1: The measured PXRD pattern of the CrPS_4 starting material. The ticks mark positions of reflections calculated from single crystal structure data [2].

9.2.1 Discovery and synthesis of $\text{Ni}_3\text{Cr}_2\text{P}_2\text{Q}_9$ ($\text{Q} = \text{S}, \text{Se}$)

CrPS_4 was synthesized by first reacting stoichiometric amounts of the elements in a sealed silica tube at $500\text{ }^\circ\text{C}$ for 12 hours and cooling to room temperature over 12 hours. The reaction product was then ground into a fine powder using an agate mortar and pestle, sealed in an evacuated silica tube and heated at $500\text{ }^\circ\text{C}$ for an additional 100 hours. After cooling to room temperature over 12 hours the product was removed from the tube and analyzed using powder X-ray diffraction (PXRD). Comparison of the PXRD pattern with reported data showed the product to be single phase CrPS_4 (see Figure 9.1).

This material was then mixed with Ni and S powders in varying ratios by grinding and pressed into pellets. The loadings were chosen to perform a cursory exploration of the CrPS_4 - NiS and the CrPS_4 - NiS_2 phase diagrams by examining

the $\text{CrPS}_4:\text{NiS}_x$ ratios of 1:2, 1:1, and 2:1. One set of the pellets were sealed in evacuated silica tubes and heated at 500 °C for 48 hours and then cooled to room temperature over 10 hours. A second identical set was heated at 800 °C for 48 hours and then cooled over 24 hours. PXRD analysis of the products showed the presence of new reflections in the NiS containing samples which were heated to 800 °C. All of the reflections observed from the other samples could be attributed to known phases, primarily CrPS_4 and NiPS_3 , with other minor phases.

Microprobe analysis of black hexagonal plate-like crystals from these reactions suggested that the composition was near “ Ni_2CrPS_5 ”. Much effort was spent trying to synthesize a single phase sample at this composition, and to solve the crystal structure of this phase from single crystal X-ray diffraction to confirm the true composition. The structure could not be solved from the single crystal experiments due to poor data quality. Diffraction spots were often smeared, and when indexing of the cell did not fail, it gave widely varying results depending on the individual crystal and intensity threshold, for example. The plate-like crystals were easily delaminated which suggested a layered structure with only weak interlayer bonding (like graphite or mica), and likely was responsible in part for the poor diffraction data.

Attempts were also made to synthesize analogues of this compound, like “ $\text{Ni}_2\text{CrPSe}_5$ ”, “ $\text{Ni}_2\text{CrAsS}_5$ ”, “ Ni_2InPS_5 ”, and “ Pd_2CrPS_5 ”. Success was only realized for the Se analogue. The Se compound formed as smaller nearly perfect hexagons, and after many attempts a good single crystal data set and structure solution was obtained. This results showed the actual composition to be $\text{Ni}_3\text{Cr}_2\text{P}_2\text{Se}_9$. Comparison of PXRD data suggest strongly that the sulfur compound is isostructural to the selenide and has the composition $\text{Ni}_3\text{Cr}_2\text{P}_2\text{S}_9$ (*vide infra*).

9.2.2 Crystal structure of $\text{Ni}_3\text{Cr}_2\text{P}_2\text{Se}_9$

Ni, Cr, P, and Se were loaded in a 2:1:1:5 ratio into a silica tube which was then sealed under vacuum. The mixture was heated at 700 °C for 300 hours and then slowly cooled to 166 °C over 400 hours. The product consisted of black powder with many small ($\lesssim 100 \mu\text{m}$) hexagonal black plates. Several of these crystals were selected for single crystal X-ray diffraction studies. A good data set was collected from a small thin plate, and the results of the structure refinements are shown in Table 9.1. Atomic positions are listed in Table 9.2. Anisotropic displacement parameters are given in Table 9.3. Note that there are two sets of atomic positions in Table 9.2. This is due to disorder in the structure which will be addressed in the following Section.

The crystal structure of this compound is shown in Figure 9.2. The structure contains layers of edge sharing octahedra which form a honeycomb network, with TM sites at the centers of the octahedra and Se at the vertices. Two such layers are fused together by face sharing of the octahedra. In the holes of the honeycomb net are P-TM-P units, with each of the three atoms bonded to three Se atoms. Thus the P atoms are in four-fold coordination, and this TM atom is in a trigonal bipyramidal environment. The coordination environments and interatomic distances are shown in Figure 9.3

The assignment of the occupancy of the metal sites deserves some attention. We will see below that this compound behaves as a semiconductor, which suggests that it is charge balanced. In order to assign formal charges we will consider a sort of hybrid model in which the P-Se interactions are considered as covalent and the transition metal bonds to P and Se are considered to be ionic. Each unit cell contains four M(1) sites, four M(2) sites, and two M(3) sites. There are also 12 Se(1) sites which are each bonded to a single P atom, and six “iso-

Table 9.1: Single crystal refinement data for Ni₃Cr₂P₂Se₉.

Empirical formula	Ni ₃ Cr ₂ P ₂ Se ₉
Temperature	175(5) K
Wavelength	0.71073 Å
Crystal system, space group	Hexagonal, P6 ₃ /m
Unit cell dimensions	a = 6.244(4) Å c = 18.479(19) Å
Volume	623.9(8) Å ³
Z, Calculated density	2, 5.603 g/cm ³
Crystal size	0.080 × 0.060 × 0.008 mm ³
Theta range for data collection	2.20 to 33.12 deg.
Limiting indices	-7 ≤ h ≤ 9, -8 ≤ k ≤ 6, -27 ≤ l ≤ 28
Reflections collected / unique	7546 / 824 [R(int) = 0.0636]
Completeness to theta = 33.12°	99.9%
Data / restraints / parameters	824 / 4 / 33
Goodness-of-fit on F ²	0.805
Final R indices [I > 2σ(I)]	R ₁ = 0.0235, wR ₂ = 0.0342
R indices (all data)	R ₁ = 0.0420, wR ₂ = 0.0356
Largest diff. peak and hole	1.420 and -1.752 eÅ ⁻³

$$R_1 = \frac{\sum ||F_o| - |F_c||}{\sum |F_o|} \quad wR_2 = \left[\frac{\sum w(F_o^2 - F_c^2)^2}{\sum w(F_o^2)^2} \right]^{\frac{1}{2}}$$

$$w^{-1} = [\sigma(F_o^2) + (aP)^2 + bP] \quad \text{where } P = [\max(F_o^2, 0) + 2F_c^2] / 3$$

Table 9.2: Atomic coordinates and equivalent isotropic displacement parameters (\AA^2) for $\text{Ni}_3\text{Cr}_2\text{P}_2\text{Se}_9$. U_{eq} is defined as one third of the trace of the orthogonalized U_{ij} tensor. The second set of atoms, Se(11) through P(11), are included to model disorder (stacking faults) in the crystal (*vide infra*).

Atom	x	y	z	U_{eq}
Se(1)	0.3333(1)	0.0009(1)	0.0850(1)	0.006(1)
Se(2)	0.2968(1)	0.3337(2)	0.2500	0.005(1)
Cr(1)/Ni(1)	0.3333	0.6667	0.1618(1)	0.006(1)
Cr(2)/Ni(2)	0	0	0.1625(1)	0.005(1)
Ni(3)	0.6667	0.3333	0.2500	0.005(1)
P(1)	0.6667	0.3333	0.1323(1)	0.004(1)
Se(11)	0.6666(2)	0.6676(1)	0.0850(1)	0.006(1)
Se(21)	0.6301(2)	0.0004(2)	0.2500	0.005(1)
Cr(11)/Ni(11)	0.6667	0.3333	0.1618(1)	0.006(1)
Cr(21)/Ni(21)	0.3333	0.6667	0.1625(1)	0.005(1)
Ni(31)	0	0	0.2500	0.005(1)
P(11)	0	0	0.1323(1)	0.004(1)

Table 9.3: The anisotropic displacement parameters (\AA^2) for the compound $\text{Ni}_3\text{Cr}_2\text{P}_2\text{Se}_9$. The exponent of the anisotropic displacement factor is of the form: $-2\pi^2(h^2a^*{}^2U_{11}+\dots+2hka^*b^*U_{12})$. The second set of atoms, Se(11) through P(11), are included to model disorder (stacking faults) in the crystal (*vide infra*).

Atom	U_{11}	U_{22}	U_{33}	U_{23}	U_{13}	U_{12}
Se(1)	0.005(1)	0.005(1)	0.007(1)	-0.001(1)	-0.001(1)	0.002(1)
Se(2)	0.004(1)	0.006(1)	0.007(1)	0	0	0.003(1)
Cr(1)/Ni(1)	0.005(1)	0.005(1)	0.009(1)	0	0	0.003(1)
Cr(2)/Ni(2)	0.004(1)	0.004(1)	0.006(1)	0	0	0.002(1)
Ni(3)	0.005(1)	0.005(1)	0.005(1)	0	0	0.003(1)
P(1)	0.005(1)	0.005(1)	0.002(1)	0	0	0.002(1)
Se(11)	0.005(1)	0.005(1)	0.007(1)	-0.001(1)	-0.001(1)	0.002(1)
Se(21)	0.004(1)	0.006(1)	0.007(1)	0	0	0.003(1)
Cr(11)/Ni(11)	0.005(1)	0.005(1)	0.009(1)	0	0	0.003(1)
Cr(21)/Ni(21)	0.004(1)	0.004(1)	0.006(1)	0	0	0.002(1)
Ni(31)	0.005(1)	0.005(1)	0.005(1)	0	0	0.003(1)
P(11)	0.005(1)	0.00(1)	0.002(1)	0	0	0.002(1)

lated" Se(2) sites. The singly bonded Se atoms are formally 1-, while the isolated Se atoms are formally 2-. The P atoms are bonded to three Se atoms and are therefore formally neutral. There are then 24 charges to be distributed among the metal cations. Assuming the usual oxidation states of Ni²⁺ and Cr³⁺ suggest that there are four Cr atoms and six Ni atoms per unit cell. This gives the stoichiometry of Ni₃Cr₂P₂Se₉.

The two metal sites which are in octahedral coordination will for now be denoted M(1) and M(2). Octahedral coordination is common for both Cr and Ni. The trigonal bipyramidal coordination of the third metal site M(3) is unusual for transition metals. Thus, based on coordination environments alone, no conclusions can be drawn regarding the occupancy of these sites. Comparison of M-Se bond distances in Figure 9.3 shows that the two octahedral environments are essentially identical, which also gives no insight into the correct occupancies, since reported Ni-Se and Cr-Se distances in six-fold coordination are very similar (2.50 in NiSe [3] and 2.51-2.54 in Cr₂Se₃ [4]).

Comparison of bond valence sums can be helpful in determining site occupancies, but in this case were also inconclusive. In these calculations, the length of each bond to a particular atom is used to calculate a bond order, which is half the number of electrons involved in the bond. The sum of all bonds to an atom then gives the total number of electrons it is using for bonding, or equivalently its valence state. One expects 3 for Cr and 2 for Ni. Bond valence sums were calculated for both Ni and Cr at each of the three metal sites in the structure. The program EUTAX [5] was used for the calculations, and the results are shown in Table 9.4. Inspection of these results shows that the bond valence sums for both Ni or Cr are equally close to the expected values for all three metal sites, and thus do not help in the assignment of occupancies.

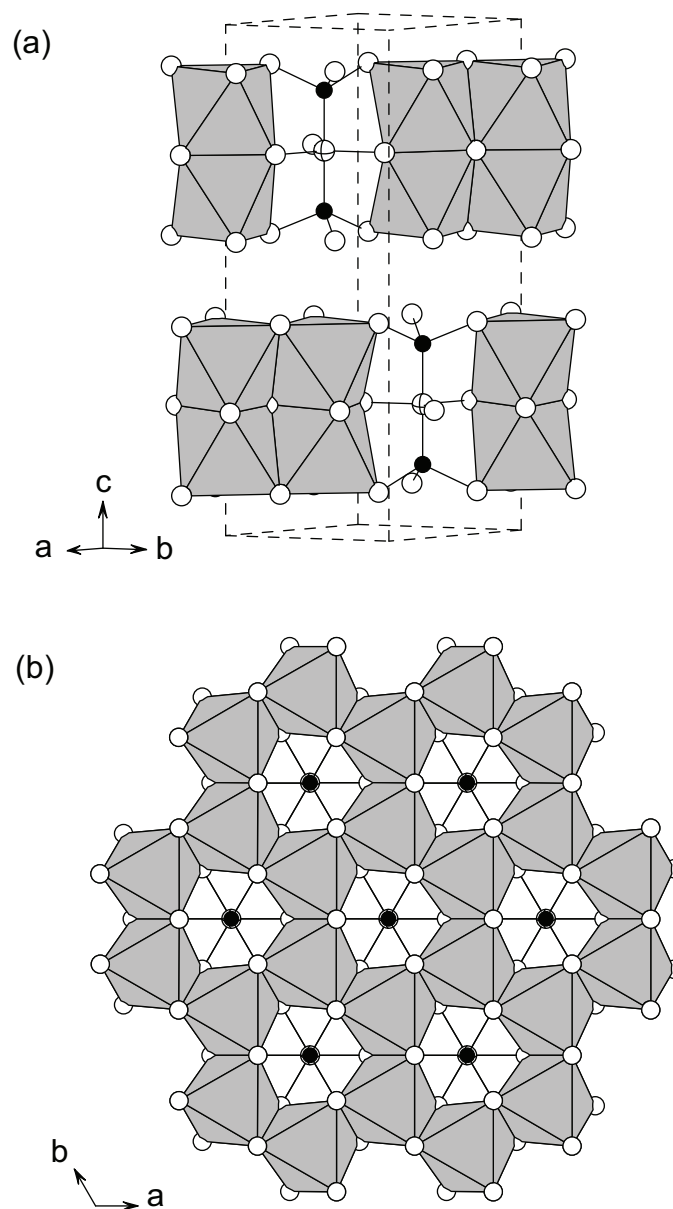


Figure 9.2: The crystal structure of $\text{Ni}_3\text{Cr}_2\text{P}_2\text{Se}_9$. Mixed sites occupied by Cr(1)/Ni(1) and Cr(2)/Ni(2) are at the centers of the grey octahedra. Se is white, P is black, and Ni(3) is striped. The unit cell edges are outlined in (a). Note the layered nature of the structure, with only weak van der Waals inter-layer interactions between the Se atoms. A view perpendicular to the layers is shown in (b).

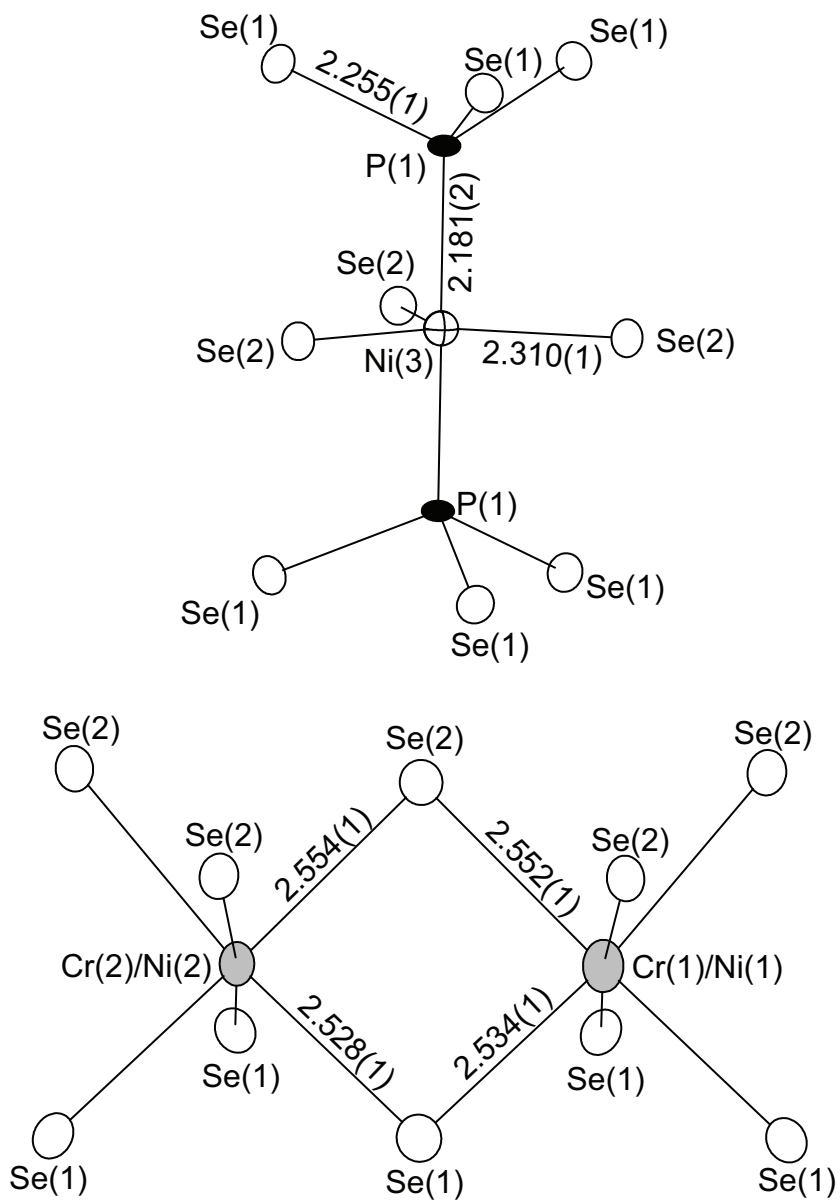


Figure 9.3: Coordination environments in $\text{Ni}_3\text{Cr}_2\text{P}_2\text{Se}_9$. Displacement ellipsoid are shown and bond distances (Å) are labeled.

Table 9.4: Bond valence sums for the two octahedral metal sites M(1) and M(2) and the bipyramidal metal site M(3) in $\text{Ni}_3\text{Cr}_2\text{P}_2\text{Se}_9$.

	Ni	Cr
M(1)	2.04	3.06
M(2)	2.03	3.04
M(3)	1.89	2.84

We are therefore left with only the X-ray data to determine the atom assignments of the metal sites. However, due to the similar scattering power of the two types of atoms, refinement of the ratio of Ni:Cr on these sites is not straightforward. Various distributions of Ni and Cr atoms over the three metal sites which maintain charge balance were investigated, and the results are presented in Table 9.5. From this Table it is clear that fully ordered arrangements of Ni and Cr are the least consistent with the X-ray data (higher R values, and displacement parameters which suggest the pure Ni site needs less scattering power and the pure Cr site needs more). This suggests that these two sites may be occupied by a mixture of Ni and Cr. It is common for Ni and Cr to share atomic sites due to their similar sizes (as in the common alloys chromel, nichrome, and stainless steel, and the sulfide series $\text{Ni}_x\text{Cr}_{3-x}\text{S}_4$ $0 < x < 1$ [6]). Allowing mixtures of Ni and Cr on all three sites while maintaining charge balance (the rightmost column in Table 9.5) gives significantly lower R values and more reasonable displacement parameters than the ordered arrangements. The refined site occupancies (in the form Ni:Cr) were: M(1) 50:50, M(2) 56:44, M(3) 87:13. This is close to equal mixtures of Ni and Cr on the octahedral sites and pure Ni on the bipyramidal site. Table 9.5 shows that there is no significant difference in the quality of the refinement between this and the freely refined case. Therefore the simpler model, with M(1) and M(2) oc-

cupied by 50:50 mixtures of Ni and Cr and M(3) occupied by Ni is likely the best description of the structure that can be realized from the present X-ray data.

More reliable information regarding the distribution of Ni and Cr over M sites could be obtained from anomalous X-ray scattering experiments. Such experiments could be carried out using the synchrotron at Cornell (CHESS), and would involve collecting diffraction datasets at two different X-ray energies, one close to and one far from the Ni absorption edge. Near the Ni absorption edge, the scattering power of the Ni atoms is reduced, while the scattering power of the other atoms are the same at both energies. The difference between the two datasets would then reflect the distribution of Ni atoms.

Table 9.5: Results from refinement of several distributions of Ni and Cr atoms on the metal sites in $\text{Ni}_3\text{Cr}_2\text{P}_2\text{Se}_9$.

	M(1)=Cr	M(1)=Ni	M(1)=Ni/Cr 1:1	Refine
	M(2)=Ni	M(2)=Cr	M(2)=Ni/Cr 1:1	M(1), M(2),
	M(3)=Ni	M(3)=Ni	M(3)=Ni	and M(3)
R_1	0.0315	0.0316	0.0235	0.0232
wR_2	0.0708	0.0857	0.0342	0.0329
M(1) U(eq)	0.001	0.013	0.006	0.006
M(2) U(eq)	0.011	0.000	0.005	0.006
M(3) U(eq)	0.005	0.005	0.005	0.004

9.2.3 Twinning and disorder in $\text{Ni}_3\text{Cr}_2\text{P}_2\text{Se}_9$

Assignment of the metal site occupancies was not the only difficulty that was encountered during the solution and refinement of the crystal structure of this compound. The crystal was also twinned. The realization of this fact and the identification of the twin law were of vital importance to the success of the refinement. No indication of twinning was seen in the diffraction pattern; that

is, all observed spots were indexed to a single unit cell. However, signs of possible twinning were seen in the analysis of the intensity data. Comparison of equivalent reflections suggested 6/mmm symmetry, but the structure could not be solved in any space group with such high symmetry. A solution of reasonable quality was found in the lower symmetry space group $P6_3/m$ (Laue class 6/m); however, the agreement factors were not as low as expected ($R_1 \approx 0.10$), some atomic displacement parameters were unphysical, and there were significant difference peaks. The difficulties with the refinement indicated that the structural model was incomplete, and the apparent higher symmetry of the intensity data suggested merohedral twinning may be source of the problems.

This type of twinning can occur when the lattice has a higher symmetry than the crystal [7, 8]. A merohedral twin law is a symmetry element of the lattice, so the diffraction patterns from each domain overlap exactly, but it is not a symmetry element of the crystal, so its presence is apparent only in the intensity data. In fact, the presence of such twinning makes the intensity data appear to have higher symmetry when there the twin fraction is near 0.5.

In the present case the twin law is a 2-fold rotation about [110], and is represented by the matrix

$$\begin{pmatrix} 0 & -1 & 0 \\ -1 & 0 & 0 \\ 0 & 0 & 1 \end{pmatrix}.$$

The refinement of the twin fraction gave $x = 0.65$, which is close to 0.5 and explains the original incorrect assignment of the Laue class. This is a common twin law in the lower symmetry trigonal, tetragonal, hexagonal, and cubic systems, which do not have this 2-fold axis as a symmetry element [8]. The twinning is illustrated in Figure 9.4. Inclusion of the twin law in the refinement of the structure improved the results significantly, lowering R_1 to 0.037 from 0.10. However, there

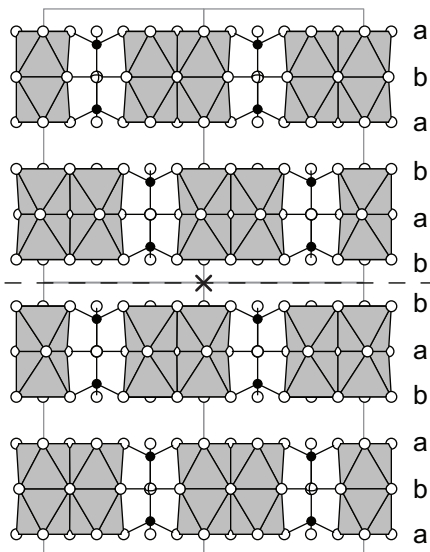


Figure 9.4: Illustration of the twinning in $\text{Ni}_3\text{Cr}_2\text{P}_2\text{Se}_9$. Mixed Ni/Cr sites are at the centers of the grey octahedra, Se is white, P is black, and Ni is striped. The grey lines separate unit cells. The view is down $[110]$. The twin law is a 2-fold rotation about this direction and is marked with a black x. The dashed line separates the two twin domains. The relationship between the twinning and the stacking of the close packed Se layers is demonstrated.

were still problems with the refinement, including some significantly elongated displacement ellipsoids and some difference peaks up to about $6 \text{ e}\text{\AA}^{-3}$. Inspection of the positions of the difference peaks lead to the further improvement of the structural model by the inclusion of a small amount of disorder.

Figure 9.5 shows the $z = 0.25$ plane of the $\text{Ni}_3\text{Cr}_2\text{P}_2\text{Se}_9$ structure. This plane contains Ni(3) and Se(2). Also shown in this Figure are the locations of the two strongest difference peaks from the refinement of the twinned structure, Q(1) and Q(2). A translation by $1/3$ along a and $2/3$ along b (Figure 9.5) moves the Ni and Se atoms to the positions of the Q's. This suggests the possibility of disorder, with some layers shifted by $(1/3, 2/3, 0)$ with respect to the bulk of the crystal. This disorder was incorporated into the structural model by adding a second set of atoms at the shifted positions (Table 9.2). The atoms were then

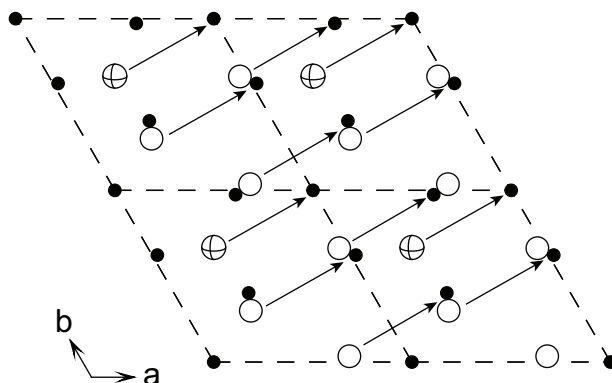


Figure 9.5: The $z = 0.25$ plane in $\text{Ni}_3\text{Cr}_2\text{P}_2\text{Se}_9$ showing the location of the two largest difference peaks (black) and their relationship to the positions of Ni(3) (striped) and Se(2) (white).

distributed over these two possible configurations and the fraction of each component was refined. The disorder fraction refined to approximately 7%. The two configurations over which the atoms are disordered are compared in Figure 9.6. The results from the refinement including the twinning and the disorder are those shown previously in Table 9.1.

The disorder shown in Figure 9.6 is a type of stacking fault which is not unusual in layered structures, due to the weak van der Waals interactions between the layers. The low level of the disorder in this particular crystal allowed the structure to still be solved and refined well. Higher concentrations of such stacking faults can significantly distort diffraction peaks which can preclude structure determination. This is likely the source of the problems encountered with the sulfur analogue $\text{Ni}_3\text{Cr}_2\text{P}_2\text{S}_9$, for which no quality single crystal diffraction data could be obtained. As noted above, indexing the single crystal data for this compound was difficult, and did not consistently return the same cell parameters. The better data sets tended to give unit cell parameters close to $a = 5.9 \text{ \AA}$ $c = 18.0 \text{ \AA}$, but often the c -axis length was double or triple this value, likely due to stack-

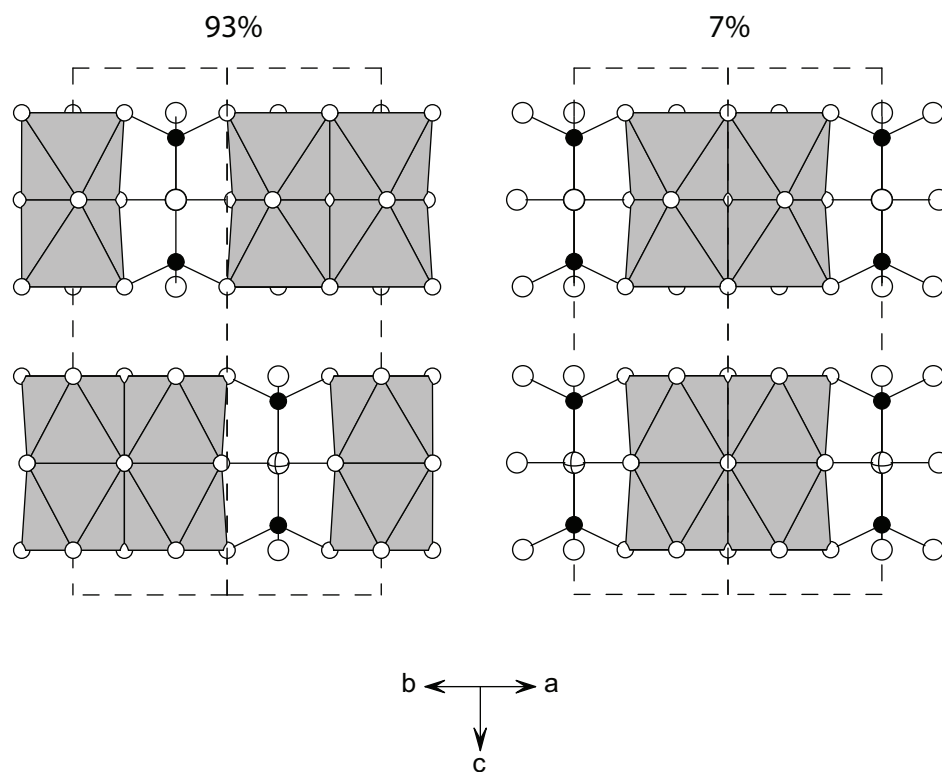


Figure 9.6: The two configurations over which the atoms in $\text{Ni}_3\text{Cr}_2\text{P}_2\text{Se}_9$ are disordered, labeled by the refined values of their population in the crystal. Mixed Ni/Cr sites are at the centers of the grey octahedra, Se is white, P is black, and Ni is striped.

ing faults. Powder X-ray diffraction results suggest the the sulfur and selenium analogues are isostructural, and will be addressed in the following Subsection.

9.2.4 Powder X-ray diffraction: $\text{Ni}_3\text{Cr}_2\text{P}_2\text{S}_9$ and $\text{Ni}_3\text{Cr}_2\text{P}_2\text{Se}_9$

Measured powder X-ray diffraction (PXRD) patterns for $\text{Ni}_3\text{Cr}_2\text{P}_2\text{S}_9$ and $\text{Ni}_3\text{Cr}_2\text{P}_2\text{Se}_9$ are shown in Figure 9.7. Neither compound has yet been made as a single phase bulk sample. The data shown in Figure 9.7 represent two of the purest samples that have been synthesized. Binary transition metal chalcogenides are present in both materials as impurities. The sulfide sample was made by reacting a stoichiometric mixture of the elements in an evacuated silica tube at 800 °C for two days and cooled to 400 °C over two days. The product contained the target phase, but with NiPS_3 as a major impurity. The sample was ground and pressed into a pellet and annealed at 700 °C for two days. This annealing treatment was then repeated. PXRD showed that the product still contained a small amount of NiPS_3 . The final annealing was performed at 700 °C for 16 days. This anneal eliminated the NiPS_3 impurity; however, peaks matching Cr_2S_3 were observed in the PXRD pattern. The selenide material represented in Figure 9.7 was made by reacting a stoichiometric mixture of the elements in an evacuated silica tube at 500 °C for two days, and then 600 °C for one day. The sample was then ground and pressed into a pellet, and annealed at 600 °C for four days. The product was again ground and pressed into a pellet for the final heating which consisted of four days at 700 °C followed by slow cooling to 250 °C over the course of four days. The resulting product contained the target compound as the main phase, with small amounts of NiSe_2 and Cr_5Se_8 as impurities.

Peak positions in these patterns were used to refine the lattice constants of each phase. The results for $\text{Ni}_3\text{Cr}_2\text{P}_2\text{Se}_9$ were $a = 6.253(1) \text{ \AA}$, $c = 18.494(4) \text{ \AA}$, in

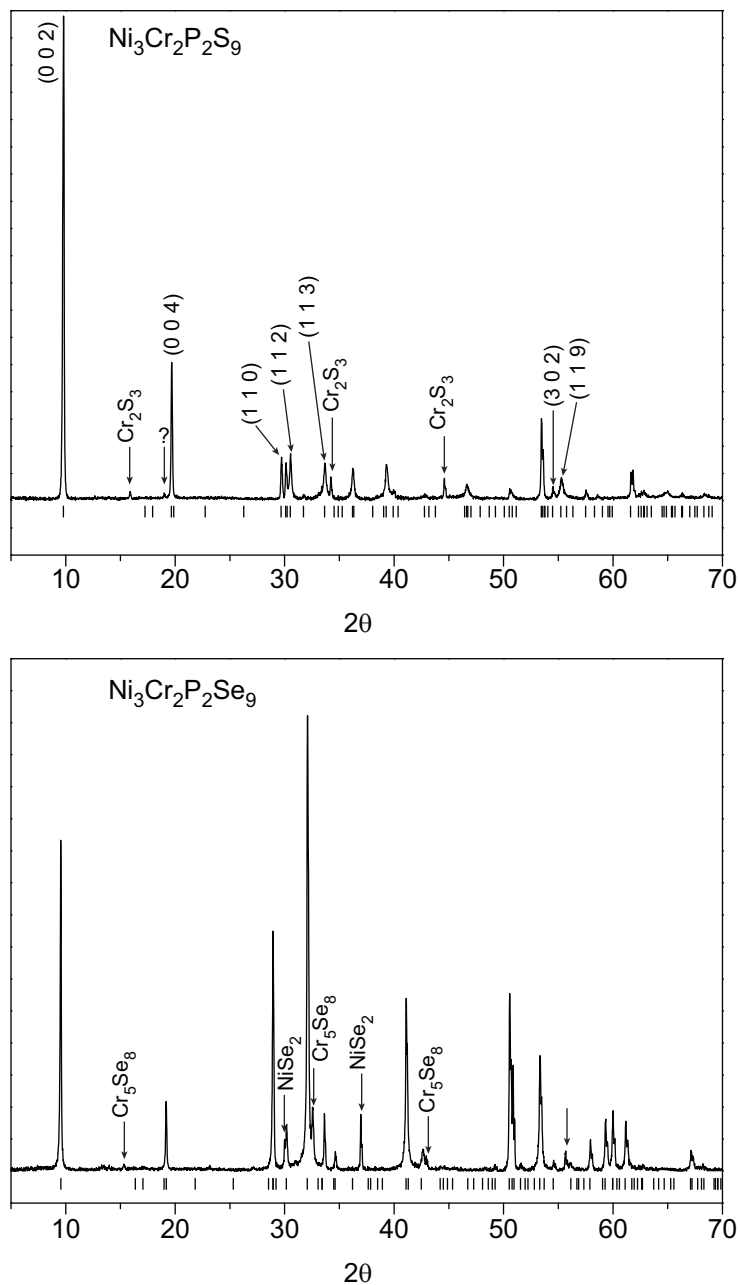


Figure 9.7: Measured PXRD patterns for $\text{Ni}_3\text{Cr}_2\text{P}_2\text{S}_9$ and $\text{Ni}_3\text{Cr}_2\text{P}_2\text{Se}_9$. Tick marks locate predicted peak positions, and observed impurity peaks are labeled.

good agreement those determined by single crystal diffraction shown in Table 9.1 (the PXRD values are a little larger since the powder data was collected at room temperature and the single crystal data was collected at 175 K). The results for $\text{Ni}_3\text{Cr}_2\text{P}_2\text{S}_9$ were $a = 5.934(1) \text{ \AA}$, $c = 18.053(4) \text{ \AA}$. These are smaller than the lattice constants of the Se compound, as expected when Se is replaced by the smaller S. Similar lattice constants were found for $\text{Ni}_3\text{Cr}_2\text{P}_2\text{S}_9$ from some single crystal diffraction experiments ($a = 5.9 \text{ \AA}$, $c = 18.0 \text{ \AA}$), although the structure could not be solved. These observations strongly suggest that $\text{Ni}_3\text{Cr}_2\text{P}_2\text{S}_9$ and $\text{Ni}_3\text{Cr}_2\text{P}_2\text{Se}_9$ are isostructural.

Several of the single indexed reflections from $\text{Ni}_3\text{Cr}_2\text{P}_2\text{Se}_9$ are labeled by their hkl values in Figure 9.7. It is clear that reflections of the form (0 0 l) and (h k 0) are sharp, while "mixed" reflections of the form (h k l) are significantly broadened. This is typical of layered materials which contain stacking faults, displacements of the layers perpendicular to the stacking direction (the c-direction in this case) [9]. In close packed structures these faults can be viewed as variations in the stacking sequence. As a result of the stacking sequence variation, the c-axis length becomes poorly defined, and is better described as a distribution of values. This does not affect the spacing between layers, and therefore do not affect the positions of the (0 0 l) lines. The stacking faults also do not affect the periodicity within each layer, and so do not affect positions of the (h k 0) reflections. However, the range of c-axis lengths causes reflections of the type (h k l) to occur over a range of angles in the PXRD pattern, reflecting the distribution of d-spacings caused by the variation in c.

9.2.5 Thermoelectric properties

Sample synthesis and experimental considerations

Crystals used for thermoelectric properties measurements were produced during attempts to make single phase bulk samples of several members of the solid solution between $\text{Ni}_3\text{Cr}_2\text{P}_2\text{S}_9$ and $\text{Ni}_3\text{Cr}_2\text{P}_2\text{Se}_9$. The elements were loaded into silica tubes in the ratios $\text{Ni}_3\text{Cr}_2\text{P}_2\text{S}_{9-x}\text{Se}_x$ for $x = 0, 3, 6, 9$. and treated as described above for $\text{Ni}_3\text{Cr}_2\text{P}_2\text{Se}_9$ sample used for powder X-ray diffraction. The resulting powder products contained black plate-like crystals in the shapes of hexagons or half-hexagons. The samples with nominal compositions of $\text{Ni}_3\text{Cr}_2\text{P}_2\text{S}_9$, $\text{Ni}_3\text{Cr}_2\text{P}_2\text{S}_6\text{Se}_3$, and $\text{Ni}_3\text{Cr}_2\text{P}_2\text{S}_3\text{Se}_6$ produced crystals large enough to allow measurements of electrical resistivity and the Seebeck coefficient (typical sizes were about 400–800 μm). $\text{Ni}_3\text{Cr}_2\text{P}_2\text{Se}_9$ did not form crystals large enough to characterize. The S:Se ratios were measured by energy dispersive electron microprobe analysis on several crystals produced by these reactions. The measured ratios were 1.2:1 for the sample of nominal composition $\text{Ni}_3\text{Cr}_2\text{P}_2\text{S}_6\text{Se}_3$ and 1:3.5 for the sample of nominal composition $\text{Ni}_3\text{Cr}_2\text{P}_2\text{S}_3\text{Se}_6$. These measurements indicate that the crystals are richer in selenium than expected from the loaded compositions. This may be attributed to the more volatile nature of sulfur.

Thermoelectric properties measurements were performed using the DiSalvo lab's home built apparatus [1]. Van der Pauw type resistivity measurements were performed on the plate-like crystals by contacting them with silver paste (Dupont Conductor Composition 4922N). The thicknesses of the crystals were measured with a non-contact optical surface profiler. Seebeck coefficient measurements were performed by mounting the crystals on a small glass plate with a heater attached to one end with Stycast black epoxy. The same epoxy was used to attach the other end of the glass was attached to the sample stage on the probe.

The heater was used to establish a temperature gradient along the glass plate, and the temperature and voltage difference across the sample were measured with thermocouples attached to each end of the sample with Epotek H20E silver epoxy. Measurements were carried out between 80 K and 300 K. The maximum uncertainty in these measurements is estimated to be $\pm 10\%$. Thermal conductivity measurements could not be performed on such small specimens.

Measurement results and discussion

The results of the resistivity and Seebeck coefficient measurements are shown in Figure 9.8. The resistivity of all three materials show semiconducting or activated behavior, with room temperature values on the order of 100 m Ω cm. This is two orders of magnitude higher than typical good thermoelectric materials. The Seebeck coefficients are positive, indicating p-type behavior. The $x = 3$ sample has moderately high thermopower, close to that of optimized Bi₂Te₃ alloys. However, the high resistivities make all of these compounds poor thermoelectric materials. Among the samples the usual relationship is seen between S and ρ , with the more resistive samples having higher Seebeck coefficients. No smooth trend is observed as x increases. The $x = 3$ sample has higher S and ρ than both the $x = 0$ and $x = 6$ samples.

The nonlinear behavior seen in the inset in the resistivity plot shows that the resistivity is not well described by a simple activation law, especially for the Se containing samples. The higher temperature $\log(\rho)$ vs. $1/T$ data for Ni₃Cr₂P₂S₉ are fairly linear, and a fit suggests an activation energy of about 0.02 eV. The $\log(\rho)$ vs. $1/T$ data for these three compounds can be fit to power laws, as predicted by variable range hopping models [10]. These models, originally developed by Mott [11], are often used to describe disordered semiconductors, amorphous materials, and doped semiconductors at very low temperature. They con-

sider conduction by hopping of electrons from one localized site to another. The exponents from the power law fits ($\log(\rho) \propto (1/T)^p$), which in the simplest models should depend only on the dimensionality of the system, do not agree for the three samples ($p(x=0)=0.51$, $p(x=3)=0.16$, $p(x=3)=0.10$). However, the low activation energy approximated by the high temperature fit to the $x = 0$ sample suggests that such hopping models should not be a good description of the conduction in these materials. The conduction may involve more than one type of activation, for example there may be both intrinsic and extrinsic carriers involved, or perhaps the mobilities are strongly temperature dependent.

9.2.6 Magnetic properties of $\text{Ni}_3\text{Cr}_2\text{P}_2\text{S}_9$

Sample synthesis and experimental considerations

Several crystals which adopted the half-hexagon plate-like morphology suggestive of the target phase were extracted from the $\text{Ni}_3\text{Cr}_2\text{P}_2\text{S}_9$ reaction product described above (from which the crystals used for transport measurements were also selected). These were ground in an agate mortar into a fine powder. An overnight PXRD scan showed the powder to be phase pure. The sample (3.0 mg) was then loaded into a gelcap for magnetic susceptibility measurements. Measurements were performed in a Quantum Design MPMS SQUID magnetometer, in an applied field of 2 T over a temperature range of 5–400 K. The diamagnetic response of an empty gelcap was measured separately and subtracted from the raw data to give the moment of the sample.

Measurements were also conducted on oriented single crystals of $\text{Ni}_3\text{Cr}_2\text{P}_2\text{S}_9$. These crystals were produced by reacting stoichiometric amounts of the elements in an evacuated silica tube at 800 °C for two days followed by cooling to 400 °C over four days. Three of the largest crystals were selected from

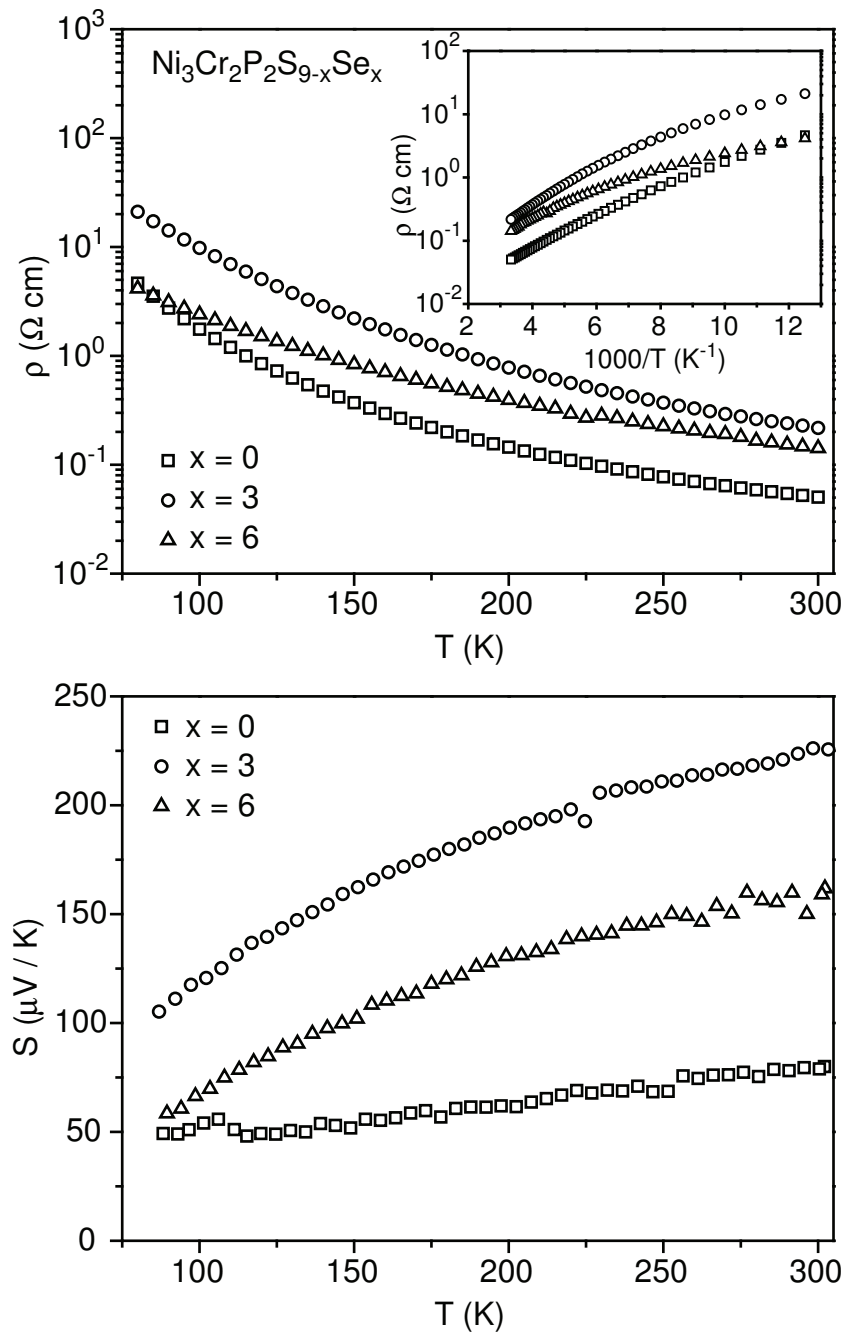


Figure 9.8: The measured resistivity ρ and Seebeck coefficient S of three members of the solid solution series $\text{Ni}_3\text{Cr}_2\text{P}_2\text{S}_{9-x}\text{Se}_x$ labeled by their nominal composition. The maximum uncertainty in these measurements is estimated to be $\pm 10\%$.

the product and used for magnetic measurements. The plate-like crystals were mounted onto a specially designed sample holder with a very small amount of non-magnetic cement (GC Electronics, Radio-TV Service Cement). The total mass of the crystals was measured to be 0.54 ± 0.02 mg. The mass was determined by repeated measurement on an electronic balance. After each measurement the crystals were removed from the weighing pan and the pan returned to the balance. If the mass returned to 0.00000 g, the measurement was deemed good. Eight such good measurements were averaged to determine the mass, and the uncertainty was estimated as the standard deviation of the measurements. Two sets of magnetic susceptibility measurements were performed on the crystals, one with H directed along the c-axis (perpendicular to the plates), and one with H in the ab-plane. Both measurements were carried out from 5 K up to 400 K in an applied field of 2 T.

The sample holder is shown in Figure 9.9, and was made by filing a small notch in a 1/8 inch diameter phenolic rod. Kapton tape was wound around the upper and lower end of the rod to achieve a snug fit inside a plastic drinking straw, which is attached to the sample holder rod of the MPMS. Holes were punched in the straw above and below the tape to help keep the sample holder stationary. The rod is long enough so that it spans the measurement area as the sample is moved through the SQUID susceptometer. Therefore, the only magnetic contribution from the holder is from the notch. The notch is a missing piece of diamagnetic material, and thus produces a paramagnetic signal when it passes through the SQUID. The magnetic moment of the empty sample holder was measured in an applied field of 2 T (Figure 9.9). The measured moment is nearly temperature independent above about 50 K. Below 50 K the moment decreases sharply with decreasing T. The origin of this behavior is unclear. The data shown

in Figure 9.9 was used to correct the raw data from the sample measurements to obtain the moment of the $\text{Ni}_3\text{Cr}_2\text{P}_2\text{S}_9$ crystals.

Measurement results and discussion

The field dependence of the magnetic moment M , measured at 20 K and at 350 K, is shown in Figure 9.10. Inspection of the M vs. H curves reveals non-linear behavior indicative of the presence of a small ferromagnetic impurity. The data collected at 20 K shows evidence of hysteresis as well. No impurity phases were detected by PXRD; however, PXRD is typically only sensitive to impurities present in amounts greater than a few weight percent.

The measured molar magnetic susceptibility χ of the powdered sample of $\text{Ni}_3\text{Cr}_2\text{P}_2\text{S}_9$ (not corrected for the unidentified ferromagnetic impurity) is shown in Figure 9.11. The inset shows the inverse molar susceptibility vs. T , which deviates significantly from Curie-Weiss type behavior, especially at lower temperatures. In particular, just above 100 K there is a knee in χ vs. T (a dip in the $1/\chi$ vs. T plot). The temperature intercept of a line drawn through the high temperature inverse susceptibility data is seen to be negative, suggesting anti-ferromagnetic interactions. The presence of the unidentified impurity phase in this sample complicates further analysis of the data. More reliable data, obtained through measurements of single crystals, are reported and discussed next.

The field dependence of the magnetic moment of the $\text{Ni}_3\text{Cr}_2\text{P}_2\text{S}_9$ crystals is shown in Figure 9.12. The lines are linear fits to the M vs. H data points. The linear behavior indicates paramagnetism in all cases except at 50 K with H in the ab -plane. In this case the line shown on the plot is a fit the data for $M \geq 1$ T. The observed behavior (with the one noted exception) shows that the ferromagnetic impurity present in the powder sample is not present in the single crystal sample. The deviation from linear M vs. H behavior in the ab plane at 50 K may be related

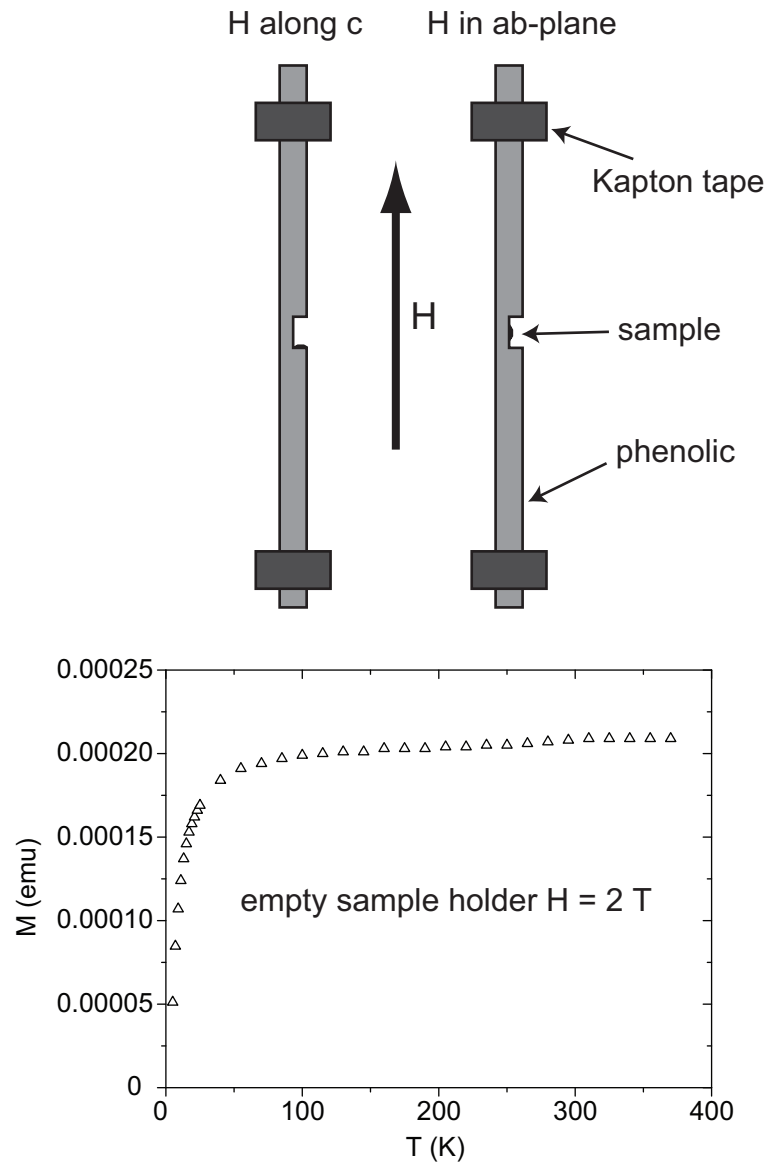


Figure 9.9: A drawing of the sample holder used for the measurement of the magnetic properties of oriented single crystals in the Quantum Design MPMS SQUID system. See the text for details. Also shown is the measured moment of the empty sample holder in an applied field of 2 T.

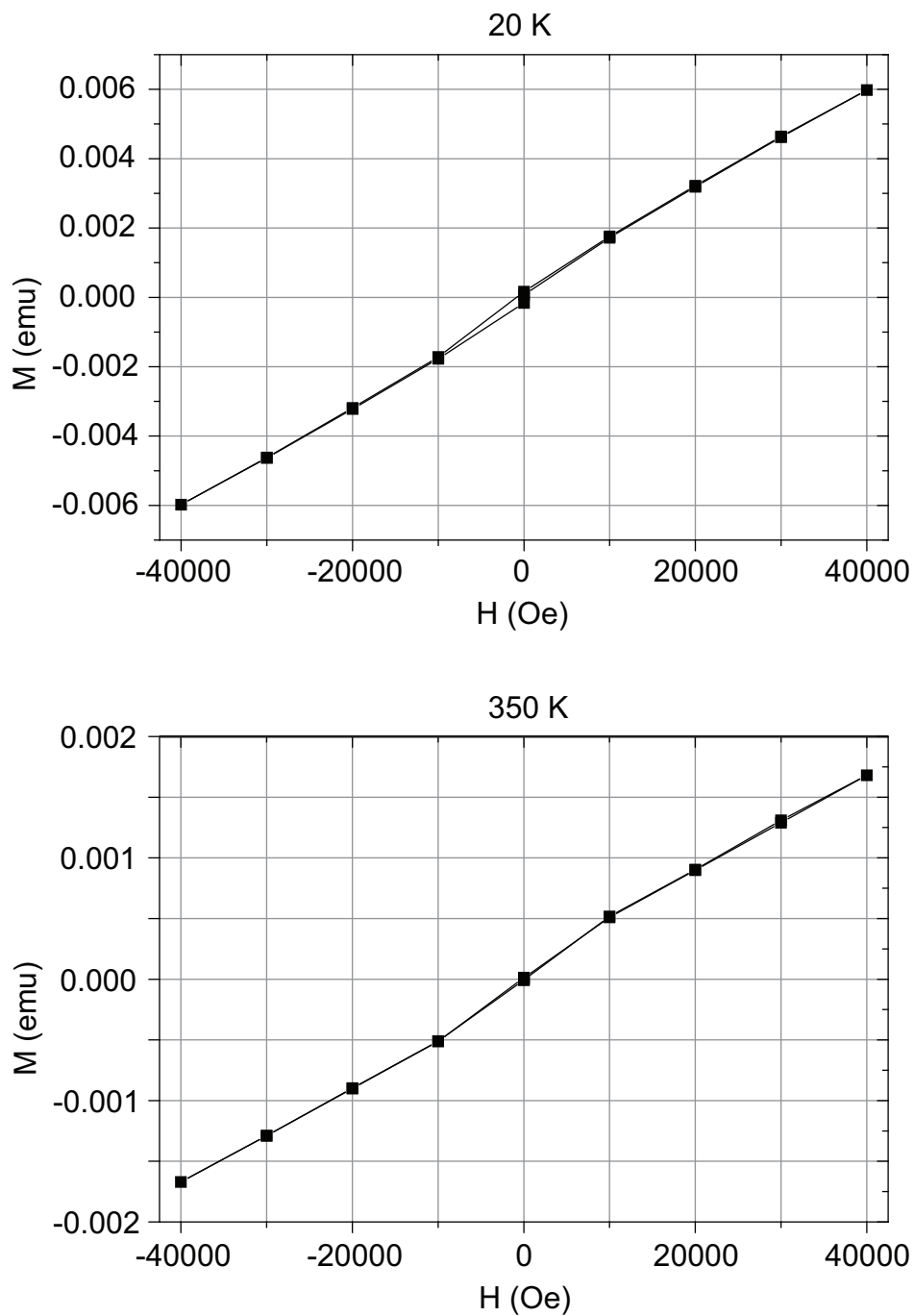


Figure 9.10: The measured field dependence of the magnetic moment of a powder sample of $\text{Ni}_3\text{Cr}_2\text{P}_2\text{S}_9$ up to 4 T at 20 K and 350 K. The lines connecting data points are meant only to guide the eye. The non-linear behavior suggest the presence of a small amount of a ferromagnetic impurity phase.

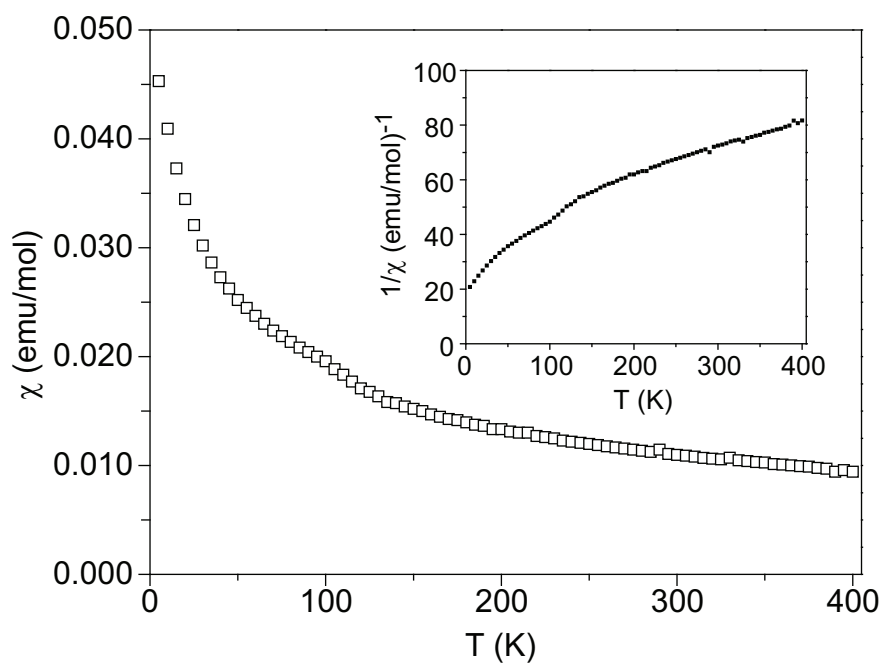


Figure 9.11: The measured magnetic susceptibility χ of a powder sample of $\text{Ni}_3\text{Cr}_2\text{P}_2\text{S}_9$ between 5 K and 400 K in an applied field of 2 T. The uncertainty in these measurements arises primarily from the sample mass measurement, and is thus estimated to be about $\pm 7\%$. The deviation from the Curie-Weiss law below about 150 K is illustrated in the inset, which shows the temperature dependence of $1/\chi$.

to the proximity in temperature to the knee near 100 K in the χ vs. T data (noted above in the powder data and discussed below in the single crystal data) which is more pronounced in the ab-plane than along the c-direction.

Figure 9.13 shows the measured molar susceptibility χ and inverse molar susceptibility $1/\chi$ vs. temperature. Over the entire temperature range, the susceptibility determined from the single crystal data is less than that determined from the powder data (Figure 9.11). This is attributed to the ferromagnetic impurity detected in the powder but not in the single crystal sample. Little difference is seen between the two crystal orientations, suggesting little magnetic anisotropy. The most notable difference is the more pronounced knee near 105 K in the data collected with H in the ab-plane.

Above about 200 K the $1/\chi$ vs. T data can be fit reasonably well with a linear model (Figure 9.13). This is characteristic of Curie-Weiss behavior [12], although the applicability of such molecular field models to 2-dimensional systems is questionable [13]. Here the Curie-Weiss law will be applied as a first step toward understanding the magnetic properties of $\text{Ni}_3\text{Cr}_2\text{P}_2\text{S}_9$. Within this model, the magnetic susceptibility χ at high temperature (above the Curie or Neel temperature) is described by

$$\chi = \frac{C}{T - \theta}. \quad (9.2)$$

In Eq. 9.3, C is the Curie constant and θ is the paramagnetic Curie temperature or Weiss temperature. The values of θ determined from the fits are -180 K and -200 K for data collected in the ab-plane and along the c-axis, respectively. These large negative values indicate strong antiferromagnetic interactions. The fitted values of C are 4.0 emuK/mol and 3.9 emuK/mol for data collected in the ab-plane and along the c-axis, respectively. These can be compared with values calculated for the expected spin arrangement in this compound.

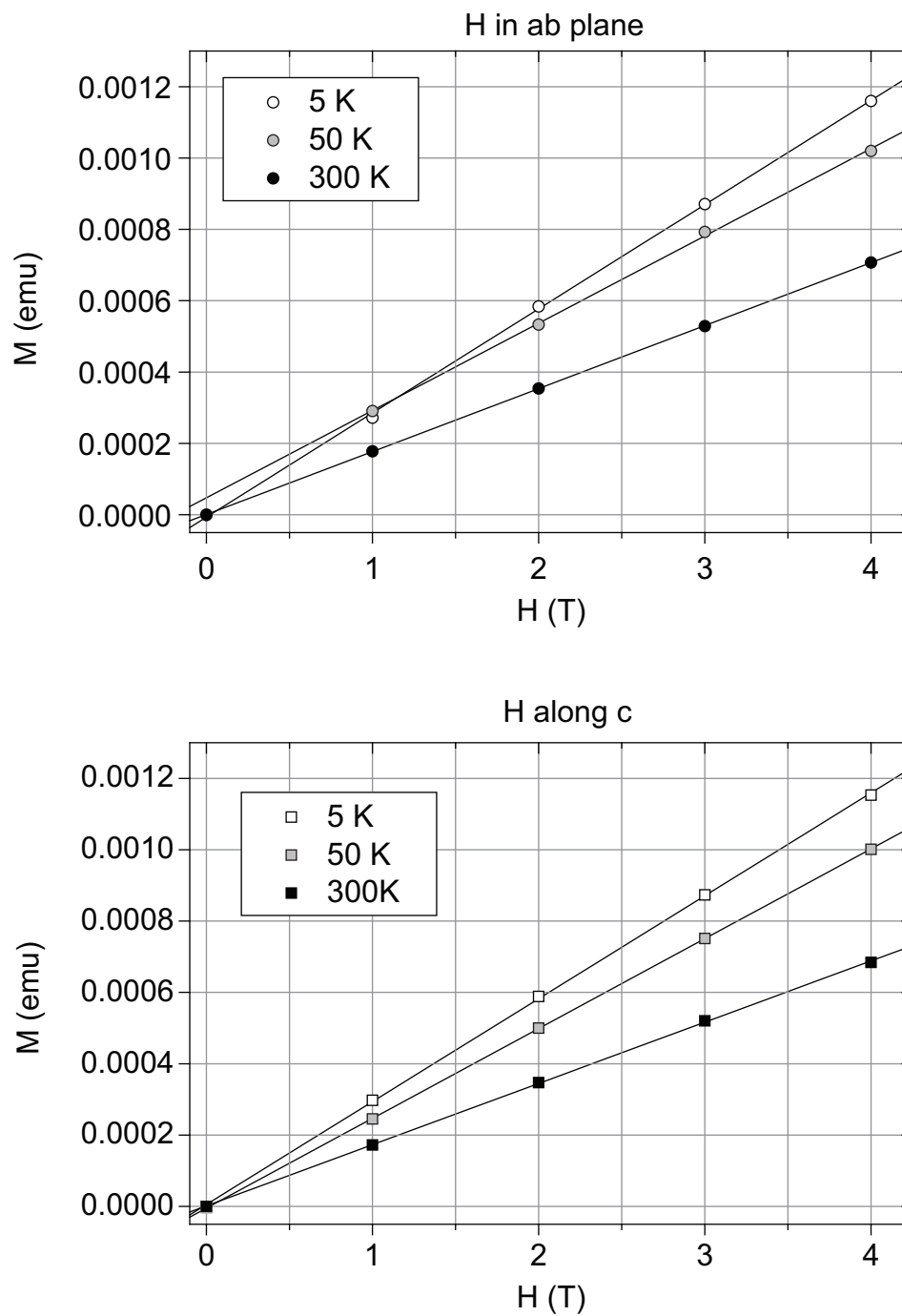


Figure 9.12: The field dependence of the magnetic moment of $\text{Ni}_3\text{Cr}_2\text{P}_2\text{S}_9$ crystals (and sample holder) up to 4 T measured at 5 K, 50 K, and 300 K. The linear fits to all curves show paramagnetic behavior with the exception of that measured with H in the ab-plane at 50 K, for which the linear fit to the data between 1 T and 4 T is shown.

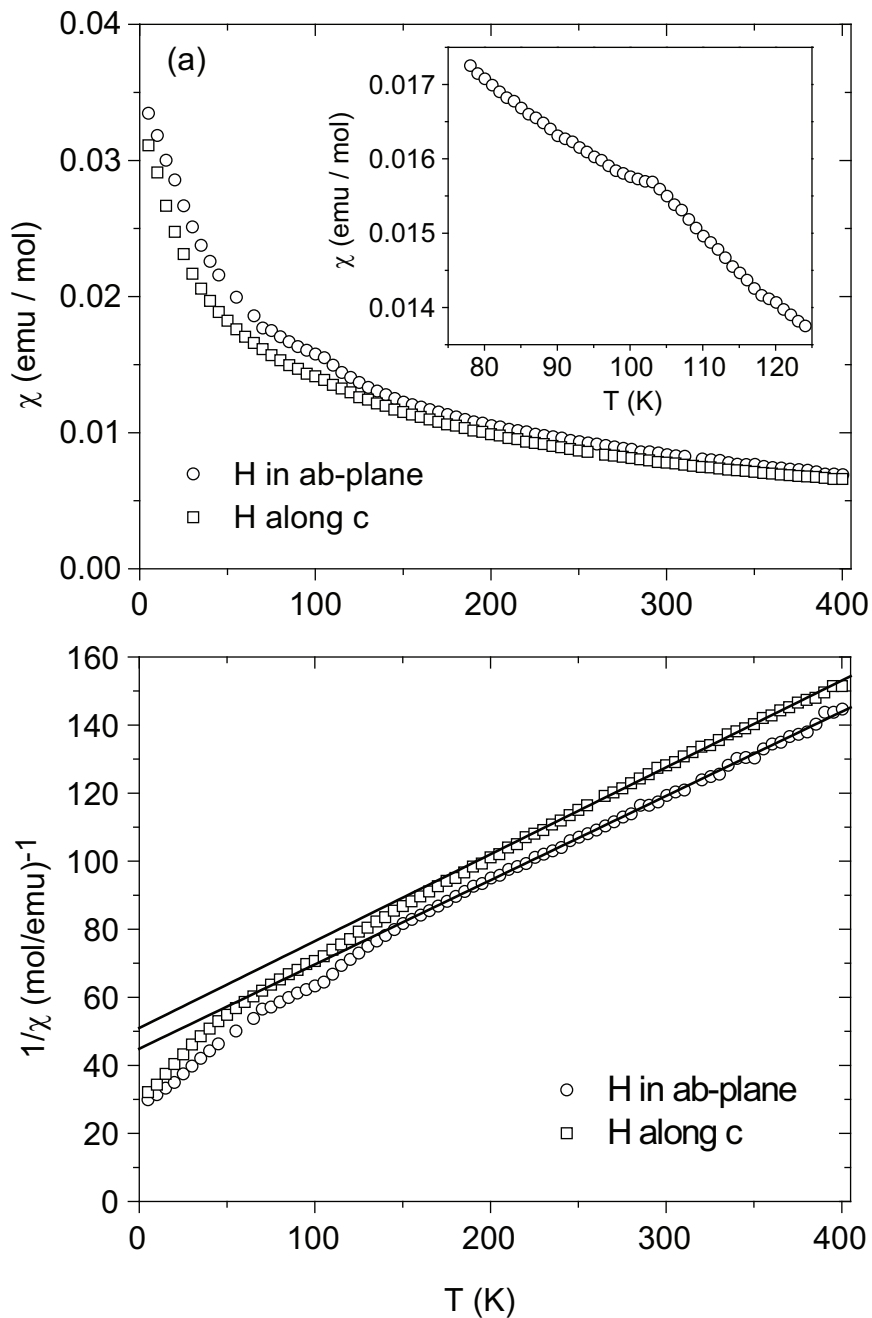


Figure 9.13: (a) The measured magnetic susceptibility χ of $\text{Ni}_3\text{Cr}_2\text{P}_2\text{S}_9$ crystals (corrected for sample holder contribution) between 5 K and 400 K oriented with the applied field ($H = 2$ T) in the ab-plane and along the c axis. The inset shows the kink near 105 K on a finer scale. (b) The inverse susceptibility $1/\chi$ vs. T , showing deviations from Curie-Weiss behavior below about 150 K. The solid lines are linear fits to data above 200 K. The uncertainty in these measurements arises primarily from the sample mass measurement, and is thus estimated to be about $\pm 4\%$.

Based on the crystal structure determined from X-ray data (*vide supra*), there are expected to be two Cr atoms and two Ni atoms in distorted octahedral environments and one Ni in trigonal bipyramidal coordination per formula unit. Octahedral and trigonal bipyramidal crystal fields split the five otherwise degenerate 3d orbitals of the transition metals as shown in Figure 9.14. The spins of the Ni and Cr atoms in these environments are also shown in this Figure. The molar Curie constant can be calculated by combining the contributions from each magnetic species [12]:

$$C = \sum_i \frac{N_i \mu_B^2}{3k_B} (\mu_{eff}^i)^2. \quad (9.3)$$

Here μ_B is the Bohr magneton, k_B is the Boltzmann constant, N_i is the number of magnetic species i per formula unit, and μ_{eff}^i is the effective moment of species i ($\mu_{eff} = 2\sqrt{S(S+1)}$). This model predicts a Curie constant of 5.75 emuK/mol. This is not consistent with the value of 3.9–4.0 emuK/mol determined from the measured data.

The octahedral coordination environments in $\text{Ni}_3\text{Cr}_2\text{P}_2\text{S}_9$ are not ideal. The degree of distortion can be described by examining the range of bond distances and angles that occur in these octahedra. The bond angles which would be 90° for a perfect octahedron vary from 84 – 96° . Less variation is seen in the bond distances, which vary only by 1–2%. It is possible that this could effect the d-orbital splitting shown in Figure 9.14, and change the expected moments on the ions. To examine this effect, extended Hückel calculations were carried out, using the exact geometry determined by the single crystal structure determination of the selenide analogue. The results showed that the doubly degenerate (e_g) states remain degenerate, while the t_{2g} levels are split into a single level about 0.2 eV below a pair of degenerate levels. Since the e_g states remain degenerate, Ni is expected to remain in the high spin configuration ($S = 1$). The splitting of the t_{2g} states is small compared to typical pairing energies (which are usually sev-

eral eV [14]), and so Cr is expected to also be in the high spin configuration ($S = 3/2$). Thus, the distortion of the octahedra cannot explain the lower than expected measured moment (Curie constant) of this material. A similar calculations for the bipyramidal site showed the $a1g'$ site to be about 6 eV above the eg' levels, suggesting that the low spin state shown in Figure 9.14 ($S = 0$) is likely to be the configuration adopted by Ni(3).

The value of the measured moment may be influenced by the disorder on the octahedral transition metal sites, which current X-ray structure data suggest contain mixtures of Ni/Cr. Random occupation of these positions could result in exchange constants that vary from site to site, producing a complex array of magnetic interactions. If some of these interaction are strong enough to result in antiferromagnetic correlations at high temperature (> 400 K), the moment measured below 400 K would be lower than the value expected if all the spins were free.

Although the $1/\chi$ vs. T data are well modeled by a linear fit at above about 200 K, the applicability of the Curie-Weiss law is somewhat questionable. Typically, this law is valid only for T significantly greater than θ , and here data is only available up to about $T = 2\theta$. In addition, complex behavior often occurs in low dimensional magnetic systems, and, as noted above, the simple Curie-Weiss model is not necessarily reliable in lower dimensional systems [13].

Despite the indications of strong antiferromagnetic interactions (large negative Weiss temperatures), no signs of long range antiferromagnetic ordering are seen in the susceptibility data in Figure 9.13. Such behavior is sometimes attributed to geometrical frustration of the antiferromagnetic interactions. This often occurs cases with triangular nets of magnetic ions (see for example Refs. [15, 16, 17, 18]). However, the octahedral transition metal sites in $Ni_3Cr_2P_2S_9$ make up a honeycomb net (actually the double layered structure of this com-

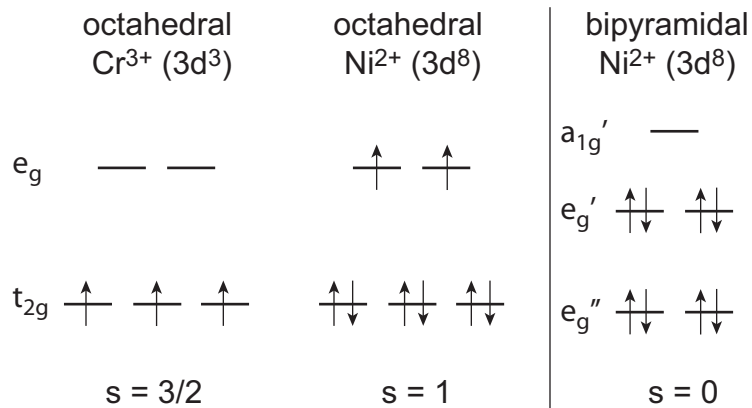


Figure 9.14: A possible spin configurations for Cr³⁺ and Ni²⁺ in Ni₃Cr₂P₂S₉, expected for ideal octahedral and trigonal bipyramidal configurations.

pound makes a double layer honeycomb net, as shown in Figure 9.2) which is not geometrically frustrated. Another possible explanation for the absence of ordering in this compound is related to its layered crystal structure.

It has been shown that no ordered antiferromagnetic (or ferromagnetic) ground states exist for isotropic one- and two-dimensional Heisenberg models [19]. However, most layered materials do undergo ordering transitions. These are usually attributed to interlayer coupling which makes the magnetic system three-dimensional, or to anisotropic intralayer couplings which have been shown to lead to ordered states through the so called Kosterlitz and Thouless (KT) transition [20]. For example, BaNi₂V₂O₈ has honeycomb nets of magnetic Ni atoms in edge sharing NiO₆ octahedra which are separated by from neighboring nets by Ba atoms and VO₄ tetrahedra. This compound orders antiferromagnetically at 50 K [21] in what is believed to be a KT transition [22]. Another, perhaps more closely related, example is NiPS₃, which is made up of layers edge sharing NiS₆ octahedra which form a honeycomb net with P–P dimers in the holes forming ethane-like P₂S₆ units [23]. The layers seen in Ni₃Cr₂P₂Q₉ can be derived from the layers in NiPS₃ by fusing two of the layers together, and then replacing two

P atoms on neighboring P–P units with a Ni atom to form the P–Ni–P units. NiPS₃ orders antiferromagnetically at 155 K [24]. This compound adopts a monoclinic crystal structure, and the ordered magnetic state has ferromagnetic chains coupled antiferromagnetically to one another (the ordered state has the same unit cell as the disordered state). However, as noted above, no such ordering is seen in Ni₃Cr₂P₂S₉. This suggests that this compound may behave more like an isotropic two-dimensional Heisenberg magnet than others.

9.2.7 Conclusions

The new quaternary compounds Ni₃Cr₂P₂S₉ and Ni₃Cr₂P₂Se₉, and the solid solution between them, were discovered, but not found to have promising thermoelectric properties. However, interesting structural and magnetic properties were observed. The layered structures of these compounds contain unusual five-coordinate Ni atoms, and the magnetic properties show strong antiferromagnetic interactions and an unexplained knee at about 105 K, but no magnetic ordering. An explanation of the magnetic properties may lie in a better understanding of the crystal structure, in particular the distribution of Cr and Ni over the transition metal sites.

9.3 Arsenic-Containing Bi₂Te₃-Based Alloys

Prof. John Badding's research group at The Pennsylvania State University investigates how the physical properties of materials change under pressure. They have observed significant enhancements in the thermoelectric properties of bismuth telluride based thermoelectric materials. They estimate a value of $ZT = 2.2$ at 1.7 GPa from measured resistivity and thermopower data [25]. The authors suggest that the observations (in particular the peak in S at about 1.7 GPa)

are consistent with an electronic topological transition (ETT) [26]. An ETT occurs when an extremum of a band crosses the chemical potential. This causes a sharp increase in the density of states at the chemical potential and therefore can enhance the thermopower.

Similar enhancements in ZT might be possible by mimicking applied pressure using chemical substitutions. Like applied pressure, substitutions which replace larger atoms with smaller ones can reduce the unit cell dimensions. Arsenic is a good candidate, since it is isovalent with Sb and Bi, yet is smaller than both (covalent radii: As 1.20 Å, Sb 1.40 Å, Bi 1.46 Å). The size difference between As and Sb or Bi is close to the maximum for which chemical substitutions typically can occur ($\sim 15\%$). In addition, As_2Te_3 adopts a monoclinic structure (C2/m) and is not isostructural with Bi_2Te_3 and Sb_2Te_3 . These observations suggest that only a small amount of As_2Te_3 may be soluble in these alloys. Indeed, a previous study found that less than 1% of As_2Te_3 could be dissolved in Bi_2Te_3 [27]. However, As_2Te_3 may be more soluble in Sb_2Te_3 rich alloys, since the size difference between As and Sb is slightly less than that between As and Bi. It is well established that significant amounts of Sb_2Se_3 can be dissolved in these alloys, even though it is not isostructural to the other members (Sb_2Se_3 is orthorhombic, space group Pnma). Bi_2Te_3 based thermoelectric alloys typically contain about 3-5% Sb_2Se_3 .

In this study we examined the effects of adding As_2Te_3 to alloys with compositions close to that which gives the best p-type thermoelectric properties: $(\text{Bi}_2\text{Te}_3)_{25}(\text{Sb}_2\text{Te}_3)_{72}(\text{Sb}_2\text{Se}_3)_3$. To optimize carrier concentration these alloys are typically doped with iodine; however, in this preliminary study of the solubility of As_2Te_3 in this system and its effects on the thermopower no intentional doping was performed. Three sets of alloys were synthesized. The first two examined the effects of replacing the Sb_2Se_3 in the optimized alloy composition with

As_2Te_3 . The third set contained no Sb_2Se_3 and involved simply the addition of varying amounts of As_2Te_3 to $(\text{Bi}_2\text{Te}_3)_{25}(\text{Sb}_2\text{Te}_3)_{72}$. The nominal composition of each alloy sample is listed in Table 9.6. In what follows the individual samples will be referred to by the alloy set to which they belong and their value of x . The Bi_2Te_3 structure is recalled in Figure 9.15.

Table 9.6: The loaded composition of each member of the three alloy sets described in this Section.

<i>Alloy sets 1 and 2: $(\text{Bi}_2\text{Te}_3)_{25}(\text{Sb}_2\text{Te}_3)_{72}(\text{As}_2\text{Te}_3)_x(\text{Sb}_2\text{Se}_3)_{3-x}$</i>	
Label	Nominal composition
$x = 3$	$(\text{Bi}_2\text{Te}_3)_{25}(\text{Sb}_2\text{Te}_3)_{72}(\text{As}_2\text{Te}_3)_3(\text{Sb}_2\text{Se}_3)_0$
$x = 2$	$(\text{Bi}_2\text{Te}_3)_{25}(\text{Sb}_2\text{Te}_3)_{72}(\text{As}_2\text{Te}_3)_2(\text{Sb}_2\text{Se}_3)_1$
$x = 1$	$(\text{Bi}_2\text{Te}_3)_{25}(\text{Sb}_2\text{Te}_3)_{72}(\text{As}_2\text{Te}_3)_1(\text{Sb}_2\text{Se}_3)_2$
$x = 0$	$(\text{Bi}_2\text{Te}_3)_{25}(\text{Sb}_2\text{Te}_3)_{72}(\text{As}_2\text{Te}_3)_0(\text{Sb}_2\text{Se}_3)_3$

<i>Alloy set 3: $(\text{Bi}_2\text{Te}_3)_{25}(\text{Sb}_2\text{Te}_3)_{72}(\text{As}_2\text{Te}_3)_x$</i>	
Label	Nominal composition
$x = 3$	$(\text{Bi}_2\text{Te}_3)_{25}(\text{Sb}_2\text{Te}_3)_{72}(\text{As}_2\text{Te}_3)_3$
$x = 2$	$(\text{Bi}_2\text{Te}_3)_{25}(\text{Sb}_2\text{Te}_3)_{72}(\text{As}_2\text{Te}_3)_2$
$x = 1$	$(\text{Bi}_2\text{Te}_3)_{25}(\text{Sb}_2\text{Te}_3)_{72}(\text{As}_2\text{Te}_3)_1$
$x = 0$	$(\text{Bi}_2\text{Te}_3)_{25}(\text{Sb}_2\text{Te}_3)_{72}(\text{As}_2\text{Te}_3)_0$

9.3.1 Synthesis of the Alloys

Bi_2Te_3 , Sb_2Te_3 , Sb_2Se_3 , and As_2Te_3 were synthesized from the elements (Bi shot 99.99%, Sb powder 99.999%, As pieces, Se pellets (99.99%), and Te ingot 99.999%) by heating stoichiometric mixtures at 550 °C for 48 hours, 500 °C for 48 hours, 650 °C for 24 hours, and 500 °C for 24 hours, respectively. The phase purity of the products was verified by powder X-ray diffraction. Alloys of Bi_2Te_3 , Sb_2Te_3 , Sb_2Se_3 , and As_2Te_3 were then made by thoroughly grinding mixtures of

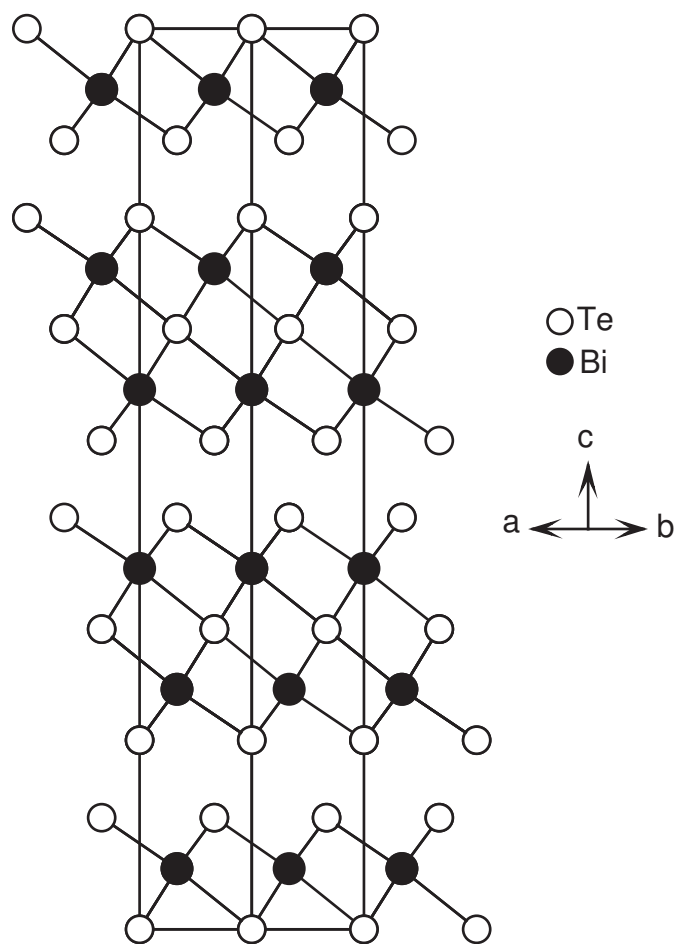


Figure 9.15: A view of the crystal structure of Bi_2Te_3 . The hexagonal unit cell is outlined.

the previously synthesized binary compounds together with an agate mortar and pestle (about 1.5 g total mass for each sample). Four sample composition were loaded for each alloy set as listed in Table 9.6. The mixtures were then sealed in evacuated silica tubes and heated to 600 °C, which is slightly above the liquidus temperature of $(\text{Bi}_2\text{Te}_3)_{25}(\text{Sb}_2\text{Te}_3)_{75}$. The reaction mixtures were held at this temperature for two days to allow thorough mixing in the liquid phase. This temperature was chosen since melting the binaries together at higher temperatures (650 °C) produced small clear As and Te crystals on the wall at the upper end of the tube. At the end of the reaction time the furnace was shut off and allowed to cool to room temperature naturally. To make pellets to be used for properties measurements, the samples were ground thoroughly in an agate mortar, pressed into cylindrical pellets, and annealed for several weeks at 250-300 °C. Pellets which were annealed at 400 °C showed signs of decomposition, with rounded pellet edges and black plate crystals, small clear crystals, round silver blobs, and glassy looking black blobs on the tube wall. Pellets annealed at 300 °C retained their sharp edges and formed only a few small black crystals on the tube wall near the pellets. The densities of the pellets of alloy set 3 were calculated from their masses and dimensions. All four pellets were 83-84% dense, when compared to the density calculated from the loaded compositions and the lattice constants determined from powder X-ray diffraction studies. This is typical for materials prepared by cold pressing and sintering.

9.3.2 Powder X-ray Diffraction Results: Unit Cell Parameters

Powder X-ray diffraction (PXRD) analysis was performed on each alloy with a Scintag 2000 theta-theta diffractometer using $\text{Cu-K}\alpha$ radiation. PXRD data were collected from alloy sets 1 and 2 after the long annealing step. PXRD data

were collected from alloy set 3 after the mixtures of binaries were melted together. A piece was cut or broken away from each sample, ground, and mixed with a Si standard. Data were collected from $2\theta = 5^\circ$ to 90° in step mode using 0.01° steps and a counting time of 5 seconds per step. Unit cell parameters were determined from the measured diffraction patterns by performing Le Bail refinements using the program Fullprof. Le Bail refinements are similar to Rietveld refinements with the one important exception: the intensity of each peak is refined independently. These refinements give accurate fits to the lattice constants, without the complications associated with the refinement of atomic positions and displacement factors. Refined parameters include zero offset, lattice constants of the alloy phase, and overall peak shape and half width parameters for both the alloy phase and the Si standard. The results of the refinements are shown in Figures 9.16, 9.17, and 9.18.

As expected, little difference is seen among the PXRD patterns for the different alloys. The observed data are modeled well by a phase isostructural to Bi_2Te_3 and the Si standard. One small unaccounted for peak is seen in the patterns from alloy set 1 (Figure 9.16), just to the left of the strongest peak near 28° . This peak could not be matched to any likely impurity phase. Upon closer inspection it was seen also in the Sb_2Te_3 starting material. This is consistent with the observation that the intensity of this peak is nearly the same in each sample. The other alloy sets were made from a different batch of Sb_2Te_3 and do not show this reflection. Other than this peak, there is no indication of secondary phases formed during the reactions. The typical detection limit for PXRD is around 1-5% by weight, and the loaded As_2Te_3 content is definitely below this limit. However, effects of the addition of As_2Te_3 the structure can be seen in the refined lattice constants listed in Table 9.7 and plotted in Figure 9.19.

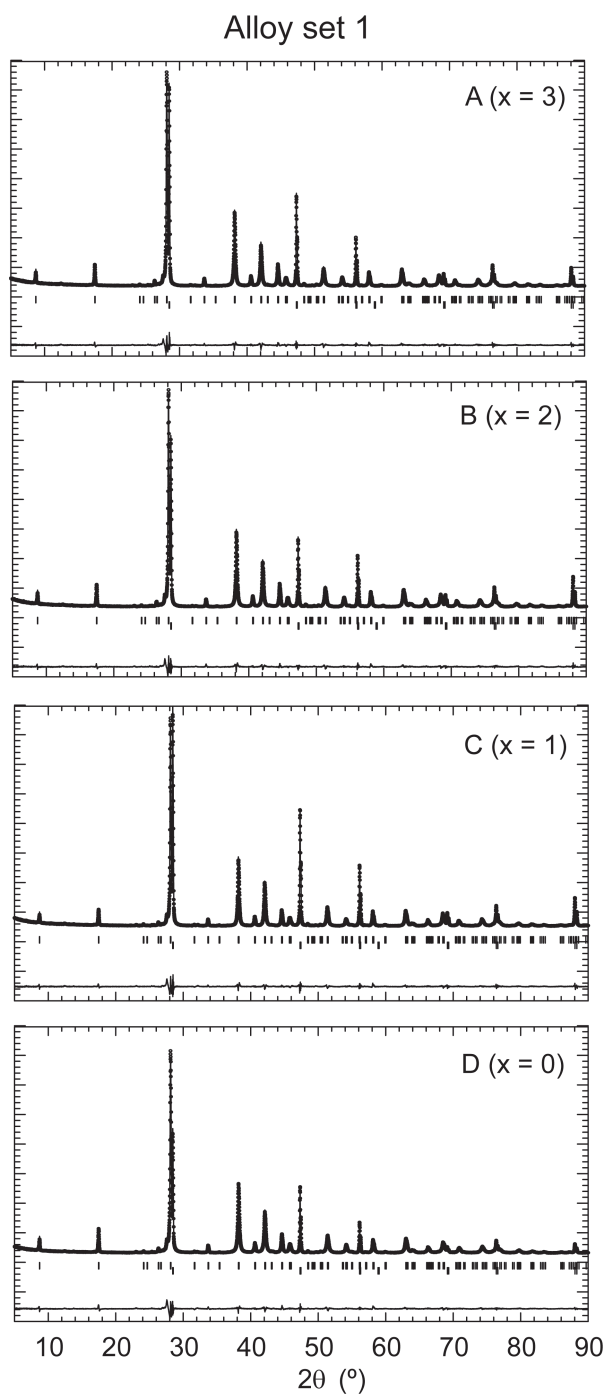


Figure 9.16: Results from Le Bail refinement of alloy set 1 with nominal compositions $(\text{Bi}_2\text{Te}_3)_{25}(\text{Sb}_2\text{Te}_3)_{72}(\text{As}_2\text{Te}_3)_x(\text{Sb}_2\text{Se}_3)_{3-x}$. The measured data points and fitted profiles (solid line) are shown, as well as the difference patterns (at bottom). The upper ticks locate predicted reflections for the alloy phase and the lower ticks denote reflections from the internal Si standard.

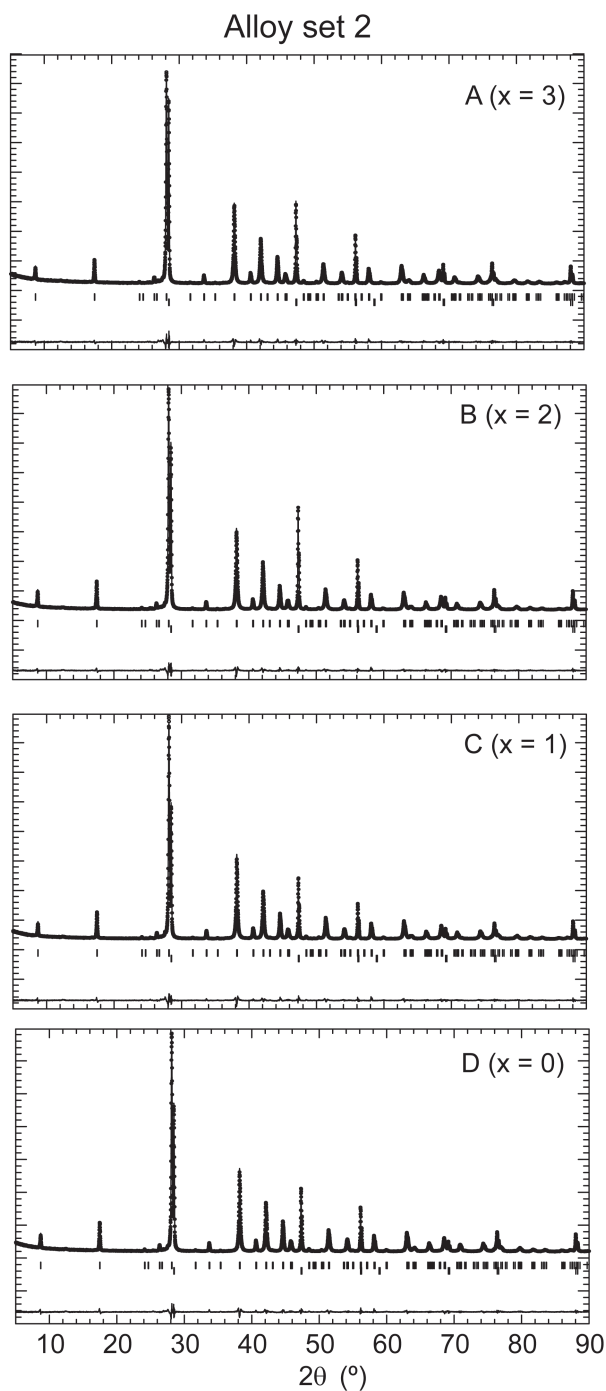


Figure 9.17: Results from Le Bail refinement of alloy set 2 with nominal compositions $(\text{Bi}_2\text{Te}_3)_{25}(\text{Sb}_2\text{Te}_3)_{72}(\text{As}_2\text{Te}_3)_x(\text{Sb}_2\text{Se}_3)_{3-x}$. The measured data points and fitted profiles (solid line) are shown, as well as the difference patterns (at bottom). The upper ticks locate predicted reflections for the alloys phase and the lower ticks denote reflections from the internal Si standard.

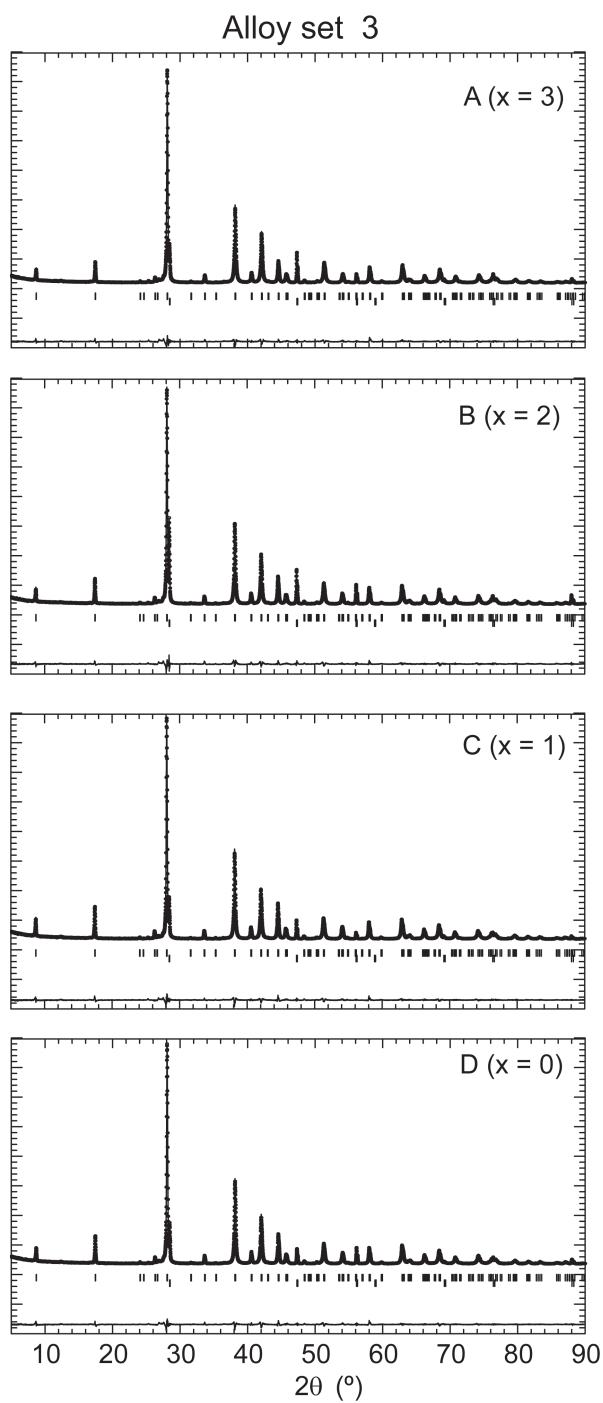


Figure 9.18: Results from Le Bail refinement of alloy set 3 with nominal compositions $(\text{Bi}_2\text{Te}_3)_{25}(\text{Sb}_2\text{Te}_3)_{72}(\text{As}_2\text{Te}_3)_x$. The measured data points and fitted profiles (solid line) are shown, as well as the difference patterns (at bottom). The upper ticks locate predicted reflections for the alloy phase and the lower ticks denote reflections from the internal Si standard.

Table 9.7: Hexagonal unit cell parameters for Bi_2Te_3 based alloys determined from PXRD. The average errors for the parameters reported by the fitting software were 0.00005 \AA for a , 0.0005 \AA for c , and 0.01 \AA^3 for V .

<i>Alloy set 1: $(\text{Bi}_2\text{Te}_3)_{25}(\text{Sb}_2\text{Te}_3)_{72}(\text{As}_2\text{Te}_3)_x(\text{Sb}_2\text{Se}_3)_{3-x}$</i>			
	a (Å)	c (Å)	V (Å³)
x = 3	4.29436	30.48152	486.816
x = 2	4.29378	30.47295	486.547
x = 1	4.29304	30.46545	486.258
x = 0	4.29032	30.45394	485.457

<i>Alloy set 2: $(\text{Bi}_2\text{Te}_3)_{25}(\text{Sb}_2\text{Te}_3)_{72}(\text{As}_2\text{Te}_3)_x(\text{Sb}_2\text{Se}_3)_{3-x}$</i>			
	a (Å)	c (Å)	V (Å³)
x = 3	4.2914	30.4825	486.16
x = 2	4.2910	30.4709	485.89
x = 1	4.2907	30.4624	485.68
x = 0	4.2896	30.4508	485.25

<i>Alloy set 3: $(\text{Bi}_2\text{Te}_3)_{25}(\text{Sb}_2\text{Te}_3)_{72}(\text{As}_2\text{Te}_3)_x$</i>			
	a (Å)	c (Å)	V (Å³)
x = 3	4.2923	30.4804	486.30
x = 2	4.2940	30.4794	486.68
x = 1	4.2962	30.4858	487.30
x = 0	4.2982	30.4912	487.84

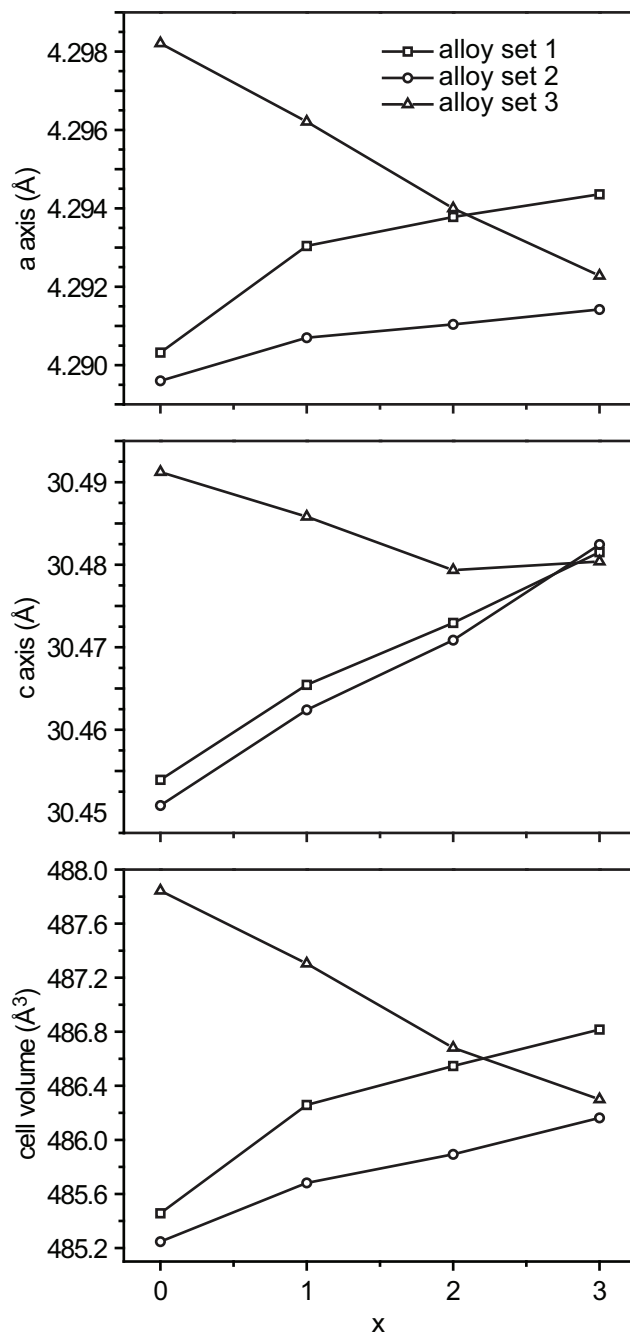


Figure 9.19: Unit cell parameters determined by PXRD for alloy sets 1 and 2 with nominal compositions $(\text{Bi}_2\text{Te}_3)_{25}(\text{Sb}_2\text{Te}_3)_{72}(\text{Sb}_2\text{Se}_3)_{3-x}(\text{As}_2\text{Te}_3)_x$ and alloy set 3 with nominal compositions $(\text{Bi}_2\text{Te}_3)_{25}(\text{Sb}_2\text{Te}_3)_{72}(\text{As}_2\text{Te}_3)_x$ as a function of the As_2Te_3 content x .

Several observations can be made regarding the refined unit cell parameters. First the discrepancy between alloy sets 1 and 2 which have the same nominal compositions must be addressed. The unit cells of set 1 are significantly larger than those of set 2. This may be attributed to the impurity in the Sb_2Te_3 used to make set 1. Such an impurity would result a lower than expected Sb_2Te_3 content, making all of the samples Bi_2Te_3 rich compared to set 2. Since Bi_2Te_3 has a larger unit cell than Sb_2Te_3 , this would result in a systematic increase in the cell parameters. The observed difference in the dependence of the cell parameters on x may be due to different annealing treatments which may change the amount of As_2Te_3 incorporated into the alloys. For $x = 3$ the nominal composition of all of the alloy set is the same, $(\text{Bi}_2\text{Te}_3)_{25}(\text{Sb}_2\text{Te}_3)_{72}(\text{As}_2\text{Te}_3)_3$. One therefore expects that the cell parameters for the $x = 3$ member of each alloy set to be equal. In this respect alloy set 1 is clearly different than sets 2 and 3, which agree fairly well with each other. This again points to a deviation in set 1 from the nominal compositions, likely due to the impurity noted above.

In the $(\text{Bi}_2\text{Te}_3)_{25}(\text{Sb}_2\text{Te}_3)_{72}(\text{Sb}_2\text{Se}_3)_{3-x}(\text{As}_2\text{Te}_3)_x$ alloys (sets 1 and 2) the unit cell is expanded as Sb_2Se_3 is replaced by As_2Te_3 (Figure 9.19). This observation alone could be attributed simply to the decreasing Sb_2Se_3 content and does not prove that As_2Te_3 is being incorporated into the alloys. However, as noted above, the similar lattice constants for $x = 3$ in sets 2 and 3 suggest that As_2Te_3 is replacing Sb_2Se_3 in the structure. The overall increase in unit cell parameters of alloy sets 1 and 2 as a function of x is therefore due to the replacement of the smaller Se atoms of Sb_2Se_3 with the larger Te atoms of As_2Te_3 . We note that without alloy set 3 we could not definitively show that As_2Te_3 was incorporated into the alloys of sets 1 and 2. Indeed this was the initial motivation for synthesizing alloy set 3.

In the $(\text{Bi}_2\text{Te}_3)_{25}(\text{Sb}_2\text{Te}_3)_{72}(\text{As}_2\text{Te}_3)_x$ alloys (set 3) the unit cell is contracted as the amount of As_2Te_3 is increased (Figure 9.19). This is consistent with the

smaller As atoms replacing the larger Sb and Bi atoms. That the decrease in unit cell volume continues steadily up to $x = 3$ suggests that a significant amount of As_2Te_3 can be dissolved in the alloys. Without microscopic chemical analysis of the samples, it is not possible to say how much As_2Te_3 is actually incorporated into the alloy in each case. It is possible to do such analysis with an electron microprobe; however, the most As rich sample contains less than 0.7 wt. % As, which is approaching the lower limits of this technique (~ 0.1 wt. %). Such measurements were not performed and all we can say is that as the nominal value of x increases in each alloy set the amount of As_2Te_3 dissolved in the alloy increases from 0 to $\lesssim 3\%$.

Finally, we note the unusual behavior of the c -axis of alloy set 3 for larger values of x . The length of c does not continue to decrease from $x = 2$ to $x = 3$. To exclude the possibility of this being an artifact of the unit cell refinements, individual diffraction peaks were examined. This is shown in Figure 9.20. This Figure shows that the (110) line shifts monotonically toward higher angles (smaller d spacing) as x is increased. The position of this diffraction peak is sensitive to the length of a but not the length of c , and its behavior agrees well with the fitted a parameters (Figure 9.19). The position of the (006) line shifts toward higher angle as x is increased up to $x = 2$, and then changes little between $x = 2$ and $x = 3$. This is consistent with the fitted c parameters (Figure 9.19). The (006) reflection is at relatively low angle, and therefore less sensitive to changes in c than say the (0018) line. However, higher order reflections of this type were either overlapping with neighboring reflections, too low in intensity, or too broad to serve as a better comparison than (006). Close inspection of the behavior of c in alloy sets 1 and 2 reveals a sharper increase from $x = 2$ to $x = 3$ than is seen between $x = 1$ and $x = 2$. This observation may be related to the "unusual" behavior seen in alloy set 3. It is not clear why this behavior should occur; however, it suggests that the in-

corporation of As into the alloys is more complicated than simple substitution on the Bi/Sb site, at least at higher As concentrations. One possibility which would account for the expansion of the lattice in the c-direction is the intercalation of As into the van der Waals gap between the Te layers (Figure 9.15). The plane between these Te layers contain distorted octahedral holes, contracted along c. The sites at the centers of these holes are 2.84 Å from Te atoms in Sb_2Te_3 , and 2.86 Å from Te atoms in Bi_2Te_3 . This is well within the range of distances seen in the As_2Te_3 structure, which contains octahedral and square pyramidal As atoms with As-Te distances of 2.65-3.16 Å [28]. The possibility of intercalation of As into these layers is therefore not unreasonable, and may be the source of the increase in c observed at the highest As content investigated in alloy set 3.

9.3.3 Thermoelectric Properties

Pieces cut from the samples were sent to Tom Scheidemantel in Prof. John Badding's research group at the Pennsylvania State University for thermopower measurements. Measurements were performed at ambient pressure and temperature, and in a diamond anvil cell [25, 29] at ambient temperature and applied pressures up to about 7 GPa.

The results of the thermopower measurements are shown in Figure 9.21. For alloy set 1, ambient condition measurements were performed on the $x = 0$, 1, and 3 samples, and show a decrease in S with increasing x. All four members of alloy set 3 were measured and showed an increase in S with increasing x up to $x = 2$, and a decrease in going from $x = 2$ to $x = 3$. Thus, we see that with the exception of the $x = 3$ member of alloy set 3 the thermopower under ambient conditions increases with decreasing unit cell volume (Figure 9.19). It could be that the anomalous behavior of the thermopower of the most As rich member

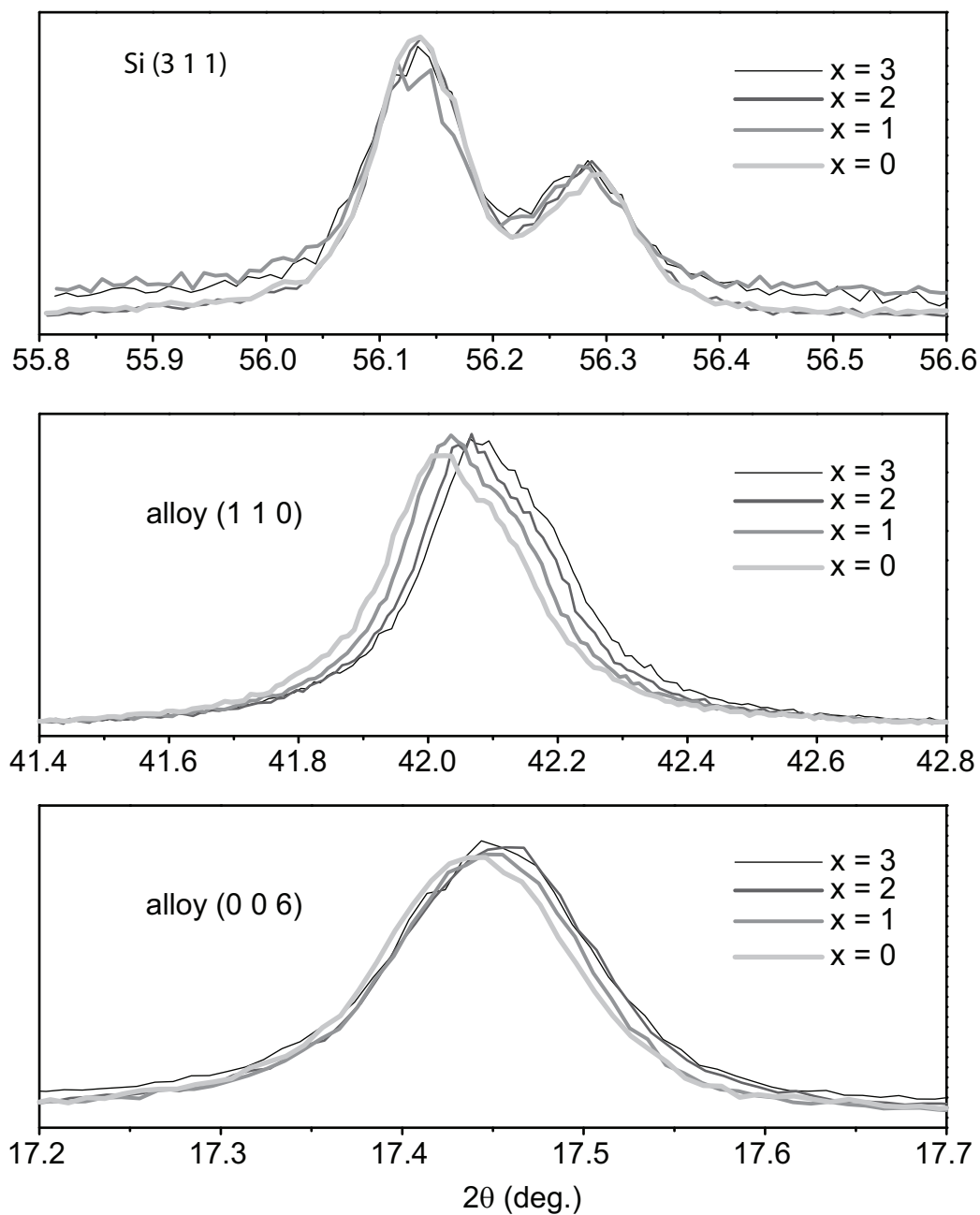


Figure 9.20: Selected diffraction peaks from alloy set 3, with the refined zero point correction applied. Panel (a) shows the (311) peak of the internal Si standard which coincides for all four alloy samples. Panel (b) shows the (110) line of the alloys, which is sensitive to the length of a but not c . Panel (c) shows the (006) line of the alloys, which is sensitive to the length of c but not a .

of alloy set 3 is related to the anomalous behavior in the c-axis length discussed above.

The pressure dependence of the thermopower of the $x = 1$ samples of alloy sets 1 and 2 are shown in Figure 9.21b. S is seen to steadily decrease with increasing pressure. This is likely due to the narrowing of the band gap as the atoms are squeezed together. At the highest pressures S has decreased to a value typical of a metal ($\sim 5 \mu\text{V}/\text{K}$).

The significant peak in S which was reported for the optimally doped p-type alloys (Ref. [25]) is not seen in Figure 9.21. This may be attributed to the difference in the location of the chemical potential in the two cases. Optimally doped alloys are heavily degenerate, and therefore their chemical potential is expected to be deeper within the valence band than for the nominally undoped samples presented here. If the peak in S in the doped alloys is due to an ETT, it would be caused by a lower valence band moving up and touching the chemical potential before the gap is sufficiently narrowed. Upon further application of pressure, the effects of the band gap narrowing begins to dominate and S declines. The measurements reported here suggest that the ETT does not occur in the undoped alloys before the narrowing of the gap significantly degrades S . This is consistent with the higher chemical potential in the undoped material. The above description of course neglects the effects of the As atoms on the pressure dependence of S , which is difficult to predict yet may be significant.

The electrical resistivities of the four members of alloy set 3 were also measured. The temperature dependence of ρ is shown in Figure 9.22. The data show behavior typical of narrow band gap semiconductors or semimetals. For comparison, the resistivity of optimally doped Bi_2Te_3 alloys is near $1 \text{ m}\Omega\text{cm}$. Finally we report the calculated power factors ($\text{PF} = S^2/\rho$) for alloy set 3 at room tempera-

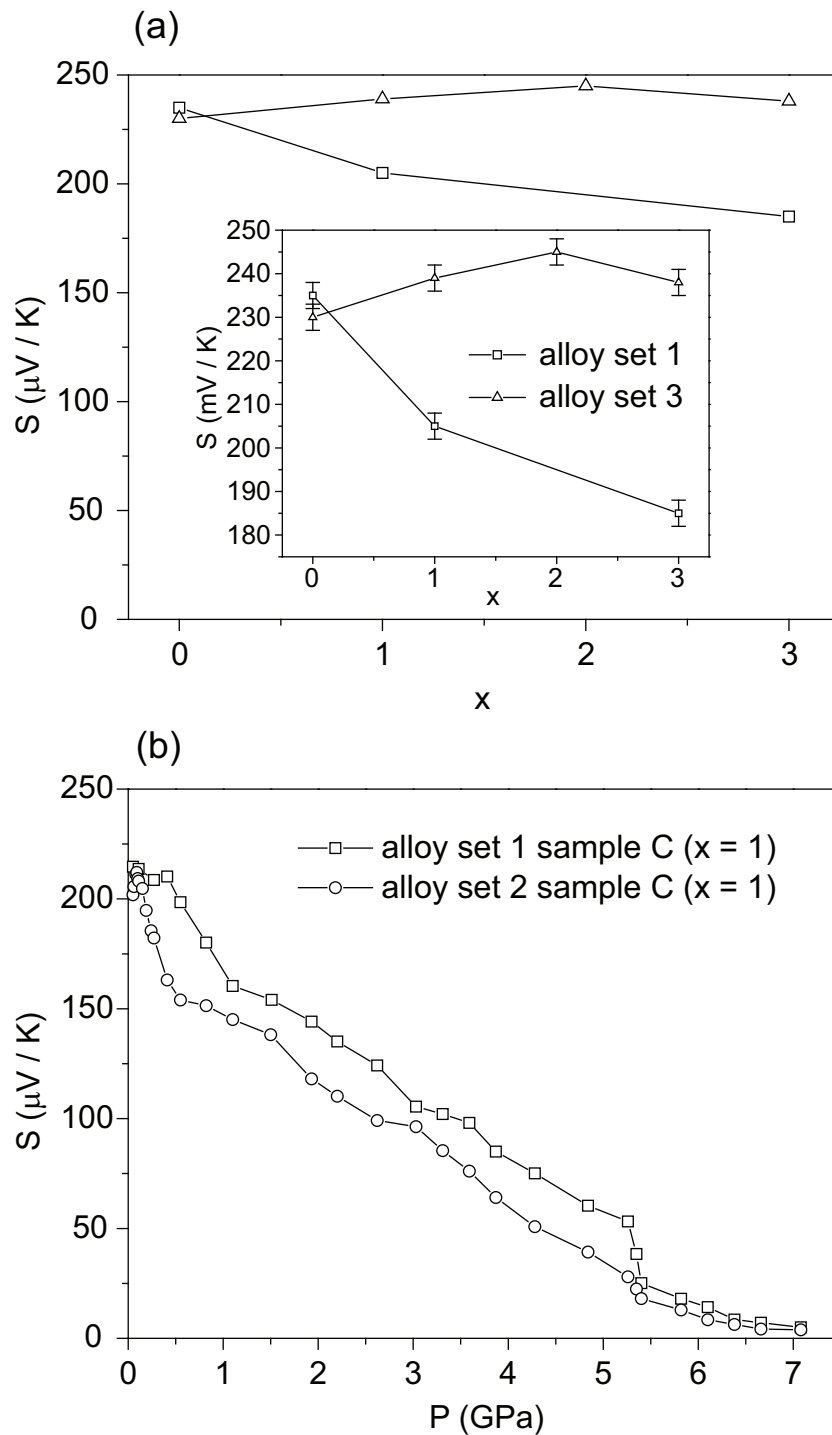


Figure 9.21: The measured thermopower of the Bi_2Te_3 based alloys. Measurements under ambient conditions are shown in panel (a). The inset in (a) shows the same data on a smaller scale. Measurements performed under pressure at ambient temperature in a diamond anvil cell are shown in panel (b).

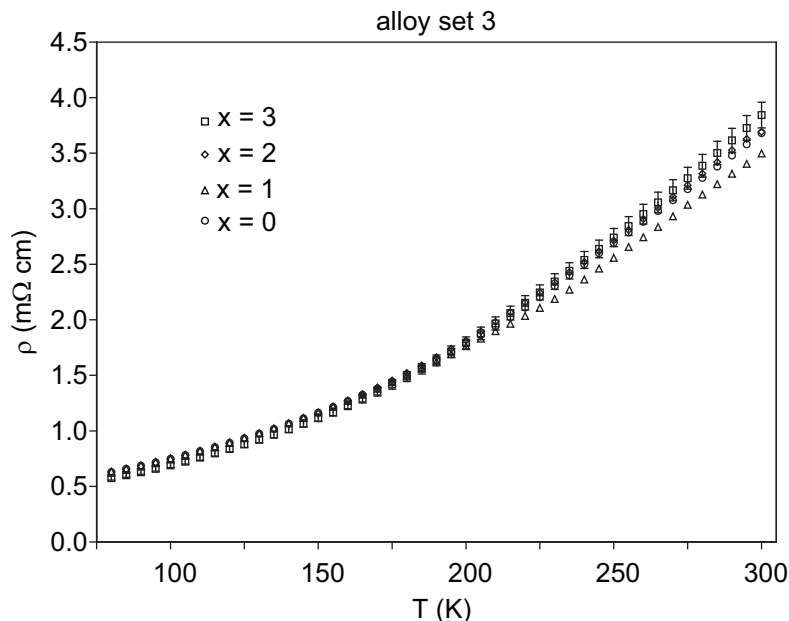


Figure 9.22: The measured electrical resistivity of alloy set 3 with compositions $(\text{Bi}_2\text{Te}_3)_{25}(\text{Sb}_2\text{Te}_3)_{72}(\text{As}_2\text{Te}_3)_x$. The error bars represent the estimated uncertainty in the geometrical measurements of the sample.

ture in Figure 9.23. The results show that the PF increases with the addition of small amounts of As but begins to decline for $x = 3$.

9.3.4 A Final Comment

The resistivity and thermopower of alloy set 3 was measured again about 18 months after the measurements reported above were made. Significant differences were observed between the two sets of data. In particular, after sitting at room temperature for 18 months in air, the measured thermopower of all four samples increased to 257–262 $\mu\text{V}/\text{K}$, varying smoothly with nominal composition; however, unlike the previous measurements (Figure 9.21), the thermopower was seen to *decrease* with increasing As content. In addition, significant differences were seen in the measured resistivities. After the samples had sat in air for 18 months, the measured resistivities were seen to be in general lower than

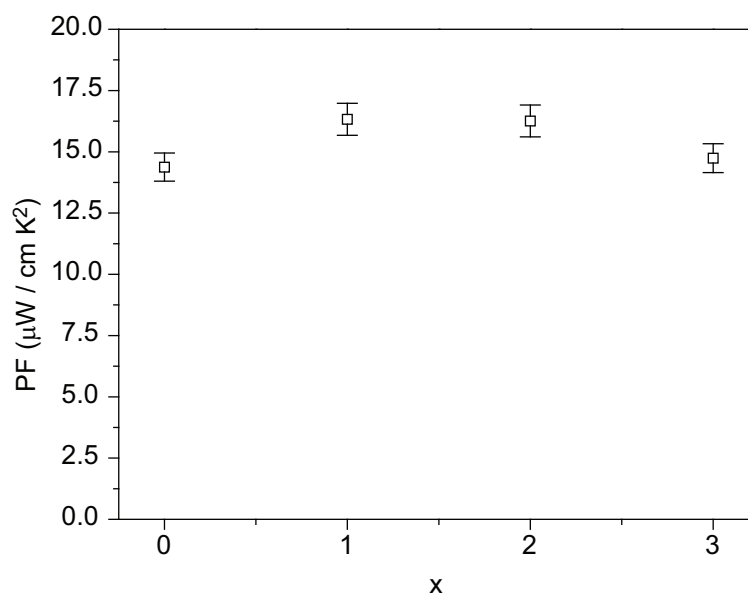


Figure 9.23: The thermoelectric power factor ($PF = S^2 / \rho$) of alloy set 3 with compositions $(\text{Bi}_2\text{Te}_3)_{25}(\text{Sb}_2\text{Te}_3)_{72}(\text{As}_2\text{Te}_3)_x$. The error bars represent the estimated uncertainty due to the uncertainties in S and ρ .

the previous measured values, varying from 2.8–3.8 $\text{m}\Omega\text{cm}$, and decreasing with increasing As content. It is unclear why the properties changed over time, but it could be an indication of phase separation. Solid solubilities usually increase with increasing temperature. Perhaps the solubility of As in these alloys is significantly higher at the temperatures at which the alloys were annealed (250–300 °C) than at room temperature. If this were the case, one would expect As or As_2Te_3 to precipitate out of the alloy at room temperature over time. A conservative estimate of the diffusion constant for elements in low melting solids near room temperature is $10^{-12} \text{ cm}^2/\text{s}$. This would result in a diffusion distance of about 70 μm over the course of 18 months. The grains in these polycrystalline alloy samples are not expected to be larger than this, so phase separation of As could occur over this time. Because this could affect not only the chemical composition of the

grains but also the properties of the grain boundaries, it is not clear how such phase separation would effect the thermoelectric properties of the bulk samples.

9.3.5 Conclusions

The results from these initial investigation into the addition of As_2Te_3 to Bi_2Te_3 based thermoelectric alloy materials are interesting, and may warrant further study. Powder X-ray diffraction analysis shows that an increasing amount of As_2Te_3 is incorporated into the structure up to a nominal concentration of 3%. This strongly suggests that the solubility of As_2Te_3 in the Sb_2Te_3 - Bi_2Te_3 alloys may be significantly higher than that previously reported for pure Bi_2Te_3 [27]. The dependence of the lattice constants on the As_2Te_3 concentration is interesting, and may indicate intercalation of As into the gap between Te layers. The measured thermoelectric properties indicate a small enhancement of performance for small As_2Te_3 content, but no further enhancement was seen under applied pressure. It may be interesting to study doped As_2Te_3 containing alloys, or higher As_2Te_3 concentrations in the future. Finally we note that although a correlation is seen between the thermopower and the unit cell volume in these samples, it is not possible to rule out other more indirect relationships between the thermopower and As_2Te_3 content. In particular, the observed variation in thermopower could be caused by subtle changes in dopant/defect chemistry and concentration produced by the addition of As_2Te_3 . Evidence which questions the stability of these solid solutions at room temperature was also noted.

9.4 High-Pressure, High-Temperature Treatment of PbTe

Lead Telluride (PbTe) is a good thermoelectric material. Its crystal structure is recalled in Figure 9.24. This compound and its use in thermoelectric power

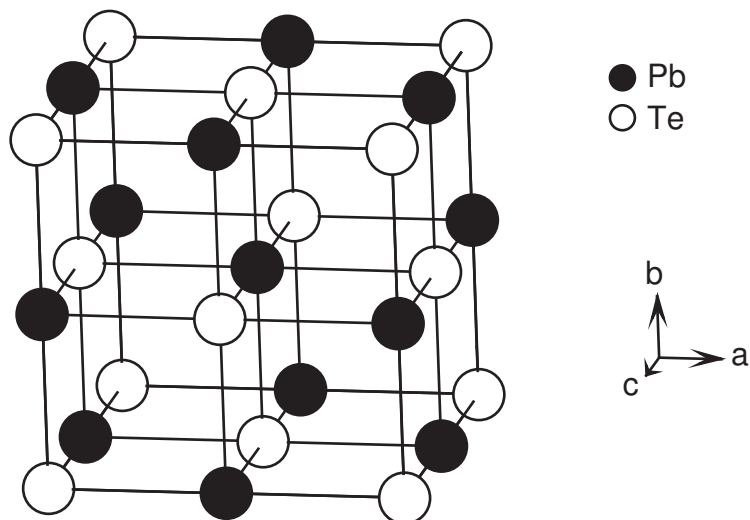


Figure 9.24: The crystal structure of PbTe, which adopts the rocksalt (NaCl) structure type.

generation devices was discussed briefly in Chapter 1. As noted there, recent reviews of the thermoelectric properties of PbTe [30] and its use application to power generation [31] have been published. Although this material has been extensively studied for many years, researcher are still working toward improving the thermoelectric performance of PbTe. As with other thermoelectric materials, considerable work has been devoted to understanding the effects synthetic techniques and of materials processing on the properties of PbTe [32, 33, 34]. Since many devices are made from sintered polycrystalline materials, the effects of the hot-pressing process is of particular relevance.

Recently, a research group in China has reported large improvements in the thermoelectric properties of PbTe which was synthesized under high-pressure high-temperature (HPHT) conditions [35]. In contrast to hot-pressing, in which powdered PbTe is sintered at elevated temperatures (but below the melting point of PbTe which is near 910 °C) under applied pressure, the technique used by this group involved loading Pb and Te powders into a pressure cell and

reacting them under pressure at high temperature to form PbTe. The reactions were carried out at 925 °C, near or just above the melting point of PbTe, at pressures ranging up to about 5 GPa. The thermoelectric properties of the products were then measured at room temperature. The reported resistivity and thermopower of samples produced in this way are reproduced in Figure 9.25. The data at zero pressure represent PbTe made in the conventional way, by melting the elements together in a silica tube and cooling to form a crystalline ingot. The authors report a remarkably strong dependence of ρ on the synthesis pressure, which changed by two orders of magnitude over the pressure range investigated. The thermopower also decreased as the synthesis pressure was increased. Less dependence on synthesis pressure was seen in the thermal conductivity, which increased with increasing pressure, and ranged from about 11–16 mW/cmK, smaller than that reported for cast PbTe (23 mW/cmK) [36]. The result is a significant improvement in ZT , which changed from about 0.04 for the cast sample to 0.87 for the sample made at the highest pressure (5.2 GPa). This result attracted the attention of former DiSalvo group member Dr. Sami Malik, a scientist at Diamond Innovations, Inc. in Columbus, OH. We have been working with Sami toward understanding the effects of HPHT synthesis and treatment of PbTe.

Measurements of thermoelectric properties under applied pressure are common, and results of such measurements on Bi_2Te_3 alloys were discussed earlier in this Chapter. Similar studies have been conducted on PbTe [37, 38, 39, 40]. These results, and X-ray structural studies [41], show evidence for a structural phase transition near 6 GPa. Below this transition, the electrical resistivity was seen to decrease with increasing applied pressure, changing by about two orders of magnitude between 0 and 5 GPa. The thermopower displayed complex behavior, but in general decreased in absolute value as the applied pressure was in-

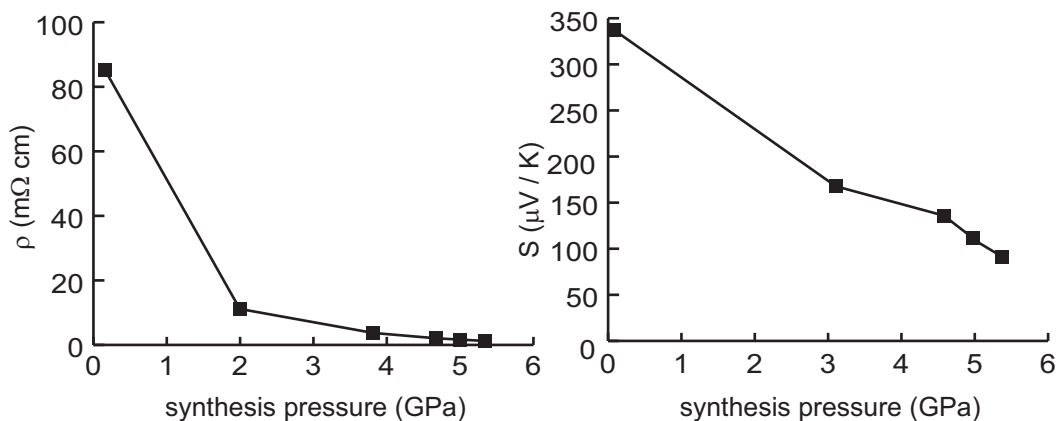


Figure 9.25: Adapted from Zhu et al. [35]. The reported dependence of the electrical resistivity ρ and the thermopower S of PbTe on the pressure applied during the HPHT synthesis.

creased. The authors report the changes to be reversible with respect to pressure, and no residual improvements in the thermoelectric properties were reported.

The ambient pressure thermoelectric properties and doping behavior of conventionally synthesized PbTe have been extensively studied and can be found in the literature [30, 42]. Some relevant information will be summarized here. The PbTe phase diagram is reproduced in Figure 9.26. PbTe can be prepared Pb-rich (n-type, with Te vacancies) or Te-rich (p-type, with Pb vacancies), but the true phase width is not well established as seen by comparison of the two assessments shown in Figure 9.26. The melting composition is reported to be just off stoichiometry, near $\text{PbTe}_{1.003}$ [32]. Due to higher mobilities for electrons than holes, stoichiometric, intrinsic PbTe is expected to be n-type [42]. Materials used for applications are always doped, with halogens which substitute for Te to make n-type PbTe, or with monovalent cations like alkali metals or Ag which substitute for Pb to make p-type PbTe.

In what follows, measured thermoelectric properties of nominally undoped PbTe samples will be reported and discussed. The initial motivation for

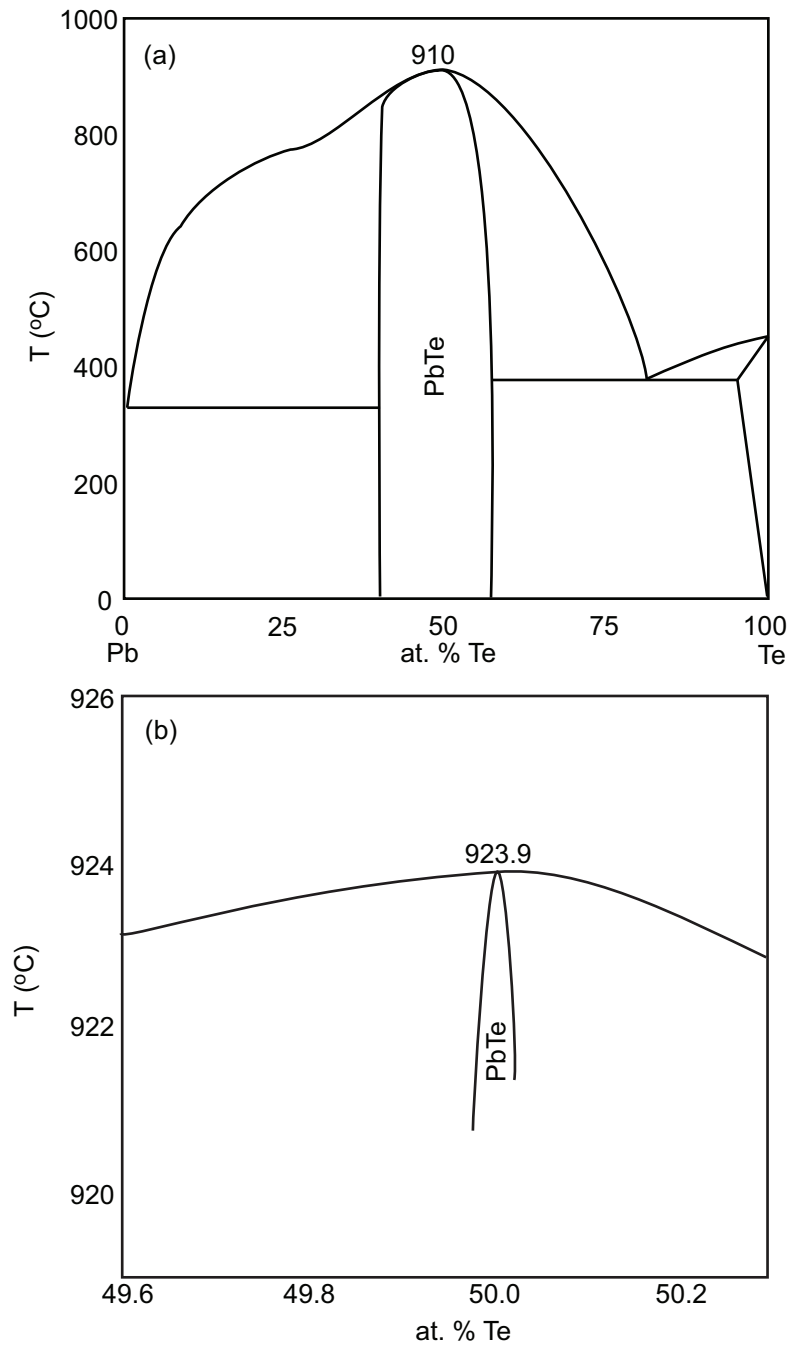


Figure 9.26: (a) The Pb-Te binary phase diagram from Ref. [43]. (b) The Pb-Te phase diagram near the melting point of PbTe from Ref. [44].

this work, as pointed out above, is the reports by Zhu et al. of significant improvements in ZT for samples synthesized at high pressures [35]. Thus, we first compare the properties of samples made by conventional methods to those synthesized using HPHT techniques similar to those used by Zhu et al. We then examine the effects of HPHT treatment of pre-synthesized PbTe samples, which may be relevant to understanding the properties of hot-pressed PbTe thermoelectric materials.

9.4.1 Conventional and HPHT synthesized PbTe

Conventional Synthesis of PbTe

Ingots of PbTe can be made easily by heating a 1:1 molar ratio of the elements above about 920 °C in an evacuated silica tube. The best ingots, which included the fewest and smallest voids, were made by heating at 930 °C for one hour and then cooling to 850 °C over six hours. A rectangular parallelepiped sample was cut from the ingot for properties measurements. The PbTe ingots are fairly hard and quite brittle, making cutting difficult. The best results were obtained by cutting very slowly using a diamond wire saw.

HPHT synthesized PbTe

HPHT synthesis of PbTe was carried out by Dr. Sami Malik at Diamond Innovations, Inc. in a hydraulic press at ~ 5 GPa and ~ 900 °C, starting from Pb and Te powders. The first attempts were made using Ta containers, and PXRD results of the products showed significant amounts of unreacted Pb. Better results were realized by improving the seal on the Ta containers, and PXRD suggested samples prepared in this way were single phase PbTe. X-ray fluorescence (XRF) measurements suggested that a sample made with a 1:1 starting mixture (later re-

ferred to as “HPHT1”) of Pb:Te was Te deficient ($\text{PbTe}_{0.8}$), while a Te rich starting mixture (1:1.32) gave a product (later referred to as “HPHT2”) with 1:1 stoichiometry as measured by XRF. However, the differences between these compositions is close to the $\pm 5\%$ limit for these standardless XRF measurements. PXRD analysis of both of these samples showed only peaks corresponding to PbTe, with no evidence of excess Pb or any other secondary phases.

These 24 mm diameter, 2 mm thick cylindrical samples were cut using wire EDM (electrical discharge machining) into rectangular samples for thermoelectric properties measurements. The sample surfaces were cleaned with SiC paper to remove any contaminants from the EDM process before measurements were performed.

Measured thermoelectric properties

Measurements of thermoelectric properties were performed in the DiSalvo lab using the home built apparatus described elsewhere [1]. Based on measurements of reference materials with similar values of S and κ , and on errors associated with geometrical measurements, the uncertainty in these measurements is estimated to be $\pm 3\%$ for the S , $\pm 5\%$ for ρ , and $\pm 15\%$ for κ .

Copper was plated onto the ends of the samples so that good thermal and electrical contacts could be made using indium metal for the measurement of thermal conductivity, thermopower, and electrical resistivity. The plating solution was made by dissolving CuSO_4 in dilute sulfuric acid (30 g CuSO_4 , 15 ml H_2SO_4 , 250 ml water). A small amount of the solution was added to a small glass vial. The positive electrode of a dc power supply was connected to a coil of copper wire placed in the bottom of the vial. The negative electrode was connected (via an alligator clip) to a pair of stainless steel tweezers. The sample was held in the tweezers and lowered to just touch the surface of the plating solution,

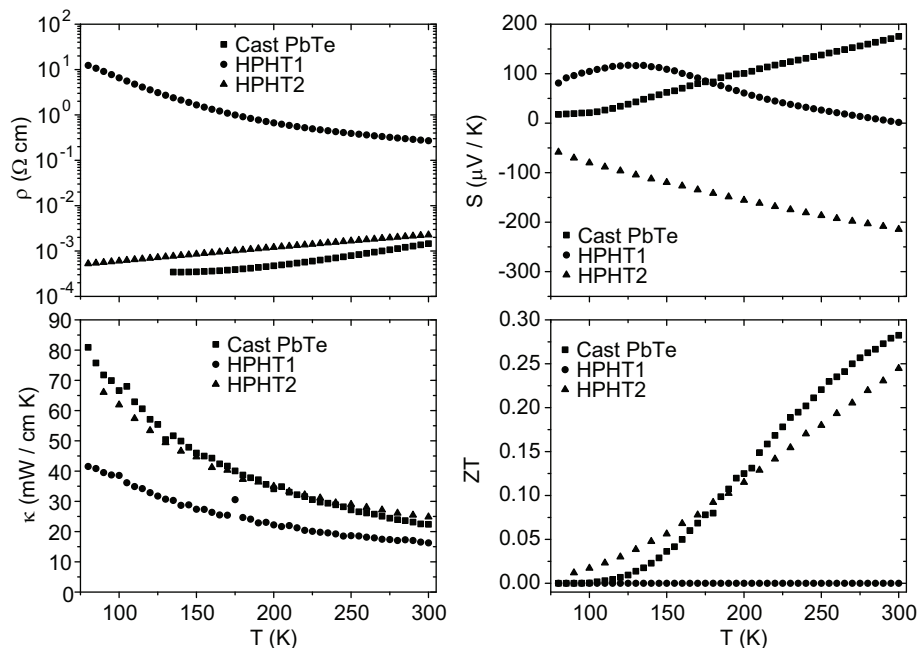


Figure 9.27: The measured electrical resistivity ρ , thermopower S , and thermal conductivity κ of conventionally synthesized PbTe and two samples of HPHT synthesized PbTe. Also shown is $ZT = S^2/\rho\kappa$ calculated from the measured data. Based on measurements of reference materials and on errors associated with geometrical measurements, the uncertainty in these measurements is estimated to be $\pm 3\%$ for the S , $\pm 5\%$ for ρ , and $\pm 15\%$ for κ . These same uncertainty estimates apply to all measurements reported in this Section.

then slightly raised to form a meniscus between the end of the sample and the solution. Plating was carried out at 3–5 V. The current during plating was not carefully monitored, but adjusted by hand to get uniform coverage that was not easily rubbed off. The best results were achieved using a pulsed method, plating for a few seconds, removing the sample from the solution, then repeating. The voltage contacts for the resistivity measurements were made using fine gauge copper wire and silver paste (Dupont Conductor Composition 4922N).

The results of the properties measurements are shown in Figure 9.30. The cast sample (conventionally synthesized PbTe) is p-type with a moderate thermopower at room temperature and resistivity in the range of that often seen for

good thermoelectric materials (about $1 \text{ m}\Omega\text{cm}$). The p-type conduction suggest that the sample may be Te rich. Similar behavior is seen in HPHT2, except it is n-type. HPHT1 behaves completely differently, with lower thermal conductivity, higher resistivity, and lower thermopower above 150 K. The increased resistivity of HPHT1 reduces this samples ZT values dramatically below those of the cast sample and HPHT2.

To gain better insight into the compositions of these samples, electron microprobe analysis was performed. Composition maps, in which less dense regions appear darker and more dense regions appear lighter, are shown for these three samples in Figure 9.28. The results show the cast sample to be essentially single phase, while the HPHT synthesized samples show the presence of at least three phases in significant amounts. Wavelength dispersive compositional analysis showed the light grey matrix to be PbTe, while the medium grey inclusions contained only Pb and Te, but were rich in Te with compositions near "PbTe₃". The dark grey inclusions contained Pb and Te, with more Pb than Te. Oxygen was also detected in the dark regions (Figure 9.28d), which explains why they appear darker than the regions which contain only Pb and Te. The oxygen likely entered through the Pb powder, which when exposed to air would form PbO on the surface. The multiphase nature of the HPHT samples explains the origin of the unusual behavior of their thermoelectric properties noted above. It is not clear why the impurities did not show up in the PXRD patterns. Perhaps the inclusions are too poorly crystalline to produce sharp diffraction peaks. Due to the difficulties with these HPHT synthesized samples, further work on the HPHT treatment of PbTe was carried out using PbTe that had been previously synthesized by conventional methods using clean Pb and Te handled in an argon filled drybox.

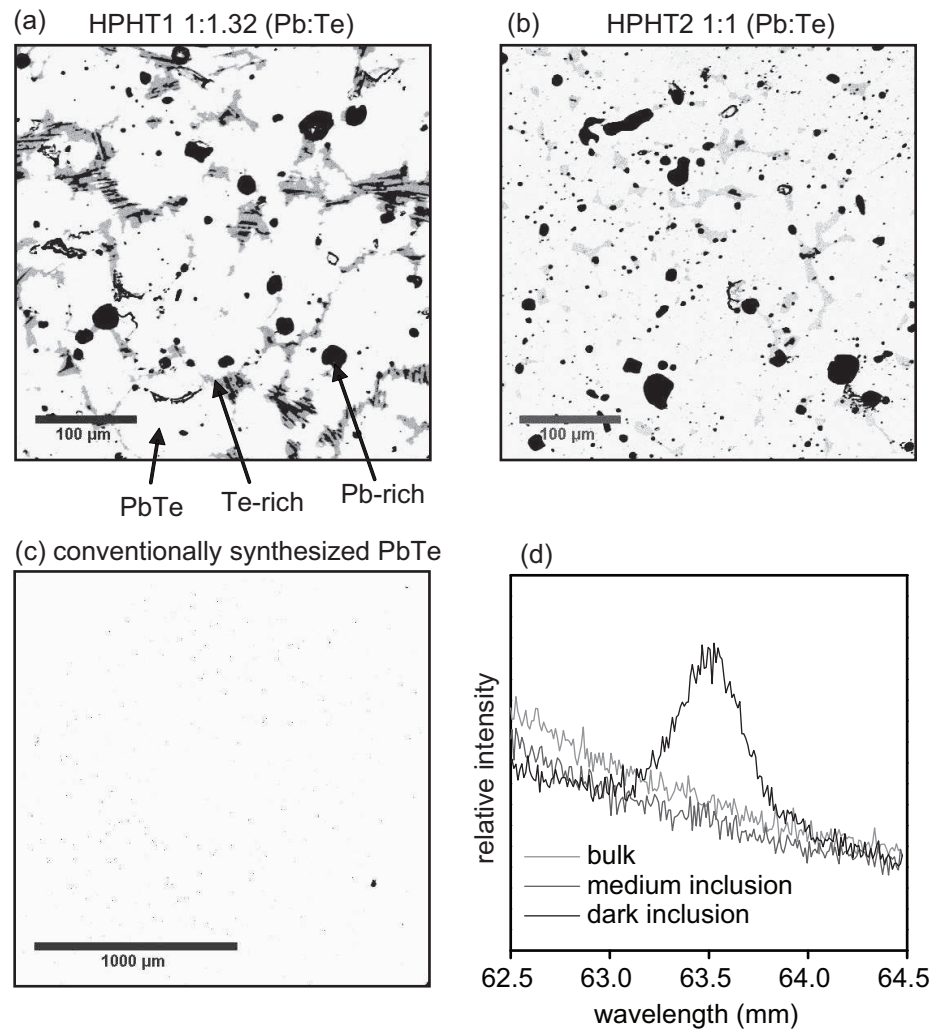


Figure 9.28: Composition maps of PbTe samples from electron microprobe analysis are shown in (a-c). Wavelength dispersive spectra showing the presence of oxygen in the Pb rich inclusions in the HPHT synthesized samples.

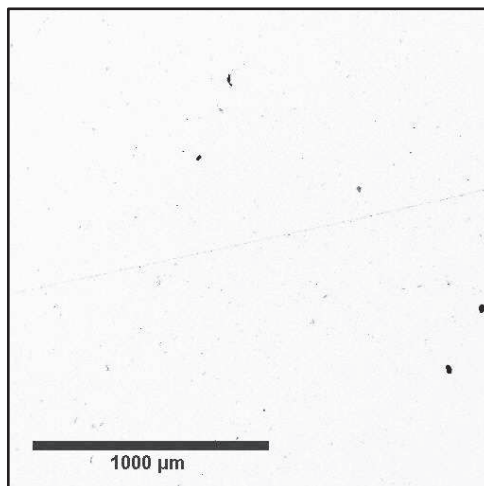


Figure 9.29: Composition map of PbTe samples from electron microprobe analysis showing the nearly single phase nature of the sample.

9.4.2 Effects of HPHT treatment of conventionally synthesized PbTe

Figure 9.29 shows the composition map of a PbTe sample that was made by conventional methods, then given HPHT treatment at ~ 900 °C and ~ 5 GPa. This map looks similar to that obtained from the material before HPHT processing (Figure 9.28c) and shows the sample to be single phase. PXRD showed the presence of no phases other than PbTe.

After HPHT treatment, the sample was cut into several rectangular parallelepiped samples using wire EDM. The thermoelectric properties of two of these pieces are shown in Figure 9.30, along with the data from the cast sample before HPHT treatment for comparison. The HPHT processing had little effect on the measured thermal conductivity, but dramatically changed the thermopower and resistivity. The resistivity increased by over two orders of magnitude, and the temperature dependence changed to display more of an activated type of behavior. HPHT treatment changed the sign of the thermopower, indicating that the

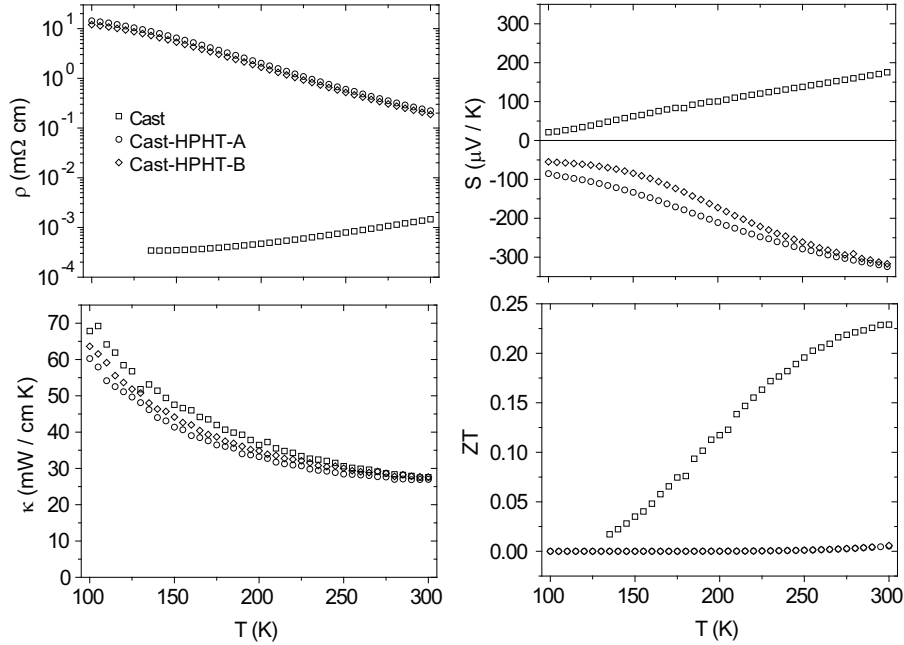


Figure 9.30: The measured electrical resistivity ρ , thermopower S , and thermal conductivity κ after HPHT treatment of conventionally synthesized PbTe. Also shown is $ZT = S^2/\rho\kappa$ calculated from the measured data.

conduction is dominated by electrons in the HPHT processed sample. Due to the large increase in resistivity, the ZT of the HPHT treated material is significantly diminished.

The n-type conduction, larger thermopower, higher resistivity, and activated behavior of the material after HPHT treatment suggest that these samples are closer to intrinsic PbTe than the cast material. We expect that this is due to the “squeezing out” of Pb vacancies (effectively p-type dopants) from the cast material by the HPHT treatment. To test this hypothesis, a HPHT treated sample was annealed for 12 hours at 500 °C, and then again for 12 hours at 600 °C, in an evacuated silica tube after cleaning the surfaces of the pellet with a small file and SiC paper, rinsing it in hexanes, and pumping on it with a vacuum line overnight. The thermoelectric properties of the sample were measured after each anneal. It is expected that annealing should allow vacancies to diffuse back into the bulk.

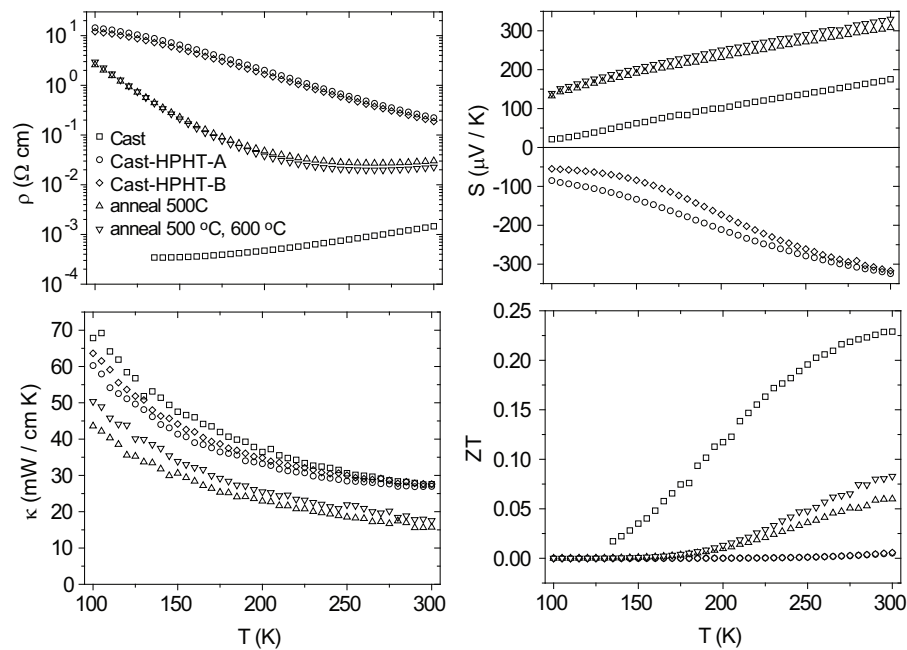


Figure 9.31: The measured electrical resistivity ρ , thermopower S , and thermal conductivity κ after annealing of HPHT treated, conventionally synthesized PbTe. Also shown is $ZT = S^2/\rho\kappa$ calculated from the measured data.

The results of the properties measurements after the annealings are shown in Figure 9.31. Annealing the samples is seen to have decreased the resistivity to values and behavior intermediate between the cast material and HPHT treated samples. After annealing, the thermopower was again positive, but greater than that in the cast sample. These observations indicate that the density of p-type dopants increased during annealing, but not up to the level present in the cast sample. This is consistent with Pb vacancies beginning to diffuse back into the bulk of the material from grain boundaries. The thermal conductivity of the annealed samples is lower than that of the cast sample and the HPHT treated samples.

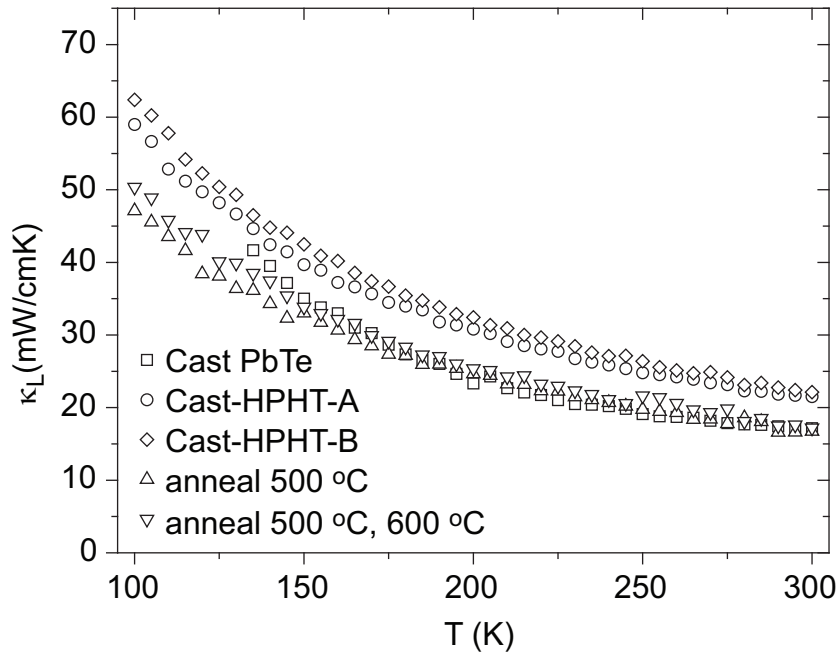


Figure 9.32: The lattice thermal conductivity of PbTe samples as cast, after HPHT treatment, and after subsequent annealing. The electronic contribution was subtracted from the measured total thermal conductivity using the Wiedemann-Franz law [45].

To understand the behavior of the thermal conductivity in this series of measurements, it is instructive to consider only the lattice thermal conductivity by subtracting away the electronic contribution using the Wiedemann-Franz law [45]. The results are shown in Figure 9.32. HPHT treatment clearly increased the lattice thermal conductivity. This is consistent with defects (vacancies) being removed by HPHT processing. Subsequent annealing then decreased the lattice thermal conductivity, consistent with vacancies diffusing back into the material.

9.4.3 Conclusion, comments, and future work with PbTe

The initial goal of this project, to reproduce the ZT enhancements reported in the literature [35], was not realized. However, HPHT tuning of the thermo-

electric properties of PbTe was demonstrated. The effects of HPHT processing on pre-synthesized PbTe presented above are satisfactorily explained by the removal of defects by HPHT treatment, and their reintroduction through annealing. This may prove to be a technologically important observation, since PbTe thermoelectric materials are sometimes prepared by hot-pressing.

We note there that in a continuation of this work, longer annealing times were tried. A sample annealed for five days at 500 °C surprisingly had a negative thermopower. This is not consistent with the explanation given above for the effects of the shorter anneals, and may indicate that impurities had been accidentally introduced into the material. Evidence of the formation of PbTe crystals within the surface of the pellet and on the tube walls during the longer anneal was also observed. This may also indicate the presence of some impurities in the tube which acted as vapor transport agents for the crystals.

Further explorations of the effects of HPHT treatment on PbTe are currently underway. PbTe has been purchased from Aesar and processed using various pressures and temperatures. The effects of these processing parameters through properties measurements and annealing are ongoing. Plans are also in place to study the behavior of HPHT treated doped PbTe samples, including the construction of a device for measuring electrical resistivity and thermopower up to about 550 °C. Construction of this apparatus is underway and testing is expected to begin in the next month. A future group member will continue this work in the coming year.

REFERENCES

- [1] T. K. Reynolds, *Design, Synthesis, and Characterization of New Materials for Thermoelectric Applications*, PhD thesis, Cornell University, 2003.
- [2] R. Diehl and C. D. Carpentier, *Acta Crystallogr. B* **33**, 1399 (1977).
- [3] E. Rost and E. Vestersjo, *Acta Chemica Scandinavica* **22** (1968).
- [4] Y. Adachi et al., *J. Phys. Soc. Japan* **63** (1994).
- [5] M. O'Keeffe and N. Brese, *J. Am. Chem. Soc.* **113**, 3226 (1991).
- [6] D. C. Colgan and A. V. Powell, *J. Mater. Chem.* **7** (1997).
- [7] R. Herbst-Immer and G. M. Sheldrick, *Acta Cryst. B* **54**, 443 (1998).
- [8] S. Parsons, *Acta Cryst. D* **59**, 1995 (2003).
- [9] A. Guinier, *X-Ray Diffraction in Crystals, Imperfect Crystals, and Amorphous Bodies*, W. H. Freeman and Company, 1963.
- [10] D. Yu, C. Wang, B. L. Wehrenberg, and P. Guyot-Sionnest, *Phys. Rev. Lett.* **92**, 216802 (2004).
- [11] N. F. Mott, *J. Non-Cryst. Solids* **1**, 1 (1968).
- [12] J. S. Smart, *Effective Field Theories of Magnetism*, Saunders Company, 1st edition, 1966.
- [13] L. J. de Jongh, ed., *Magnetic Properties of Layered Transition Metal Compounds*, Kluwer Academic Press, 1990.
- [14] J. E. Huheey, *Inorganic Chemistry: Principles of Structure and Reactivity*, Harper and Row, 1st edition, 1972.
- [15] H. Karunadasa, Q. Huang, B. G. Ueland, P. Schiffer, and R. J. Cava, *Phys. Rev. B* **71**, 144414 (2005).
- [16] G. C. Lau, R. S. Freitas, B. G. Ueland, P. Schiffer, and R. J. Cava, *Phys. Rev. B* **72**, 054411 (2005).
- [17] N. P. Ong and R. J. Cava, *Science* **305**, 52 (2004).
- [18] I. S. Hagemann, Q. Huang, X. P. A. Gao, A. P. Ramierz, and R. J. Cava, *Phys. Rev. B* **86**, 894 (2001).
- [19] N. D. Mermin and H. Wagner, *Phys. Rev. Lett.* **17**, 1133 (1966).
- [20] J. M. Kosterlitz and D. J. Thouless, *J. Phys. C* **6**, 1181 (1973).

- [21] N. Rogado et al., *Phys. Rev. B* **65**, 144443 (2002).
- [22] M. Heinrich, H.-A. von Nidda, A. Loidl, N. Rogado, and R. J. Cava, *Phys. Rev. Lett.* **91**, 137601 (2003).
- [23] J. R. G. Ouvrard, R. Brec, *Mater. Res. Bull.* **20**, 1181 (1985).
- [24] P. A. Joy and S. Vasudevan, *Phys. Rev. B* **46**, 5425 (1992).
- [25] D. A. Polvani, J. F. Meng, N. V. C. Shekar, J. Sharp, and J. V. Badding, *Chem. Mater.* **66** (2001).
- [26] N. V. Chandra Shekara, D. A. Polvani, J. F. Meng, and J. V. Badding, *Physica B* **358** (2005).
- [27] E. I. Yarembash and E. S. Vigileva, *Russian J. Inorg. Chem.* **7** (1962).
- [28] A. C. Stergiou and P. J. Rentzeperis, *Z. Kristallogr.* **172** (1985).
- [29] D. A. Polvani, J. F. Meng, M. Hasegawa, and J. V. Badding, *Rev. Sci. Instrum.* **70** (1999).
- [30] Z. H. Dughaish, *Physica B* **322**, 205 (2002).
- [31] J. Yang and T. Caillat, *MRS Bull.* **31**, 224 (2006).
- [32] I. K. Avetisov, A. Y. Mel'kov, A. Y. Zinov'ev, and E. V. Zharikov, *Crystallogr. Rep.* **50**, S124 (2005).
- [33] K. Kishimoto, M. Tsukamoto, and T. Koyanagi, *J. Appl. Phys.* **92**, 5331 (2002).
- [34] K. Kishimoto and T. Koyanagi, *J. Appl. Phys.* **92**, 2544 (2002).
- [35] P. Zhu et al., *Chem. Phys. Lett.* **359**, 89 (2002).
- [36] A. F. Ioffe, *Can. J. Phys.* **34**, 1342 (1956).
- [37] V. V. Shchennikov, S. V. Ovsyannikov, and A. Y. Derevskov, *Phys. Solid State* **44**, 1845 (2002).
- [38] S. V. Ovsyannikov, V. V. Shchennikov, S. V. Popova, and A. Y. Derevskov, *Phys. Stat. Sol. B* **235**, 521 (2003).
- [39] S. V. Ovsyannikov and V. V. Shchennikov, *Phys. Stat. Sol. B* **241**, 3231 (2004).
- [40] S. V. Ovsyannikov and V. V. Shchennikov, *Physica B* **344**, 190 (2004).
- [41] G. Rousse et al., *Phys. Rev. B* **71**, 224116 (2005).
- [42] R. Heikes and R. Ure Jr., *Thermoelectricity: Science and Engineering*, Interscience Publishers Inc., 1st edition, 1961.

- [43] W. Lugscheider, H. Ebel, and G. Langer, *Z. Metallkunde* **56**, 851 (1965).
- [44] E. Miller, K. Komarek, and I. Cadoff, *Trans. Am. Inst. of Mining, Metallurgical and Petroleum Engineers* **215**, 882 (1959).
- [45] N. Ashcroft and N. Mermin, *Solid State Physics*, Holt, Rinehart and Winston, 1976.

Chapter 10

Conclusions and Outlook for TE Materials

Research

The work in this Dissertation did not produce any advanced thermoelectric materials; however, many new compounds were discovered and characterized. Although high ZT values were not measured for any of these materials, some displayed interesting structural, electrical, and magnetic properties. That is a nice side effect of this type of research. Although good thermoelectric materials are what we hope to find, bad thermoelectric materials can have other fascinating properties, and any new compound holds promise for exciting chemistry and physics.

As demonstrated by the Tl compounds reported here, low lattice thermal conductivity is easily achieved with heavy elements. Values less than about 1/2 that of Bi_2Te_3 alloys were demonstrated. If this could be achieved along with the thermopower and electrical resistivity of optimized Bi_2Te_3 alloys, this would lead to materials with $ZT = 2-3$. The greatest difficulty lies in achieving high S and low ρ in the same material at the same doping level. This depends directly on the electronic structure of the material, which of course can not be determined without knowing the crystal structure. Since all but the simplest crystal structures cannot be predicted, the materials must be made and their structures determined experimentally. Only then can their suitability as a thermoelectric material be determined. This is the rate limiting step in the quest for high ZT . The field needs more talented makers and measurers of materials, to increase the rate at which new compounds are screened. However, the possible compositions of new complex materials is practically limitless, and search must be guided by theoretical

understanding. I believe that this type of research will produce bulk materials with high ZT, and that it will be the prepared searchers, the ones who know where to look and are able to identify promising materials, who will find them.

I will conclude by noting two of the most exciting recent developments in thermoelectrics materials research, and how they might guide further efforts. The first is Na_xCoO_2 (see Chapter 2). This compound has metallic resistivity with high S (about 10 times that of most metals). As pointed out in Chapter 2, it is thought that the high S could be attributed to spin entropy carried by holes as they hop from Co^{3+} to Co^{4+} . Could other systems be found with this type of enhanced thermopower? Perhaps rare earth compounds, which can have large moments and therefore large hopping entropy, could have even higher S than Na_xCoO_2 . Rare earth compounds with geometrically frustrated structures (to prevent ordering of the moments and loss of hopping entropy) should be investigated. Could a compound like KSmSe_2 be doped with Ba to realize hopping between Sm^{2+} ($J = 0$) and Sm^{3+} ($J = 5/2$)?

The second recent interesting development, in my opinion, is the discovery of good thermoelectric behavior in Zintl phases. This was pointed out during the discussion of Chevrel phase thermoelectrics in Chapter 6. Zintl phases are a fascinating class of materials with structural properties that could lead to enhanced thermoelectric performance. Conventional Zintl phases combine electropositive elements A (like alkali metals, alkaline earths, or rare earths) with one or more early p-block elements B. In more exotic Zintl phases B can also be a transition metal. Their structures are composed of covalently bonded frameworks (or sometimes clusters) of B atoms surrounding isolated A atoms, giving them the structural features needed for “rattling”. Simple, but powerful, electron counting rules can be used to understand the electronic structure and bonding in these materials. The donation of electrons from the electropositive elements

A results in unusual oxidation states for B. To satisfy their needs for filled octets the B atoms form bonds with one another, producing the covalent framework. The number of electrons donated by A and the number of valence electrons of B determine the connectivity in the B network, and thus control the adopted crystal structure. This simplified view of bonding in Zintl phases is surprisingly powerful. Zintl systems include remarkably diverse compositions and structure types, in which the relationships between crystal structure and physical properties can be explored and understood, starting from this simple model of bonding.

Although some Zintl phases behave like semimetals, the closed shell nature of the B framework often results in semiconducting compounds with small band gaps between bonding and antibonding states. Since both the valence band and conduction band arise primarily from the covalent B framework and not the isolated A atoms, appropriate doping of these materials should produce mobile holes or electrons. In addition, aleovalent substitutions on the A sites represents an ideal doping strategy for Zintl phases. The substitutions should only affect the number of electrons donated to the B framework and have minimal influence on the mobility of the carriers. These compounds also often adopt complex structures with large unit cells which lead to low lattice thermal conductivities. Finally, the sharp peaks in the density of states associated with the incorporation of rare earth elements and transition metals into these materials can lead to enhanced TE performance.

It is clear then that Zintl phase systems are likely to produce semiconducting compounds with the structural and electronic features needed for good TE materials, and at the same time provide a means for effective doping. They also tend to have high melting points, giving them good thermal stability. These properties suggest to me that Zintl compounds are an ideal class of materials for efficient TE waste heat recovery.